The Characterisation of Velocity Amplified Vibration Energy Harvesters

UNIVERSITY of LIMERICK

OLLSCOIL LUIMNIGH

Declan O'Donoghue, B. Eng (Hons)

CONNECT, Stokes Laboratories

School of Engineering

Faculty of Science & Engineering

University of Limerick

Supervisors

Dr. Jeff Punch & Dr. Ronan Frizzell

Submitted to the University of Limerick for the degree of

Doctor of Philosophy (PhD)

January 2017

Declaration

The substance of this thesis is the original work of the author, and due reference and acknowledgement has been made, where necessary, to the work of others. No part of this thesis has been submitted in candidature for any degree.

Declan O'Donoghue (Candidate)

Dr. Jeff Punch (Co-Supervisor)

Dr. Ronan Frizzell (Co-Supervisor)

This thesis was defended on January 5th, 2017.

Examination committee

External examiner	Dr. Steve Burrow	University of Bristol
Internal examiner	Dr. David Corcoran	University of Limerick

Abstract

Vibration energy harvesters (VEHs) scavenge ambient vibrational energy, offering an alternative to batteries for the autonomous operation of low power electronics. VEHs are typically spring-mass-dampers that extract mechanical energy from a vibrating source, converting it into useful electrical energy. A number of transduction mechanisms can be utilised, with electromagnetic induction of interest herein. Velocity amplification, a technique used to increase velocity through impacts, is employed in this thesis to improve the power output and operational bandwidth of multiple-degree-of-freedom (multi-DoF) piecewise linear (PWL) VEHs, compared to linear resonators. Such a harvester is referred to as a velocity amplified electromagnetic generator (VAEG), with a gain in power achieved by increasing the relative velocity between the magnet and coil in the transducer.

In this thesis, VAEGs were investigated numerically and experimentally under sinusoidal excitation, for a range of parameters. An analysis of the influence of mass configuration on multi-DoF VAEGs was undertaken. It was determined that under forced excitation, contrary to velocity amplification theory, 2-DoF configurations achieve higher RMS velocities and, hence, voltages than systems with greater numbers of DoFs. With increasing mass ratio, despite the RMS velocity increasing, the RMS voltage actually decreases, as the increase in velocity does not compensate for the reduction in transducer size.

A 2-DoF VAEG with a mass ratio of $R = 3$ was selected for in-depth investigation. The harvester was characterised with frequency sweeps for a range of base acceleration levels and gap lengths—a key geometric parameter. A shift in peak output power towards lower frequencies is observed with increasing gap, due to the decreasing effective stiffness, while RMS velocity also increases. The acceleration level required to achieve large amplitude oscillations increases with gap, however. An optimisation of the 2-DoF VAEG is presented, resulting in the prediction of a relatively high volume figure of merit ($FoM_V = 2.83\%$) at high accelerations (10 m/s^2) and low frequencies (16.4 Hz).

It is demonstrated that the hysteresis behaviour and dependence of RMS response on initial conditions associated with non-linear VEHs is not present in the VAEGs herein. Consequently, the frequency responses presented are independent of initial conditions, which is significant for the applicability of VAEGs.

To determine the influence of scale on the harvester response, the 2-DoF VAEG was fabricated at three length scales ($s = Volume^{1/3}$), with the electrical and mechanical systems considered separately—a number of deviations from linear scaling methodologies were required to achieve this. It was determined that the gap does not scale, while the load power is predicted to scale as $P_L \propto s^{5.51}$, suggesting that achieving high power densities in a VAEG at low device volumes is extremely challenging.

VAEG configurations with 2-DoFs and low mass ratios demonstrate the highest power densities, while the optimal gap is dependent on the excitation conditions and increases with increasing acceleration amplitude, at the optimal frequency. VAEGs are found to be most suitable for applications with high acceleration levels and low frequencies, where high power densities can be achieved.

Acknowledgements

I would like to express my sincerest gratitude to my co-supervisors Dr. Jeff Punch and Dr. Ronan Frizzell, for their guidance and encouragement in carrying out this project.

I am grateful to all at Bell Labs for being so welcoming and helpful during my stay, particularly Ger Kelly, Kevin Nolan and Ollie Burns.

Thanks to the Irish Research council and CONNECT for their financial support of this work.

To all of the students and staff at Stokes Laboratories and further afield in UL, thank you for making the last three years so enjoyable (mostly). Special mentions include: my Italian colleagues, Valeria and Betta—for the much needed culture they brought to the Energy Harvesting Department; Paddy O'Regan and Fionnuala O'Connell—for being so helpful and supportive of my work; the guys in The Glen—for teaching me that being wrong is rarely a reason to concede an argument; and to Hil-dog—for being my wine-buddy!

Finally, thanks to my family for encouraging and supporting me in all my pursuits, be they educational or otherwise.

Contents

List of Tables xi

List of Figures xiii

Nomenclature xxi

1 Introduction 1

1.1 Motivation . . . 1
1.2 Energy conversion . . . 3
1.2.1 Electromagnetic transduction . . . 4
1.2.2 Piezoelectric transduction . . . 4
1.2.3 Electrostatic transduction . . . 5
1.2.4 Power processing circuitry . . . 6
1.3 Single-DoF Linear energy harvesters . . . 6
1.4 Broadband energy harvesting methods . . . 8
1.4.1 Frequency tuning methods . . . 9
1.4.2 Multi-modal methods . . . 11
1.4.3 Non-linear methods . . . 13
1.5 Comparison of VEHs from the literature . . . 19
1.6 Objectives of this work . . . 22
1.7 Thesis compendium . . . 23

2 Theory 25

2.1 Linear inertial oscillator . . . 25
2.2 Electrical system . . . 30
2.2.1 Electromagnetic induction . . . 30

2.2.2 Modelling the transduction factor . . . 33
2.2.3 Electrical circuit representation . . . 34
2.2.4 Coupled model . . . 35
2.3 Velocity amplification . . . 36
2.4 Closure . . . 40

3 Experimentation and methods 43
3.1 Drop-test . . . 43
3.1.1 Drop-testing apparatus . . . 44
3.1.2 Image processing . . . 45
3.2 Forced excitation . . . 47
3.3 Uncertainty analysis . . . 50
3.3.1 Experimental uncertainty . . . 51
3.3.2 Power measurement . . . 52
3.3.3 High-speed imaging—velocity measurement . . . 52
3.3.4 LDV—velocity measurement . . . 53
3.3.5 Accelerometer—acceleration measurement . . . 54
3.4 Closure . . . 54

4 Non-linear analysis of piecewise linear harvesters 55
4.1 Single-DoF PWL harvesters . . . 55
4.1.1 Single-DoF PWL harvester in phase space . . . 56
4.1.2 Single-DoF PWL harvester sweep analysis . . . 60
4.2 Velocity amplified multi-DoF PWL harvesters . . . 75
4.2.1 Multi-DoF PWL harvesters in phase space . . . 76
4.2.2 Sweep analysis of velocity amplified multi-DoF PWL harvesters . . . 79
4.3 Closure . . . 95

5 Influence of mass configuration on multi-DoF VAEGs 101
5.1 Multi-DoF VAEG design . . . 101
5.2 Drop-test . . . 104
5.3 Forced excitation . . . 106
5.3.1 Fixed transducer size . . . 107

5.3.2 Proportional transducer scaling . . . 113
5.4 Closure . . . 115

6 Optimisation and characterisation of a 2-DoF VAEG 117
6.1 2-DoF VAEG design . . . 118
6.2 Transducer design and optimisation . . . 122
6.2.1 Transducer configurations . . . 122
6.2.2 Transducer optimisation . . . 126
6.3 Characterisation sweeps . . . 134
6.4 Performance metrics . . . 144
6.5 Closure . . . 146

7 Scaling of a 2-DoF VAEG 149
7.1 Scaling theory . . . 150
7.1.1 Scaling of a linear electromagnetic harvester . . . 150
7.1.2 Mechanical damping scaling . . . 151
7.2 Scaling of a 2-DoF VAEG . . . 153
7.2.1 Influence of scaling on energy conversion in a VAEG . . . 154
7.2.2 Influence of scale on mechanical damping in a VAEG . . . 164
7.3 Closure . . . 166

8 Conclusions and recommendations 169
8.1 Conclusions . . . 169
8.2 Recommendations for future work . . . 174

References 177

Appendix A: Publications 195

List of Tables

1.1 Summary of electromagnetic VEHs reported in the literature. . . 21

4.1 Model parameters used in single-DoF PWL harvester frequency sweeps. 63
4.2 Model parameters used in multi-DoF PWL harvester sweeps. . . . 80
4.3 RMS velocities from time traces in figure 4.20. 91

5.1 Proof mass of each VAEG configuration; note: $m_1 = 80$ g. 102

6.1 Model parameters used in optimisation tests. 129
6.2 Model parameters used in forward-frequency sweeps. 137
6.3 Comparison of peak power and corresponding RMS absolute velocity and frequency in experimental and simulation frequency sweeps, for $Acc = 10$ m/s^2. 138
6.4 Highest NPD and FoM_V for $d_{mag} = 8$ mm, air-gap $= 2.6$ mm. . . 145
6.5 Highest NPD and FoM_V for $d_{mag} = 12$ mm predicted from simulation sweeps—coil wound directly around the Teflon tube, air-gap $= 1.8$ mm. 146

7.1 Scaling relationships employed in the simulation scaling analysis of a 2-DoF VAEG. 159

List of Figures

1.1 Acceleration power spectral densities (PSD) of real vibration sources (NiPS, 2012); (a) car engine, (b) train floor, (c) lathe, and (d) bridge. 3
1.2 Schematics of linear inertial energy harvesters; (a) cantilever beam spring with piezoelectric strip, and (b) helical spring with inductive transducer. 7
1.3 Schematics of tuning mechanisms: (a) mechanical tuning of a simply supported beam by application of a compressive axial load, (b) magnetic tuning using the attractive force between magnets. . . . 10
1.4 Schematics of multi-modal energy harvesters: (a) cantilever array (plan-view), (b) 2-DoF cantilever (side-view), (c) 2-DoF inverted (plan-view), and (d) L-shaped (side-view). 11
1.5 (a) Potential function and (b) restoring force for linear, softening, hardening, and bistable behaviour in a Duffing-type oscillator. . . 13
1.6 Schematics of different Duffing-type oscillators with adjustable nonlinear stiffness, capable of monostable and bistable operation—(a,b,c) piezoelectric and (d,e) inductive. 14
1.7 Potential function of a bistable Duffing-type oscillator, showing potential barriers of deep (——) and shallow (- - - -) double potential wells. 16
1.8 (a) Inductive PWL oscillator, with a one-sided stopper, and (b) its force-displacement diagram showing bilinear stiffness. 18

2.1 Lumped parameter model of linear inertial electromagnetic energy harvester. 26

LIST OF FIGURES

2.2 Normalised power as a function of frequency ratio ω/ω_n for a range damping ratios. 28

2.3 (a) Magnetic flux through a single coil loop of radius r_m and length l_w—the coil is moving at velocity $\dot{z}$ relative to the magnet, through the non-uniform magnetic field B; (b) wire loop moved from z_1 to z_2—A_l is the cylindrical lateral area which results from the coil movement. 32

2.4 (a) Magnetic flux density of a cylindrical permanent magnet with flux lines (right half only shown)—white rectangle represents coil at zero-position, (b) radial flux B_r along the axial direction at a range of radial distances from the surface of the magnet—average radial flux over coil radial thickness shown as dashed black line, and (c) transduction factor K for varying coil positions relative to the magnet. This process is implemented in chapters 4, 6, and 7. . 34

2.5 (a) Electrical circuit representation of an electromagnetic generator, and (b) multi-turn coil showing the geometric properties of the coil. 35

2.6 System of sequentially smaller vertically stacked impacting masses. The velocity of a mass before an impact is v, while the velocity after is V. 37

2.7 Velocity gain as a function of the number of masses and the mass ratio for $e = 1$. 39

3.1 Drop-testing mechanism developed to achieve sequential pair-wise collisions between masses, in open position (masses released). . . . 44

3.2 Schematic of high-speed imaging set-up. 45

3.3 (a) High contrast raw image captured by high-speed camera. (b) Filtered grey-scale image from pixel intensity 0–1 (black–white) with individual masses isolated. (c) Gradient of pixel intensity across cross-section of mass in consecutive images. (d) Cross-correlation of gradients and fitted Gaussian model. 46

3.4 Velocity profile of drop-test for 4-DoF configuration showing initial free-fall followed by sequential pair-wise collisions. 47

3.5 Schematic of the experimental set-up used in forced excitation tests for voltage measurements—LabVIEW used as shaker controller. . 48
3.6 Accelerometer time-trace from shaker demonstrating an approximately sinusoidal profile with a VAEG in operation. 50
3.7 Schematic of the experimental set-up used in forced excitation tests for voltage and velocity measurements—Dactron Comet shaker control system employed. 50
3.8 Photograph of the experimental set-up used in forced excitation tests for voltage and velocity measurements. 51

4.1 (a) Schematic of a single-DoF PWL oscillator and (b) its force-displacement relationship. 57
4.2 (a) Linearly extended phase space and (b) phase-plane; solution trajectory plotted for periodic orbit crossing switching surfaces S^{-1} and S^{+1}. 59
4.3 (a) Experimental and (b) simulation load voltage and absolute velocity-time histories for bidirectional frequency sweeps—Acc = 7 m/s^2, $g_0 = 6.7$ mm; arrow denotes sweep direction. 61
4.4 Comparison of experimental (——) and simulation (- - - -) (a) load voltage and (b) absolute velocity-time traces—$Acc = 7$ m/s^2, $f = 12.5$ Hz, $g_0 = 6.7$ mm. 62
4.5 Continuously and periodically sampled voltage-time histories for (a) frequency forward-sweep and (b) reverse-sweep. (c) Voltage-time trace at 32 Hz, and (d) corresponding phase portrait and Poincaré map, with switching surface S^{-1}—$Acc = 0.5$ m/s^2, g_0 = 2 mm; arrow denotes sweep direction. 65
4.6 Continuously and periodically sampled voltage-time histories for (a) frequency forward-sweep and (b) reverse-sweep. (c) Voltage-time trace at 25 Hz, and (d) corresponding phase portrait and Poincaré map, with switching surfaces S^{-1} and S^{+1}—$Acc = 3$ m/s^2, $g_0 = 2$ mm; arrow denotes sweep direction. 66

4.7 Continuously and periodically sampled voltage-time histories for (a) frequency forward-sweep and (b) reverse-sweep; voltage-time trace at (c) 28 Hz, and (e) 12 Hz; (d,f) corresponding phase portrait and Poincaré map, with switching surfaces S^{-1} and S^{+1}—Acc = 10 m/s^2, $g_0 = 2$ mm; arrow denotes sweep direction. 68
4.8 Continuously and periodically sampled voltage-time histories for (left column) frequency forward-sweeps and (right column) reverse-sweeps—$Acc = 10$ m/s^2; (a,b) $g_0 = 0.5$ mm, (c,d) $g_0 = 3$ mm, and (e,f) $g_0 = 10$ mm; arrow denotes sweep direction. 70
4.9 Continuously and periodically sampled voltage-time histories for (a,c) acceleration forward-sweeps and (b,d) reverse-sweeps—g_0 = 2 mm, (a,b) $f = 15$ Hz and (c,d) $f = 24$ Hz; arrow denotes sweep direction. 71
4.10 Continuously and periodically sampled voltage-time histories for (a) gap forward-sweep (increasing g_0) and (b) reverse-sweep (decreasing g_0)—$Acc = 10$ m/s^2, $f = 24$ Hz. 71
4.11 Amplitude of voltage response as a function of frequency for a single-DoF linear harvester. 72
4.12 Schematic of a 2-DoF PWL harvester; (a) m_1 and m_2 at positions $z_1 = 0$ and $z_2 = 0$, respectively, with springs and dampers; (b) displaced masses detached from springs, showing base ($y(t)$), absolute ($x_{1,2}$), and relative ($z_{1,2}$) displacement. 76
4.13 Continuously and periodically sampled voltage-time histories for (left column) frequency forward-sweeps and (right column) reverse-sweeps—(a–d) $g_0 = 0$ mm, (e–h) $g_0 = 3$ mm; (a,b,e,f) Acc = 5 m/s^2, (c,d,g,h) $Acc = 10$ m/s^2; mass ratio $R = 5$; arrow denotes sweep direction. 81
4.14 2-DoF PWL periodic response: (a) phase space (z_1, z_2) solution trajectory with switching surfaces S^{-1}, S^{+1}, and S^{+2}, (b) velocity-time history $\dot{z}_1$ and $\dot{z}_2$, (c) phase diagram of m_1 and m_2, with Poincaré maps—$Acc = 5$ m/s^2, $f = 30$ Hz, $g_0 = 0$ mm, $R = 5$. . . 83

4.15 2-DoF PWL chaotic response: (a) phase space (z_1, z_2) solution trajectory with switching surfaces S^{-1}, S^{+1}, and S^{+2}, (b) velocity-time history $\dot{z}_1$ and $\dot{z}_2$, (c) phase diagram of m_1 and m_2, with Poincaré maps—$Acc = 10$ m/s^2, $f = 18$ Hz, $g_0 = 3$ mm, $R = 5$. . . 85
4.16 Continuously and periodically sampled voltage-time histories for frequency forward-sweeps—(a) $g_0 = -0.5$ mm, (b) $g_0 = 0.5$ mm, (c) $g_0 = 2$ mm, (d) $g_0 = 10$ mm; $Acc = 10$ m/s^2, mass ratio $R = 5$. 86
4.17 Continuously and periodically sampled voltage-time histories for frequency forward-sweep for (a) $R = 3$, (b) $R = 5$, (c) $R = 10$, (d) $R = 20$—$Acc = 10$ m/s^2, $g_0 = 3$ mm. 87
4.18 2-DoF PWL velocity-time history and power spectrum for (a,b) $R = 5$ and (c,d) $R = 20$—$Acc = 10$ m/s^2, $f = 20$ Hz, and $g_0 = 3$ mm. 88
4.19 Continuously and periodically sampled voltage-time histories for frequency forward-sweep for (a,b) 2-DoF, (c,d) 3-DoF, and (e,f) 4-DoF; (a,c,e) $R = 5$ and (b,d,f) $R = 20$—$Acc = 10$ m/s^2, $g_0 = 3$ mm. 89
4.20 Velocity-time histories of each of the masses in the (a) 2-DoF, (b) 3-DoF, and (c) 4-DoF stacked mass systems—$R = 20$, $Acc = 10$ m/s^2, $g_0 = 3$ mm, and $f = 20$ Hz. 90
4.21 Amplitude of voltage response as a function of frequency for a 2-DoF linear energy harvester—mass ratio $R = 3$. 92
4.22 RMS velocity of m_2 as a function of time, for a range of initial conditions—$f = 22$ Hz, $Acc = 10$ m/s^2, $g_0 = 3$ mm. 94

5.1 Schematic representation of 2-, 3- and 4-DoF configurations for $R = 10$—without transducer. 102
5.2 Model of the 3-DoF $R = 5$ VAEG—with transducer present. . . . 103
5.3 Experimental velocity gain from drop-tests for a range of mass configurations compared to theory with $e = 0.97$. 106
5.4 VAEG (a) RMS load voltage and (b) RMS velocity of the final mass for fixed transducer size under sinusoidal excitation—$Acc = 1$ g, $R_L = 425\ \Omega$. 111

5.5 Velocity traces of each mass and corresponding power spectra for (a,b) the 2-DoF $R = 5$ system, and (c,d) the 4-DoF $R = 10$ system—$Acc = 1$ g. 112
5.6 VAEG (a) RMS load voltage and (b) voltage normalised by proof mass for proportional transducer scaling under sinusoidal excitation—$Acc = 1$ g, $R_L = 425\ \Omega$. 114

6.1 (a) Model of $d_{mag} = 8$ mm scale harvester and support structure, (b) tube inner structure showing active components, (c) plan view of inertial masses showing ridged edge design, and (d) cross section of the left half of the coil-magnet arrangement. 119
6.2 Photograph of the $d_{mag} = 8$ mm 2-DoF VAEG. 120
6.3 Cross sections of the three magnet configurations (Magnet I, II, III), each with two coil arrangements (Coil I—top row; Coil II—bottom row). 123
6.4 Flux distribution and density for the right half of the three magnet configurations. The coil locations implemented to find K in figure 6.5 are shown as white boxes (Coil I—solid box, Coil II—dashed and solid box). 124
6.5 Left column: average radial flux density $\bar{B}_r$ over coil radial thickness for the three magnet configurations, Magnet I, II and III. Right column: electromagnetic transduction factor K for the two coil arrangements, Coil I and II, for each magnet configuration—$d_{mag} = 12$ mm, $h_{mag} = 19.2$ mm, $ct_{rad} = 5$ mm, $ct_{ax} = (2/3)h_{pitch}$ ($h_{pitch} = h_{mag} + h_{pole}$), and air-gap = 1.2 mm. 125
6.6 Electromagnetic transduction factor as a function of magnet-pole height ratio. Magnet stack height is constant. 127
6.7 Power generated as a function of coil axial thickness ct_{ax} and coil radial thickness ct_{rad} for each of the magnet-coil configurations. Results from numerical simulation of $d_{mag} = 12$ mm system. . . . 130
6.8 Power density as a function of coil axial thickness ct_{ax} and coil radial thickness ct_{rad} for each of the magnet-coil configurations. Results from numerical simulation of $d_{mag} = 12$ mm system. . . . 131

6.9 (a) Power and (b) normalised power density as a function of coil axial thickness ct_{ax} and coil radial thickness ct_{rad} for $d_{mag} = 12$ mm—magnet-coil configuration: Magnet II - Coil II, air-gap = 3.9 mm. 133
6.10 Experimental forward (——) and reverse (- - -) frequency sweeps showing load power for a range of acceleration levels; $g_0 = 2.2$ mm. Results from experimental testing of $d_{mag} = 8$ mm system. 135
6.11 Sample load resistance sweep—$Acc = 4$ m/s^2, $g_0 = 0.8$ mm, $f = 24$ Hz. Results from experimental testing of $d_{mag} = 8$ mm system. 136
6.12 Experimental power (left column (a), (c), (e)) and simulated power (right column (b), (d), (f)) versus frequency forward-sweeps—$Acc = 2$–10 m/s^2, $g_0 = -0.2,\ 0.8,\ 2.5$ mm. Results from $d_{mag} = 8$ mm system. 139
6.13 Experimental power (left column (a), (c), (e)) and simulated power (right column (b), (d), (f)) versus frequency forward-sweeps—$Acc = 2$–10 m/s^2, $g_0 = 5.5,\ 10.5,\ 18.5$ mm. Results from $d_{mag} = 8$ mm system. 140
6.14 Experimental (left column (a), (c), (e)) and simulated absolute velocity (right column (b), (d), (f)) versus frequency forward-sweeps—$Acc = 2$–10 m/s^2, $g_0 = -0.2,\ 0.8,\ 2.5$ mm. Results from $d_{mag} = 8$ mm system. 141
6.15 Experimental (left column (a), (c), (e)) and simulated absolute velocity (right column (b), (d), (f)) versus frequency forward-sweeps—$Acc = 2$–10 m/s^2, $g_0 = 5.5,\ 10.5,\ 18.5$ mm. Results from $d_{mag} = 8$ mm system. 142
6.16 Voltage-time trace for (a) $g_0 = -0.2$ mm and (b) $g_0 = 10.5$ mm at $Acc = 10$ m/s^2. Results from experimental testing of $d_{mag} = 8$ mm system. 144

7.1 Normalised power as a function of length scale showing asymptotic scaling relationships $P_L \propto s^5$ and $P_L \propto s^7$, for linear inertial energy harvesters. 152
7.2 Schematic showing the cross section of a 2-DoF VAEG at scales s_1 and s_2, with the dimensional scaling relationships. 156

7.3 (a) Peak electromagnetic transduction factor K and (b) coil resistance R_C as a function of length scale s for scaled wire diameter ($d_w \propto s$ - - -) and constant wire diameter ($d_w = const.$ ——). . . . 158
7.4 Absolute (- - - -) and relative (——) RMS velocity of m_2 for simulation forward frequency sweeps at a range of gaps—$Acc = 10$ m/s^2, $R = 3$, $s \approx 19$ mm. 161
7.5 Experimental and simulation effective transduction factor, K_{eff}, as a function of length scale, for a range of g_0; (a) $Acc = 10$ m/s^2 and (b) $Acc = 6$ m/s^2. Experimental results from $d_{mag} = 6$, 8, and 12 mm systems. The main graphs are plotted on logarithmic scales, while the embedded graph are plotted on linear scales. . . 162
7.6 Simulation frequency forward-sweeps showing RMS velocity of magnet stack for a range of length scales; (a) $c_m \propto s^3$, (b) $c_m \propto s^2$, and (c) $c_m \propto s$—$Acc = 10$ m/s^2, $g_0 = 2.2$ mm. 166

Nomenclature

Symbol	Description	Unit
Roman		
A	area within coil loop	m^2
A_l	lateral cylindrical area	m^2
A_w	coil wire cross sectional area	m^2
Acc	base acceleration amplitude	m/s^2
B	normal magnetic flux density	T
B_r	radial magnetic flux density	T
$\bar{B}_r$	average radial magnetic flux density	T
B_{res}	residual magnetic flux density	T
B_z	axial magnetic flux density	T
c_e	electrical damping coefficient	Ns/m
c_e^{loss}	electrical loss damping coefficient	Ns/m
c_L	load resistance damping coefficient	Ns/m
c_m	mechanical damping coefficient	Ns/m
c_{m_f}	frictional damping coefficient	Ns/m
c_{m_s}	spring damping coefficient	Ns/m
c_T	total damping coefficient	Ns/m
ct_{ax}	coil axial thickness	m
ct_{rad}	coil radial thickness	m
d_{mag}	magnet diameter	m

d_w	coil wire diameter	m
$e_{k,k-1}$	coefficient of restitution	-
F	force	N
F_c	damping force	N
F_e	Lorentz force	N
F_k	restoring force	N
F_m	mechanical damping force	N
f	frequency	Hz
f_f	coil fill factor	-
f_n	natural frequency	Hz
f_r	frequency sweep rate	Hz/s
G_n	final velocity gain	-
g	acceleration due to gravity	m/s^2
g_0	initial gap	m
h_{mag}	magnet height	m
h_{pitch}	pitch height	m
h_{pole}	pole height	m
h_{spr}	spring height	m
h_{mass}	mass height	m
i	current	A
k	spring stiffness	N/m
k_{eff}	effective spring stiffness	N/m
K	transduction factor	Vs/m
K_{eff}	effective transduction factor	Vs/m
L_C	coil inductance	H
l_{px}	pixel length	m
l_w	coil wire length	m
m	mass	kg
N	number of coil turns	-

P	power	W
P_{av}	average power	W
P_e	electrical power	W
P_L	load power	W
P_{max}	maximum average power	W
PD	power density	W/m^3
$q_{n+1,n}$	initial velocity ratio	-
R	final mass ratio	-
R_C	coil resistance	Ω
R_L	load resistance	Ω
r_i	coil inner radius	m
r_m	coil mean radius	m
$r_{n,n+1}$	pairwise mass ratio	-
r_o	coil outer radius	m
$S^{\pm 1}$	switching surface	-
s	length scale	m
t	time	s
t_{impact}	impact time	s
V	voltage	V
V_{ind}	induced voltage	V
V_{coil}	coil volume	m^3
V_L	load voltage	V
Vol	volume	m^3
v	velocity	m/s
x	mass displacement	m
$\dot{x}$	mass velocity	m/s
$\ddot{x}$	mass acceleration	m/s^2
x_{px}	pixel displacement	m

Y	base displacement amplitude	m
y	base displacement	m
Z_L	coil impedance	Ω
z	relative displacement of mass and base	m
Z_{lim}	mass displacement limit	m
Z_{max}	maximum mass displacement	m

Greek

α	velocity gain on impact	-
γ	phase angle between excitation and response	rad
ζ	damping ratio	-
ζ_e	electrical damping ratio	-
ζ_e^{loss}	electrical loss damping ratio	-
ζ_f	frictional damping ratio	1/s
ζ_L	load resistance ratio	-
ζ_m	mechanical damping ratio	-
ζ_s	spring damping ratio	-
ζ_T	total damping ratio	-
δx	mass displacement	m
θ	excitation angle	rad
ρ	density	kg/m^3
ρ_{cop}	resistivity of copper	Ωm
τ	period of excitation	s
ϕ	magnetic flux	Wb
ω	frequency	rad/s
ω_n	natural frequency	rad/s
ω_0	initial frequency	rad/s
ω_r	frequency sweep rate	rad/s^2
ω_R	uncertainty in variable R	(R)

Subscripts

Au	gold
av	average
ax	axial
C	coil
e	electrical
eff	effective
ff	free-fall
i	inner
ind	induced
l	lateral
L	load
m	mean
m	mechanical
mag	magnet
max	maximum
n	mass number
o	outer
px	pixel
r	radial direction
rad	radial
res	residual
spr	spring
T	total
w	wire
z	axial direction
0	initial

Acronyms

DAQ	data acquisition
DoF	degree-of-freedom
EDAM	electrical domain analogue matching
IoT	internet of things
LDV	laser Doppler vibrometer
MEMS	microelectromechanical systems
ODE	ordinary differential equation
PSD	power spectral density
PWL	piecewise linear
PZT	lead zirconate titanate
RMS	root mean square
SMA	simple moving average
VAEG	velocity amplified electromagnetic generator
VEH	vibration energy harvester

Abbreviations

const	constant
exp	experimental
multi	multiple
sim	simulation

Chapter 1

Introduction

This thesis examines energy harvesting from ambient vibrational energy as an alternative to batteries for the autonomous operation of low-power electronics. Discussed in this chapter, is the motivation behind the need for energy harvesting technologies, particularly from vibrational energy, along with a review of the state-of-the-art in vibration energy harvesting.

1.1 Motivation

Recent advancements in low-power electronics have increased the feasibility of wireless sensor networks (WSNs) for the pervasive monitoring of environmental conditions. This technology has garnered much attention, as it comprises a significant portion of the technology behind the highly touted Internet of Things (IoT)—the globally interconnected network of smart objects (Miorandi *et al.*, 2012; Shaikh and Zeadally, 2016). WSNs consist of distributed networks of static sensor nodes, which have evolved such that they can operate effectively at extremely low power levels (< 50 μW) (Baert *et al.*, 2006; Bracke *et al.*, 2007). This technology has a vast range of applications, including human and structural health monitoring, building energy management, and monitoring of transportation systems (Libelium, 2013).

Contemporary sensor nodes rely on battery technology for power; batteries, however, suffer from multiple issues, foremost among them being their finite operational lifetime and environmental impact (Penella *et al.*, 2009). Energy har-

vesting technologies seek to scavenge unused ambient energy such as light, heat and vibrational energy, to supplement or replace batteries for the unlimited autonomous powering of sensor nodes (Gilbert and Balouchi, 2008). Furthermore, sensor nodes may be employed in remote, hostile, or inaccessible environments, such as inside the human body, or inside rotating machinery, where battery replacement would be costly, obstructive and potentially infeasible. An effective energy harvester for a WSN application must be cost-effective, efficient and reliable (Shaikh and Zeadally, 2016). In many environments, multiple integrated energy harvesting technologies may be necessary to achieve this (Miorandi *et al.*, 2012).

This thesis addresses vibration energy harvesting technologies. Ambient vibrational energy is pervasive, with potential sources for small-scale power generation including industrial machinery, transportation systems and human motion (Ahmed Seddik *et al.*, 2011). As such, in the last two decades vibrational energy harvesters (VEHs) have received significant research from multiple disciplines, including material sciences and electrical, civil, and mechanical engineering. VEHs, which are typically spring-mass-dampers, extract mechanical energy from a vibrating source and convert it into useful electrical energy. This can be achieved through a number of transduction mechanisms (described in section 1.2), with electromagnetic induction—based on Faraday's law—of interest herein. The majority of research into VEHs initially was focused on linear VEHs (section 1.3), which allow energy to be harvested at a single frequency corresponding to the resonant frequency of the linear spring-mass-damper. The spectra of ambient vibrations, however, are often temporally varying, broadband, or random in nature—evident in the real vibration spectra illustrated in figure 1.1. Consequently, a broadband energy harvester, which can harvest energy over a range of frequencies, is desirable. A summary of broadband energy harvesting methods presented in the literature is discussed in section 1.4.

In this thesis, a velocity amplification effect is implemented to enhance the performance of multiple-degree-of-freedom (multi-DoF) electromagnetic generators by increasing the relative velocity between the transducer components (magnet and coil). Sequential impacts between free-moving masses of decreasing size are utilised to increase velocity, according to the conservation of momentum. As the

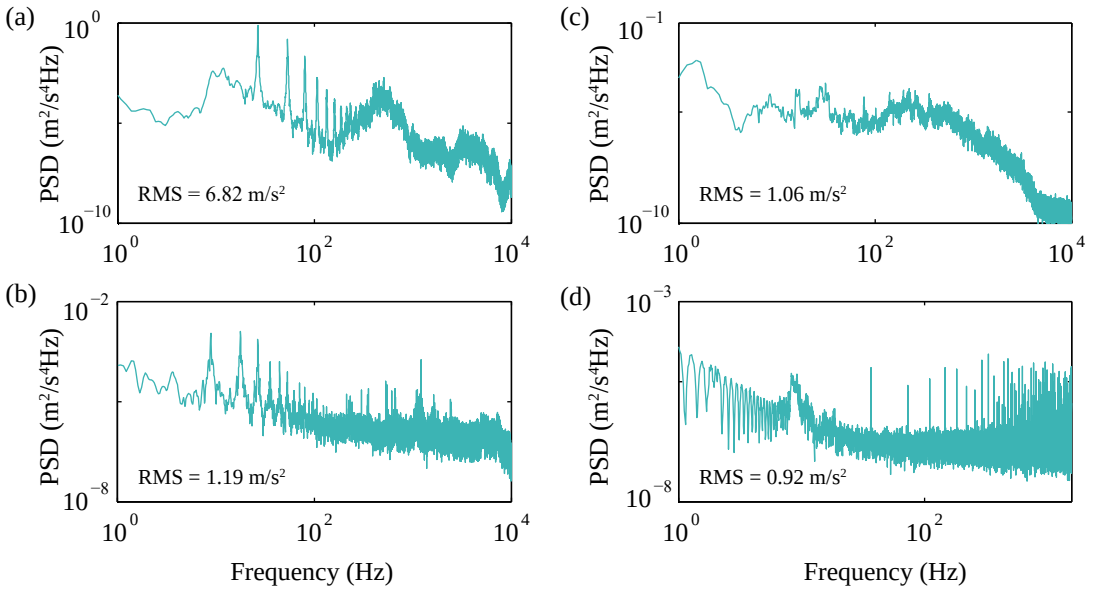

Figure 1.1: Acceleration power spectral densities (PSD) of real vibration sources (NiPS, 2012); (a) car engine, (b) train floor, (c) lathe, and (d) bridge.

masses are free-moving, there is no spring force acting against the masses in tension, allowing ballistic motion and higher velocities to be achieved. The theory of velocity amplification is presented in section 2.3, while harvesters implementing this effect, referred to as velocity amplified electromagnetic generators (VAEGs), are investigated numerically and experimentally in chapters 4–7.

The remainder of this chapter presents a review of the state-of-the-art in vibration energy harvesting. A summary of electromagnetic VEHs reported in the literature is presented in section 1.5, while the research objectives of this work and the thesis compendium are outlined in sections 1.6 and 1.7, respectively.

1.2 Energy conversion

To date, various transduction mechanisms have been implemented in VEHs in order to harvest vibrational energy as efficiently as possible. Other considerations such as scalability, cost, ease of implementation, and durability are also of importance in transducer selection. The transduction mechanisms most commonly

implemented in the literature—inductive, piezoelectric, and capacitive—are discussed in this section. Power conditioning circuitry is also briefly discussed.

1.2.1 Electromagnetic transduction

Electromagnetic induction is based on Faraday's law, whereby a change in magnetic field experienced by a conductor, typically a coil, induces a current in the conductor. The theory of electromagnetic induction—the transduction mechanism of interest in this thesis—is provided in section 2.2.1. Electromagnetic induction is realised in VEHs by moving a permanent magnet relative to a coil. The coil is usually stationary, with the source vibrations causing the inertial mass, which is coupled to a magnet, to oscillate relative to the coil. Both macro-scale harvesters, composed of discrete components (Beeby *et al.*, 2007; Cepnik *et al.*, 2011; Elvin and Elvin, 2011; Mallick *et al.*, 2015), and micro-scale harvesters, constructed using micro-fabrication techniques (Kulkarni *et al.*, 2008; Liu *et al.*, 2014; Park *et al.*, 2010; Wang *et al.*, 2009), have been presented in the literature.

Electromagnetic generators feature inherently low voltages (often $\ll 1$ V) (Roundy, 2005). In a macro-scale device, the voltage can be increased by increasing the coil turns. In a MEMS (micro electromechanical system) device, the number of turns is limited by volume; as a consequence, the voltage is always likely to be low in micro-scale harvesters. Methods of increasing the voltage for rectification and storage include step-up transformers, which, undesirably, require power to operate (James *et al.*, 2004). Inductive energy conversion methods are usually preferred in macro-scale harvesters, as scaling of the technology results in the power density decreasing significantly (Arnold, 2007). The influence of scale on power density in electromagnetic generators is discussed in detail in chapter 7.

1.2.2 Piezoelectric transduction

Piezoelectricity was discovered by Pierre and Jacques Curie in 1880. They found that subjecting certain crystals to external mechanical stress resulted in the crystals becoming electrically polarised, with the degree of polarisation proportional to the strain. Conversely, piezoelectric crystals deform when an electric field is

applied (Tichý *et al.*, 2010). VEHs employ the former effect to convert mechanical energy from vibrations to useful electrical energy by straining a piezoelectric material. These materials are available in many forms including single crystals such as quartz, piezoceramics such as lead zirconate titanate (PZT), and thin films such as sputtered zinc oxide (Beeby *et al.*, 2006).

Piezoelectric VEHs can achieve relatively high output voltages (of the order 10^1 V); the current flow is low, however, due to the high impedance and, consequently, the power generated is reduced (Roundy, 2005). They are typically implemented in fixed-free (cantilever) (Inman and Erturk, 2009; Lin *et al.*, 2010; Roundy and Wright, 2004; Stanton *et al.*, 2010; Yang and Yang, 2008) or fixed-fixed beams (Daqaq, 2012; Masana and Daqaq, 2011*b*; Sneller *et al.*, 2011), and are often preferred to inductive harvesters due to their greater power density (Roundy *et al.*, 2003).

1.2.3 Electrostatic transduction

An initial voltage is required in electrostatic energy harvesters to create a charge on two capacitor plates, resulting in the generation of an electrostatic force between the plates (Mitcheson *et al.*, 2008). As a result of the source vibration, the overlapping area or separation distance between the plates changes—working against the electrostatic force—causing a change in capacitance and, consequently, current flows in the circuitry. These devices are effectively mechanical variable capacitors, allowing the transferral of mechanical energy to the electrical domain.

Electrostatic energy harvesters benefit as a result of their relative ease of integration with MEMS technology, in comparison with inductive and piezoelectric systems. Significant output voltages can also be achieved, which is important for power conditioning. However, the requirement of a separate voltage source for the initial charge is a disadvantage which reduces the applicability of this energy harvesting technology. Furthermore, mechanical end stops are required to prevent the capacitor electrodes from coming into contact and short circuiting the system. These end stops limit the displacement range, as well as increasing the mechanical damping. Examples of electrostatic energy harvesters presented

in the literature include Hoffmann *et al.* (2009); Le *et al.* (2012); Meninger *et al.* (2001); Naruse *et al.* (2009) and Tvedt *et al.* (2010).

1.2.4 Power processing circuitry

The function of power processing circuitry in energy harvesters is to extract power from the transducer element and deliver a steady DC voltage to the electronic device or storage system (Mitcheson *et al.*, 2007). As the output from an energy harvester is AC, rectification is essential. The simplest rectification topologies are passive, such as the full-bridge rectifier, which is the most common method reported in the literature (James *et al.*, 2004; Mitcheson *et al.*, 2008; Rahimi, 2012). In electromagnetic energy harvesters, the voltage output is also typically low; hence, a mechanism to increase this voltage to allow for power conditioning may be necessary. This can be done passively through transformers, which are bulky and, so, require a large volume. Active switched-mode power electronics can provide a much more efficient method of rectification and voltage multiplication, in a more compact volume (Le *et al.*, 2006); however, a portion of the harvested energy is required to operate the circuitry. An additional consideration is that it is desirable for the power processing circuitry to maintain the electrical damping condition resulting in maximum power generation during operation (James *et al.*, 2004).

In the harvesters discussed in this thesis, the power dissipated in a load resistor is measured. The delivery of power to the electrical system, which would require rectification and possibly voltage boosting, is considered beyond the scope of this thesis, although extensive work in this area has been reported in the literature (Ferrari *et al.*, 2009; Marin *et al.*, 2013; Mitcheson *et al.*, 2007; Zhu *et al.*, 2011).

1.3 Single-DoF Linear energy harvesters

Having described the most commonly employed transduction mechanisms, VEHs reported in the literature are now discussed. In the years following the first reported VEH by Williams and Yates (1995), the majority of the focus on VEHs was on linear systems—spring-mass-dampers with a linear force-displacement

relationship—the theory of which is described in section 2.1. Examples of linear harvesters presented in the literature, and their associated issues, are discussed in this section. Figure 1.2 illustrates the most common linear energy harvester architectures—a cantilever beam with a tip-mass, and an inertial mass attached to a helical spring, with piezoelectric and inductive generators, respectively.

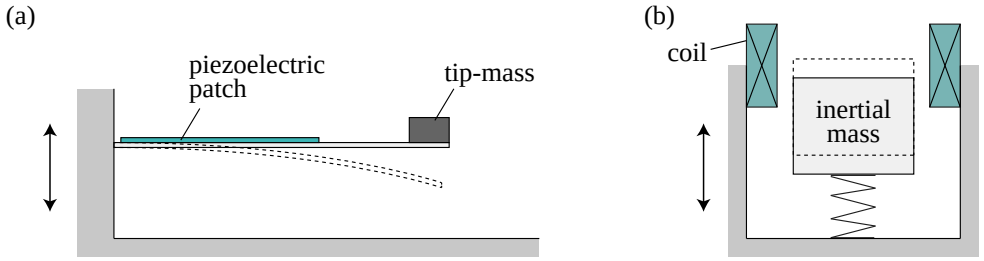

Figure 1.2: Schematics of linear inertial energy harvesters; (a) cantilever beam spring with piezoelectric strip, and (b) helical spring with inductive transducer.

The earliest vibration energy harvesting implementations were reported by a group from the University of Sheffield (Williams and Yates, 1996; Williams *et al.*, 2001; Williams and Yates, 1995). The authors developed the basic theory of linear inertial energy harvesters, and demonstrated the principle with micro-machined inductive generators. The first implementation achieved a power output of 100 μW at an excitation frequency of 330 Hz and acceleration of 129 m/s^2 in a volume of 0.25 cm^3. The output voltage from the device was low due to the limited number of coil turns which could be implemented with integrated circuit technology. In such a system, increasing the number of coil turns would actually reduced the power generated, despite increasing the voltage, due to the increasing coil resistance. A further issue with micro-scale harvesters is the associated high resonant frequency, with the majority of micro-scale harvesters presented in the literature having resonant frequencies of hundreds or even thousands of Hz (Koukharenko *et al.*, 2006; Kulkarni *et al.*, 2006). This is an issue, as the highest power available from ambient vibrations is typically at frequencies < 100 Hz (figure 1.1). Lower resonant frequencies can be achieved at micro-scales by developing compliant springs (Ching *et al.*, 2002).

Significant work on electromagnetic macro-scale linear harvesters, fabricated from discrete components, has been presented by a group from the University of Southampton. El-hami *et al.* (2001) developed a cantilever harvester with a C-shaped core attached to the free end, which oscillated relative to a stationary coil. This design was enhanced by Glynne-Jones *et al.* (2004), with an improved magnetic circuit in a volume of 3.15 cm^3. A miniaturised version of this device was presented by Beeby *et al.* (2007) and Torah (2007) which achieved a power output of 58 μW at 50 Hz and 0.6 m/s^2 in a volume of 0.15 cm^3. A spin-out company from this group, Perpetuum Ltd., offer vibration powered electromagnetic generators for a range of applications. PMG 17, a commercially available harvester from Perpetuum Ltd., can deliver 1 mW of conditioned power at 100 Hz, under just 0.25 m/s^2 of excitation. Increasing the acceleration to 2.5 m/s^2, the device can deliver 2 mW over a 20 Hz bandwidth, as a result of the increased electrical damping, with a peak power of 10 mW. The device volume of 135 cm^3 is relatively large, however.

Although some of the devices described above demonstrate significant power densities, the major issue afflicting them is the narrow bandwidth. In many of these devices, a slight deviation in excitation frequency away from the resonant frequency, results in the power generated dropping off drastically. Real vibration spectra are rarely at a single frequency, with the dominant frequency component of many vibration sources varying temporally. The spectrum may also have broadband characteristics, or may even be random in nature (figure 1.1). A number of broadband energy harvesting techniques, which have been developed to increase the effective operational frequency range of VEHs, are discussed in the following section.

1.4 Broadband energy harvesting methods

An overview of the broadband energy harvesting methods reported in the literature is presented in this section. These methods include frequency tuning, multi-modal, and non-linear methods.

1.4.1 Frequency tuning methods

Frequency tuning has received significant investigation as a method of increasing operational bandwidth in energy harvesters. Adjusting the resonant frequency of a system requires either the mass or stiffness to be changed. Of these, the stiffness is more practical to adjust. The most common tuning mechanisms employed are mechanical, magnetic, and electrical, each of which can be further categorised as active or passive. Constant power input is required for active frequency tuning in applications where the excitation frequency changes quickly, while passive tuning requires intermittent power input to adjust the system resonant frequency where the frequency varies slowly. The latter mode remains in standby until the excitation frequency shifts and, therefore, has a much lower power requirement than the active tuning mode. An effectively designed tuning mechanism should be able to cover the entire source excitation frequency range, be able to self-detect the shift in frequency and adjust the tuning parameter accordingly, and the additional power generated must compensate for the power requirement of the tuning mechanism.

The most common mechanical tuning method employs a compressive axial load to adjust the stiffness of a simply supported beam (figure 1.3a). Below the critical buckling load, increasing the axial load results in a reduction in the resonant frequency. In theory, the resonant frequency goes to zero at the critical buckling load; however, achieving such a low frequency in practice is not possible, although relatively low resonant frequencies can be obtained. When the beam buckles, it stiffens, increasing the resonant frequency again. Such an approach, implemented by Hu *et al.* (2007); Leland and Wright (2006) and Masana and Daqaq (2012), allows a significant shift in frequency to be achieved, with Masana and Daqaq (2012) experimentally demonstrating a shift in resonant frequency from 150 to 45 Hz (70%). An issue with this tuning mechanism is that the mechanical damping increases with compressive load, reducing the power output (Leland and Wright, 2006).

Magnetic tuning mechanisms utilise repulsive or attractive forces between magnets (figure 1.3b) to either increase or decrease the effective stiffness of a spring. Adjusting the position of the tuning magnet relative to the tip-magnet

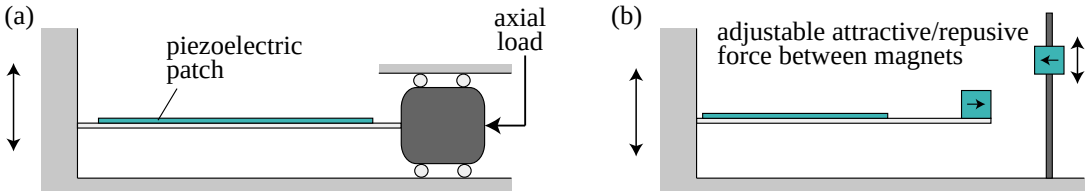

Figure 1.3: Schematics of tuning mechanisms: (a) mechanical tuning of a simply supported beam by application of a compressive axial load, (b) magnetic tuning using the attractive force between magnets.

allows the force between the magnets and, hence, the stiffness to be controlled. This frequency tuning technique was implemented by Challa *et al.* (2011, 2008), with a bidirectional tuning range of 22–32 Hz (31.3%) achieved in a volume of 50 cm^3. A time of 320 s was required between each tuning procedure to shift the resonant frequency between the maximum and minimum values, however. Clearly, this method is only effective in applications where the frequency shifts slowly with time.

Electrical tuning can be employed through a number of methods, the most common being piezoelectric and electrical damping tuning. The piezoelectric tuning mechanisms employed in the literature typically involve coupled piezoelectric beams, where one of the beams acts as an actuator to alter the beam stiffness. The second beam, which can utilise any of the previously described transduction mechanisms, then acts as the energy harvesting component. Wu *et al.* (2006) developed an actively controlled piezoelectric bimorph which had a narrow tuning range of 91.5–94.5 Hz (3.2%). Another harvester implementing piezoelectric tuning methods was presented by Peters *et al.* (2009). In this case, a broader tuning range of 66–89 Hz (29.5%) was achieved. An electrical damping resonant frequency tuning method was implemented by Mitcheson *et al.* (2011), which used a H-bridge power electronic interface to control the power transfer between the mechanical and electrical domains, allowing the damping and resonance frequency to be tuned. This method achieved a maximum resonant frequency shift of 20% around the unmodified natural frequency of 1.25 Hz in a pendulum type harvester. The most significant advantage of electrical tuning method is that active tuning is accommodated with relative ease, in comparison to the other

methods; however, the tuning range is also smaller.

In summary, frequency tuning mechanisms may be beneficial in applications where the dominant frequency is slowly varying. If, however, the frequency varies rapidly, or the excitation is random, the power requirement of the tuning mechanism is likely to exceed the additional energy harvested. Consequently, it is evident that an alternative method of broadening the response of an energy harvester is required.

1.4.2 Multi-modal methods

Rather than attempting to tune the resonant frequency of a harvester, many authors have developed multi-modal energy harvesters, which have a naturally broader frequency response. The most simple of these designs consist of arrays of linear energy harvesters—usually cantilever beams—arranged in parallel, with each beam having a distinct resonant frequency (figure 1.4a). This design has been employed by Shahruz (2006); Xue *et al.* (2008) and Sari *et al.* (2008). The concept of such a system is that, under frequency varying excitation, one of the beams will always be at resonance. Such devices suffer due to reduced power density as, at a given frequency, the majority of the harvester beams are inactive.

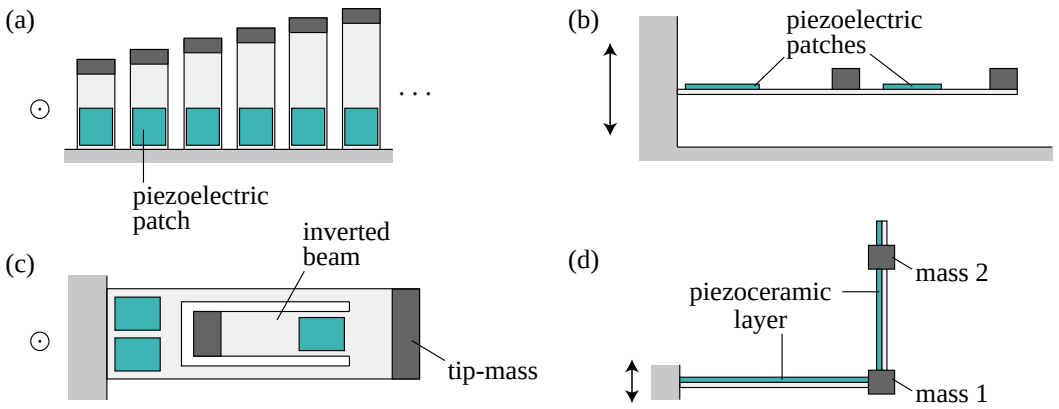

Figure 1.4: Schematics of multi-modal energy harvesters: (a) cantilever array (plan-view), (b) 2-DoF cantilever (side-view), (c) 2-DoF inverted (plan-view), and (d) L-shaped (side-view).

The multiple bending modes of multi-DoF linear systems have also been suggested as a potential method of broadening frequency response. Of these, 2-DoF linear systems—often referred to as dual-mass systems—have received the most analysis (figure 1.4b). Tang *et al.* (2012) theoretically investigated the influence of a range of parameters on the performance of the these systems including; transducer location, mass ratio, and frequency. The most significant issues affecting linear multi-DoF harvesters is that there is typically a large frequency range between the resonances, and the amplitude of the peaks vary significantly. The authors demonstrated that in order to achieve closely spaced resonant frequencies of similar amplitude, the first mass should be significantly larger, i.e. the mass ratio should be high (mass ratio is the ratio of the base mass to the final mass, discussed in greater detail in section 2.3). Geometric adjustments to multi-DoF coupled harvesters allow the spacing between resonant frequencies to be reduced. This can be done by inverting the secondary beam (figure 1.4c) (Wu *et al.*, 2012), by coupling beams to one another (Kim *et al.*, 2011; Qi *et al.*, 2010), through irregular cantilever designs such as M- and Y-shaped cantilevers (Wu *et al.*, 2015) and L-shaped cantilevers (figure 1.4d) (Erturk, Renno and Inman, 2009), or in a clover design (Iannacci *et al.*, 2016). Although these methods allow closely spaced resonant frequencies of similar amplitude to be achieved, the peak amplitude is lower than that of the first mode of a conventional multi-DoF system.

In summary, multi-model energy harvesters are relatively easy to implement as no tuning is required. The resonant frequencies in a conventionally designed multi-DoF system are far apart, however, with the amplitude of the first mode being significantly larger than the remaining modes. These issues can be mitigated by implementing irregular geometries, at the cost of reducing the amplitude of the first mode. Power density also decreases in multi-modal systems, relative to linear harvesters, due to the increased volume required for the additional masses. The harvesters under investigation in this thesis are multi-DoF and, consequently, are also multi-modal. It is only the first mode which is of interest, however.

1.4.3 Non-linear methods

The broadband harvesting method which has received the most investigation in recent years is non-linear energy harvesting. Such a harvester utilises non-linear stiffness and, consequently, non-linear restoring force to extend the coupling between excitation frequency and the energy harvester over a wider range of frequencies. Two types of non-linear oscillator are discussed in this subsection: Duffing-type oscillators and piecewise linear (PWL) oscillators.

(a) Duffing-type oscillators: This type of oscillator features a cubic non-linear spring force; whereas, in the case of a linear system, the restoring force is a linear function of the displacement. If the restoring force increases with displacement, the system behaviour is referred to as hardening; while if the restoring force decreases with displacement, softening behaviour is observed. Systems with a single stable equilibrium, demonstrating either hardening or softening behaviour, are considered monostable. Bistable behaviour occurs when the system exhibits two stable equilibrium points. The potential function—which describes the energy stored for a given spring deflection—and restoring force for different types of non-linear behaviour in a Duffing-type oscillator are illustrated in figure 1.5.

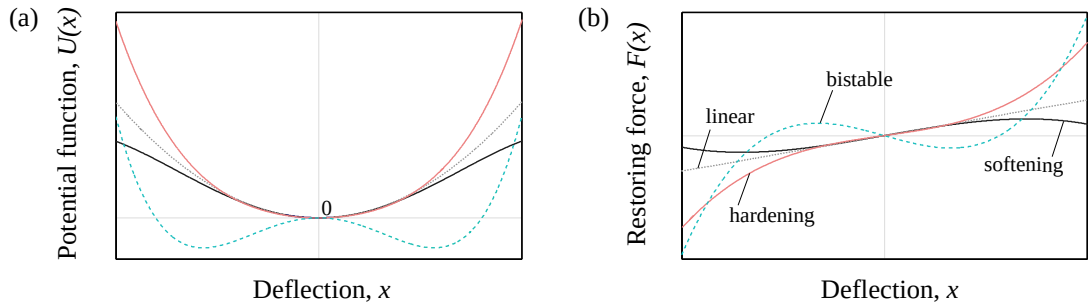

Figure 1.5: (a) Potential function and (b) restoring force for linear, softening, hardening, and bistable behaviour in a Duffing-type oscillator.

A Duffing-type oscillator can be realised through a number of mechanisms, typically using attractive or repulsive magnetic forces, or compressive mechanical forces. These mechanisms are the same as those described for frequency tuning in section 1.4.1. This is because, as well as allowing the resonant frequency

to be tuned, these mechanisms introduce non-linearity into the spring stiffness. Examples of Duffing-type oscillators presented in the literature are illustrated in figure 1.6. Each of the systems presented can adapt to operate in monostable and bistable modes by adjusting a tuning parameter.

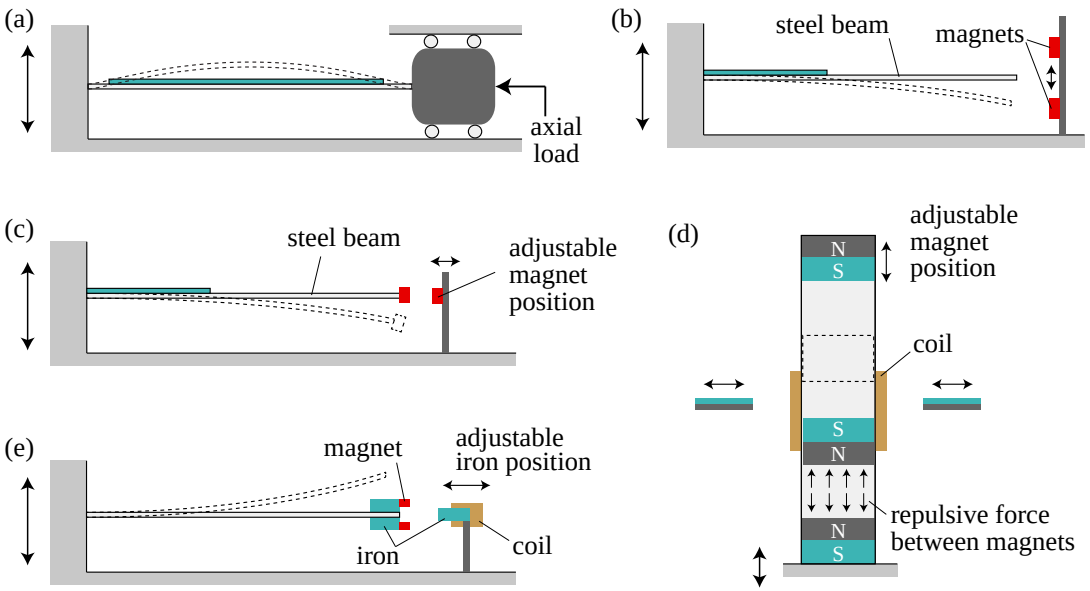

Figure 1.6: Schematics of different Duffing-type oscillators with adjustable non-linear stiffness, capable of monostable and bistable operation—(a,b,c) piezoelectric and (d,e) inductive.

Monostable harvesters: Among the first to intentionally employ non-linearities into an energy harvester were Burrow and Clare (2007) and Barton *et al.* (2010). The authors developed an inductive monostable harvester, as in figure 1.6e, which utilised the attractive force between magnets, attached to the tip of a beam, and a steel stator to achieve a non-linear hardening restoring force. Adjusting the position of the steel stator allowed the non-linear stiffness to be tuned. Following from this, a number of other monostable harvesters were developed. Mann and Sims (2009) employed magnetic levitation in an inductive harvester (figure 1.6d) to introduce a non-linear restoring force. The non-linear stiffness—of a hardening type—was tuned by adjusting the position of the magnetic springs at the cap and base. A harvester capable of both softening and hardening monostable behaviour, achieved through respective use of attractive and repulsive magnet forces, was

presented by Stanton *et al.* (2009), while a similar design was implemented by Sebald *et al.* (2011). Examples of mechanical methods of introducing non-linearity are through compressive axial loads (figure 1.6a) below the critical buckling load (Masana and Daqaq, 2011*a*,*b*; Sneller *et al.*, 2011), or through stretching of spring material (Mallick *et al.*, 2015; Marinkovic and Koser, 2009).

The monostable harvesters described above were excited harmonically with bidirectional frequency sweeps. In each case, hysteresis in response to the bidirectional sweeps was described, with the bandwidth increasing for forward-frequency sweeps in hardening systems, and for reverse-frequency sweeps in softening systems. The response achieved by a harvester at a particular frequency in this region of coexisting responses is determined by the initial conditions and its basin of attraction. The higher branch of the coexisting response is referred to as the high-energy state, while the lower branch is referred to as the low-energy state (Mallick *et al.*, 2015). A probabilistic study by Quinn *et al.* (2011) suggests that as the frequency shifts further away from the unique response, the solution tends towards the low-energy response. The presence of coexisting or non-unique responses in monostable systems severely impedes their applicability. To ensure a high-energy response, Erturk, Renno and Inman (2009) proposed employing impulse actuation though piezoelectric layers to create a disturbance, potentially by discharging a capacitor. According to Daqaq *et al.* (2014), no such physical system has been realised to date. Another issue affecting monostable harvesters is that, under low excitation amplitude, the influence of the non-linearity is small. Consequently, the extension of the bandwidth is small, with the response approaching that of a linear system. It is also important to note that the non-linearity only serves to bend the frequency response curve; the amplitude of the response does not increase relative to a linear system.

Bistable harvesters: In recent years, much of the research on non-linear energy harvesters has been focused on bistable systems. As well as for harmonic excitation, bistability has been proposed as a method of improving power generation under noise excitation. The first experimentally tested bistable harvesters were presented by Cottone *et al.* (2009) (figure 1.6c) and Erturk, Hoffmann and Inman (2009) (figure 1.6b), with the bistability introduced through the use of different arrangements of magnets.

Harmonic excitation is considered initially here. Erturk, Hoffmann and Inman (2009) and Erturk and Inman (2011) considered the main advantage of bistable systems being the ability to achieve large orbit inter-well oscillations at certain frequencies and accelerations. Their piezo-magneto-elastic device demonstrated a significantly broader bandwidth than an equivalent linear system. It was also noted, however, that lower energy solutions existed over a portion of the frequency range investigated, resulting in the same dependence on initial conditions previously described for monostable systems. These conclusions were also reached by Stanton *et al.* (2010) using a similar device to Cottone *et al.* (2009) (figure 1.6c).

The importance of the excitation and the shape of the potential energy function in bistable systems was investigated by Masana and Daqaq (2011*b*) (figure 1.6a). Both deep and shallow potential wells—illustrated in figure 1.7—were analysed. For low amplitude excitation with deep potential wells, the potential barrier was too large to achieve inter-well oscillations; consequently, small intra-well oscillations were observed. Increasing the excitation amplitude allowed the potential barrier to be crossed. Further increases in excitation resulted in large-amplitude inter-well oscillations and high voltages being achieved over a wide range of frequencies. Decreasing the potential barrier, the excitation amplitude required to achieve inter-well oscillations was much lower. Further reductions in the potential well depth, however, would eventually result in the system losing its bistability, reducing its effectiveness, particularly at higher excitation levels. Again, coexisting responses, which affect the energy that can be harvested in practice, were demonstrated by the authors.

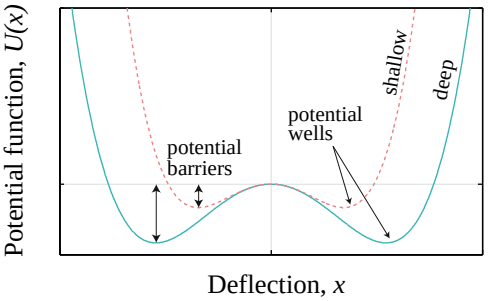

Figure 1.7: Potential function of a bistable Duffing-type oscillator, showing potential barriers of deep (——) and shallow (- - - -) double potential wells.

The response of bistable systems to noise excitation has been the focus of much investigation recently (Cottone *et al.*, 2009; Daqaq, 2011; Ferrari *et al.*, 2010; Friswell *et al.*, 2012; Gammaitoni *et al.*, 2009; Litak *et al.*, 2010). The inverted pendulum design of Cottone *et al.* (2009) (figure 1.6c)—the first bistable system investigated experimentally—was tested under Gaussian white noise. In this design, a magnet was placed at the tip of the beam, while a repulsively polarised magnet was placed oppositely. By adjusting the distance between these magnets, the non-linearity was controlled. At relatively large distances between the magnets, the system behaviour was monostable. Reducing this distance, the device transitioned to bistable behaviour, with two potential wells located either side of the adjustable magnet. An improvement in power generation of as much as 600% was demonstrated by the optimally configured non-linear harvester, compared to an equivalent linear system. It was noted by both Cottone *et al.* (2009) and Daqaq (2012) that, in order to achieve this improved performance, prior knowledge of the noise intensity is required to implement the optimal potential barrier height.

In summary, bistable harvesters suffer from the same reliance on excitation amplitude as monostable non-linear harvesters—this applies to both harmonic and noise excitation. If the excitation is too small, large inter-well oscillations will not occur, and the device performance will not improve, relative to a monostable system. Decreasing the depth of the potential wells to allow for inter-well oscillations at lower accelerations, the system becomes weakly bistable, again, approaching the performance of a monostable harvester. Even if the excitation amplitude is sufficiently large, it is necessary to know the amplitude of the excitation to implement the optimal potential barrier. For harmonic excitation, the presence of regions consisting of coexisting responses and the resultant dependence on initial conditions remains a significant issue. The complex relationship between the performance of bistable harvesters and the excitation and geometrical parameters, significantly hinders their potential application.

(b) PWL oscillators: Non-linearity in VEHs can also be realised through a PWL restoring force, which is bilinear in its simplest form. This is typically introduced using impacts with stoppers, which limit the displacement of an inertial

mass. Although the restoring force is linear, the system dynamics are non-linear. The first example of a PWL harvester in the literature was presented by Soliman *et al.* (2008), a schematic of which, is illustrated in figure 1.8, along with its force-displacement relationship. A symmetrical force-displacement relationship could be achieved by implementing a second stopper at the opposite side of the cantilever beam. The device behaves as a linear oscillator until the beam displacement is sufficient to impact the stopper, resulting in a large increase in effective stiffness and an induced hardening effect. Consequently, on the frequency forward-sweep, the response extends beyond the linear resonance. On the frequency reverse-sweep, the response again follows that of a linear system until the stopper is reached, with the same response observed as for the forward-sweep for the remainder of the frequency range. Although the frequency response is significantly increased on the forward-sweep, the presence of the stopper limits the displacement, reducing the peak amplitude at resonance. Further investigation into the design and optimisation of this system was presented by Soliman *et al.* (2009). As with the non-linear harvesters previously discussed, this system is affected by coexisting responses, with the response achieved depending on initial conditions. To be effective in practice, a mechanism to ensure entry into the high-energy state would be necessary.

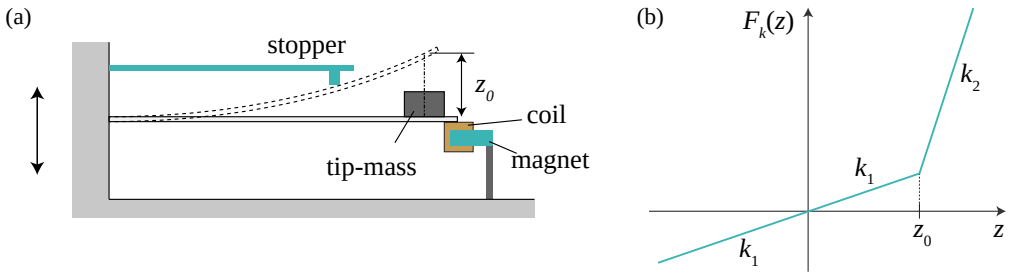

Figure 1.8: (a) Inductive PWL oscillator, with a one-sided stopper, and (b) its force-displacement diagram showing bilinear stiffness.

Similar systems have been investigated at both macro- and micro-scale by a number of authors. Blystad and Halvorsen (2011) and Dhakar *et al.* (2013) employed impacts with mechanical end stops in macro-scale piezoelectric harvesters, while MEMS implementations, with both single and double end stops,

have been demonstrated in piezoelectric and electrostatic harvesters by Blystad *et al.* (2010); Gu (2011); Hoffmann *et al.* (2009); Le and Halvorsen (2012); Le *et al.* (2012) and Liu *et al.* (2012*a*). Impacts were used by Ahmed Seddik *et al.* (2011) to increase the velocity of a seismic mass, through the use of piezoelectric actuators that induced controlled impacts. This technique required artificial input to increase velocity, however, which is undesirable. All of the above systems employed anchored springs, connecting the base to the inertial mass.

Impacts between masses have also been used to improve the performance of energy harvesters, by increasing the relative velocity in an electromagnetic generator. This effect, referred to as velocity amplification, was first implemented for high acceleration shock testing by Rodgers *et al.* (2009). It is this effect, applied to VEHs, that is under investigation in this thesis. The theory of velocity amplification and its application in electromagnetic generators is discussed in section 2.3. Cottone *et al.* (2013) first developed a VAEG, employing velocity amplification in VEHs. VAEGs with 2- and 3-DoFs were tested against a single-DoF system, with the multi-DoF systems offering an improvement in power generation, compared to the single-DoF system tested. More recently, Frizzell *et al.* (2016) investigated different implementations of 2-DoF VAEGs, while Nico *et al.* (2016) utilised magnetic springs in a 2-DoF VAEG to achieve a high power output at relatively low frequencies. In comparison with the harvesters employing impacts with end stops and controlled piezoelectric actuators previously described, the VAEGs described herein achieve this naturally through their geometry and configuration of masses. The VAEGs utilize free-moving masses and, hence, do not require anchored springs. This is beneficial as there is no spring force acting against the masses, allowing ballistic motion and higher velocities to be achieved. This thesis investigates the influence of a range of parameters on the non-linear behaviour of VAEGs using detailed numerical and experimental techniques.

1.5 Comparison of VEHs from the literature

A number of performance metrics have been proposed to allow the comparison of energy harvesters of different scales, acting under different excitation conditions. Of these, the most widely used are the normalised power density (NPD) described

by Beeby *et al.* (2007), and the volume figure of merit (FoM_V) described by Mitcheson *et al.* (2008).

NPD is the power per unit volume normalised by the acceleration amplitude squared:

$$NPD = \frac{P}{Acc^2 Vol} \tag{1.1}$$

This metric does not account for the excitation frequency or bandwidth.

The FoM_V compares the power output from a device, with the power generated by an equivalent linear resonator. This equivalent harvester has a cubic geometry, a proof mass composed of gold occupying half the volume, an internal displacement range occupying the remaining half, and is excited at the same frequency and acceleration:

$$FoM_V = \frac{P}{\frac{1}{16}\omega Acc Vol^{4/3} \rho_{Au}} \tag{1.2}$$

Although this metric accounts for excitation frequency, it also does not account for bandwidth.

The NPD and FoM_V values of harvesters reported in the literature are listed in table 1.1, along with the corresponding excitation, geometric, and transduction properties, to allow for comparison. As this thesis is primarily focused on electromagnetic generation, only inductive harvesters are presented. The performance values achieved by the harvesters in this thesis are discussed in section 6.4.

The harvester performance values achieved by the device of Beeby *et al.* (2007) are significantly higher than those of the remaining harvesters in the literature. Their design was a linear cantilever with a very high quality factor, Q (level of underdamping), resulting in an extremely narrow peak at the resonance frequency and a relatively high power output at low acceleration levels, resulting in a very high NPD. The issue with this harvester design is the narrow frequency response; consequently, it is only suitable for applications with a stationary frequency response.

Overall analysis of the presented harvester performance metrics shows that large numbers of low power density electromagnetic VEHs have been presented in the literature. More careful manufacturing and assembly, along with a greater

effort to improve the design of magnetic circuitry would allow higher power densities to be achieved.

Table 1.1: Summary of electromagnetic VEHs reported in the literature.

Reference	Vol (cm^3)	Acc (m/s^2)	f (Hz)	Power (μW)	NPD (kgs/m^3)	FoM_v (%)
El-hami *et al.* (2001)	0.24	102.3	322.0	530	0.21	0.142
Ching *et al.* (2002)	2.00	34.4	66.0	830	0.35	0.191
Sasaki *et al.* (2005)	25.00	3.2	2.0	170	0.66	0.479
Spreemann *et al.* (2006)	1.50	28.0	80.0	3000	2.55	1.028
Beeby *et al.* (2007)	0.15	0.6	52.0	46	883.97	24.838
Yuen *et al.* (2007)	3.80	4.6	80.0	120	1.49	0.072
Kulkarni *et al.* (2008)	0.10	5.5	8080.0	0.2	0.05	0.000
Saha *et al.* (2008)	12.70	0.4	8.0	14.6	7.93	0.213
Soliman *et al.* (2008)	72.00	1.4	95.0	83	0.59	0.003
Ferro (2009)	170.00	1.0	60.0	5200	30.59	0.121
Xing *et al.* (2009)	69.00	5.6	54.0	5000	2.31	0.077
Hatipoglu and Ürey (2010)	4.10	1.0	24.4	144	35.12	1.185
Park *et al.* (2010)	0.60	7.9	54.0	115	3.07	0.702
Cepnik *et al.* (2011)	10.00	9.9	50.0	20600	21.15	2.554
Cepnik and Wallrabe (2011)	1.20	1.0	143.0	12	10.00	0.087
Galchev *et al.* (2011)	3.75	9.8	10.0	13.6	0.04	0.031
Zorlu *et al.* (2011)	3.00	11.8	10.0	545	1.30	1.407
Elvin and Elvin (2011)	2.30	1.0	112.3	8	3.48	0.031
Zhu *et al.* (2012)	12.10	4.9	45.0	150	0.51	0.032
Perpetuum (2013)	135.00	2.0	100.0	20000	37.04	0.190
Ashraf *et al.* (2013)	27.38	9.8	18.0	9360	3.56	0.847
Munaz *et al.* (2013)	9.05	4.9	6.0	4840	21.92	11.412
Nico *et al.* (2016)	8.12	3.9	11.5	2060	16.51	2.600

1.6 Objectives of this work

At present, commercially-available VEHs are typically linear oscillators, which harvest energy over a narrow frequency range. Non-linear techniques have been developed to increase the effective operational frequency range and power density of VEHs; however, these devices suffer due a dependence on initial conditions, as discussed in section 1.4.3. This thesis investigates VAEGs as a potential alternative to the presently available VEHs.

The first publication on VAEGs by Cottone *et al.* (2013) investigated single-, 2-, and 3-DoF harvesters under exponentially correlated Gaussian noise. A more recent publication by Frizzell *et al.* (2016) investigated a range of 2-DoF VAEG designs—featuring attached and detached masses—for both stacked and embedded mass configurations (Frizzell *et al.*, 2016), while Nico *et al.* (2016) focused on developing a 2-DoF VAEG with magnetic springs and an optimised transducer. A number of open questions remain regarding the influence of a range of parameters on the dynamic and electrical response of VAEGs. This thesis seeks to investigate the influence of these parameters, such that a more complete understanding of VAEGs can be obtained.

The objectives of this thesis are:

- to develop a model which can accurately represent the dynamic and electrical behaviour of VAEGs, such that the parameters of significance can be isolated, and their influence investigated fully;
- to determine the influence of mass configuration—number of DoFs and mass ratio—on the relative performance of VAEGs, i.e. what is the optimal number of DoFs and mass ratio to maximise the power density of a VAEG;
- to geometrically and electrically optimise a VAEG, maximising power density;
- to characterise a VAEG for a range of excitation and geometric parameters, i.e. frequency, acceleration and a geometric parameter referred to as the initial gap, to understand their influence; and

- to demonstrate the influence of scaling on the electrical and mechanical behaviour of a VAEG and gain an insight into the challenges which affect the development of a VAEG approaching MEMS scale.

1.7 Thesis compendium

The remainder of this thesis is organised as follows:

- *Chapter 2* outlines the theory of linear inertial oscillators, electromagnetic induction employed in VEHs, and velocity amplification.
- *Chapter 3* presents the experimental apparatus and measurement techniques employed in the testing of the various VAEG configurations, including velocimetry, and voltage measurement for drop-test and forced excitation test conditions.
- *Chapter 4* develops a model for single- and multi-DoF PWL harvesters. Non-linear analysis mechanisms such as bidirectional sweeps, stroboscopic maps, phase diagrams and Poincaré maps are utilised to describe the dynamic behaviour with changing geometric and excitation conditions.
- *Chapter 5* investigates experimentally the influence of mass configuration—number of DoFs and mass ratio—on the output voltage of multi-DoF VAEGs. Drop-test and forced excitation test conditions are employed.
- *Chapter 6* utilises simulations to optimise the transducer of a VAEG in terms of power density. A 2-DoF VAEG is fabricated and characterised with frequency sweeps, experimentally and numerically, at a range of accelerations and for a range of values of the geometric parameter referred to as the initial gap. The performance of the 2-DoF VAEG relative to harvesters presented in the literature is discussed.
- *Chapter 7* details the influence of scaling on a 2-DoF VAEG, which is fabricated at three scales. The electrical and mechanical systems are considered separately for comparison to linear systems.

- *Chapter 8* draws conclusions from the presented numerical and experimental data, and makes recommendations for future work.
- Peer-reviewed journal and conference publications from this work, as well as articles currently under review, are listed in Appendix A.

Chapter 2

Theory

This chapter provides a basic overview of the theory of inertial electromagnetic generators. The equation of motion for a linear oscillator coupled to an electromagnetic transducer is derived for both constant and spatially varying magnetic flux gradient. The theory of velocity amplification, the principle on which velocity amplified electromagnetic generators (VAEGs) are based, is also described.

2.1 Linear inertial oscillator

A single-degree-of-freedom (DoF) linear inertial VEH, usually referred to as a spring-mass-damper is first described. Such a device, as depicted in figure 2.1, consists of a mass m attached to a linear spring of stiffness k, and a transduction mechanism to convert mechanical energy to electrical energy. The displacement of the mass is $x(t)$, the base excitation displacement is $y(t)$, and the relative displacement of the mass and base (spring deflection) is $z(t) = x(t) - y(t)$.

The inertial force on the mass ($F = m\ddot{y}$) is due to the input vibrations applied to the base. This inertial force results in relative motion of the mass and the device frame, allowing energy to be extracted from the system.

Energy dissipated from the system is modelled by a damper, illustrated as a dash-pot. The mechanical damping coefficient c_m is a measure of the parasitic losses. c_m is highly dependent on the device design, with the most common mechanical damping mechanisms being:

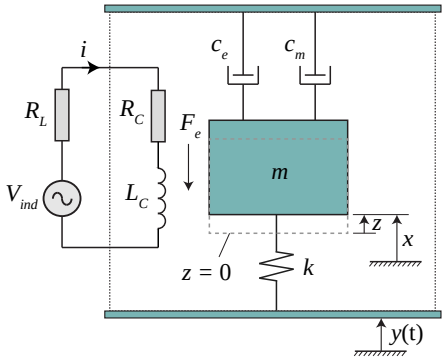

Figure 2.1: Lumped parameter model of linear inertial electromagnetic energy harvester.

- friction—as a result of sliding surfaces; this becomes more significant as scale is reduced as the surface-to-volume ratio increases;
- thermoelastic damping—due to the generation of heat from compression and expansion in a flexural body, i.e. a cantilever or helical spring;
- squeeze-film damping—caused by gas becoming squeezed between structures moving relative to one another; and
- air resistance—due to viscous drag.

The electrical damping coefficient c_e is a result of the energy extraction mechanism, in this case an electromagnetic transducer. This electrical subsystem, described in greater detail in section 2.2, consists of a coil of resistance R_C and inductance L_C, and a load resistance R_L, while the load voltage is V_L and i is the current flowing in the coil. The total damping coefficient of the system is the sum of the mechanical and electrical damping coefficients, $c_T = c_e + c_m$. It is assumed that the damping force is proportional to velocity, an assumption which is valid for electromagnetic transduction; however, it requires alteration to accurately model alternative transduction mechanisms.

The general model to describe the conversion of mechanical to electrical energy in a linear inertial VEH was first proposed by Williams and Yates (1996). Their model assumes that the source is infinite; therefore, it is unaffected by the

harvesting device. By applying a force balance to the inertial mass, the equation of motion is found:

$$m\ddot{x} + c_e(\dot{x} - \dot{y}) + c_m(\dot{x} - \dot{y}) + k(x - y) = 0 \tag{2.1}$$

The relative displacement between the mass and the base is $z = x - y$. Inserting this relationship into equation 2.1 yields:

$$m\ddot{z} + (c_e + c_m)\dot{z} + kz = -m\ddot{y} \tag{2.2}$$

The power dissipated in the damper (i.e. the power extracted by the transduction mechanism, and the losses due to mechanical damping) is given by:

$$P = \int_0^{\dot{z}} F_c d\dot{z} \tag{2.3}$$

where the damping force $F_c = c_T\dot{z}$. If both c_T and the velocity $\dot{z}$ are constant, the power is simply the product of force and velocity, $P = F_c\dot{z}$. Where the velocity is not constant the power becomes:

$$P = c_T \int_0^{\dot{z}} \dot{z} d\dot{z} \tag{2.4}$$

Solving equation 2.4 gives an expression for the power dissipated:

$$P = \frac{1}{2} c_T \dot{z}^2 \tag{2.5}$$

Assuming the excitation is harmonic—$y(t) = Y sin(wt)$, where Y is the base excitation amplitude and ω is the excitation frequency—equation 2.2 can be solved for z. Differentiating and inserting the solution into equation 2.5 yields an expression for the average power dissipated per cycle.

$$P_{av} = \frac{m\zeta_T\omega^3\left(\frac{\omega}{\omega_n}\right)^3 Y^2}{\left(1 - \left(\frac{\omega}{\omega_n}\right)^2\right)^2 + \left(2\zeta_T\frac{\omega}{\omega_n}\right)^2} \tag{2.6}$$

where $w_n = \sqrt{k/m}$ is the natural frequency of the system, ζ_m is the mechanical damping ratio, ζ_e is the electrical damping ratio and ζ_T is the total damping

ratio ($\zeta_T = \zeta_e + \zeta_m$, where $\zeta = c/2m\omega_n$). A plot of normalised average power as a function of frequency ratio ω/ω_n is shown in figure 2.2, for a range of damping ratios. Evidently the highest power occurs at resonance ($\omega = \omega_n$). With increasing damping ratio, the power at resonance decreases; however, the bandwidth increases.

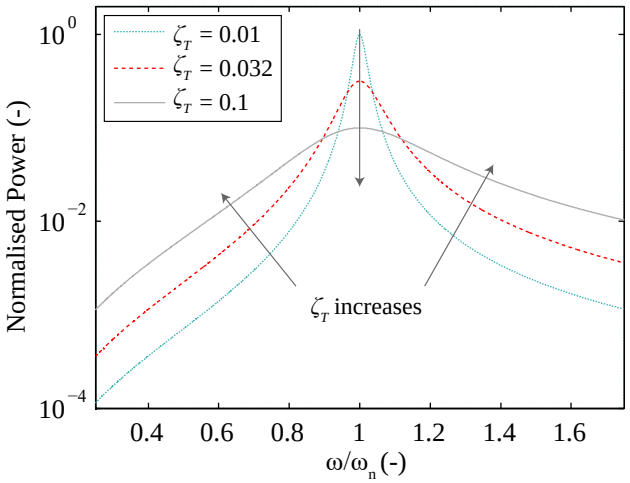

Figure 2.2: Normalised power as a function of frequency ratio ω/ω_n for a range damping ratios.

At resonance, equation 2.6 reduces to equation 2.7.

$$P_{av} = \frac{m\omega_n^3 Y^2}{4\zeta_T} \tag{2.7}$$

Substituting the amplitude of the acceleration, $Acc = \omega^2 Y$, yields:

$$P_{av} = \frac{mAcc^2}{4\omega_n\zeta_T} \tag{2.8}$$

Inserting $\zeta_T = Y/2Z_{max}$ gives the average power in terms of peak displacement, Z_{max}:

$$P_{av} = \frac{1}{2}m\omega_n^3 Y Z_{max} \tag{2.9}$$

The average power delivered to the electrical domain at resonance is:

$$P_e = \frac{m\zeta_e\omega_n^3 Y^2}{4(\zeta_e + \zeta_m)^2} \tag{2.10}$$

Taking $dP_e/d\zeta_e = 0$, the relationship which maximises power flow into the electrical domain, $\zeta_e = \zeta_m$, is determined. This is valid as ζ_e and ζ_m are independent. However, as there are further losses in the electrical domain, the condition which is actually desirable is to maximise the power delivered to the electrical load.

The electrical damping can be subdivided as $\zeta_e = \zeta_L + \zeta_e^{loss}$, where ζ_L and ζ_e^{loss} are load resistance and electrical loss damping ratios, respectively. The losses from the electrical and mechanical domains can be grouped as $\zeta_{loss} = \zeta_e^{loss} + \zeta_m$. The average load power at resonance is then:

$$P_L = \frac{m\zeta_L\omega_n^3 Y^2}{4(\zeta_L + \zeta_{loss})^2} \tag{2.11}$$

As ζ_L and ζ_e^{loss} are not independent, taking $dP_L/d\zeta_L = 0$ to maximise power delivered to the load is not valid. The domain in which the load matching is applied must be the domain to which power is delivered (Stephen, 2006).

The electrical damping coefficient is given by $c_e = K^2/(R_L + R_C)$, where K is the electromagnetic transduction factor (equation 2.22). The electrical load and electrical loss damping coefficients are then $c_L = K^2 R_L/(R_L + R_C)^2$ and $c_e^{loss} = K^2 R_C/(R_L + R_C)^2$, respectively. Inserting these equations into equation 2.11, and rearranging, with $\zeta = c/2m\omega_n$ yields:

$$P_L = \frac{m^2\omega_n^4 Y^2 K^2 R_L}{2(c_m(R_L + R_C) + K^2)^2} \tag{2.12}$$

Taking $dP_L/dR_L = 0$ yields a relationship for the maximum power delivered to the load:

$$R_L = R_C + \frac{K^2}{c_m} \tag{2.13}$$

This approach is known as electrical domain analogue matching (EDAM) (Stephen, 2006), as it contains the electrical analogue of mechanical damping, and is the optimisation approach which should be employed in the design of a linear energy

harvester. Inserting this relationship into equation 2.12 gives an expression for the maximum power delivered to the load at the optimal load resistance:

$$P_L = \frac{m^2\omega_n^4 Y^2 K^2}{8c_m(c_m R_C + K^2)} \tag{2.14}$$

Equation 2.14 can be used in the design of a resonant energy harvester to maximise the power delivered to the load. Reintroducing ζ_m into equation 2.14, it can be shown that $P_L \propto \omega_n^3$. Based on this relationship, it might be assumed that the highest harmonic should be targeted in the design of a linear energy harvester for a particular application. However, this analysis assumes the base displacement amplitude Y is independent of excitation frequency. In reality it is likely that Y will decrease with increasing excitation frequency; therefore, the highest power would be at a lower frequency. This is evident in the real vibration spectra presented in section 1.1 (figure 1.1). It is clear that the source vibrations should be analysed closely before designing an energy harvester.

2.2 Electrical system

The transduction mechanism utilised herein is an electromagnetic transducer. This type of transducer can be implemented in an inertial oscillator in a number of ways. Usually the inertial mass is either partially or entirely composed of the magnet or magnet stack, and this mass oscillates relative to a stationary coil. The theory of electromagnetic induction, and its implementation in a VEH model is described in this section. The scaling theory of electromagnetic energy harvesters is presented in section 7.1.

2.2.1 Electromagnetic induction

The transduction mechanism in an electromagnetic generator is based on Faraday's Law. When a conductor experiences a change in magnetic field, a voltage, V_{ind}, is induced, which is equal to the temporal rate of change of magnetic flux, ϕ. This can be rewritten as the product of the magnetic flux gradient and the

relative velocity between the coil and magnetic field:

$$V_{ind} = -\frac{d\phi}{dt} = -\frac{d\phi}{dz}\dot{z} \tag{2.15}$$

In oscillatory energy harvesters, an electromagnetic transducer can be configured in multiple ways to achieve a temporally-varying flux. These transducer configurations can be broadly characterised by two designs: magnet-through-coil and magnet-across-coil, where the relative motion of the magnet and coil is axial and transverse, respectively (Cheng and Arnold, 2010; Spreemann *et al.*, 2008; Yamamoto and Trimble, 2016). In this thesis, the magnet-through-coil configuration is employed as it is readily implemented in VAEGs by including a magnet in the smallest mass with a coil arranged concentrically to it (figure 2.3a). The remaining theory is specific to magnet-through-coil configurations.

Considering initially a conductor composed of a single wire loop of radius r_m and length $l_w = 2\pi r_m$, which is moved through a non-uniform magnetic field from position z_1 to z_2, as illustrated in figure 2.3. The flux in the loop, ϕ, at z_1 is defined as:

$$\phi = \int B_{z_1} dA \tag{2.16}$$

where B_z is the magnetic flux density perpendicular to the coil area and $A = \pi r_m^2$ is the area enclosed by the coil. Hence, the change in flux in the coil in moving from z_1 to z_2 is:

$$d\phi = \int B_{z_1} dA - \int B_{z_2} dA \tag{2.17}$$

The difference in the flux cutting the coil perpendicular to its surface at z_1 and z_2 is the radial flux which cuts A_l, the virtual cylindrical surface resulting from the motion of the coil loop from z_1 to z_2. This can be seen clearly in figure 2.3b. Considering this relationship between B_z and B_r allows a new expression for the change in flux to be derived:

$$d\phi = \int B_r dA_l \tag{2.18}$$

where B_r is the radial flux density.

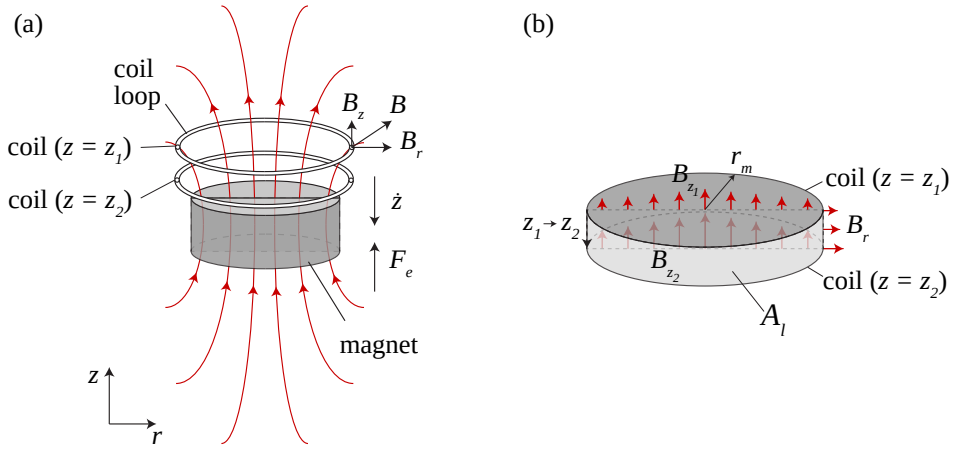

Figure 2.3: (a) Magnetic flux through a single coil loop of radius r_m and length l_w—the coil is moving at velocity $\dot{z}$ relative to the magnet, through the non-uniform magnetic field B; (b) wire loop moved from z_1 to z_2—A_l is the cylindrical lateral area which results from the coil movement.

The flux gradient is then the change in flux divided by the displacement over which it occurs:

$$\frac{d\phi}{dz} = \frac{\int B_r dA_l}{dz} \tag{2.19}$$

Assuming that the coil area and length are constant, the average radial flux density $\bar{B}_r$ can be taken to eliminate the integral:

$$\frac{\int B_r dA_l}{dz} = \frac{A_l}{dz}\bar{B}_r \tag{2.20}$$

Inserting lateral area $A_l = l_w dz$:

$$\frac{d\phi}{dz} = \frac{A_l}{dz}\bar{B}_r = \frac{l_w dz}{dz}\bar{B}_r = \bar{B}_r l_w \tag{2.21}$$

The flux gradient, often termed as the transduction factor, K, is the link between the mechanical and electrical domains:

$$K = \frac{d\phi}{dz} = \bar{B}_r l_w \tag{2.22}$$

Substituting equation 2.22 into equation 2.15 gives a new expression for the in-

duced voltage:

$$V_{ind} = -K\dot{z} \tag{2.23}$$

Applying this derivation to a multi-turn coil yields the same result, with l being the total length of the coil, rather than the length of a single turn.

The movement of the coil through the magnetic field also results in an electrical damping force known as the Lorentz force, F_e. This damping force—which opposes the relative motion of the coil and magnet—is a consequence of the energy extracted from the system:

$$F_e = Ki \tag{2.24}$$

where i is the current.

2.2.2 Modelling the transduction factor

For simplicity, the transduction factor K is often assumed to be constant in the analysis of electromagnetic energy harvesters. This assumption is valid if the displacement of the inertial mass is small. VAEGs, however, exhibit relatively large displacements. Therefore, to accurately model a VAEG, a transduction factor that varies with axial displacement, $K(z)$, is necessary. The process used to determine $K(z)$ in this thesis, outlined below, is illustrated in figure 2.4.

- A plot of the magnetic flux density produced by a cylindrical permanent magnet is shown in figure 2.4a. Only half of the magnet is shown as the magnetic field is symmetrical about its axis. The permanent magnet is modelled using COMSOL multi-physics—this requires a residual flux density, B_{res}, and magnet orientation as input parameters. A multi-turn coil is shown at its zero position relative to the magnet, as a white rectangle.

- The radial magnetic flux density B_r in the axial direction is shown in figure 2.4b, at a range of radial distances. For the given coil arrangement, the average radial flux density $\bar{B}_r$ is calculated by averaging B_r in the coil radial direction.

- The transduction factor is then the product of $\bar{B}_r$ over the total coil length, as derived in equation 2.21. This is calculated for a range of coil positions

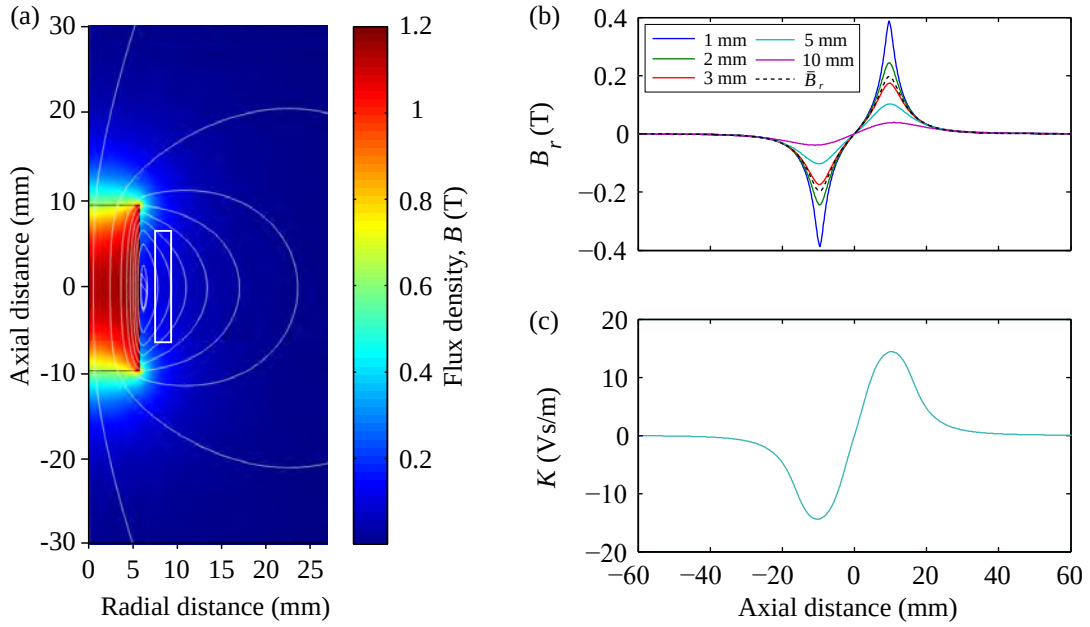

Figure 2.4: (a) Magnetic flux density of a cylindrical permanent magnet with flux lines (right half only shown)—white rectangle represents coil at zero-position, (b) radial flux B_r along the axial direction at a range of radial distances from the surface of the magnet—average radial flux over coil radial thickness shown as dashed black line, and (c) transduction factor K for varying coil positions relative to the magnet. This process is implemented in chapters 4, 6, and 7.

relative to the magnet. A function is fitted to the result such that K can be determined for any relative coil-magnet position (figure 2.4c).

2.2.3 Electrical circuit representation

The electrical circuit of the electromagnetic energy harvester implemented in this thesis is presented in figure 2.5a. It consists of a generator connected in series with a coil resistance R_C, load resistance R_L, and coil inductance L_C.

Applying Kirchhoff's voltage law to the circuit:

$$V_{ind} = K(z)\dot{z} = L_C\frac{di}{dt} + i(R_C + R_L) \tag{2.25}$$

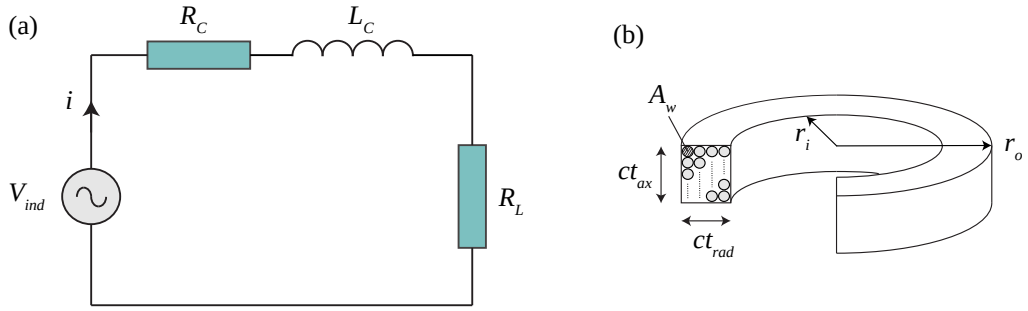

Figure 2.5: (a) Electrical circuit representation of an electromagnetic generator, and (b) multi-turn coil showing the geometric properties of the coil.

where i is current. The coil resistance is given by:

$$R_C = \frac{\rho_c l}{A_w} \tag{2.26}$$

where ρ_c is the resistivity of copper, and A_w is the coil wire cross sectional area. The coil inductance (in μH) is calculated using the Wheeler approximation (Wheeler, 1928):

$$L_C = \frac{0.8(r_m^2 N^2)}{0.0254(6r_m + 9ct_{ax} + 10ct_{rad})} \tag{2.27}$$

where the mean coil radius $r_m = (r_o + r_i)/2$, N is the number of coil turns, ct_{ax} is the coil thickness in the axial direction, and ct_{rad} is the coil thickness in the radial direction (figure 2.5b). Rearranging equation 2.25 and substituting $i = V_L/R_L$ (Ohm's Law) results in a first order ordinary differential equation (ODE) for the load voltage, with a variable electromagnetic transduction factor:

$$\dot{V_L} = K(z)\dot{z}\frac{R_L}{L_C} - \frac{V_L}{L_C}(R_C + R_L) \tag{2.28}$$

This electrical circuit equation is coupled to the equation of motion to model both the mechanical and electrical subsystems.

2.2.4 Coupled model

The coupled mechanical and electrical equations are a system of ODEs which can be solved analytically or numerically. Equation 2.29a is found by inserting

equation 2.24 into equation 2.2 in place of $F_e = c_e\dot{z}$, and substituting $i = V_L/R_L$.

$$m\ddot{z} + c_m\dot{z} + K(z)\frac{V_L}{R_L} + kz = -m\ddot{y} \tag{2.29a}$$

$$\dot{V}_L = K(z)\dot{z}\frac{R_L}{L_C} - \frac{V_L}{L_C}(R_C + R_L) \tag{2.29b}$$

It is evident from equation 2.29b that the load voltage increases with the relative velocity between the magnet and coil, $\dot{z}$. If the excitation frequency is low, the inductor impedance is small ($Z_L = j\omega L_C$) and the impedance is purely resistive. Ignoring the coil inductance, the load voltage is then:

$$V_L = K(z)\Big(\frac{R_L}{R_L + R_C}\Big)\dot{z} \tag{2.30}$$

Evidently, the load voltage is proportional to the relative velocity ($V_L \propto \dot{z}$). The power in the load is then given by:

$$P_L = \frac{V_L^2}{R_L} \tag{2.31}$$

Therefore, the load power is proportional to the velocity squared ($P_L \propto \dot{z}^2$). A gain in output power is achieved by increasing the relative velocity between the coil and magnetic field. The technique implemented in this thesis to increase $\dot{z}$ and, hence, P_L is referred to as velocity amplification. The theory of velocity amplification is described in the following section.

2.3 Velocity amplification

Velocity amplification is a technique used to collisionally transfer kinetic energy from one mass to a lighter mass in order to increase the velocity of the lighter mass. It is achieved by utilising sequential collisions in a series of free moving masses, where the number of masses and mass ratio control the system performance (Cottone *et al.*, 2013). For electromagnetic generators, an increase in power generation is achieved by increasing the relative velocity between the coil and magnetic field.

Velocity amplification can be employed in multiple-DoF VEHs by coupling of the masses to a transducer. This can be achieved in a number of ways. Permanent magnets can be incorporated into one or more of the masses, which move relative to either a stationary coil, or a coil attached to a different mass in the system. The coil can also function as the proof mass moving relative to a stationary magnetic field. In this thesis, one or multiple magnets are incorporated in the final mass in the stacked mass system, which then oscillates axially relative to a coil (magnet-through-coil) attached to the harvester base.

The velocity amplification technique was investigated in a high acceleration shock testing machine by Rodgers *et al.* (2009). A simple schematic of the vertically stacked, sequentially smaller multi-mass system developed by the authors is shown in figure 2.6. For the sequential pairwise collisions shown, the velocity of the smaller mass increases after each collision until the final mass, m_n, is impacted and rebounds with a velocity significantly higher than the initial velocity of m_1—according to the conservation of momentum. The VAEGs implemented in this thesis are composed of vertically stacked systems of free-moving, monotonically decreasing mass, as in figure 2.6, with springs interposed between the masses to achieve high restitution impacts.

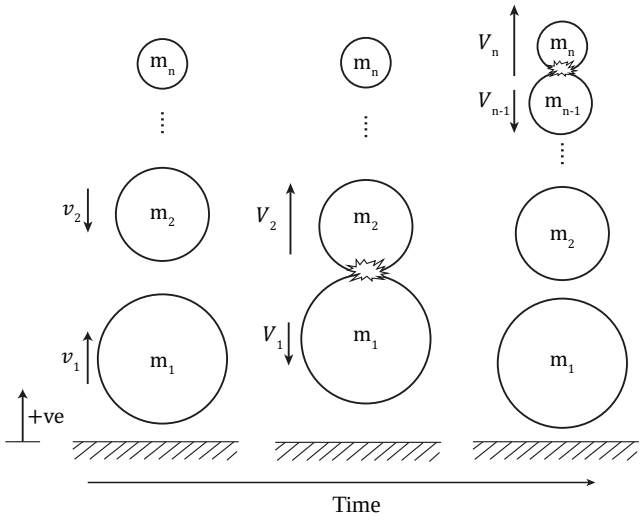

Figure 2.6: System of sequentially smaller vertically stacked impacting masses. The velocity of a mass before an impact is v, while the velocity after is V.

Rodgers *et al.* (2009) derived a set of equations for the velocity amplification achieved by each mass in this system. The dynamics of the impact between two sequential masses, for example m_1 and m_2 (figure 2.6) where $m_1 > m_2$, are described for rigid body mechanics. Applying the conservation of momentum results in:

$$m_1 V_1 + m_2 V_2 = m_1 v_1 + m_2 v_2 \tag{2.32}$$

The energy lost in the impact is accounted for through the coefficient of restitution, e, which is described by equation 2.33 for the impact between m_1 and m_2:

$$e_{2,1} = -\frac{V_2 - V_1}{v_2 - v_1} \tag{2.33}$$

For perfectly elastic collisions $e = 1$.

By combining equation 2.32 and equation 2.33, a relationship for the velocity amplification of m_2 can be derived:

$$\alpha_2 = \frac{V_2}{v_2} = 1 - \frac{1}{1 + 1/r_{1,2}}(1 + e_{2,1})(1 - \frac{1}{q_{2,1}}) \tag{2.34}$$

where the mass ratio $r_{1,2}$ and the initial velocity ratio $q_{2,1}$ of the masses are defined as:

$$r_{1,2} = \frac{m_1}{m_2} \tag{2.35}$$

$$q_{2,1} = \frac{v_2}{v_1} \tag{2.36}$$

Given a system of n masses, with base mass m_1, final mass m_n and a uniform coefficient of restitution, the maximum velocity gain that can be attained by m_n is achieved by choosing the pairwise mass ratio according to the power-law relationship described by equation 2.37:

$$r_{k-1,k} = R^{\frac{1}{n-1}} \tag{2.37}$$

where R is the final mass ratio:

$$R = \frac{m_1}{m_n} \tag{2.38}$$

This relationship has been demonstrated by a number of authors—Hart and Herman (1968); Kerwin (1972); Thorsten and Brilliantov (2001)—and is the relationship employed to determine the intermediate masses in the multi-DoF systems in chapters 4 and 5.

The overall velocity gain G_n, achieved by an n-DoF system is then:

$$G_n = (1 + e_{1,0}) \prod_{k=2}^{n} \left(\frac{1 + e_{k,k-1}}{1 + r_{k,k-1}} \right) - 1 \tag{2.39}$$

It is evident from equation 2.39 and equation 2.35 that the smaller m_2 is relative to m_1, the greater the velocity gain. Velocity amplification of the final mass in the system also increases with increasing number of intermediate masses (number of masses between the base mass and the final mass) provided the coefficient of restitution is sufficiently high. The theoretical velocity gains achieved by n-DoF systems for elastic collisions ($e = 1$), as described by equation 2.39, are shown in figure 2.7.

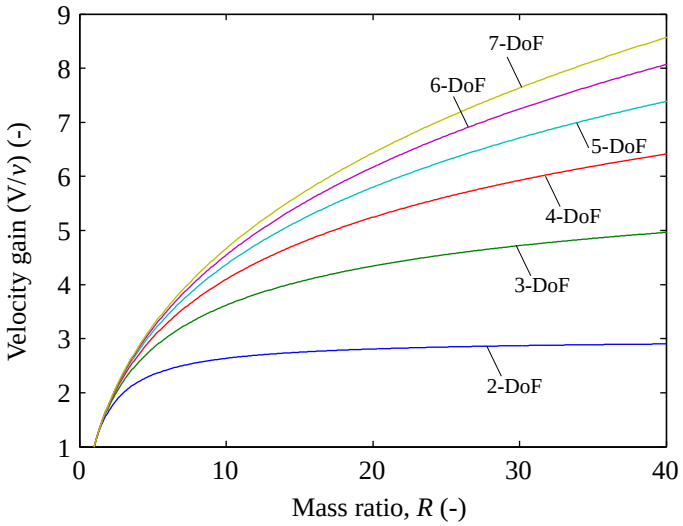

Figure 2.7: Velocity gain as a function of the number of masses and the mass ratio for $e = 1$.

For realistic systems where the collisions are inelastic ($e < 1$), the velocity gain does not increase monotonically with increasing number of masses because the extra losses due to additional impacts ultimately dissipate too much energy

from the system. This is demonstrated experimentally in section 5.2. The final velocity gain that can be achieved decreases rapidly with decreasing coefficient of restitution such that no velocity amplification occurs at values of $e < 0.35$ (Rodgers *et al.*, 2009). The experimentally measured coefficient of restitution values exhibited by the harvesters developed in this thesis are in the range $e = 0.9$–0.97.

The phasing of impacts in a velocity amplified system is also very important. For drop-tests, the impacts are sequential and pairwise (i.e. optimally phased). Under forced excitation this will not always be the case, resulting in lower velocity gains. This is due to the changing sequence in which the masses impact each other and the housing, as a result of the device being excited by sinusoidal vibrations. If the velocity of the larger mass is negative at the time of impact with a smaller mass, then the velocity gain of the smaller mass will be < 1 (i.e. this leads to a decrease in velocity and subsequent degradation of output power). Velocity amplification under forced excitation is described in further detail for 2-, 3-, and 4-DoF stacked mass systems through simulation in section 4.2.2, and experimentally in section 5.3.

2.4 Closure

The general equations describing a linear inertial energy harvester based on the equation of motion have been developed, while EDAM, the condition for maximising the power delivered to the load in such as system, was described.

The theory of electromagnetic induction and its application in an energy harvester has been described for spatially varying flux within a coil. A set of coupled ODEs describing the mechanical and electrical subsystems of the linear inertial electromagnetic energy harvester have been presented. It has been shown that the output voltage and power increase with the relative velocity between the coil and magnetic field. The equations presented are expanded upon in chapter 4 to model single- and multi-DoF PWL harvesters and investigate their non-linear behaviour. The model is further employed in chapters 6 and 7 to investigate the influence of a range of geometric and excitation parameters, as well the effect of scaling on a VAEG.

Velocity amplification, the principle on which VAEGs are built has also been described. The relative velocity between a coil and magnetic field is increased through collisions between masses in multi-DoF stacked mass systems. The final velocity gain increases with both number of DoFs and mass ratio. A high coefficient of restitution is also important in achieving a high velocity gain. These results are valid for sequential pairwise collisions, which is investigated experimentally in section 5.2 through drop-tests. The performance of such systems under forced excitation is the focus of much of the rest of this thesis, with the influence of mass ratio, number of DoFs, excitation frequency and acceleration, and the initial gap (a geometric parameter) investigated experimentally and numerically in chapters 4–7.

Chapter 3

Experimentation and methods

A description of the methods of experimentation employed in this thesis is provided in this chapter. A drop-testing mechanism employing high-speed imagery for measuring velocity amplification under optimal conditions is described, along with a sub-pixel resolution object tracking algorithm. Sinusoidal forced excitation—using a permanent magnet shaker—was the primary method of testing. The forced excitation experimental set-up and control system is described, along with the measurement techniques and sensors utilised; these included a laser Doppler vibrometer (LDV) and high-speed camera for velocity measurement, an accelerometer to measure the acceleration of the shaker head, and the measurement of the harvester voltage across a load resistor. Finally, the uncertainty associated with each experimental technique is discussed.

3.1 Drop-test

Velocity amplification theory states that the velocity gain on impact in a series of masses increases with mass ratio and number of DoFs. The validity of this theory is tested initially under optimal sequential pairwise collisions, before being tested under forced excitation. A drop-testing facility was developed to validate the theoretical velocity amplification model, presented in section 2.3, with experimental data. A high-speed camera recorded each drop-test, and an image processing technique was developed to track the motion of the masses with sub-pixel reso-

lution. The drop-testing apparatus and object tracking technique, described in this section, are implemented in section 5.2 and 5.3.

3.1.1 Drop-testing apparatus

The drop-testing facility—shown in figure 3.1—provides sequential, pairwise collisions between the masses in a multi-DoF stacked mass system. It consists of adjustable support arms upon which the masses rest. The number of arms, and their position, is configurable with that of the masses, ensuring sequential pairwise collisions between the masses. The system is actuated by rotating its central spine. A cam component in the cap and base of the system, upon rotation, causes outward translation of the support arms, allowing each of the masses to fall at the same instant.

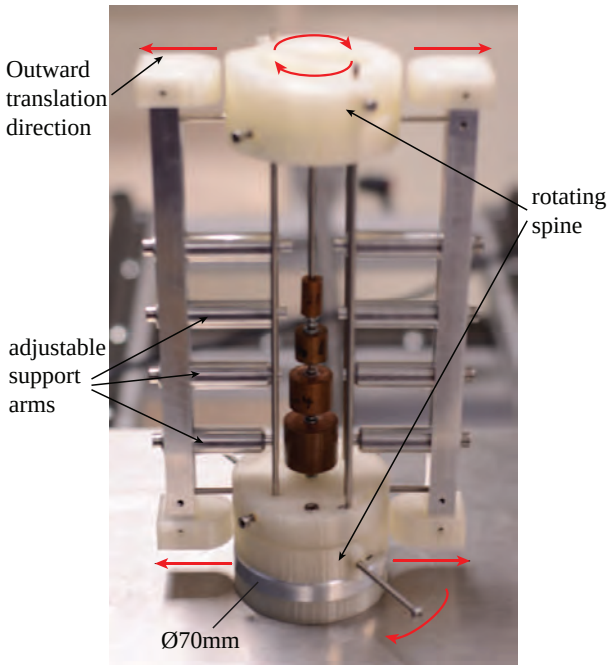

Figure 3.1: Drop-testing mechanism developed to achieve sequential pair-wise collisions between masses, in open position (masses released).

A Phantom high-speed camera (model v311) was employed to record each drop-test. To temporally resolve the impacts between the masses and, hence, the peak velocities, a high frame rate of 2000 frames per second (fps) was used. Each

test was repeated ten times to ensure independent and identically distributed observations. A schematic of the experimental set-up is shown in figure 3.2. A Nikkor 300 mm f/4D telephoto lens was used in order to achieve an orthographic view of the masses, hence limiting perspective effects. The images were backlit by placing an illuminated screen behind the system being tested. The resulting images of the masses were high contrast and rectilinear, which permitted accurate object detection.

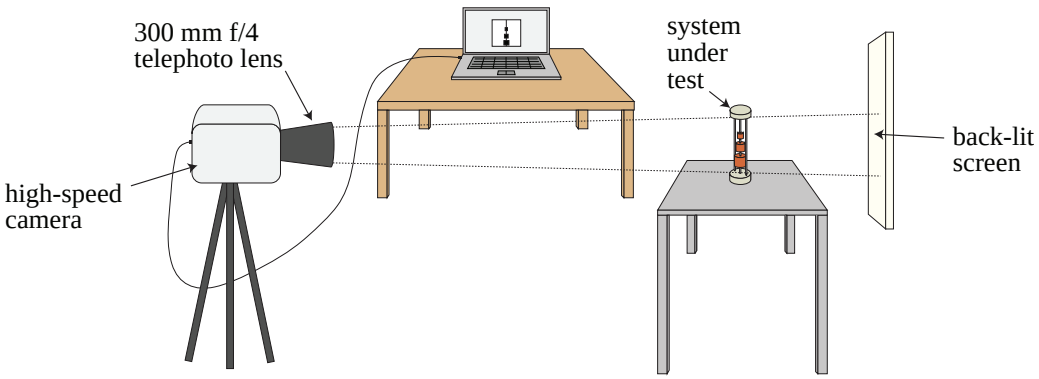

Figure 3.2: Schematic of high-speed imaging set-up.

3.1.2 Image processing

For the drop-test calculations, it was necessary to accurately measure the velocity of each of the masses recorded in the high-speed video. The accuracy of a first order approach to object tracking was limited by the resolution of the camera, which was 1280 pixels in the vertical direction. It was found that measurement of the peak velocity was subject to considerable spatial aliasing using this technique; therefore, a sub-pixel resolution approach was developed.

The algorithm worked by converting each frame of the high-speed video to a greyscale image (figure 3.3a and b) and examining the gradient along the vertical direction (figure 3.3c). This gradient was used to find the mass edges, and a one-dimensional cross-correlation of this data was calculated. A Gaussian distribution was fitted to the output of the cross-correlation function (figure 3.3d). This method allowed the displacement of the masses to be assumed in a manner that was not limited by the pixel resolution of the camera. The time-step between

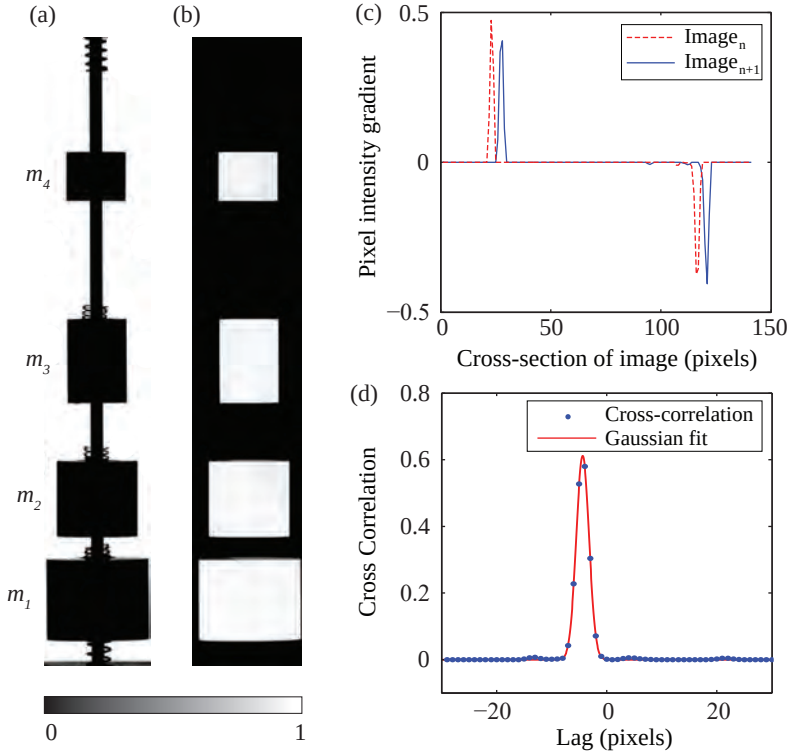

Figure 3.3: (a) High contrast raw image captured by high-speed camera. (b) Filtered grey-scale image from pixel intensity 0–1 (black–white) with individual masses isolated. (c) Gradient of pixel intensity across cross-section of mass in consecutive images. (d) Cross-correlation of gradients and fitted Gaussian model.

images allowed the velocity of the masses to be calculated from the displacement data. Similar methods have been employed to increase the accuracy of two-dimensional displacement measurements in particle image velocimetry (PIV) for flow visualisation (Fore, 2010; Nobach and Honkanen, 2005; Westerweel, 1997).

An example of the velocity profiles achieved using this tracking method is shown in figure 3.4. The initial downward slope in the velocity of all the masses shows that each of them are released at approximately the same instant and fall at constant acceleration (under gravity). The base mass, m_1, rebounds off the base and impacts the next mass, m_2. This process continues until the final mass, m_4, is impacted. The increase in velocity of each mass after it has been impacted by a heavier mass is evident, with the final mass moving at a significantly higher velocity (2.18 m/s) than the initial velocity of the base mass (0.46 m/s). The

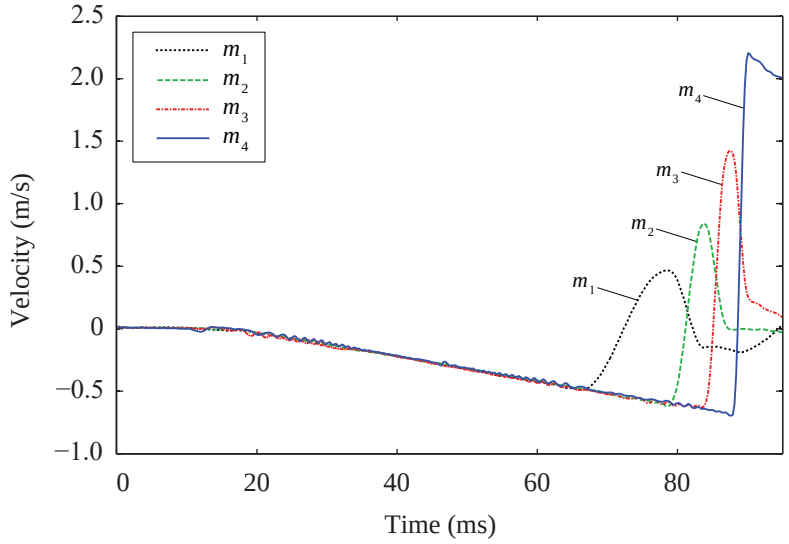

Figure 3.4: Velocity profile of drop-test for 4-DoF configuration showing initial free-fall followed by sequential pair-wise collisions.

shape of the velocity profile of m_4 differs from the profiles of the other masses as, after impact, m_4 moves freely, decelerating under the influence of gravity. The masses lower down the chain, meanwhile, experience impacts immediately after reaching their peak velocity.

3.2 Forced excitation

In an application environment, VEHs are excited by forced excitation. A significant issue in designing an energy harvester is that the spectra of real vibrations vary significantly with the vibrating source, ranging from harmonic excitation to white noise (Green *et al.*, 2012*a*). The measured spectra of some real vibrating sources were presented in section 1.1 (figure 1.1). In this thesis, harmonic excitation only is considered, with the experimental apparatus employed to provide sinusoidal forced excitation to the systems under test described in this section. Harmonic excitation was deemed an appropriate characterisation method as many vibrating sources demonstrate significant peaks in the spectral response (for example, the vibrations from a car engine illustrated in figure 1.1a).

Experimental results under sinusoidal forced excitation are presented in chapters 4–7. Two variations of this experimental apparatus were employed, with the most significant difference between the two being the control mechanism used.

A schematic of the first variation of the experimental set-up—implemented in chapter 5—is illustrated in figure 3.5. The system under test, a 3-DoF VAEG in the schematic, was mounted on the head of the V406 permanent magnet shaker. The shaker excited the system sinusoidally at the desired frequency and acceleration. To achieve these desired excitation conditions, a PID controller—developed with LabVIEW—was used to supply a voltage signal to the shaker through a power amplifier. A high sensitivity (508 mV/g) PCB Piezotronics accelerometer mounted on the shaker head measured the acceleration of the shaker, with the output signal providing feedback control to LabVIEW, relayed to the attached PC through a National Instruments data acquisition (DAQ) card. In each case, the harvesters were positioned vertically, as shown in figure 3.5. A high-speed camera was employed—as described in section 3.1.1—to analyse the system dynamics under forced excitation for the test series in section 5.3.1.

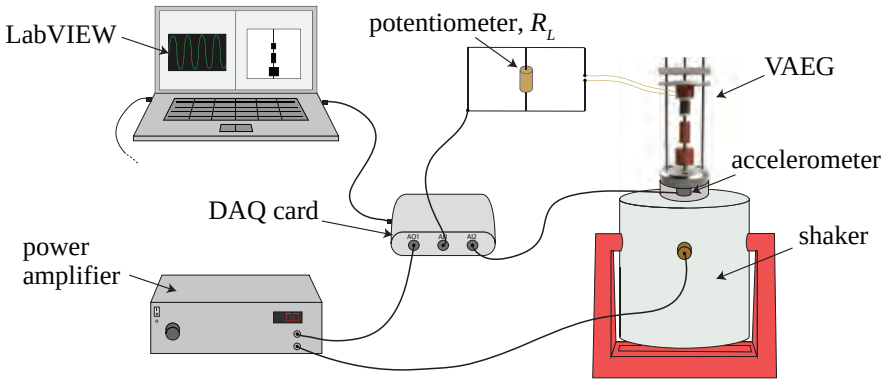

Figure 3.5: Schematic of the experimental set-up used in forced excitation tests for voltage measurements—LabVIEW used as shaker controller.

The harvesters under investigation in this thesis (VAEGs) utilised electromagnetic induction to extract electrical energy from the mechanical system. Measuring the output from the electrical system involved attaching the coil to a load of a known resistance value. The voltage generated in the coil was then recorded across this load resistor using LabVIEW.

As the masses in the multi-DoF velocity amplified systems could detach from the springs, the force experienced by the shaker head was discontinuous, i.e. the force changed depending on whether the masses were in contact with the springs anchored to the base and cap. Active control of the excitation was difficult, with large accelerations which were not a result of the input signal being registered by the accelerometer as a result of the discontinuous force acting on the shaker head. To counteract this issue, the masses were locked in place until the controller reached the input frequency and acceleration. The closed loop control system was then deactivated, fixing the driving signal, and the masses were released. This allowed the shaker to continue vibrating at the desired frequency and acceleration. The locking mechanism—which was a spacer placed underneath the base mass—prevented the masses from decoupling themselves from the springs, thus, mitigating the effect of impacts between the masses and the base and cap. The spacer used was light relative to the overall mass of the harvester system; therefore, it can be assumed that it did not have a significant influence on the final amplitude of the driving signal. A similar approach to the one described above was previously implemented by Frizzell *et al.* (2016).

The second variation of the experimental set-up was employed in chapters 4, 6, and 7. In this case, the shaker excitation was controlled by a Dactron Comet shaker control system, with the accelerometer again providing feedback to the controller. This controller allowed bidirectional frequency sweeps to be employed. The previous issues with active control were mitigated by reducing the mass of the oscillating components of the harvesters, while increasing the total mass of the system. Total mass was increased by adding a copper base to the harvesters. The impacts between the masses and the base, thus, had a lesser effect on the shaker acceleration profile, distorting the signal only marginally. A sample time-trace from the accelerometer is shown in figure 3.6 demonstrating that the response is approximately harmonic. An LDV was also employed in this set-up to measure the velocity of the magnet stack under forced excitation. A schematic of this second forced excitation experimental apparatus is shown in figure 3.7 (photograph in figure 3.8).

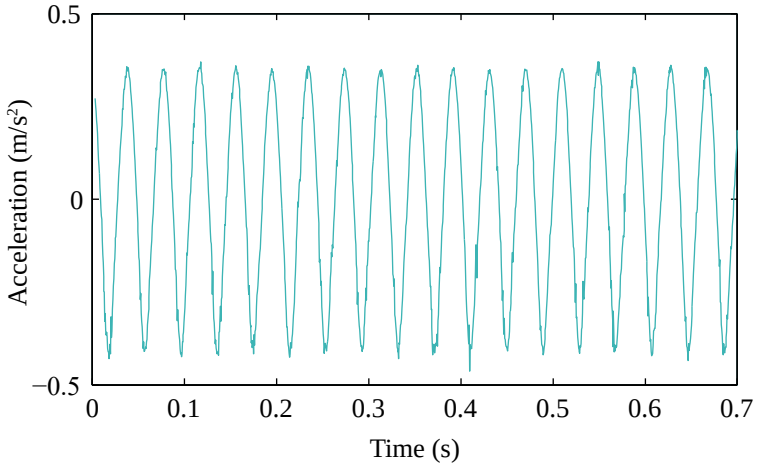

Figure 3.6: Accelerometer time-trace from shaker demonstrating an approximately sinusoidal profile with a VAEG in operation.

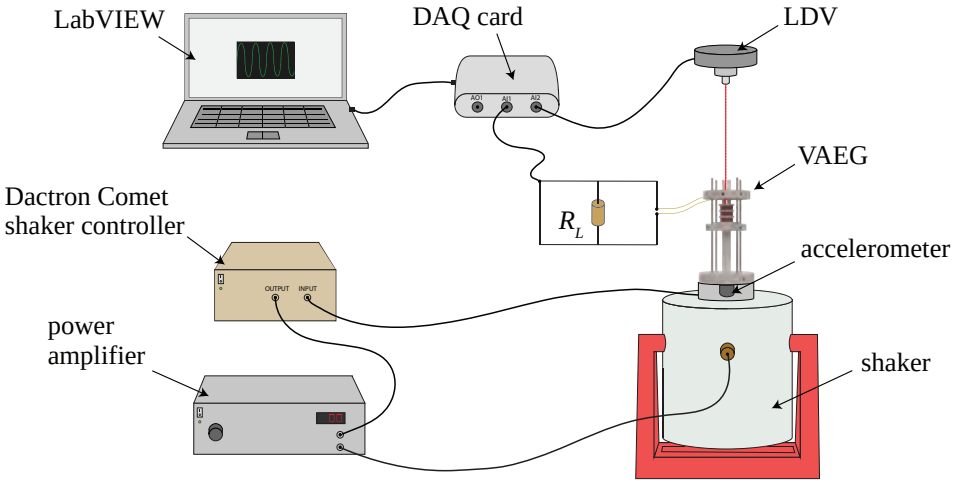

Figure 3.7: Schematic of the experimental set-up used in forced excitation tests for voltage and velocity measurements—Dactron Comet shaker control system employed.

3.3 Uncertainty analysis

Experimental error is defined as the difference between a measured value and its true value. In most situations, the true value is unknown; hence, the term uncertainty is used to describe the value the error may have (Holman, 1971; Kline and McClintock, 1953; Moffat, 1988). The different types of error which can affect a measurement, described by Holman (1971), are significant, fixed and

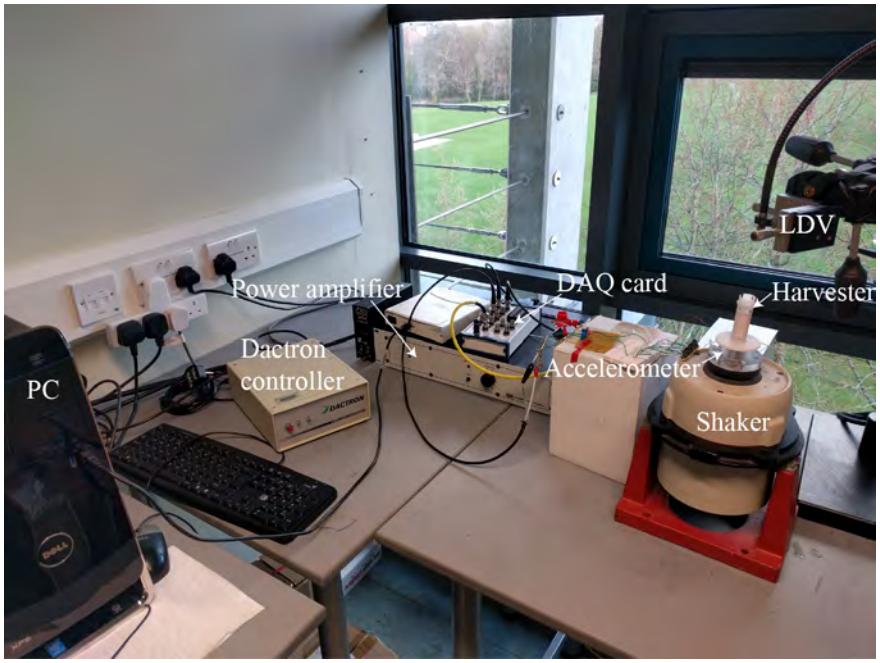

Figure 3.8: Photograph of the experimental set-up used in forced excitation tests for voltage and velocity measurements.

random errors. Efforts were made to mitigate these errors in the experimental work herein. A method of estimating uncertainty in experimental systems is described in this section, followed by a discussion of the uncertainty in the data measured.

3.3.1 Experimental uncertainty

Kline and McClintock (1953) presented a method of determining the uncertainty present in the measurement of a parameter, which is a function of n primary variables—$R = R(x_1, x_2, ..., x_n)$—where the uncertainty of each can be stated with the same confidence. The equation describing the uncertainty in the calculated result, w_R, is:

$$w_R = \left[\left(\frac{\delta R}{\delta x_1} w_1 \right)^2 + \left(\frac{\delta R}{\delta x_2} w_2 \right)^2 + ... + \left(\frac{\delta R}{\delta x_n} w_n \right)^2 \right]^{\frac{1}{2}} \tag{3.1}$$

The uncertainty in derived quantities (i.e. functions of experimental primary measurements), determined using equation 3.1, are outlined in the following subsections, along with the uncertainties in the primary measurements.

3.3.2 Power measurement

Sources of uncertainty in the calculated power include voltage and load resistance measurement. Applying equation 3.1 to equation 2.31 describing the load power, P_L, yields:

$$\frac{w_{P_L}}{P_L} = \left[4\left(\frac{w_{V_L}}{V_L}\right)^2 + \left(\frac{w_{R_L}}{R_L}\right)^2\right]^{\frac{1}{2}} \tag{3.2}$$

The output voltage from the harvester was measured by a National Instruments DAQ device (NI PCI-6251), which had a stated accuracy of $\pm 1\%$. A multimeter with an accuracy of $\pm 0.7\%$ was employed to measure the load (potentiometer) resistance. Inputting these parameters into equation 3.2 yields an uncertainty of 2.12% in the power measurements. This uncertainty is small and would not be significant graphically; consequently, uncertainty bars are not presented with the power data.

3.3.3 High-speed imaging—velocity measurement

The drop-test and forced excitation tests were recorded at frame rates of 2000 and 1000 fps, respectively. These frame rates were significantly higher than the frequency of the motion under the test conditions, so the frequency of the response was deemed to be captured accurately.

Equation 3.3 gives the velocity of a mass moving in the vertical plane, which is calculated as the mass displacement between an image pair, δx, divided by the time interval, δt. The displacement, δx, is a product of the pixel displacement, x_{px}, and the pixel length, l_{px}:

$$\dot{x} = \frac{\delta x}{\delta t} = \frac{x_{px} l_{px}}{\delta t} \tag{3.3}$$

The uncertainty in the high-speed imagery velocity measurements can, thus, be

calculated using equation 3.4, derived from equation 3.1.

$$\frac{w_{\dot{x}}}{\dot{x}} = \left[\left(\frac{w_{x_{px}}}{x_{px}}\right)^2 + \left(\frac{w_{l_{px}}}{l_{px}}\right)^2 + \left(\frac{-w_{\delta t}}{\delta t}\right)^2\right]^{\frac{1}{2}} \tag{3.4}$$

The uncertainty in the measurement of each of the independent variables is as follows:

- The pixel displacement, x_{px}, determined from the Gaussian sub-pixel tracking algorithm (section 3.1.2), is dependent on the peak of the Gaussian fit. Forliti *et al.* (2000) demonstrates that the bias error is small using this method, as the image intensity tends toward a Gaussian profile. For the purpose of this analysis, an uncertainty of 5% in the pixel displacement measurement is assumed.

- The pixel length, l_{px}, was calibrated from a known distance in each set of images. This known distance was the diameter of the base mass, measured with a micrometer with an accuracy of ± 2.5 μm. The image length was 1280 pixels in each test; however, in terms of distance, the image length varied, with the longest pixel length being 0.13 mm (for the 4-DoF configuration with a mass ratio of $R = 3$, i.e. the tallest configuration). An uncertainty of 1.9% is assumed to be present in the measurement of the pixel length.

- The time interval between pairs of images is a function of the frame rate, $\delta t = 1/\text{frame rate}$. The timing was accurate to 2×10^{-8} s (from the high-speed camera operating manual), while the minimum time interval between images was 5×10^{-4} s (1/2000 fps). The uncertainty in timing is 0.004% and, therefore, is assumed to be negligible.

Inputting the above values into equation 3.4 yields an uncertainty in velocity measurement of 5.35%.

3.3.4 LDV—velocity measurement

The LDV—Polytec OFV-3001 laser vibrometer controller and OFV-501 fibre interferometer—was utilised to measure the absolute velocity of the oscillating

masses throughout this thesis. Measuring the velocity was of importance as it provides a measure of the harvester performance, with the voltage generated being proportional to velocity. It also allowed for parameter fitting for the single- and multi-DoF models employed in chapters 4, 6 and 7. The voltage output from the LDV controller was multiplied by a conversion factor of 0.125 m/sV to calculate the velocity in m/s. An uncertainty of $\pm 1\%$ in the amplitude of the velocity is assumed to apply (from the LDV operating manual).

3.3.5 Accelerometer—acceleration measurement

The sensor used for measuring the acceleration of the shaker head was a high sensitivity (508 mV/g) PCB Piezotronics accelerometer—model number 353B51. To convert to SI units (m/s^2), the voltage signal from the accelerometer was multiplied by a conversion factor of 19.311 m/s^2V. The frequency response of the accelerometer was linear in the range 1–2000 Hz $\pm$ 5%, with a resonant frequency of 14 kHz. The frequency range of interest in this thesis (< 50 Hz) is orders of magnitude lower than the maximum accurately measurable frequency; hence, uncertainty in frequency is deemed to be negligible.

3.4 Closure

The methods of experimentation employed in this thesis were outlined in this chapter. A drop-testing apparatus employing high-speed imagery, along with a sub-pixel accurate object tracking algorithm was presented. The forced excitation set-ups were described for different methods of shaker control. Finally, the uncertainties in the various experimental measurements were evaluated and discussed. The uncertainties are, in general, $< 2.2\%$, with the exception of the velocity from the high-speed imagery (5.3%).

Chapter 4

Non-linear analysis of piecewise linear harvesters

The multi-DoF VAEGs presented in this thesis are modelled as piecewise linear (PWL) inertial oscillators. Although the dynamics of PWL systems are linear almost everywhere, their global behaviour is non-linear. In this chapter, non-linear analysis techniques are utilised to investigate the influence of geometric and excitation parameters on the dynamics of single-DoF (section 4.1) and multi-DoF (section 4.2) PWL energy harvesters. These non-linear analysis techniques include bidirectional sweeps, stroboscopic maps, phase diagrams, Poincaré maps, and power spectra. Simulations are used as the dynamics of the complete system can be readily analysed, whereas measurement of the effect of the full range of parameters would be non-trivial.

4.1 Single-DoF PWL harvesters

The energy harvesters discussed herein—VAEGs—utilise impacts in free moving masses to achieve velocity amplification, as described in section 2.3. Linear springs interposed between the masses, base, and cap facilitate high restitution impacts. Each mass can, therefore, be forced upon by a spring or can be free of any spring force, resulting in piecewise-linearity or discontinuity. Discontinuity in dynamical systems is a common issue in many engineering applications. It often

arises due to the clearance tolerances in machinery, resulting in play or backlash, which can lead to increased stress and strain, and instability (Kleczka *et al.*, 1992). As such, these discontinuous dynamical systems have received significant investigation in the field of non-linear dynamics (Budd *et al.*, 1995; Hinrichs *et al.*, 1997; Ing *et al.*, 2008; Kleczka *et al.*, 1992; Shaw and Holmes, 1983). Discontinuities arising from impacts have also been investigated to improve the performance of VEHs in systems referred to as impact oscillators (Bendame *et al.*, 2014; El Aroudi *et al.*, 2014; Frizzell *et al.*, 2016; Haroun *et al.*, 2015; Le *et al.*, 2012; Soliman *et al.*, 2009; Wu *et al.*, 2014).

Single-DoF PWL harvesters are analysed in this section as an introduction to the more complex velocity amplified systems, which are described as multi-DoF PWL harvesters. Firstly, the single-DoF model is developed, which is then used to investigate the non-linear behaviour of the system.

4.1.1 Single-DoF PWL harvester in phase space

Considering a single-DoF PWL oscillator, in which the mass oscillates freely between two springs, i.e. the mass can be in contact with either one of the springs, or can be entirely free of any spring force. This gives rise to a discontinuity. A schematic of such a system and its force-displacement diagram are shown in figure 4.1. The initial gap between the mass and the spring affixed to the cap—the stopper spring—is referred to as g_0. The single-DoF PWL energy harvester design is not novel; similar systems have been investigated by Shaw and Holmes (1983) and Kleczka *et al.* (1992) in the field of non-linear dynamics, and by Bendame *et al.* (2014), Haroun *et al.* (2015) and Frizzell *et al.* (2016) for energy harvesting applications. However, as mentioned above, this system is introduced here to aid in the understanding of the more complex multi-dof velocity amplified PWL energy harvesters discussed throughout the remainder of this thesis.

The equation of motion for this system is given by equation 4.1. Unlike the linear system considered in section 2.1, the forces on the mass are not symmetrical; hence, gravity ($g = 9.81$ m/s^2) is included in the equation of motion. A transducer—employed to extract useful energy from the system—is also included

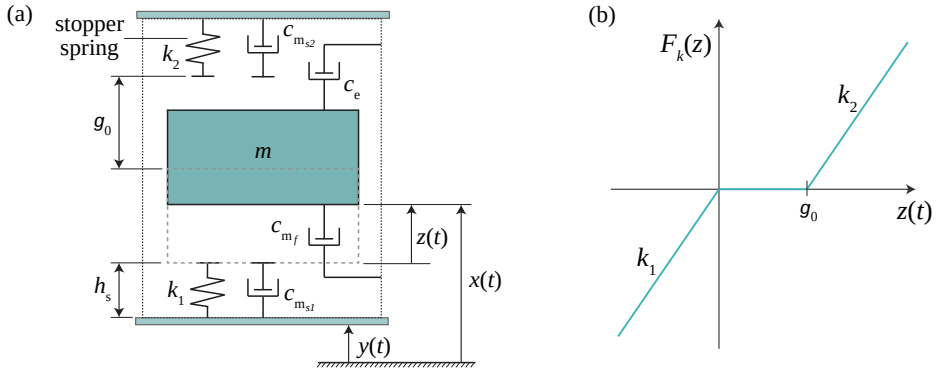

Figure 4.1: (a) Schematic of a single-DoF PWL oscillator and (b) its force-displacement relationship.

in the model.

$$m\ddot{z} + (c_m(z) + c_e)\dot{z} + k(z)z(t) = mg - m\ddot{y} \tag{4.1}$$

where the force due to the PWL stiffness is given by:

$$F_k(z) = k(z)z(t) = \begin{cases} k_1 z(t) & \text{if } z(t) \leq 0 \\ 0, & \text{if } 0 < z(t) < g_0 \\ k_2(z(t) - g_0), & \text{if } z(t) \geq g_0 \end{cases} \tag{4.2}$$

The mechanical damping is modelled by a discontinuous viscous damper, $F_m(z)$. A single viscous damping force, due to friction and air resistance, is applied to the mass when it is disconnected from the springs ($F_f = c_{m_f}\dot{z}$). An additional viscous damping force is applied when in contact with the springs ($F_s = c_{m_s}\dot{z}$). This damping force is due to thermoelastic damping in the springs. The PWL mechanical damping force is then the sum of the damping forces acting for a particular $z(t)$:

$$F_m(z) = c_m(z)\dot{z} = \begin{cases} (c_{m_f} + c_{m_{s1}})\dot{z} & \text{if } z(t) \leq 0 \\ c_{m_f}\dot{z} & \text{if } 0 < z(t) < g_0 \\ (c_{m_f} + c_{m_{s2}})\dot{z} & \text{if } z(t) \leq g_0 \end{cases} \tag{4.3}$$

The damping ratio ζ_s of the spring is equivalent to the damping ratio of the linear

harvester described in section 2.1:

$$\zeta_s = \frac{c_{m_s}}{2m\omega_n} \tag{4.4}$$

As c_{m_f} is not influenced by the spring stiffness, it is assumed to be proportional to mass, and the corresponding damping ratio is, therefore:

$$\zeta_f = \frac{c_{m_f}}{m} \tag{4.5}$$

The dynamics of the system can be analysed by plotting the solution trajectories in the phase plane (z,$v = \dot{z}$). Solving the equation of motion analytically becomes difficult, due to the discontinuous stiffness and damping. Alternatively, numerical ODE solvers can be employed. The MATLAB numerical ODE solver ode45 is utilised to find the solution trajectory for a set of geometric and excitation parameters. This solver requires the second-order system to be represented as a set of first-order ODEs. Time is introduced as an additional state variable to form an extended phase space. For a periodically forced system, the phase angle of the harmonic excitation, $\theta = t \ mod \ 2\pi$, can be included (Jordan and Smith, 1977; Kleczka *et al.*, 1992). The 3-dimensional phase space is defined as:

$$Z = (z, v, \theta) \in \mathbb{R}^2 \times S^1, \quad S^1 = [0, 2\pi) \tag{4.6}$$

Under harmonic excitation, the set of first order equations then becomes:

$$\begin{bmatrix} \dot{z} \\ \dot{v} \\ \dot{\theta} \end{bmatrix} = \begin{bmatrix} v \\ (-k(z)z - c_m(z)\dot{z})/m + g + \omega^2 Y sin(\theta) \\ 1 \end{bmatrix} \tag{4.7}$$

The electrical subsystem, which represents the transducer, is initially ignored in the analysis presented, as it has already been described in section 2.2.

Within the phase space are a number of subspaces, each demonstrating a different type of linear behaviour, i.e. the mass attached and detached from the springs. The PWL function is non-smooth at the interfaces separating these subspaces. These interfaces are called switching surfaces, and intersection of the solution trajectory with one results in a non-smooth change in dynamics between

linear behaviours. The switching surfaces are defined as:

$$S^{-1} = \{(z, v, \theta) \in \mathbb{R}^2 \times S \mid z = 0\} \tag{4.8a}$$

$$S^{+1} = \{(z, v, \theta) \in \mathbb{R}^2 \times S \mid z = g_0\} \tag{4.8b}$$

The switching surfaces are illustrated in extended phase space in figure 4.2a, along with a solution trajectory for a periodic response, which crosses both switching surfaces. Figure 4.2b presents the corresponding phase portrait. The locations where the solution trajectory crosses the switching surfaces are labelled 1–4, while the solutions at $\theta = (0, 2\pi)$ are labelled 0. A Poincaré map can be established by sampling the solution trajectory at an arbitrary, but fixed, phase angle, θ_0, in the range 0–2π (Jordan and Smith, 1977). For a periodic solution, the Poincaré map will be a point. In the analysis presented in this chapter, the Poincaré map is sampled at $\theta_0 = 0$.

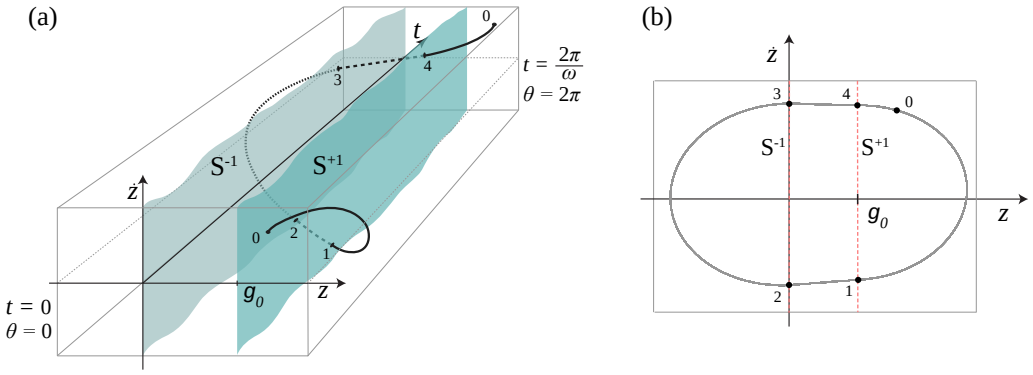

Figure 4.2: (a) Linearly extended phase space and (b) phase-plane; solution trajectory plotted for periodic orbit crossing switching surfaces S^{-1} and S^{+1}.

The set of equations described in equation 4.7 are used to solve for the dynamics of the PWL system. Reintroducing the transduction mechanism into the model, a new system of first order equations is found, allowing the load voltage

to be determined.

$$\begin{bmatrix} \dot{z} \\ \dot{v} \\ \dot{\theta} \\ \dot{V}_L \end{bmatrix} = \begin{bmatrix} v \\ (-k(z)z - c_m(z)\dot{z} - K\frac{V_L}{R_L})/m + g + \omega^2 Y sin(wt) \\ 1 \\ K(z)\dot{z}\frac{R_L}{L_C} - \frac{V_L}{L_C}(R_C + R_L) \end{bmatrix} \tag{4.9}$$

The first order ODE describing the load voltage in an electromagnetic generator was derived in equation 2.29b. The addition of the load voltage equation results in the coupled equations becoming stiff, i.e. the numerical method of solving the equation becomes unstable, as the equations contain terms which can rapidly change the solution. In this case, the MATLAB numerical ODE solver ode15s is a more effective solver. Equation 4.9 is used in the non-linear analysis presented in the following subsection. The velocity component of phase space (figure 4.2) is replaced by load voltage, which is appropriate as the load voltage is proportional to the relative velocity. The 3-dimensional phase space is now defined as $Z = (z, V_L, \theta)$.

4.1.2 Single-DoF PWL harvester sweep analysis

Although the restoring force of the single-DoF PWL oscillator described is linear almost everywhere, the global behaviour is non-linear, due to the discontinuity arising from intersection with a switching surface when the mass either leaves or contacts a spring. This simple system can demonstrate complicated dynamic behaviour such as chaotic motion and coexisting attractors, that is, two different responses can occur under the same excitation. The non-linear behaviour of the system was analysed using bidirectional sweeps, with the influence of the geometric parameter g_0, and the excitation parameters ω and Acc on the dynamics and voltage output of the harvester investigated. The response of the single-DoF PWL system is compared to an equivalent linear harvester at the end of this section.

It was first necessary to determine the parameters to be used in the model, by matching the simulation and experimental responses to bidirectional frequency sweeps. The experimental set-up employed in the sweeps was described in section 3.2 (figure 3.7). A single mass system was used for the validation in the

harvester structure employed in chapters 6 and 7, while the transducer consisted of a magnet and a single coil (see figure 6.1). A linear frequency sweep rate of $f_r = 0.177$ Hz/s was employed in the frequency range 8–40 Hz, resulting in a sweep time of 180 s. Frequency sweeps with the coil removed, were performed to allow the mechanical damping parameters to be fitted. This was done by varying the mechanical damping ratios (ζ_s and ζ_f) until the simulation velocity-frequency response matched the experimental velocity-frequency response. The remaining model parameters were directly measurable, or were known *a priori*. These model parameters, which are representative of the physical system, are listed in table 4.1. The velocity-frequency and voltage-frequency time history responses for simulation and experimental bidirectional frequency sweeps are plotted in figure 4.3. A section of the voltage and velocity-time histories is highlighted in figure 4.4 to directly compare the experimental and simulation responses. Clearly, the model captures both the amplitude and shape of both the velocity and load voltage,

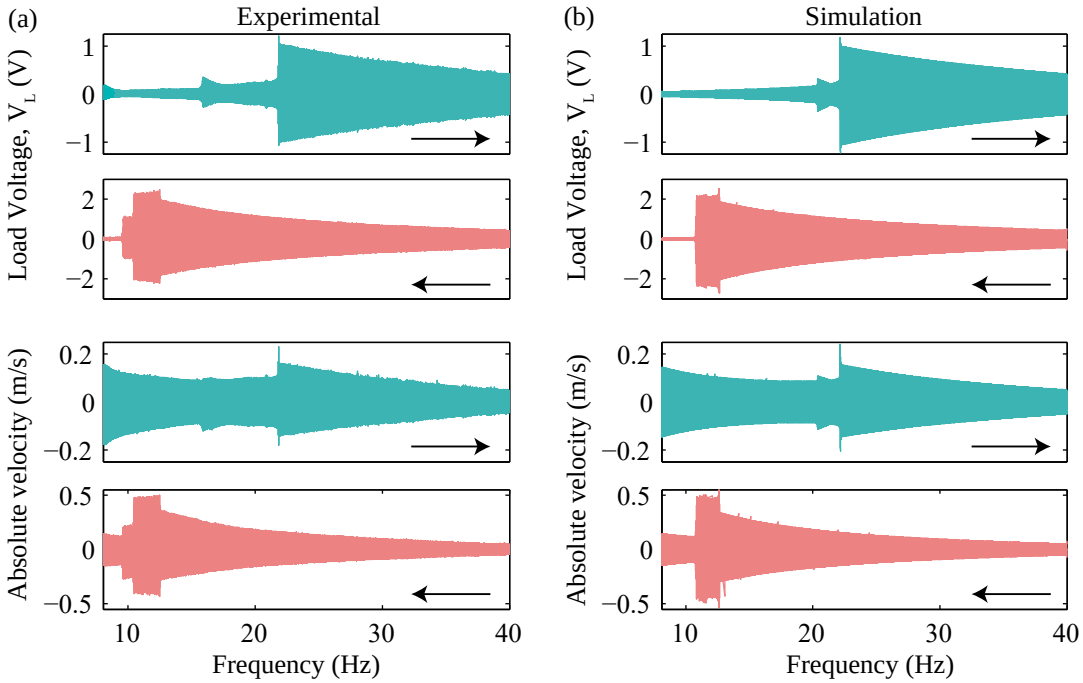

Figure 4.3: (a) Experimental and (b) simulation load voltage and absolute velocity-time histories for bidirectional frequency sweeps—$Acc = 7$ m/s^2, $g_0 = 6.7$ mm; arrow denotes sweep direction.

while the hysteresis behaviour is also captured. An in-depth description of the dynamics is provided later in this section. Since the model has been shown to capture the harvester response, only simulation results are now presented.

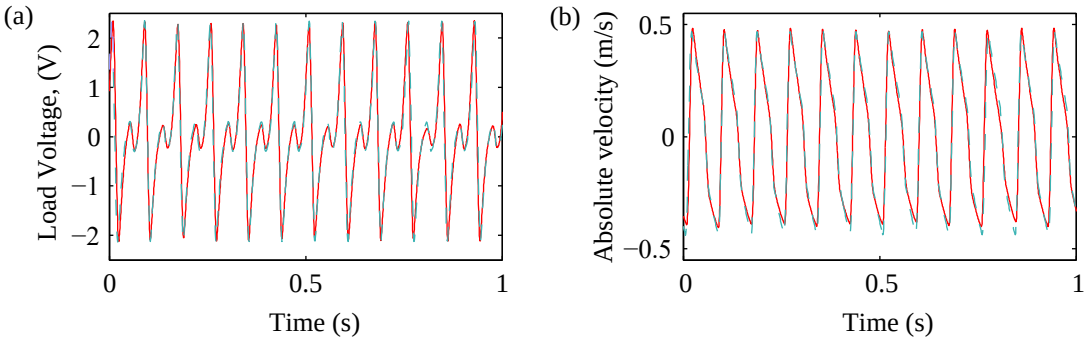

Figure 4.4: Comparison of experimental (——) and simulation (- - - -) (a) load voltage and (b) absolute velocity-time traces—$Acc = 7$ m/s^2, $f = 12.5$ Hz, $g_0 = 6.7$ mm.

A variable electromagnetic transduction factor $K(z)$, as described in section 2.2.2, was implemented in the electrical model validation. For simplicity, in the following simulations, K was taken as a constant. Consequently, the load voltage, V_L, varies linearly with relative velocity, $\dot{z}$. The model parameters used were those listed in table 4.1, with the exception of a constant transduction factor of $K = 5$ Vs/m, which replaced the magnet and coil geometric parameters.

The changing dynamics of the single-DoF PWL system are described using simulated bidirectional frequency sweeps. A linear sweep rate of $f_r = \omega_r/2\pi = 0.375$ Hz/s was employed in the range 5–50 Hz, giving a total sweep time of 120 s. In figures 4.5–4.8, the frequency sweeps are presented as continuously and periodically (stroboscopically) sampled load voltages. Continuous sampling gives the amplitude of the voltage response. Black dots represent the periodic sampling, or stroboscopic map, obtained by sampling the voltage time series at $\theta(t)/2\pi$ (i.e. $\theta_0 = 0$), where $\theta(t) = (\omega_0 + \frac{1}{2}\omega_r t)t$ is a function of the initial frequency ω_0, sweep rate ω_r, and time t. This stroboscopic map reveals the periodicity of the response as a function of excitation frequency. Continuous lines represent a periodic response, while a chaotic response is represented by dispersed dots (Mann and Owens, 2010). Bidirectional sweeps with stroboscopic maps have previously

Table 4.1: Model parameters used in single-DoF PWL harvester frequency sweeps.

Parameter	Value	Unit
m	20.08	g
k_1	910	N/m
k_2	910	N/m
h_{spr}	10	mm
d_{mag}	12	mm
B_{res}	1.35	T
r_i	8.4	mm
r_o	12.8	mm
ct_{ax}	10	mm
N	3412	-
R_C	556	Ω
R_L	653	Ω
L_C	0.2715	H
ζ_s	0.02	-
ζ_f	4.26	1/s
θ_0	0	rad

been utilised to analyse non-linear energy harvesters by Mann and Owens (2010); Masana and Daqaq (2011*b*) and Liu *et al.* (2013).

The significance of sampling the stroboscopic map at $\theta_0 = 0$ is that information about the phase angle between the mass and base can be extracted from stroboscopic map plotted on the time history response. The reason for this is as follows: the base velocity is modelled as $\dot{y} = \omega Y cos(\omega t)$, meaning that, at $\theta_0 = 0$, the velocity of the base is at its peak on the upward trajectory. Consequently, if the stroboscopic map follows the upper edge of the response, the motion of the mass and base are in phase, i.e. the peak upward velocity of the mass corresponds to the peak upward velocity of the base. If the stroboscopic map follows the lower edge of the response, the motion of the mass and base are π radians out of phase, i.e. the peak downward velocity of the mass corresponds to the peak upward

velocity of the base.

Voltage-time traces, and Poincaré maps plotted on phase diagrams are also presented, to aid in the description of the response behaviour. A single frequency, represented by a grey dashed line in the frequency sweeps plots, is selected for analysis in the voltage-time traces and phase diagrams. The switching surfaces are plotted as dashed red lines in the phase diagrams.

The dynamics of a PWL oscillator at a range of acceleration levels is first described. An initial gap of $g_0 = 2$ mm was taken, resulting in switching surfaces S^{-1} and S^{+1} located at $z(t) = 0$ and 2 mm, respectively. The range of dynamics shown by the single-DoF PWL harvester are described as modes of operation:

- **Mode 1—Periodic oscillator:** (figure 4.5, $Acc = 0.5$ m/s^2, sample frequency $f = 32$ Hz) the acceleration amplitude is low and the displacement of the mass is too small to reach the first switching surface, located at the free length of the spring ($z(t) = 0$). Due to the gravitational force, mg, the rest position of the mass is at $z(t) = -0.22$ mm. Provided the displacement of the mass does not exceed the initial displacement, the spring remains in compression, and the system behaves as a linear oscillator; i.e. the response is harmonic with a resonant peak at the linear natural frequency, and there is no hysteresis in the bidirectional sweeps. The Poincaré map is then a single point. The stroboscopic map (the black line formed by the periodically sampled load voltage in figures 4.5a and b) shows that the mass and base motion are in phase (phase angle, $\gamma \approx 0$) at low frequencies, where the stroboscopic map follows the peak of the positive load voltage. Phase angle increases as the frequency is increased, before switching to out of phase motion beyond the resonant frequency ($\gamma \approx \pi$ radians), seen by the stroboscopic mappings following the negative voltages.

- **Mode 2—Single-impact oscillator**: (figure 4.6, $Acc = 3$ m/s^2, sample frequency $f = 25$ Hz) the acceleration is large enough for the displacement of the mass to reach the first switching surface, S^{-1}. The mass leaves the spring for a portion of each cycle, during which it experiences no spring force (seen in the distortion of the voltage-time history and phase portrait).

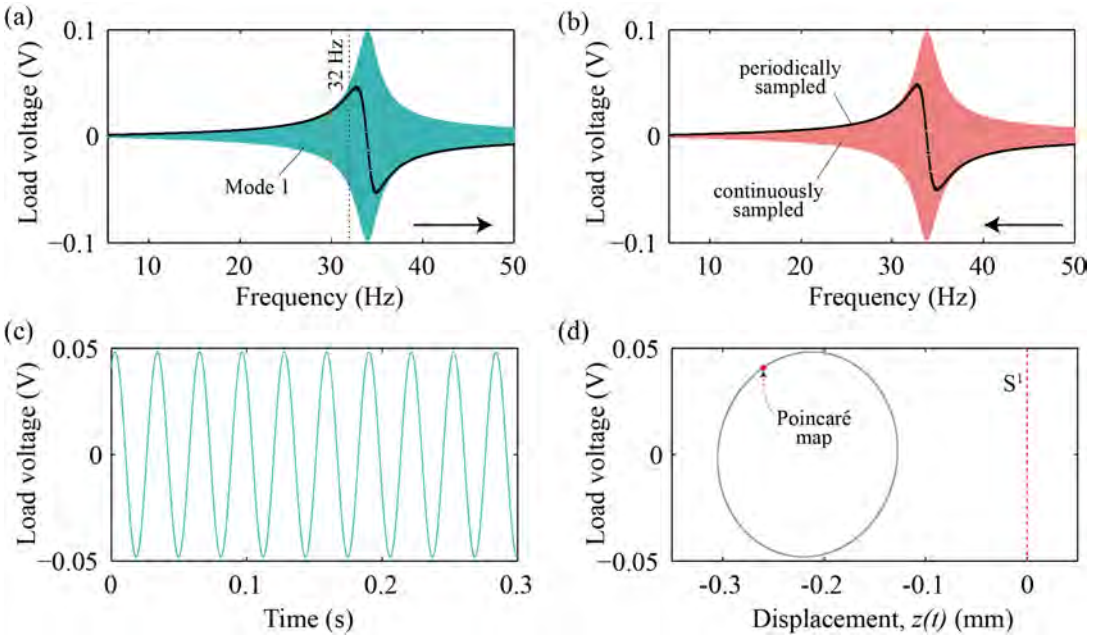

Figure 4.5: Continuously and periodically sampled voltage-time histories for (a) frequency forward-sweep and (b) reverse-sweep. (c) Voltage-time trace at 32 Hz, and (d) corresponding phase portrait and Poincaré map, with switching surface S^{-1}—$Acc = 0.5$ m/s^2, $g_0 = 2$ mm; arrow denotes sweep direction.

This results in a reduction of the effective spring stiffness, which is the time averaged stiffness per cycle given by equation 4.10:

$$k_{eff} = \frac{2\pi}{\omega} \int_0^{2\pi} k dt \tag{4.10}$$

The portion of the cycle in which the mass is in contact with the spring is considered an impact. A system such as this is referred to as an impact oscillator (Bendame *et al.*, 2014; Budd *et al.*, 1995).

In this Mode 2 operation, the motion of the mass and base are $\sim \pi$ radians out of phase, i.e the downwards trajectory of the mass corresponds to the upward trajectory of the base, resulting in maximum energy transfer on impact. This is evident from the stroboscopic map in figure 4.6a and b, with the black dots forming a continuous line on the lower edge of the continuously sampled load voltage for Mode 2 operation. The amplitude of the displacement response is dependent on the excitation frequency; the

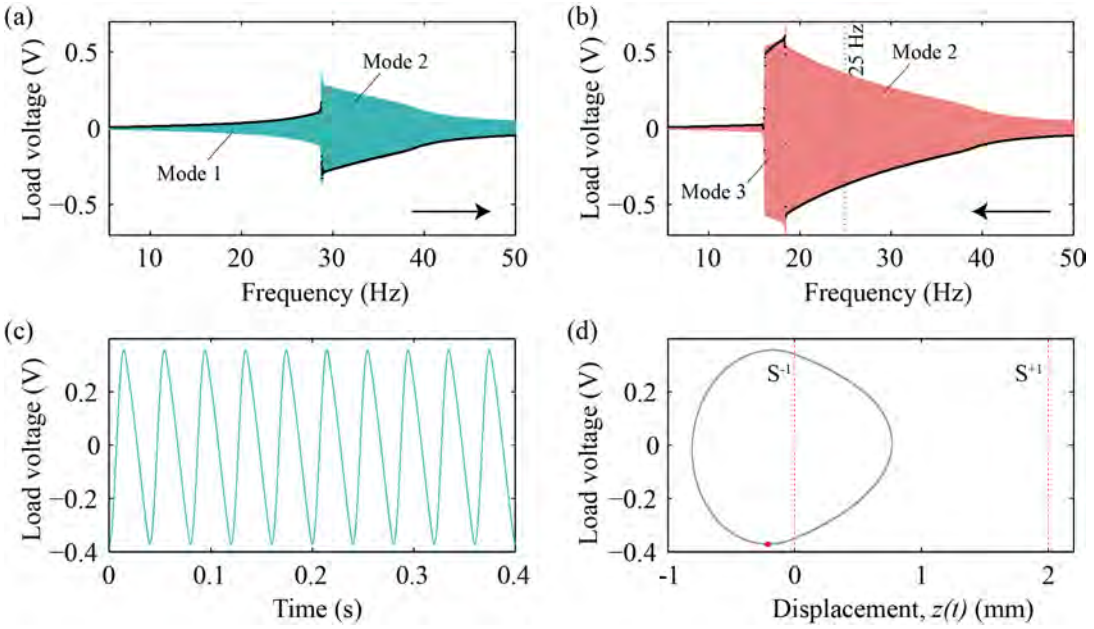

Figure 4.6: Continuously and periodically sampled voltage-time histories for (a) frequency forward-sweep and (b) reverse-sweep. (c) Voltage-time trace at 25 Hz, and (d) corresponding phase portrait and Poincaré map, with switching surfaces S^{-1} and S^{+1}—$Acc = 3$ m/s^2, $g_0 = 2$ mm; arrow denotes sweep direction.

lower the excitation frequency, the greater the displacement amplitude—assuming large amplitude oscillations can be achieved.

On the frequency reverse-sweep, the amplitude of the jump from the spring increases as the frequency is reduced. A softening non-linearity is observed, resulting in hysteresis. A jump-up frequency of $\sim$ 29 Hz is seen in the forward-sweep, while the jump-down frequency is $\sim$ 16 Hz. In the region between the jump-up and jump-down frequencies are two non-unique co-existing responses, respectively known as the high- and low-energy states (Mallick *et al.*, 2015). Entry into either the high- or low-energy state at a particular frequency in this range is dependent on the initial conditions, i.e. the initial position and velocity of the mass. In the regions of coexisting attractors, loss of out-of-phase synchrony of the impacts between the mass and base in the high-energy state results in the system jumping down to the low-energy state. The jump-down frequency is dependent on the damping

in the system; as damping increases, the phase angle changes more quickly and the mass and base loose their synchrony. The jump-down frequency then approaches the jump-up frequency, reducing the peak amplitude and the hysteresis in the response.

- **Mode 3—Double-impact oscillator:** (figure 4.7a–d, $Acc = 10$ m/s^2, sample frequency $f = 28$ Hz) the acceleration is now sufficiently high for the displacement of the mass to reach the second switching surface, S^{+1}. Once the mass reaches the spring at the second switching surface, it has reached the maximum portion of its cycle that it can spend out of contact with the spring. On the frequency forward-sweep, it impacts both springs and its effective stiffness is now increased. The frequency response curve, therefore, bends towards higher frequencies, resulting in a hardening non-linearity.

  Mode 3 operation can again be considered as a synchronisation of impacts, in this case with two impacts per cycle—between the mass and base, and the mass and cap (stopper spring). The mass and base are initially in-phase in Mode 3 operation, with the phase angle increasing as amplitude increases. Despite this not being the condition for maximum energy transfer, high velocities are achieved as a result of the additional energy transferred in the second impact. Synchrony is lost when the phase angle deviates excessively from the in phase motion; again, this is a result of damping. This type of system is referred to as a double-impact oscillator (Peterka, 2000), with Mode 3 operation resulting in high velocity oscillations and, hence, high voltages.

- **Mode 4—Chaotic response:** (figure 4.7a–b,e–f, $Acc = 10$ m/s^2, sample frequency $f = 12$ Hz) the system also demonstrates higher period and chaotic motions which are a combination of the above modes. Clearly, the response is chaotic at the frequency and acceleration level presented, with the Poincaré map becoming a strange attractor. The output from the harvester during chaotic motion contains some relatively large peaks when the impacts between the mass and base are optimally phased, resulting in

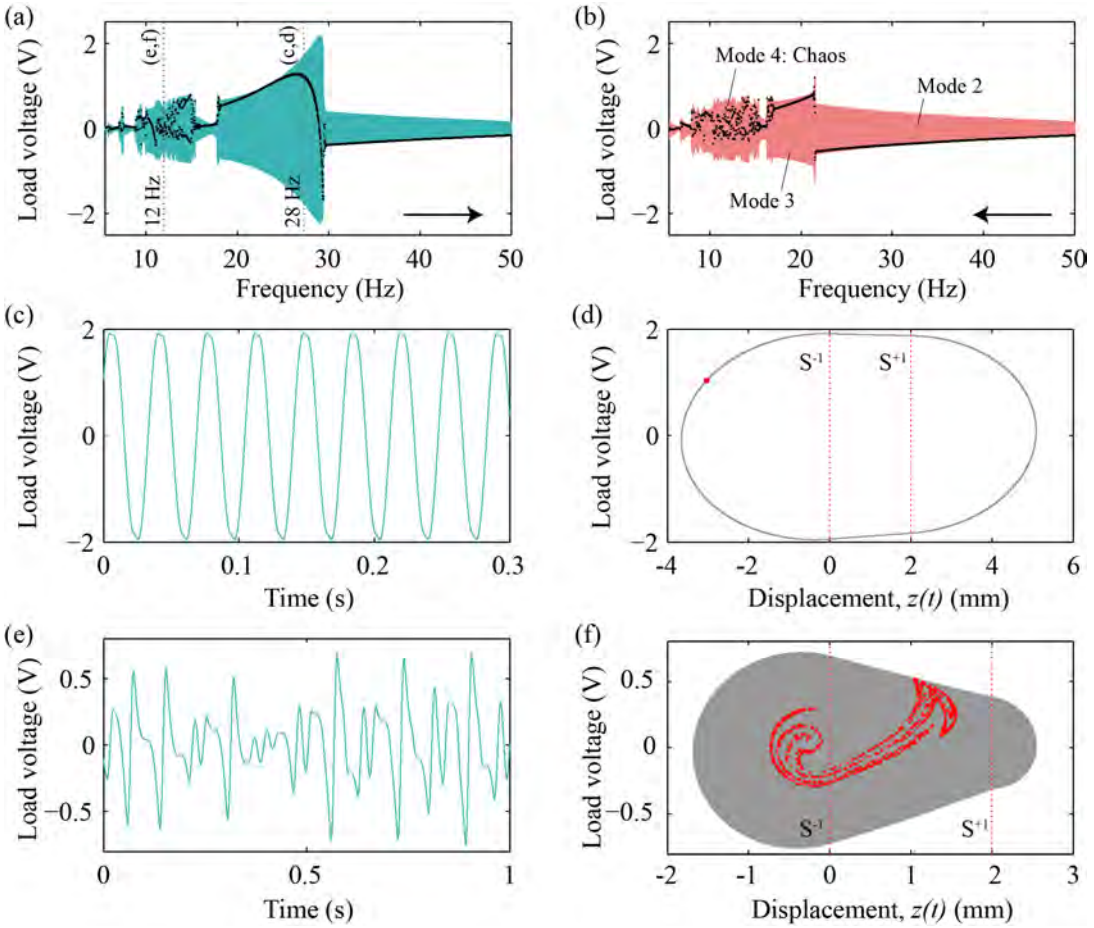

Figure 4.7: Continuously and periodically sampled voltage-time histories for (a) frequency forward-sweep and (b) reverse-sweep; voltage-time trace at (c) 28 Hz, and (e) 12 Hz; (d,f) corresponding phase portrait and Poincaré map, with switching surfaces S^{-1} and S^{+1}—$Acc = 10$ m/s^2, $g_0 = 2$ mm; arrow denotes sweep direction.

maximum energy transfer; however, the RMS voltage is low due to the lack of synchronisation between the base and mass, resulting in regions of the response where the amplitude is low. The chaotic motion demonstrated by the system is a result of a grazing impact in the transition between Mode 2 and Mode 3 operation, i.e. as the system goes from a single impact orbit to a double impact orbit. The grazing mechanism has received significant investigation in the study of discontinuous dynamical systems resulting from impacts (di Bernardo *et al.*, 2001; Ing *et al.*, 2008; Peterka, 2000). An in-

depth analysis of this chaos-inducing mechanism is, however, beyond the scope of this thesis.

The modes of operation in the impact oscillator described above have also been described by Bendame *et al.* (2014). It should be noted that the results described are for a specific set of parameters. Changing either the damping or mechanical properties of the system (mass and stiffness) would change the response for the given excitation and geometric properties. However, each of the modes of operation and the coexisting responses would still be observable.

As well as the excitation acceleration, the geometric parameter g_0 also has a significant effect on the harvester response. As g_0 increases, the portion of each cycle in which the mass can oscillate free from a spring force is greater, thus reducing the effective stiffness (equation 4.10). The synchronisation of impacts between the mass and base extends further from the linear natural frequency, resulting in the optimal frequency shifting towards lower frequencies. This applies in both Mode 2 and 3 operation (where the discontinuity is in effect), and is evident in the bidirectional frequency sweeps presented in figure 4.8, with a shift in optimal frequency from $\sim$ 32 to 20 Hz observed for an increase in g_0 from 0.5 to 10 mm. The peak amplitude of the load voltage response also rises with increasing g_0. This is due to the increased peak velocity resulting from the larger displacement range available for the mass to oscillate within.

As discussed earlier in this section, single-DoF PWL harvesters demonstrate hysteresis in response to bidirectional frequency sweeps. This hysteresis behaviour is also observed in response to sweeps of g_0 and the excitation acceleration level.

- Bidirectional acceleration sweeps for $g_0 = 2$ mm and $f = 15$ and 24 Hz are presented in figure 4.9 for accelerations in the range 0.5–12 m/s^2. The sweep time is 120 s, as in the previous sweeps. The three periodic modes of operation described for the frequency sweeps, as well as chaotic and higher period motions, are visible in the plots. Hysteresis between the forward- and reverse-acceleration sweeps is clearly evident.

- Bidirectional sweeps of g_0 between 0 and 7 mm at $Acc = 10$ m/s^2 and $f = 24$ Hz are presented in figure 4.10 to demonstrate the hysteresis in

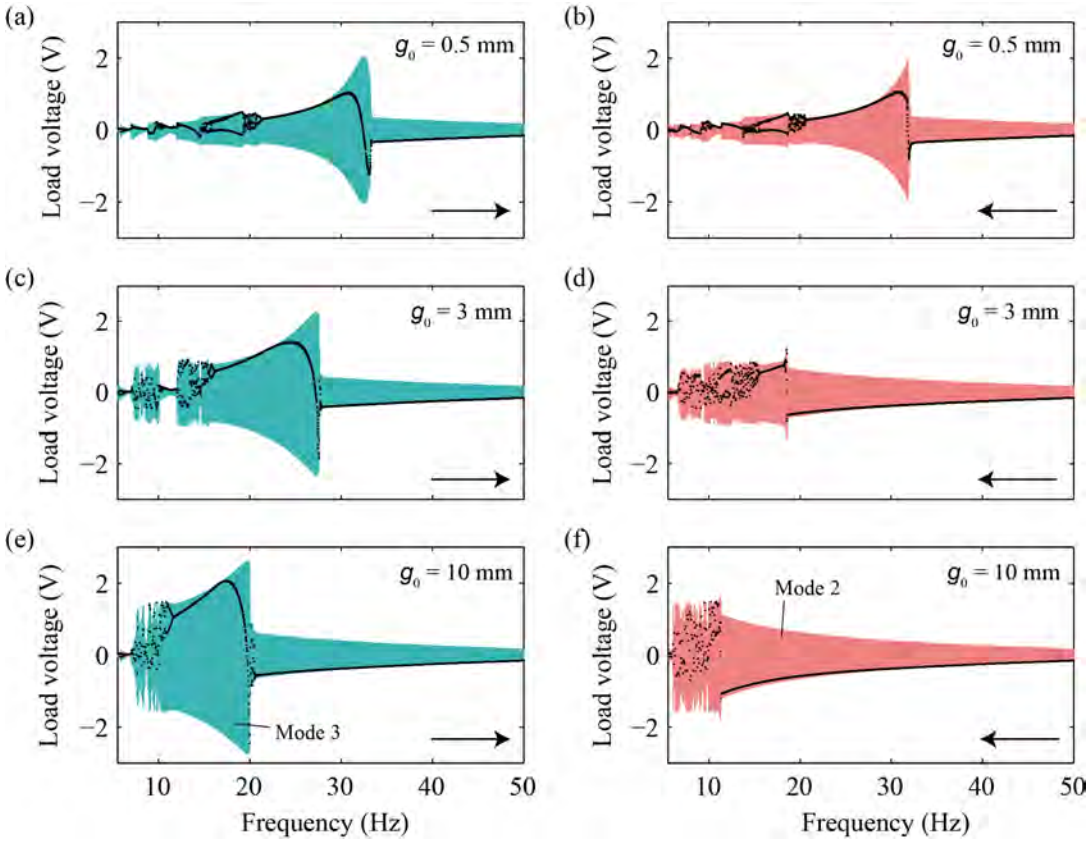

Figure 4.8: Continuously and periodically sampled voltage-time histories for (left column) frequency forward-sweeps and (right column) reverse-sweeps—$Acc = 10$ m/s^2; (a,b) $g_0 = 0.5$ mm, (c,d) $g_0 = 3$ mm, and (e,f) $g_0 = 10$ mm; arrow denotes sweep direction.

the response. A sweep length of 120 s was employed. On the frequency forward-sweep, the load voltage increases linearly with increasing g_0, with the system operating in Mode 3. At $g_0 \approx 5.5$ mm, the large oscillations can no longer be sustained, and the system jumps down to Mode 2. The cause of this jump-down, previously described for the Mode 3 double-impact oscillator, is the increase in phase angle between the mass and base as the response amplitude rises (evident in the bending of the stroboscopic map away from the upper edge of the continuously sampled load voltage in figure 4.10a). Consequently, synchronisation between impacts is lost, resulting in the response transitioning from the high- to low-energy state.

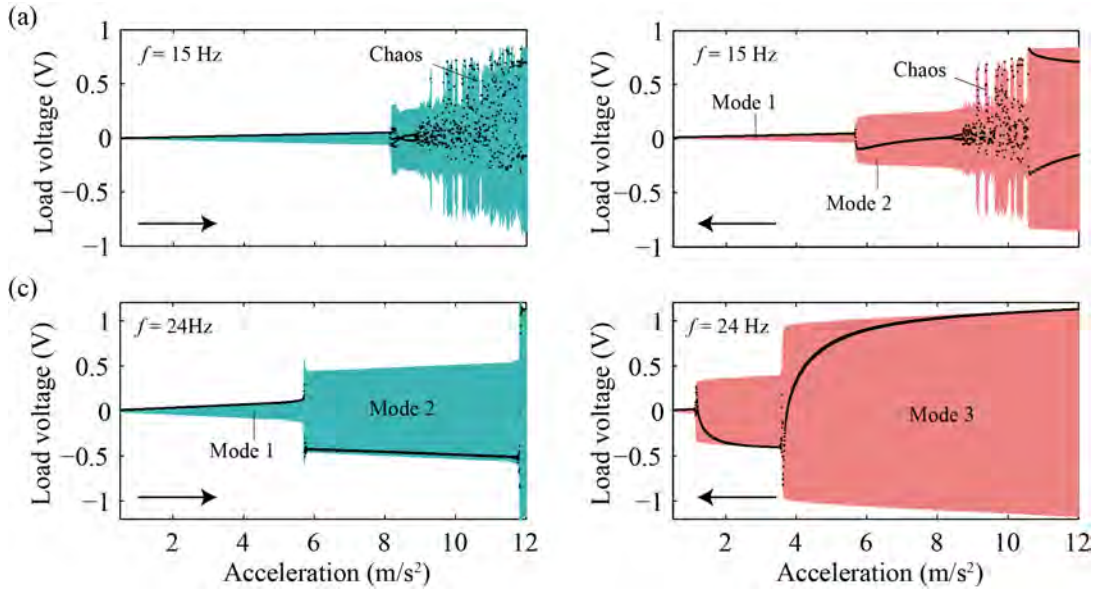

Figure 4.9: Continuously and periodically sampled voltage-time histories for (a,c) acceleration forward-sweeps and (b,d) reverse-sweeps—$g_0 = 2$ mm, (a,b) $f = 15$ Hz and (c,d) $f = 24$ Hz; arrow denotes sweep direction.

The frequency at which the jump-down frequency occurs is dictated by the damping. On the reverse-sweep, the response does not enter Mode 3 until $g_0 \approx 1.5$ mm, as the input energy is not sufficient to reach the high-energy state of operation.

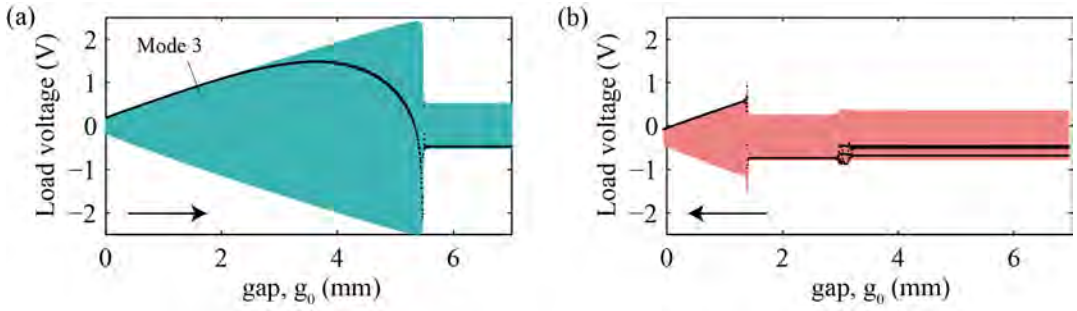

Figure 4.10: Continuously and periodically sampled voltage-time histories for (a) gap forward-sweep (increasing g_0) and (b) reverse-sweep (decreasing g_0)—$Acc = 10$ m/s^2, $f = 24$ Hz.

It is instructive to consider the difference in dynamics between the single-DoF

PWL system and its linear counterpart. For that purpose, the amplitude of the load voltage response of an equivalent single-DoF linear energy harvester, as a function of frequency, is presented in figure 4.11. In a linear system, the mass is always attached to the spring, meaning the spring transfers load to the mass in both tension and compression; whereas, the spring in the PWL system transfers load in compression only. As is evident in figure 4.11, the response of a linear single-dof harvester contains a single peak at the resonant frequency, with smooth degradation in amplitude observed at higher and lower frequencies.

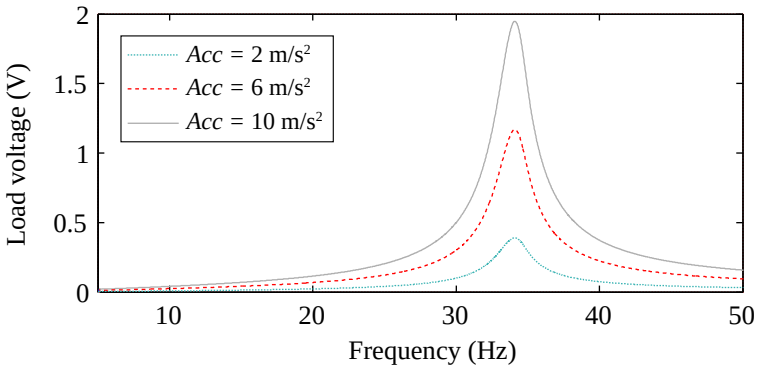

Figure 4.11: Amplitude of voltage response as a function of frequency for a single-DoF linear harvester.

Comparing the response of the single-DoF PWL harvesters (figures 4.5–4.8) with the linear system presented in figure 4.11—particularly figure 4.8 with the base acceleration of $Acc = 10$ m/s^2 in figure 4.11—the following is observed:

- The peak amplitude of the response of the PWL system is always lower than the linear system when operating in the low-energy state, while it is equal or greater when the stopper spring is engaged in the high-energy state. The PWL system can achieve a greater response amplitude than the linear system, as the displacement range is greater. Entry into either the high- or low-energy state is dependent on initial conditions. Significantly, if the initial conditions are zero ($z = 0$, $\dot{z} = 0$) in the region of non-unique coexisting responses, the system is likely to enter the low-energy state. This has been demonstrated by numerous authors including Barton *et al.* (2010); Daqaq *et al.* (2014) and Ramlan *et al.* (2010), while Quinn *et al.* (2011)

showed that the probability of entering the high-energy response decreases with greater deviation of the parameter (i.e. the frequency, acceleration, or gap) from the unique solution.

- Although the peak amplitude of the response of the PWL system in the low-energy state is lower than that of the linear system (by as much as 50%), the frequency at which the peak response is observed (optimal frequency) is significantly lower than the linear resonant frequency—the reasons for this were outlined in the discussion of the different modes of operation for figures 4.5–4.7. The reduced optimal frequency is of potential benefit, however, as it is difficult to achieve low operating frequencies at small scales. PWL systems offer potential in the low frequency operating range.

The single-DoF PWL harvester investigated in this section was introduced as an aid to understanding the more complex behaviour of the velocity amplified multi-DoF PWL harvesters, which are discussed throughout the remainder of this thesis. It was not the objective of this section to develop an effective energy harvester. Nonetheless, the applicability of this energy harvester design is discussed here:

- A significant issue affecting the applicability of the PWL energy harvester described is the presence of non-unique coexisting responses. The peak amplitude of the response is greater than or equal to an equivalent linear energy harvester if the high-energy state is reached (dependent on the initial conditions). It is lower, however, if the harvester operates in the low-energy state—which is the more likely case in practice (Quinn *et al.*, 2011). In many practical environments, the vibrating source would intermittently reach either very low amplitudes or stop entirely, e.g. a car with its engine turned off. Consequently, the initial conditions would regularly be zero. If the vibrating source was continuous, an initial perturbation could be applied on installation to achieve non-zero initial conditions. To ensure entry into the high-, rather than the low-energy state in regions of coexisting responses, some form of mechanical or electrical actuation would be necessary (Wu *et al.*, 2014). A method of ensuring entry into the high-energy

response, proposed by Erturk, Renno and Inman (2009), involved creating a perturbation by discharging a capacitor through piezoelectric layers. To date, no such device has been fabricated. Obviously, for this method to be feasible, the additional energy harvested would have to compensate for the energy requirement of the actuation mechanism.

- For a given application, g_0 could potentially be used as a tuning parameter, i.e. g_0 would be adjusted such that the excitation frequency corresponded to a large harvester response. If the excitation frequency was stable, this would only need to be done once. If, however, the excitation frequency was time varying, g_0 would have to be actively controlled. This would require an actuation mechanism; again, this would require energy to operate, which is undesirable. Frequency tuning is not pursued any further in this thesis; however, a number of tuning mechanisms have been described in section 1.4.1, which could be implemented in the current harvester (Challa *et al.*, 2011).

- The shift towards lower frequencies featured by the PWL systems discussed herein (see figure 4.8) may be advantageous for applications featuring low frequencies, such as human motion. It may, however, be simpler to design a linear harvester with an appropriate mass and spring to operate in this low frequency range. Yet, as volume is reduced, achieving a very low resonant frequency is difficult. This is because, assuming the mass and spring are scaled uniformly, the mass scales with the volume, while the spring scales with the dimension (cubed root of the volume). Consequently, the natural frequency is inversely proportional to dimension ($\omega_n = \sqrt{k/m}$). To maintain the resonant frequency with scale in a linear harvester, the spring stiffness must be scaled at the same rate as the mass. This means the spring dimensions (beam thickness in a cantilever spring, or wire diameter in a helical spring) must be scaled at a much greater rate than the device dimensions, increasing the complexity of spring fabrication. Consequently, it is difficult for springs made of conventional materials (e.g. steel) to achieve a low stiffness for MEMS-scale implementations. Alternative materials featuring low Young's modulus (such as FR4, Mallick *et al.* (2015))

offer potential as an alternative to conventional spring materials at low scales.

Non-linear analysis of a single-DoF PWL energy harvester has been presented in this section. The range of dynamics, or modes of operation, exhibited by the harvester have been presented using bidirectional sweeps for varying excitation and geometric conditions. Hysteresis in frequency, acceleration and initial gap sweeps has been demonstrated. Mode 3 operation, which is characterised by a double-impact cycle, results in high velocity and output voltage; however, entry into this high-energy state is dependent on initial conditions. This significant issue hinders the potential implementation of this type of harvester in an application environment.

The objective of the non-linear analysis of a single-dof PWL system presented in this section was not to develop an effective energy harvester; rather, it was to serve as an introduction to some of the key parameters and analysis techniques used in the investigation of the more complex multi-dof velocity amplified PWL systems. In the following section, these multi-DoF PWL energy harvesters are analysed through the same non-linear analysis mechanisms already presented.

4.2 Velocity amplified multi-DoF PWL harvesters

The non-linear analysis methods applied to single-DoF PWL oscillators in the previous section are employed to analyse VAEGs, which are considered multi-DoF PWL oscillators (with 2-, 3- and 4-DoFs) in this section. The masses in these multi-DoF harvesters are vertically stacked, with springs interposed. The largest mass in the series is at the base of the stack (referred to as the base mass), with the masses becoming monotonically smaller moving upwards. As in the single-DoF PWL harvester, the masses are decoupled from the springs, allowing unforced motion. In addition to frequency, acceleration and initial gap, the system dynamics in multi-DoF PWL oscillators change with mass ratio R, defined in equation 2.38. The influence of these parameters on the behaviour of multi-DoF PWL systems is discussed in this section.

4.2.1 Multi-DoF PWL harvesters in phase space

As an initial progression from the single-DoF PWL system towards velocity amplified multi-DoF PWL systems, 2-DoF PWL energy harvesters are investigated. A schematic of a 2-DoF PWL system is shown in figure 4.12, with the masses (a) at their zero positions ($z_1 = 0$ and $z_2 = 0$), and (b) displaced. The zero positions are located at the free length of the springs. This differs from the rest position as the initial spring deflection due to the weight of the mass is not included. As with the single-DoF PWL oscillator, the springs do not transfer load in tension, meaning that the masses can become detached from the springs.

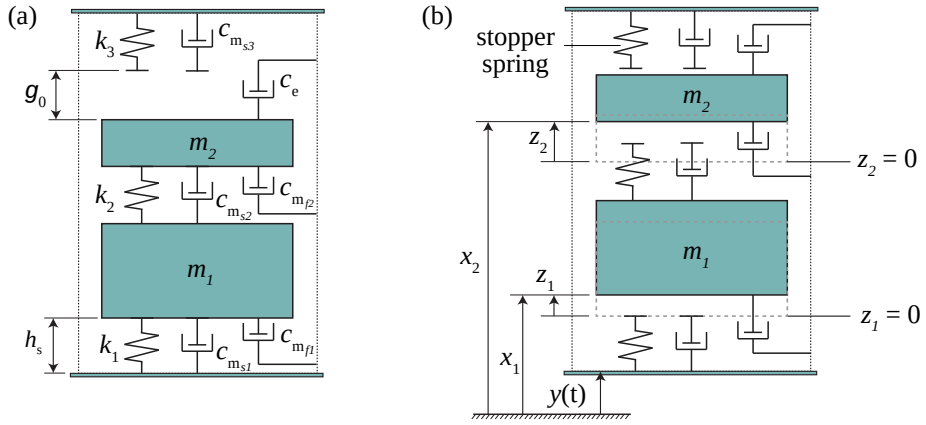

Figure 4.12: Schematic of a 2-DoF PWL harvester; (a) m_1 and m_2 at positions $z_1 = 0$ and $z_2 = 0$, respectively, with springs and dampers; (b) displaced masses detached from springs, showing base ($y(t)$), absolute ($x_{1,2}$), and relative ($z_{1,2}$) displacement.

The transducer is coupled between m_2 and the base. This involves incorporating a magnet in m_2, with a coil arranged concentrically to the mass, attached to the device housing. Therefore, the electrical damping force, $F_e = c_e(\dot{x}_2 - \dot{y})$, is applied in the equation of motion of m_2 only.

A linear 2-DoF system is considering initially, i.e. the gap is $g_0 = 0$ and the masses are non-detachable from the springs. The masses are considered to be point masses in the model; therefore, their height is zero. As this is a 2-DoF

system, there are now two equations of motion:

$$m_1\ddot{x}_1 + k_1(x_1 - y - h_s) + c_{s_1}(\dot{x}_1 - \dot{y}) - k_2(x_2 - x_1 - h_s) - c_{s_2}(\dot{x}_2 - \dot{x}_1) + c_{f_1}(\dot{x}_1 - \dot{y}) + m_1 g = 0 \quad (4.11a)$$

$$m_2\ddot{x}_2 + k_2(x_2 - x_1 - h_s) + c_{s_2}(\dot{x}_2 - \dot{x}_1) + k_3(x_2 - y - 2h_s - g_o) + c_{s_3}(\dot{x}_2 - \dot{y}) + c_{f_2}(\dot{x}_2 - \dot{y}) + c_e(\dot{x}_2 - \dot{y}) + m_2 g = 0 \quad (4.11b)$$

The relative displacements of the masses and the base are $z_1 = x_1 - y - h_s$ and $z_2 = x_2 - y - 2h_s$, while the relative velocities are then $\dot{z}_1 = \dot{x}_1 - \dot{y}$ and $\dot{z}_2 = \dot{x}_2 - \dot{y}$. As described in equation 2.24, the electrical damping force can also be written as $F_e = Ki$. Inserting these relationships into equation 4.11 yields:

$$m_1\ddot{z}_1 + k_1 z_1 + c_{s_1}\dot{z}_1 - k_2(z_2 - z_1) - c_{s_2}(\dot{z}_2 - \dot{z}_1) + c_{f_1}\dot{z}_1 = -m_1\ddot{y} - m_1 g \quad (4.12a)$$

$$m_2\ddot{z}_2 + k_2(z_2 - z_1) + c_{s_2}(\dot{z}_2 - \dot{z}_1) + k_3(z_2 - g_0) + c_{s_3}\dot{z}_2 + c_{f_2}\dot{z}_2 + Ki = -m_2\ddot{y} - m_2 g \quad (4.12b)$$

Now considering the 2-DoF system as a PWL oscillator with detachable masses, the stiffness and damping forces are discontinuous. Boundary conditions determine the forces acting on the masses at any instant:

- the base mass m_1 is attached to the spring k_1 under the condition $z_1 < 0$;
- the two masses are attached to each other through k_2 if $z_2 < z_1$; and
- m_2 is in contact with the stopper spring k_3 under the condition $z_2 > g_0$.

It should be noted that multiple boundary conditions can be satisfied concurrently. The equation describing the load voltage generated in the electrical circuit, derived in equation 2.28, is also required to model the system. In this case, the velocity term is $\dot{z} = \dot{z}_2$. The set of coupled equations describing the dynamics

and voltage output of a 2-DoF PWL electromagnetic energy harvester are then:

$$m_1\ddot{z}_1 = -m_1\ddot{y} - m_1 g - c_{f_1}\dot{z}_1 + \begin{cases} -k_1 z_1 - c_{s_1}\dot{z}_1, & \text{if } z_1 < 0 \\ 0, & \text{if } 0 \leq z_1 \leq z_2 \\ k_2(z_2 - z_1) + c_{s_2}(\dot{z}_2 - \dot{z}_1), & \text{if } z_2 < z_1 \end{cases} \tag{4.13a}$$

$$m_2\ddot{z}_2 = -m_2\ddot{y} - m_2 g - c_{f_2}\dot{z}_2 - Ki + \begin{cases} -k_2(z_2 - z_1) - c_{s_2}(\dot{z}_2 - \dot{z}_1), & \text{if } z_2 < z_1 \\ 0, & \text{if } z_1 \leq z_2 \leq g_0 \\ -k_3(z_2 - g_0) - c_{s_3}\dot{z}_2, & \text{if } z_2 > g_0 \end{cases} \tag{4.13b}$$

$$\dot{V}_L = K\dot{z}_2\frac{R_L}{L_C} - \frac{V_L}{L_C}(R_C + R_L) \tag{4.13c}$$

In order to solve these equations numerically, the second order equations of motion are represented as a set of first-order ODEs. This was demonstrated previously for the single-DoF PWL system in equation 4.9.

The additional mass also results in an additional switching surface located at the position of impact between m_1 and m_2. Unlike the switching surfaces previously described in section 4.1.1, the location of the new switching surface changes with the position of the masses. The switching surfaces for the 2-DoF PWL oscillator are defined as:

$$S^{-1} = \{(z_1, \dot{z}_1, \theta) \in \mathbb{R}^2 \times S \mid z_1 = 0\} \tag{4.14a}$$

$$S^{+1} = \{(z_2, \dot{z}_2, \theta) \in \mathbb{R}^2 \times S \mid z_2 = g_0\} \tag{4.14b}$$

$$S^{+2} = \{(z_1, \dot{z}_1, z_2, \dot{z}_2, \theta) \in \mathbb{R}^4 \times S \mid z_1 = z_2\} \tag{4.14c}$$

As described previously, intersection with a switching surface results in a non-smooth change in dynamics between linear behaviours.

The equations of motion for multi-DoF systems with more than two masses

are derived in the same manner as above. In each case, the transducer is coupled between the final mass in the stacked mass series and the base. An additional switching surface also accompanies each extra mass. In the following subsection, the dynamics of multi-DoF PWL energy harvesters are analysed.

4.2.2 Sweep analysis of velocity amplified multi-DoF PWL harvesters

The influence of frequency, acceleration, initial gap, and mass ratio on the dynamics of velocity amplified multi-DoF PWL systems is investigated in this subsection. 2-DoF PWL harvesters receive the most in-depth analysis, while 3- and 4-DoF harvesters are also discussed. Simulated bidirectional sweeps, with stroboscopic maps were utilised, along with phase diagrams, Poincaré maps and power spectra to investigate the non-linear behaviour of these systems.

The model parameters that remained constant in the simulations are listed in table 4.2. The base mass, m_1, was the same in each case, while the stiffness of each spring was also kept constant ($k_1 = k_2 = k_n$). Masses further along the stack were defined by the system mass ratio R (equation 2.38), with increasing mass ratio resulting in the final mass in the stack becoming smaller relative to the base mass, m_1. A constant electromagnetic transduction factor of $K = 2$ Vs/m was used in each system, irrespective of mass ratio or number of DoFs. This effectively means that the same transducer (magnet and coil) was used in each test. It should be noted that the electrical system implemented in the multi-DoF PWL model is different to the one used in the single-DoF PWL model, described in section 4.1, as the mass containing the magnet in the multi-DoF systems was smaller. Therefore, the amplitude of the voltage response for the single- and multi-DoF PWL systems are not comparable. The variable parameters used in the simulations—mass ratio, initial gap, acceleration, and frequency—are defined with each set of results.

A validation of the multi-DoF model is not provided in this section; for a comparison between experimental and simulation frequency sweeps for a 2-DoF PWL harvester (VAEG), see figures 6.12–6.15 in chapter 6. Only simulation results are presented in this section.

Table 4.2: Model parameters used in multi-DoF PWL harvester sweeps.

Parameter	Value	Unit
m_1	20.08	g
k_n	910	N/m
ζ_{s_n}	0.02	-
ζ_{f_n}	4.26	1/s
K	2	Vs/m
R_C	155.3	Ω
R_L	300	Ω
L_C	0.0125	H
θ_0	0	rad

Bidirectional frequency sweeps for a 2-DoF PWL harvester of mass ratio $R = 5$, are presented in figure 4.13 for base acceleration levels of $Acc = 5$ and 10 m/s^2, and gaps of $g_0 = 0$ and 3 mm. Unlike the single-DoF PWL harvester, a gap of $g_0 = 0$ mm does not result in a linear response for a 2-DoF PWL harvester. This is because, in this case, detachment from a spring still results in a discontinuous stiffness. Negative gap lengths can also be physically realised by decreasing the cap height such that the springs are initially compressed. Again, this does not mean the response will be linear. The frequency was swept between 5 and 45 Hz at a rate of 0.167 Hz/s for a total sweep time of 240 s. A longer sweep length was required for the multi-DoF sweeps, as for large sections of the sweep the response was stationary random. To achieve a statistically significant RMS value for the voltage at a particular frequency where the response is stationary random, a long test time is required. This ensured that the shape of the frequency response did not change from test to test, mitigating the effect of the stationary random nature of the data. This requirement for long sweep lengths was applied in both the experimental and simulation tests throughout chapters 5–7.

A second smaller resonant peak is present at $\sim$ 80 Hz in the 2-DoF PWL system—as in the response of the linear 2-DoF harvester presented later in figure 4.21. Frequencies above 45 Hz are ignored in the 2-DoF PWL harvester

sweeps, however, as the amplitude of the response is much larger for the lower frequency range.

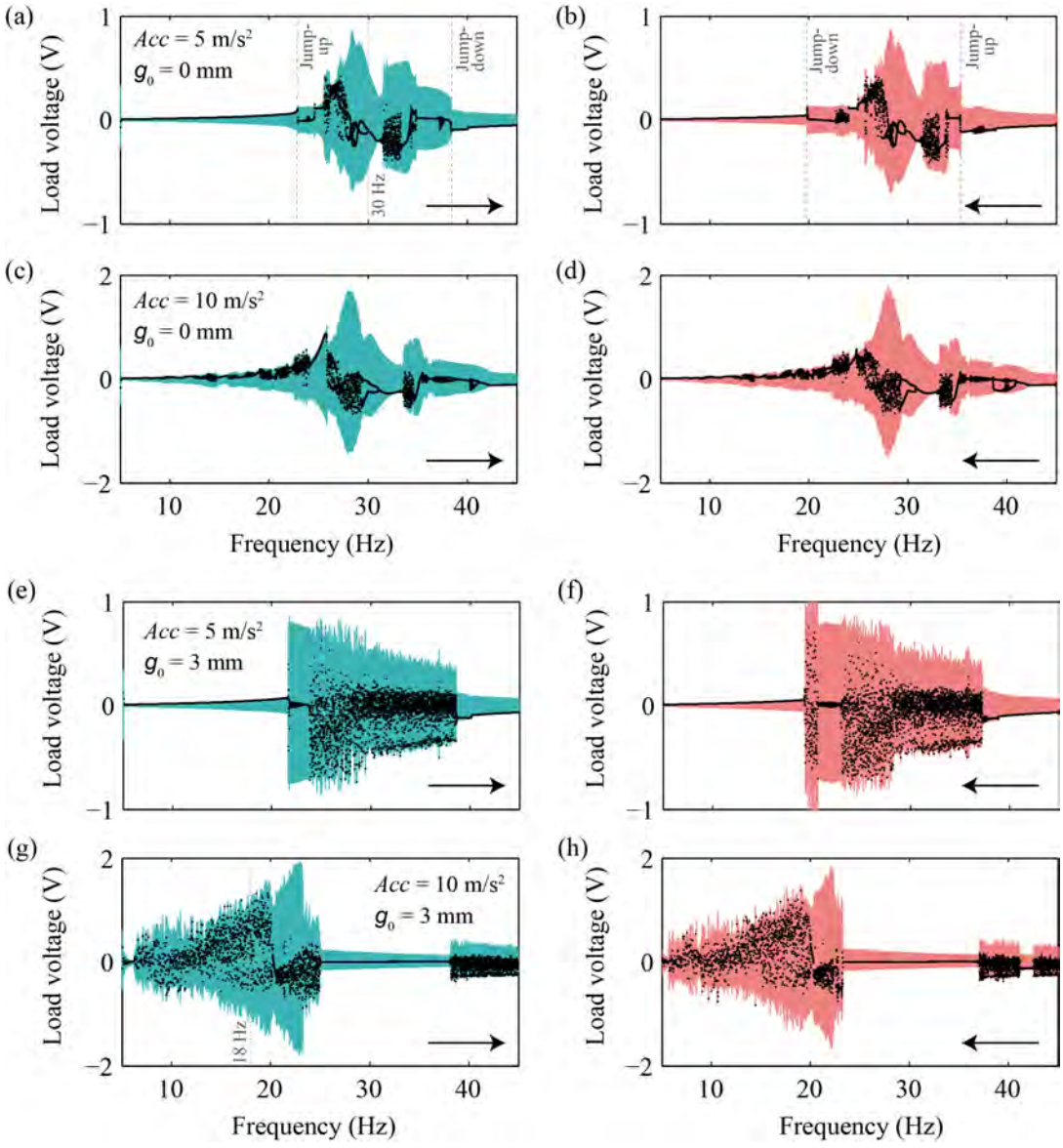

Figure 4.13: Continuously and periodically sampled voltage-time histories for (left column) frequency forward-sweeps and (right column) reverse-sweeps—(a–d) $g_0 = 0$ mm, (e–h) $g_0 = 3$ mm; (a,b,e,f) $Acc = 5$ m/s^2, (c,d,g,h) $Acc = 10$ m/s^2; mass ratio $R = 5$; arrow denotes sweep direction.

On initial analysis of the results, two significant differences between the 2-DoF

and single-DoF PWL configurations are immediately obvious:

- The dynamics of the 2-DoF configuration are significantly more complex than the dynamics of the single-DoF system, with chaotic motion being more common than periodic motion for large amplitude responses. This is a result of the additional switching surface introduced by the second mass. The reason for the chaotic motion is expanded upon later in the section, with the dynamics at individual frequencies illustrated.

- The hysteresis in the response of the 2-DoF system is either small or non-existent. Hysteresis is evident in figure 4.13a–b, with jump-up and jump-down frequencies evident in both the forward and reverse sweeps. However, the response is low in these regions, and extends only slightly to higher and lower frequencies. This is in contrast with the single-DoF system, where both the amplitude and bandwidth of the response changes significantly with sweep direction. As the hysteresis in the 2-DoF PWL system is small, only forward-sweeps are presented in the remainder of this section. This reduction of hysteresis in the response of the 2-DoF PWL system, in comparison to the single-DoF PWL system, is also exhibited by experimental systems in sections 5.3 and 6.3.

The solution trajectory of the periodic response from figure 4.13a at 30 Hz is presented in figure 4.14a. It is evident that the response is periodic as the solution trajectory and phase diagrams form lines, while the Poincaré maps form points. In order to display all three switching surfaces on a single plot, the phase space (z_1,z_2) is used. This is necessary as the location of S^{+2} changes with the position of the masses. Phase space is divided into six subspaces by the three switching surfaces, with intersection with one of these surfaces resulting in a non-smooth change in dynamics between linear behaviours. Under the geometric and excitation conditions in figure 4.14, the solution trajectory undergoes ten changes in dynamics per cycle, as a result of crossing the switching surfaces. Maintaining a stable periodic response for a large amplitude response in a multi-DoF PWL system is unlikely, as there are simply too many non-smooth changes in dynamics per cycle. This is demonstrated by the chaotic regions at frequencies above and

below 30 Hz in figure 4.13a. This example demonstrates why the dynamics of the 2-DoF PWL system presented in this section are chaotic under most operating conditions.

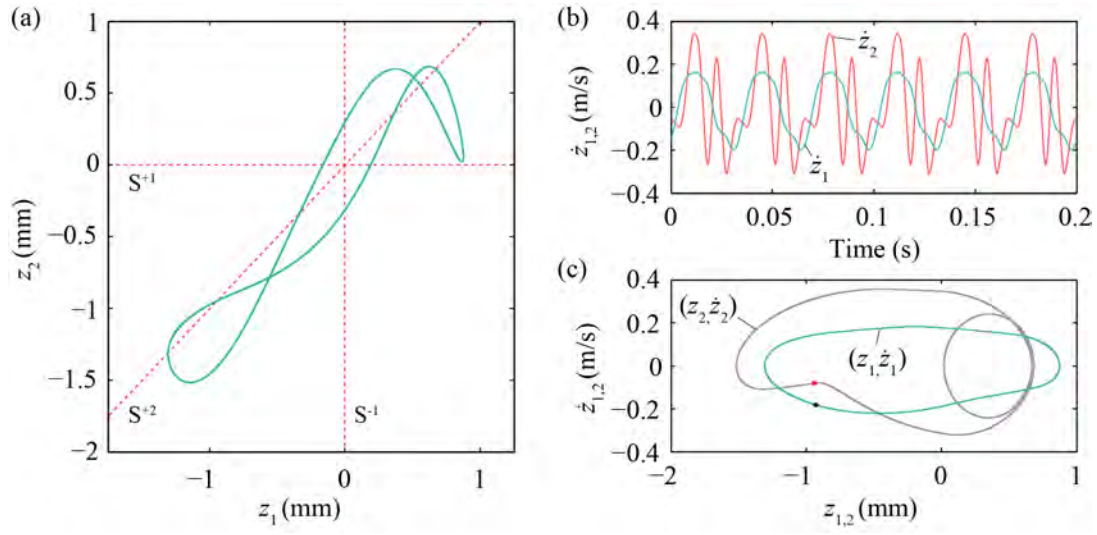

Figure 4.14: 2-DoF PWL periodic response: (a) phase space (z_1, z_2) solution trajectory with switching surfaces S^{-1}, S^{+1}, and S^{+2}, (b) velocity-time history $\dot{z}_1$ and $\dot{z}_2$, (c) phase diagram of m_1 and m_2, with Poincaré maps—$Acc = 5$ m/s^2, $f = 30$ Hz, $g_0 = 0$ mm, $R = 5$.

The velocity-time history and phase diagram are also shown in figure 4.14. Some interesting features of the response are evident from these plots:

- The velocity of the second smaller mass, $\dot{z}_2$, is significantly higher than that of the larger base mass, $\dot{z}_1$. This is an example of velocity amplification under forced excitation, which is described for experimental systems in chapters 5 and 6. The increase in velocity of the smaller mass, m_2, occurs as a result of impacts between the two masses, which results in energy transfer to m_2—provided $\dot{z}_1 > 0$. Maximum energy is transferred when the upward trajectory of m_1 corresponds to the downward trajectory of m_2. The frequency at which the peak voltage is generated is the frequency where the synchronisation of the impacts between the masses results in the highest energy transfer. This is controlled by the displacement range—which is a

function of g_0—and also the input acceleration. The effect of g_0 on the optimal frequency is described later in this section.

- While m_1 oscillates at the excitation frequency ω, m_2 undergoes a form of frequency-up conversion (Galchev *et al.*, 2009). This increase in oscillation frequency occurs as follows: m_1 impacts m_2, increasing the velocity of m_2. This mass then impacts the stopper spring and rebounds into m_1, which is still in the upward portion of its cycle, i.e. $\dot{z}_1 > 0$. The masses impact each other once again, and the process repeats itself. This cycle continues until the velocity and, hence, kinetic energy of m_1 is zero, meaning no more energy can be transferred to m_2 through an impact. In the case shown, m_2 experiences two impacts with m_1 per excitation cycle; therefore, m_2 is effectively oscillating at 2ω. Greater increases in frequency can also be achieved by increasing the mass ratio. This is demonstrated in figure 4.18 later in this section. Power density tends to diminish with decreasing excitation frequency, however, due to the increased volume required for the associated increase in displacement range. The frequency-up conversion method described allows the mass coupled to the transducer to have a large total displacement within a much smaller volume, increasing the power density at low frequencies. Other examples of frequency-up conversion through impacts were presented by Gu (2011); Gu and Livermore (2011) and Liu *et al.* (2012*b*).

The solution trajectory of the chaotic response from figure 4.13g at 18 Hz is presented in figure 4.15, along with the velocity-time history, and Poincaré maps plotted on the phase diagrams. The chaotic nature of the response is evident in the highly dispersed Poincaré maps, with a non-repeating solution trajectory (Jordan and Smith, 1977). Once again, velocity amplification and frequency-up conversion are evident; however, their occurrence is intermittent. A response such as this is a typical response from the multi-DoF PWL harvesters investigated in this section.

The influence of the initial gap, g_0, on the response of the 2-DoF PWL harvester is now investigated. The load voltages generated for forward-frequency sweeps for a range of g_0 values are plotted in figure 4.16; the remaining variable

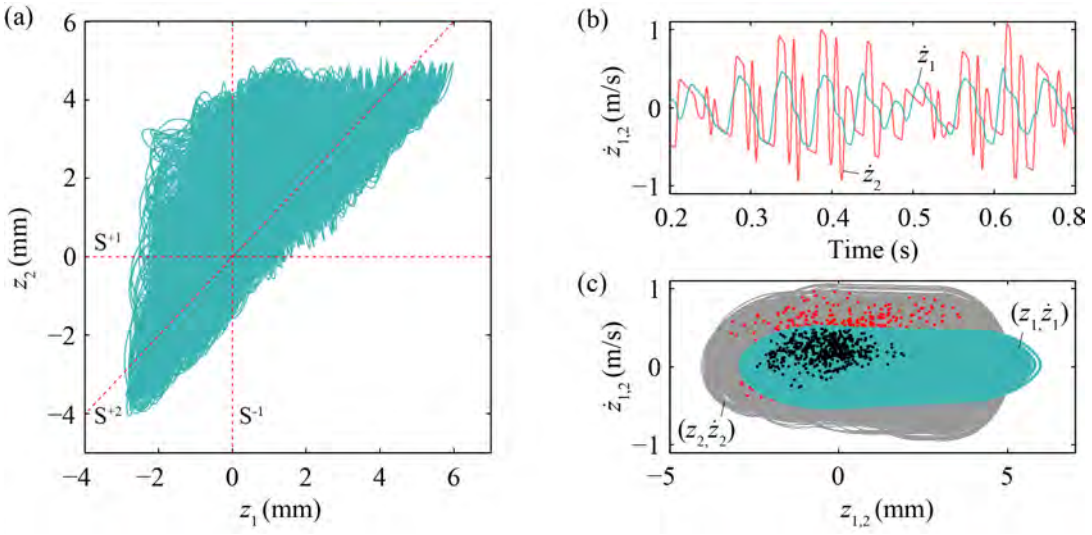

Figure 4.15: 2-DoF PWL chaotic response: (a) phase space (z_1, z_2) solution trajectory with switching surfaces S^{-1}, S^{+1}, and S^{+2}, (b) velocity-time history $\dot{z}_1$ and $\dot{z}_2$, (c) phase diagram of m_1 and m_2, with Poincaré maps—$Acc = 10$ m/s^2, $f = 18$ Hz, $g_0 = 3$ mm, $R = 5$.

parameters, listed in the figure caption, were held constant in each case. The influence of g_0 on a 2-DoF velocity amplified harvester, investigated experimentally, is presented in section 6.3.

- The gap in figure 4.16a is $g_0 = -0.5$ mm. This negative gap length results in the system approaching a linear harvester, as the masses can not easily detach from the springs, reducing the effect of the discontinuity. As for the single-DoF PWL system described in section 4.1.2, increasing g_0 results in the optimal frequency shifting towards lower frequencies. The highest energy transfer from m_1 to m_2 now occurs at a frequency lower than the resonant frequency of an equivalent linear system. Again, this is a result of the effective stiffness reducing with increasing g_0, as the masses spend a greater portion of each cycle experiencing no spring force. In this case, an increase in g_0 from -0.5 mm to 10 mm results in the optimal frequency reducing from $\sim$ 30 Hz to 18 Hz. This is a significant reduction of 40 %. A number of broadband energy harvesters described in section 1.4 attempted to broaden the frequency range over which effective operation

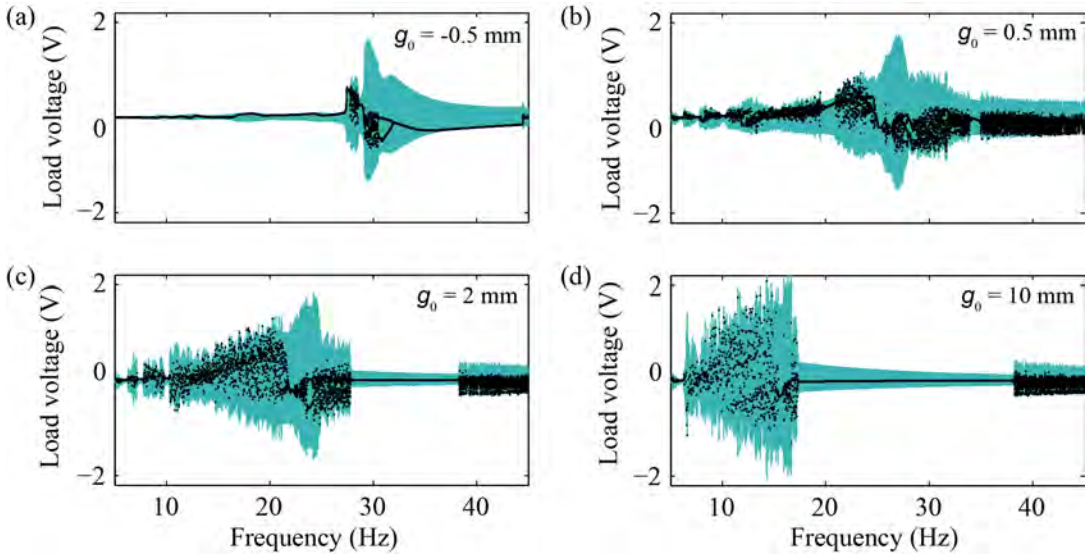

Figure 4.16: Continuously and periodically sampled voltage-time histories for frequency forward-sweeps—(a) $g_0 = -0.5$ mm, (b) $g_0 = 0.5$ mm, (c) $g_0 = 2$ mm, (d) $g_0 = 10$ mm; $Acc = 10$ m/s^2, mass ratio $R = 5$.

of their harvester was achieved, through mechanical and electrical tuning methods (Challa *et al.*, 2011; Leland and Wright, 2006; Peters *et al.*, 2009). The predicted reduction in optimal frequency of 40% in the current harvester compares favourably with these systems.

- It is also noticeable that the amplitude of the voltage response increases with g_0, due to the increasing RMS velocity of m_2. This RMS velocity increase is a result of the greater displacement range over which the masses can oscillate with larger values of g_0. A proviso to this result is that, for excessively large values of g_0, m_2 may not engage with the stopper spring, resulting in the return velocity being lower than had it impacted the stopper. In essence, the input acceleration level must be large enough to engage m_2 with the stopper; otherwise, high RMS velocities will not be achieved. A consequence of this is, the larger g_0, the greater the acceleration level required to engage the stopper spring. The frequency at which the highest RMS voltages are achieved is determined by the value of g_0.

  Furthermore, the assumption that the electromagnetic transduction factor,

K, is constant becomes less valid with increasing g_0. In practice, K reduces with increasing displacement range as the relative location of the magnet and coil is not optimal. This issue is examined further in chapters 6 and 7, with the implementation of a variable K.

The final parameter under investigation for a 2-DoF PWL harvester is the mass ratio R. Unlike the previously discussed variable parameters—frequency, acceleration and initial gap—mass ratio is specific to multi-DoF systems. The voltage response for frequency forward-sweeps with mass ratios in the range $R =$ 3–20 is presented in figure 4.17. According to the theory of velocity amplification, described in section 2.3, the velocity and, hence, load voltage would be expected to increase with R. This increase in voltage with R is clear in the frequency sweeps, with the peak voltage demonstrated for the mass ratio $R = 3$ system being approximately half the peak voltage demonstrated by the $R = 20$ system.

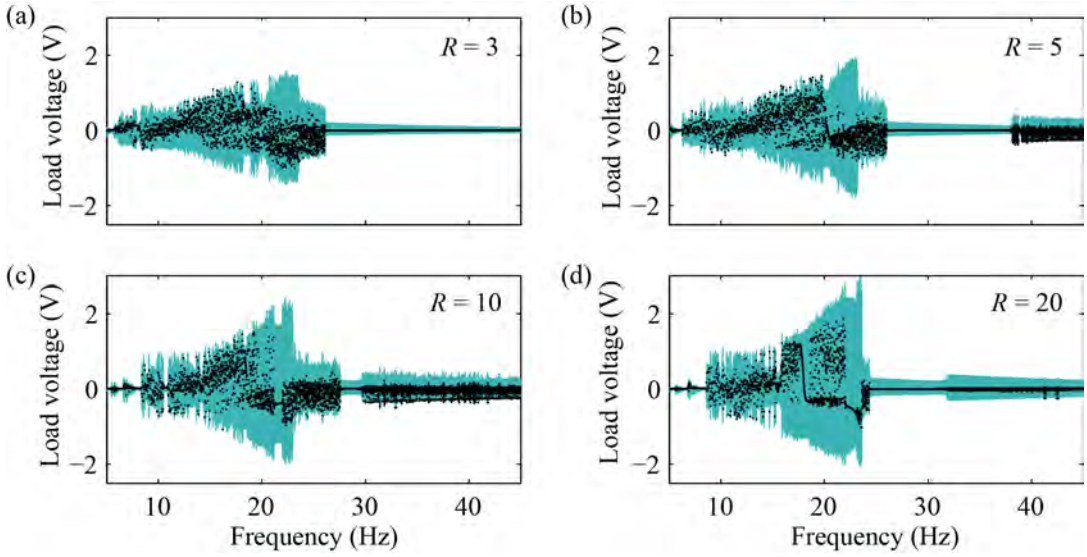

Figure 4.17: Continuously and periodically sampled voltage-time histories for frequency forward-sweep for (a) $R = 3$, (b) $R = 5$, (c) $R = 10$, (d) $R = 20$— $Acc = 10$ m/s^2, $g_0 = 3$ mm.

Velocity-time histories and power spectra of the $R = 5$ and $R = 20$ systems (figure 4.17b and d) at 20 Hz are presented in figure 4.18. The increase in velocity of m_2 with increasing mass ratio is clearly evident, as well as the complementary

increase in oscillation frequency. This increase in oscillation frequency was previously explained for the system response in figure 4.14. Mass m_2 traverses the displacement range more quickly for $R = 20$ than $R = 5$. As a result, it undergoes more impacts per cycle and oscillates at a higher frequency. The higher frequency response is also evident in the voltage power spectra. Both systems exhibit significant power at the excitation frequency, and its harmonics. However, the $R = 20$ system demonstrates high power up to much higher frequencies. It is noteworthy that K is fixed for the simulation results presented at the different mass ratios. Although the voltage output increases with mass ratio for the current parameters, it is unclear if this result would remain valid if K was maximised for each mass ratio. This is investigated experimentally in section 5.3.2.

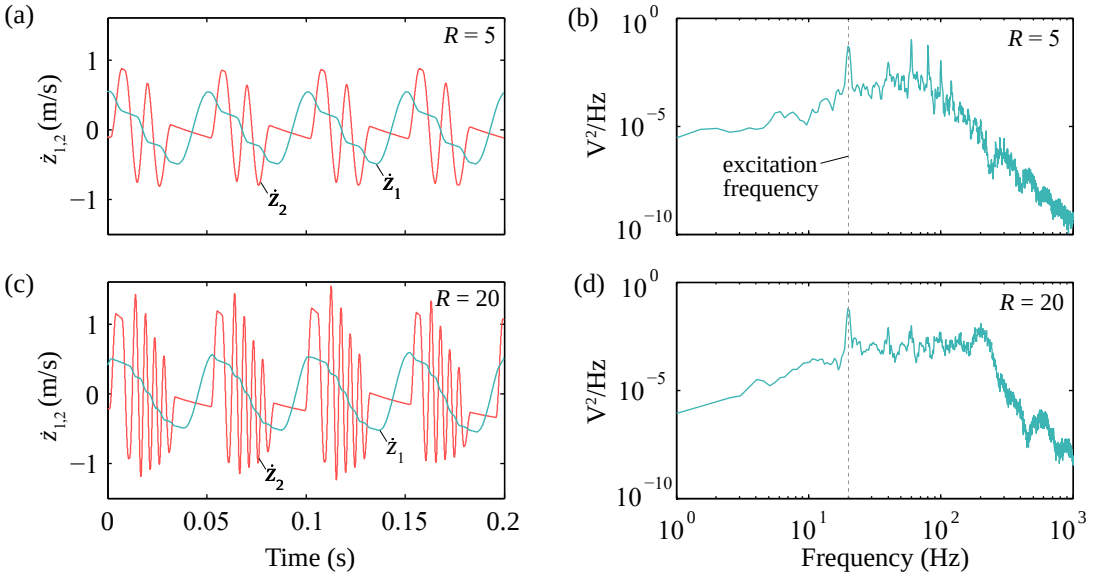

Figure 4.18: 2-DoF PWL velocity-time history and power spectrum for (a,b) $R = 5$ and (c,d) $R = 20$—$Acc = 10$ m/s^2, $f = 20$ Hz, and $g_0 = 3$ mm.

The remainder of this section on multi-DoF PWL harvesters is focused on comparing 3- and 4-DoF systems to the 2-DoF system already described. The equations of motion for the 3- and 4-DoF systems were derived in the same manner as for the 2-DoF PWL system. These equations are not presented here as they are simply extensions of the 2-DoF equations of motion, derived in equation 4.13. The transducer was coupled between the final mass and the base in each system.

Frequency forward-sweeps of the load voltage generated by 2-, 3-, and 4-DoF systems, for mass ratios of $R = 5$ and 20, are presented in figure 4.19.

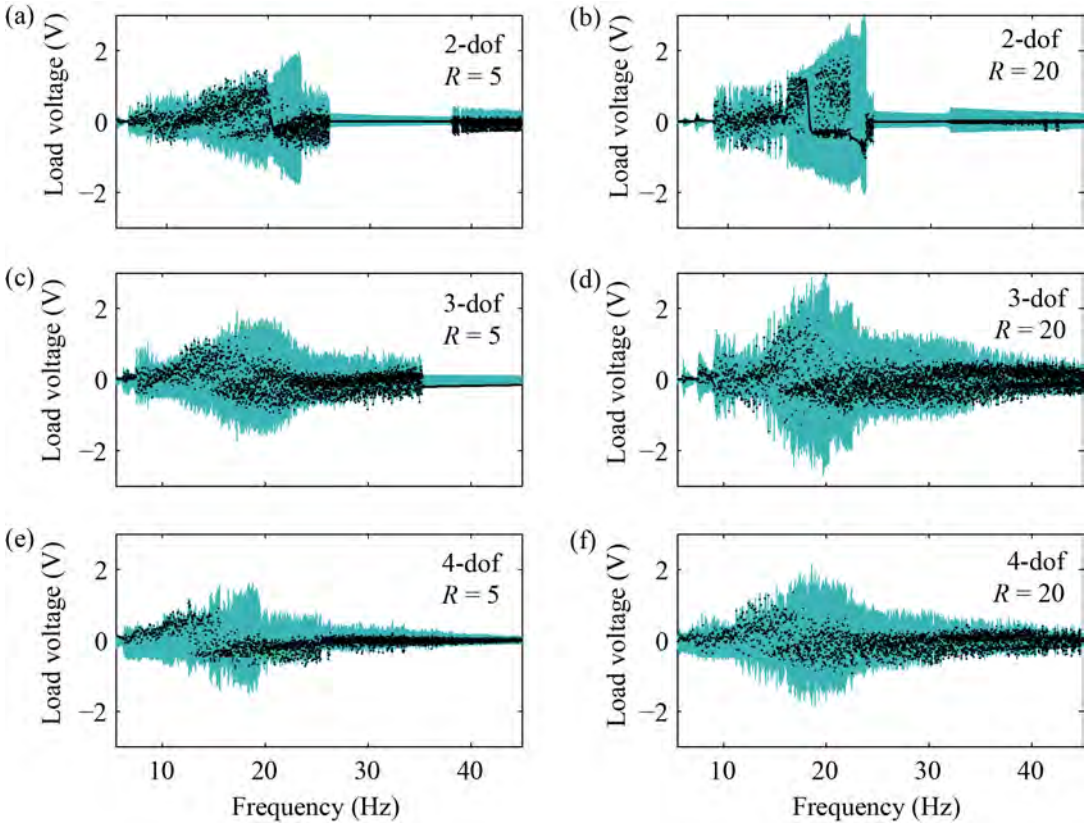

Figure 4.19: Continuously and periodically sampled voltage-time histories for frequency forward-sweep for (a,b) 2-DoF, (c,d) 3-DoF, and (e,f) 4-DoF; (a,c,e) $R = 5$ and (b,d,f) $R = 20$—$Acc = 10$ m/s^2, $g_0 = 3$ mm.

- As expected, the additional switching surfaces in the 3- and 4-DoF systems compound the effect already observed in the 2-DoF system, resulting in a chaotic response. Achieving a stable periodic response is unlikely for large amplitude oscillations, as the number of impacts (or switching surface intersections) per cycle is high.

- An increase in voltage, as a result of increased velocity of the mass coupled to the transducer, is observed with increasing mass ratio for each configuration. The explanation for this is the same as was described for the changing

mass ratio in figure 4.17 and 4.18, i.e. the velocity gain on impact increased with mass ratio, resulting in the masses traversing the displacement range more quickly, increasing the number of impacts (and amplification events) per cycle.

- Under the conditions for maximum velocity amplification, i.e. perfectly elastic sequential pairwise collisions, the final velocity gain increases with the number of DoFs. Under forced excitation, this is not the case. The load voltage profile of the 3-DoF system demonstrates a similar amplitude to the 2-DoF system, while a significant reduction in load voltage amplitude is observed in the 4-DoF response. This is a significant finding and is expanded upon in figure 4.20.

- The frequency range over which a large amplitude response is observed is broader for the 3- and 4-DoF systems than the corresponding 2-DoF system, due to the additional modes excited by the extra masses. Due to the greater total mass, the frequency at which the peak response is observed decreases with additional masses.

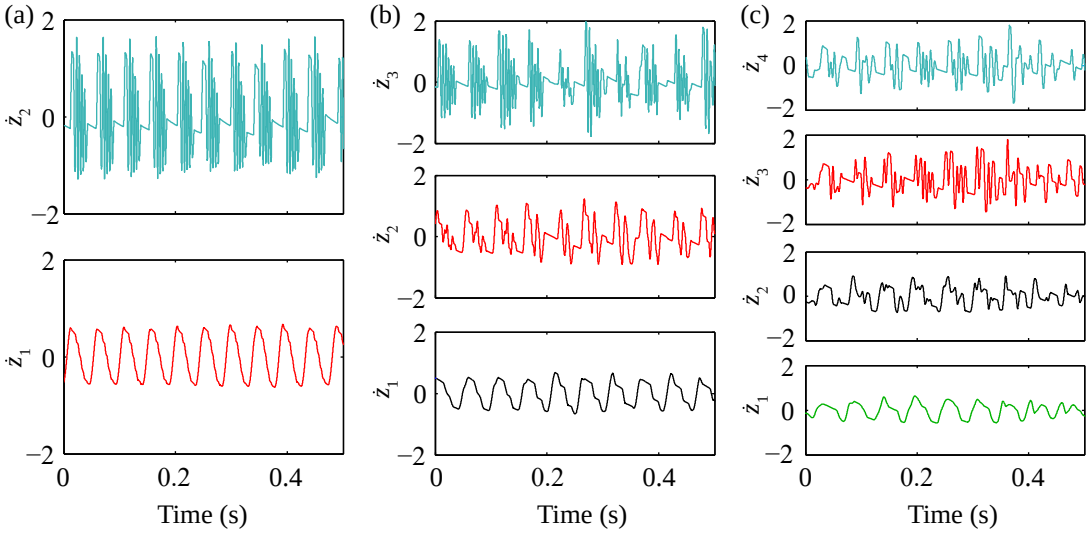

Figure 4.20: Velocity-time histories of each of the masses in the (a) 2-DoF, (b) 3-DoF, and (c) 4-DoF stacked mass systems—$R = 20$, $Acc = 10$ m/s^2, $g_0 = 3$ mm, and $f = 20$ Hz.

Velocity profiles of the individual masses are presented in figure 4.20, for the 2-, 3-, and 4-DoF configurations, with mass ratio $R = 20$ from figure 4.19, at 20 Hz. The increasingly chaotic nature of the response with increasing numbers of DoFs is evident on visual inspection of the velocity-time histories. The RMS values of the velocity of each mass in the different systems are presented in table 4.3.

Table 4.3: RMS velocities from time traces in figure 4.20.

DoFs	v_1 (m/s)	v_2 (m/s)	v_3 (m/s)	v_4 (m/s)
2	0.414	0.595	-	-
3	0.214	0.395	0.534	-
4	0.235	0.328	0.481	0.475

- Impacts between the masses in the 2-DoF system result in high velocity, high frequency oscillations of m_2 (figure 4.20a).
- This is also observed in the 3-DoF system; however, the occurrences of these frequency-up events are less regular (figure 4.20b). This is because the order in which the masses impact each other is not always sequential and pairwise. A result of this is that, although the peak amplitude of the voltage generated for the 3-DoF configuration is comparable to the 2-DoF configuration (figure 4.19), the RMS voltage generated by the 3-DoF configuration is lower.
- This issue of undesirable impact sequences is further compounded in the 4-DoF system (figure 4.20c). For this configuration, velocity amplification of the final mass in the stack, m_4, is irregular, with no significant difference observed in the amplitude of the velocities $\dot{z}_3$ and $\dot{z}_4$.

In summary, the multi-DoF PWL model has predicted that the 2-DoF configuration will generate a higher total output voltage than velocity amplified harvesters with greater numbers of DoFs. This finding is also determined experimentally in chapter 5.

For comparative purposes, the amplitude of the voltage response with frequency, for a 2-DoF linear system—equivalent to the 2-DoF PWL harvester—is plotted in figure 4.21. In a linear system, the springs transfer load to the masses in both compression and tension, with the linear response consisting of two resonant peaks. The amplitude of the peak at the lower frequency is significantly larger than the secondary peak; furthermore, the peaks are separated by a large frequency range. Ideally, a multi-modal energy harvester should have close resonances, each with significant amplitude. Clearly, the linear 2-DoF energy harvester presented here does not achieve this. Comparing the amplitude of the voltage response of the linear 2-DoF harvester in figure 4.21 and the 2-DoF PWL harvester, the amplitude of the response of the velocity amplified PWL systems is significantly larger. Taking the 2-DoF $R = 20$ system excited at $Acc = 10$ m/s^2 from figure 4.17b, the peak amplitude of the velocity amplified response is increased by a factor of ~ 4 relative to the linear 2-DoF system under the same excitation.

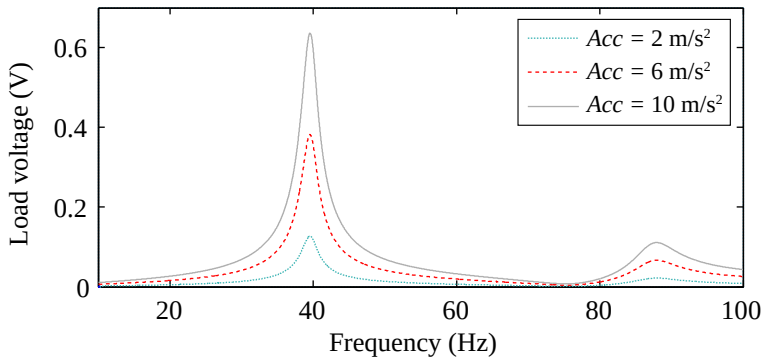

Figure 4.21: Amplitude of voltage response as a function of frequency for a 2-DoF linear energy harvester—mass ratio $R = 3$.

Simulated non-linear analysis of multi-DoF PWL oscillators has been presented in this section. The influence of frequency, acceleration, initial gap, and mass ratio on the dynamics of 2-DoF PWL harvesters has been investigated, while 3- and 4-DoF PWL harvesters were investigated for changing mass ratio and compared to the 2-DoF PWL system. Significant predictions from the multi-DoF model (with specific model parameters) include:

- under sinusoidal forced excitation, the dynamics are typically chaotic;
- hysteresis in the response is small, or not present;
- increasing g_0 results in the optimal frequency shifting towards lower frequencies;
- RMS velocity also increases with g_0, provided the acceleration level is sufficient to achieve large oscillations at the optimal frequency, which is determined by g_0;
- increasing mass ratio increases the relative velocity between the magnet and coil, resulting in the generated voltage increasing; and
- the RMS velocity of the final mass does not increase beyond 2-DoFs, as the sequence of impacts required to achieve high amplification occurs less regularly with higher numbers of DoFs—investigated experimentally in chapter 5.

These findings are valid for the set of parameters used in the multi-DoF model.

Implications of the simulation results for the applicability of multi-DoF PWL harvesters are summarised below.

- The chaotic harvester response is stationary random in nature, meaning, over time, the RMS of the output tends towards a certain value (Bendat and Piersol, 1971). Therefore, although the response of the chaotic system at a particular time is, by definition, dependent on the initial conditions, the RMS output is independent of initial conditions. A plot of the RMS velocity of m_2 against time for a range of initial conditions is shown in figure 4.22. It is clear that, irrespective of the initial conditions, the RMS of the chaotic response tends towards a certain value, over time. Also, the hysteresis exhibited by the single-DoF PWL systems in section 4.1 is significantly reduced or no longer present in the multi-dof PWL systems investigated in this section. Coupled with the stationary random nature of the response, the practical implication of this lack of hysteresis is that, for given excitation conditions, the RMS output from the harvester can be predicted prior to installation.

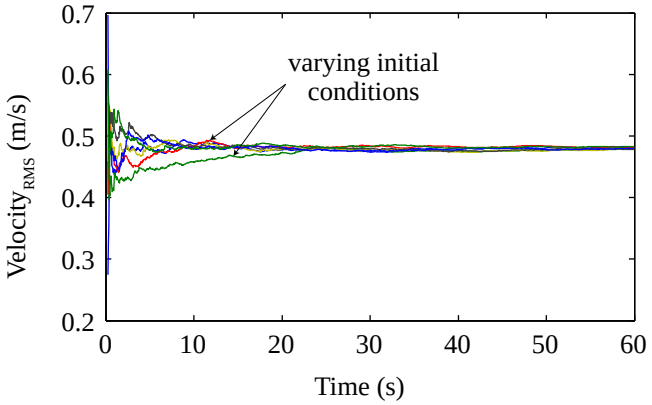

Figure 4.22: RMS velocity of m_2 as a function of time, for a range of initial conditions—$f = 22$ Hz, $Acc = 10$ m/s^2, $g_0 = 3$ mm.

- Achieving high power output at low frequencies is a significant challenge for linear VEHs. Multi-DoF PWL harvesters offer potential in this area, as the response shifts towards lower frequencies with increasing g_0, while the voltage amplitude of the response also increases. As g_0 is increased, however, the acceleration level required to achieve a significant response also increases. In general, the velocity amplified systems require large acceleration amplitudes to achieve a significant response.

- The shift in optimal operating frequency to lower frequencies with increasing g_0 offers potential as a tuning parameter. Prior to installation, the application frequency would be measured. The harvester geometry would then be adjusted to the desired value of g_0 to obtain maximum power generation. If the source vibration frequency is temporally varying, an active control mechanism may be necessary. As described for the single-DoF PWL harvester in section 4.1.2 and for harvesters employing tuning mechanisms in the literature (section 1.4.1), implementing an active control mechanism is undesirable as it would require energy to operate.

- The increased oscillation frequency of the mass coupled to the transducer, caused by the mass experiencing multiple impacts per cycle, allows large total displacements of the mass to be achieved within a small volume. This

increases the power density, which has the practical benefit of reducing the device volume required for large total displacements at low frequencies.

- The highest output is achieved by the 2-DoF configuration; this reduces the harvester volume requirements, compared to higher DoF configurations. Spatial requirements of VEHs are likely to be important in many application environments; therefore, this can be seen as a benefit.

- The amplitude of the response from the 2-DoF PWL harvester is significantly larger than that of an equivalent 2-DoF linear system, meaning the velocity amplified system can generate more power under the excitation conditions presented, although the device volume is increased for the velocity amplified system.

4.3 Closure

Single and multi-DoF PWL electromagnetic energy harvesters were modelled in this chapter, and compared to equivalent linear systems. The dynamics have been investigated through non-linear analysis methods, such as bidirectional sweeps, stroboscopic maps, phase diagrams, Poincaré maps, and power spectra. The influence of frequency, acceleration, and initial gap, g_0, was investigated for single-DoF PWL systems, while an additional variable parameter—mass ratio, R—was also investigated for the multi-DoF PWL systems. Attached to this thesis is a CD containing the MATLAB scripts with the single-, 2-, 3-, and 4-DoF models employed.

Single-DoF PWL harvesters were described initially, introducing some of the key concepts and parameters in advance of the more complex multi-DoF PWL systems:

- An extended phase space was developed to determine the solution trajectory for a set of excitation and geometric conditions. This phase space included switching surfaces—the term used to describe the position where the stiffness changed from one form of linear behaviour to another—located at the points of contact between the mass and springs. Intersection with

one of the switching surfaces, i.e. the masses coming in or out of contact with a spring, resulted in a non-smooth change in dynamics between linear behaviours.

- The single-DoF PWL system could operate in three periodic regimes, while chaotic motion was also observed. The periodic regimes were determined by the number of switching surfaces intersected. The highest velocities and voltages were achieved by the periodic regime in which both switching surfaces were crossed, i.e when the stopper spring was engaged, resulting in a double impact cycle—referred to as Mode 3 operation. The single-DoF PWL system achieved a higher amplitude response than an equivalent linear system in this Mode 3 operation.

- Both hardening and softening hysteresis behaviour was observed in bidirectional sweeps of the frequency, with the amplitude and bandwidth increasing significantly for the high-energy response. Hysteresis was also seen in bidirectional sweeps of the acceleration, and the initial gap g_0. Hysteresis in the response impacts the energy which can be extracted from such a system in an application environment, as the response is dependent on the initial conditions.

- Increasing g_0 resulted in the optimal frequency shifting to lower frequencies, due to the decreasing effective stiffness. A significant shift of 13 Hz from $\sim$ 33 Hz to 20 Hz was observed for a change in g_0 from 0 to 10 mm. This geometric parameter could potentially be implemented as a frequency tuning mechanism.

- The amplitude of the highest voltage response also increased with g_0, due to the increased RMS velocity associated with the larger displacement range; however, the acceleration level required to reach the highest energy operating regime also increased.

Velocity amplified multi-DoF PWL harvesters (referred to as VAEGs throughout the remainder of this thesis) were then investigated through simulation. The majority of the focus in this section was on 2-DoF PWL systems, while 3- and

4-DoF PWL systems were also investigated. As velocity amplification is an important feature of these systems, the masses in the stacked mass system became monotonically smaller from the base up, while the same transducer was implemented in each configuration.

- The phase space of a 2-DoF PWL system was described, including an additional switching surface to the single-DoF PWL system, located at the point of impact between the two masses.
- While periodic motion was typical in single-DoF PWL systems, chaotic motion was the standard in the 2-DoF system investigated. This was further compounded in the higher DoF systems, due to the additional switching surfaces introduced with each mass. It should be noted that the analysis presented is for a single set of parameters. Changing the mechanical and electrical damping, or mass and stiffness characteristics may result in different device behaviour. It is likely, however, that the typical behaviour of multi-DoF PWL systems, under the same excitation conditions discussed in this chapter, would be chaotic.
- The significant hysteresis exhibited by the single-DoF PWL system was effectively eliminated in the 2-DoF system. This meant that the RMS of the stationary random response was independent of initial conditions, which is significant for potential implementation in an application environment.
- The frequency shift described for the single-PWL system with changing g_0 also applied in the multi-DoF PWL systems, with a 40% reduction in optimal frequency observed for a change in g_0 of 10 mm. This frequency shift was a result of reduced effective stiffness with increasing g_0.
- The amplitude of the voltage output also increased with g_0, due to increased velocity resulting from the greater displacement range; however, the acceleration level required to engage the stopper spring and achieve large amplitude oscillations also increased with g_0.

- The velocity of the final, smallest mass in the system of stacked masses, m_n, increased with mass ratio, according to the conservation of momentum. An increase in the oscillating frequency of m_n was also observed, where the mass rebounds off the stopper spring multiple times per excitation cycle. This increased frequency allows m_n to traverse a larger total displacement at low input frequencies within a much smaller volume, thus, increasing the power density.

- The amplitude of the voltage response did not increase with increasing number of DoFs, beyond 2-DoF. The optimal sequential pairwise collisions for maximum velocity amplification occurred intermittently in the higher-DoF systems, such that the amplitude of the 4-DoF system response was actually much lower than the 2-DoF system, contrary to the theory of velocity amplification.

- The 2-DoF PWL harvester achieved a significantly higher voltage output than an equivalent linear 2-DoF system, due to the different system dynamics discussed earlier.

This chapter placed a significant emphasis on the dynamic behaviour of single- and multi-DoF PWL oscillators. The model afforded relatively easy access to the behaviour of the complete system in the various configurations, in comparison with measuring the same behaviour in an experimental system. In the remainder of this thesis, the focus shifts towards a global analysis of experimental systems; for example, measuring the RMS voltage generated, or the RMS velocity of a particular mass to assess the overall performance. The model is also implemented for deeper insight into certain behaviours, design optimisation, and to supplement experimental data.

The results of the numerical investigations presented in this chapter lead to a number of interesting questions regarding the influence of geometric and excitation parameters on the dynamics of multi-DoF velocity amplified systems. It is of interest to investigate the influence of these parameters further in later chapters. For example, the influence of mass ratio and number of DoFs on VAEGs—under drop-test and forced excitation—is investigated experimentally

in Chapter 5. Other parameters discussed in this chapter, such as g_0 and base acceleration, are investigated experimentally in chapter 6.

Chapter 5

Influence of mass configuration on multi-DoF VAEGs

A detailed experimental analysis on the influence of mass ratio and number of DoFs on the dynamic behaviour and voltage generation of macro-scale VAEGs is presented in this chapter. The experimentation addressed 2-, 3-, and 4-DoF stacked-mass configurations, with mass ratios in the range $R = 3$–20 tested under drop-test and sinusoidal forced excitation. A description of the multi-DoF systems is provided in section 5.1. From the theory of velocity amplification (Rodgers *et al.*, 2009), described in section 2.3, increasing the mass ratio and number of masses in the system results in an increase in the velocity gain, provided the coefficient of restitution is sufficiently high. In section 5.2, the validity of this theory for VAEGs is investigated for the range of mass configurations, using drop-tests. The dynamics of the different systems are analysed using high-speed imagery and compared to theory. The dynamic behaviour and voltage output of the range of VAEG configurations under sinusoidal forced excitation are described in section 5.3, for fixed transducer size and also for proportional transducer scaling.

5.1 Multi-DoF VAEG design

The systems described in this investigation are macro-scale multi-DoF systems, where the number of DoFs is equal to the number of masses. In order to

achieve velocity amplification, the masses were vertically stacked—as shown in figure 5.1—such that the heaviest mass was at the base and the remaining masses were decreased monotonically until the final, smallest mass. A schematic of 2-, 3- and 4-DoF configurations for a mass ratio of $R = 10$ (equation 2.38) is depicted in figure 5.1. To achieve a given mass ratio, the sizes of the base and final masses remained constant regardless of the number of DoFs; it was the intermediate masses between the base mass and final mass that changed. The intermediate masses were determined from equation 2.37. Configurations with 2-, 3- and 4-DoFs, and $R = 3$, 5, 10 and 20 were tested. The proof mass (sum of masses) of each configuration is shown in table 5.1.

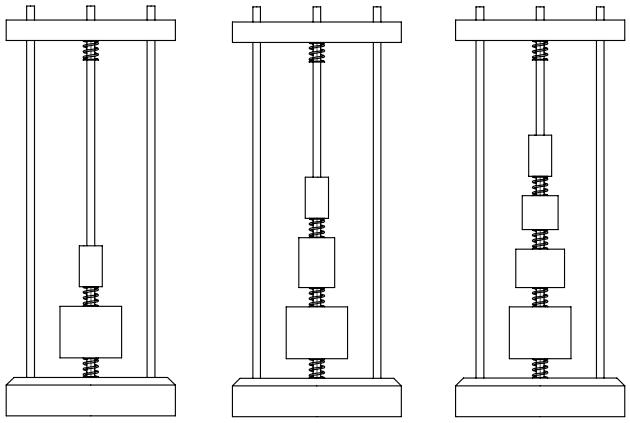

Figure 5.1: Schematic representation of 2-, 3- and 4-DoF configurations for $R = 10$—without transducer.

Table 5.1: Proof mass of each VAEG configuration; note: $m_1 = 80$ g.

Degrees of Freedom	mass ratio, R			
	3	5	10	20
	mass (g)			
2	106.67	96.00	88.00	84.00
3	152.85	131.78	113.30	101.89
4	200.60	170.14	142.37	124.33

Each VAEG was composed of a number of free-moving copper masses (i.e. not anchored to the device housing or each other), with high quality stainless steel 316

(SS316) springs interposed—SS316 was used due to its non-magnetic properties. Each mass was constrained to move in the vertical direction by an SS316 shaft, while a cap was placed on the system to constrain the total vertical displacement of the masses—as in the model of the 3-DoF VAEG illustrated in figure 5.2. The cap height was also adjustable, such that the initial gap, g_0, could be varied. As demonstrated throughout chapter 4, g_0 has a significant effect on the dynamics of PWL systems, in this case multi-DoF VAEGs. It was also necessary to be able to adjust the position of the coil relative to the magnet stack in order to maximise the change in flux experienced by the coil for each configuration. The coil position was adjusted in the same way as the cap, by moving the sliders along the guide rails. The cap and coil holder were held in place by set screws.

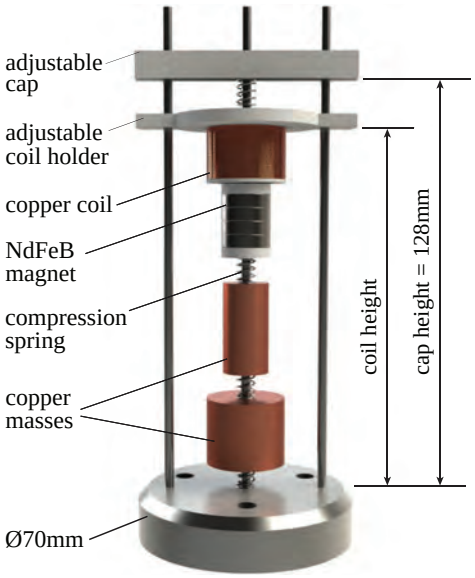

Figure 5.2: Model of the 3-DoF $R = 5$ VAEG—with transducer present.

A transducer was introduced in the forced excitation tests, as in the model of the 3-DoF VAEG in figure 5.2. This incorporated a single or multiple neodymium iron boron (NdFeB) permanent magnets in the final mass (sections 5.3.1 and section 5.3.2, respectively) and a copper coil positioned concentrically to the magnet. Ring magnets of outer diameter 16 mm and height 2 mm were used as they had a suitable mass for the tests (less than the final mass in the $R = 20$ system, i.e. the smallest mass tested). Copper wire of diameter 100 µm was used

in the coil which had an inner diameter of 18 mm, a height of 15.5 mm and a thickness of 3 mm, resulting in a coil resistance of 339 Ω. Copper was employed to supplement the magnet in each final mass to bring the total mass to the desired level. Teflon inserts were included on the bearing surface of the masses containing the magnet to achieve a low coefficient of friction contact.

The VAEG support structure was designed to provide an unobstructed view of the masses to facilitate object tracking through high speed imagery. The overall mass and volume were not constrained, as the VAEGs were designed to compare the dynamics and voltage output for a range of mass configurations. The VAEGs in this chapter were not designed to achieve a high power density.

The description of the VAEG mass configuration parameters provided in this section is relevant for both the drop-test and forced excitation tests. The transducer described was implemented in the forced excitation tests only, however, as the drop-test was simply designed to analyse the velocity gains for the various mass configurations.

5.2 Drop-test

The facility developed to determine the velocity gain in multi-DoF stacked mass configurations under drop-test was presented in section 3.1. The objective of the investigation in this section was to validate the theoretical velocity amplification model, discussed in section 2.3, with experimental data.

In order to compare the velocity amplification theory to experimental data, it was necessary to modify the theory of Rodgers *et al.* (2009). The original equations to determine velocity gain—equations 2.34 and 2.39 presented in section 2.3—describe instantaneous impacts associated with rigid-body mechanics, whereas in the drop-tests, the impacts occur over a finite time interval. Therefore, in order to achieve sequential pairwise impacts with all masses dropped at the same time, the masses higher up the chain must fall through a greater distance. Consequently, the free-fall velocities of each of the masses are not constant—as is the case for the theory described by Rodgers *et al.* (2009)—with the masses further up the chain having higher free-fall velocities at the moment of impact. Therefore, in order to calculate the new free-fall velocity of each mass the impact

times need to be added to the initial free-fall time of each sequential mass. The free-fall velocity of each mass at the time of impact is calculated using $v_{ff} = gt_{ff}$, where g is the acceleration due to gravity and t_{ff} is the free-fall time. As forces are only transferred between the spring and mass when the spring is in compression, the impact time is calculated as the half period of the spring-mass system at the natural frequency (half of full compression-extension cycle):

$$t_{impact} = \frac{\tau}{2} = \frac{1}{2f_n} = \pi\sqrt{\frac{m}{k}} \tag{5.1}$$

The parameter altered by this modification is the initial velocity ratio, q (equation 2.36).

The experimental velocity amplification data plotted over the theoretical velocity amplification is shown in figure 5.3. These respective experimental and theoretical results were determined through the drop-test described in section 3.1 and the theory presented in section 2.3, with the modification introduced above. The data points represent the experimental results for the 2-, 3- and 4-DoF configurations for mass ratios of $R = 3$, 5, 10 and 20, while the lines represent the theoretical velocity gains for a coefficient of restitution of $e = 0.97$. This value is representative of the restitution levels measured between two impacting masses in a simple 2-mass drop-test. From the theory, it is evident that increasing the mass ratio and increasing the number of masses in the system results in an increase in the velocity gain.

The velocity gain that can be achieved by a 2-DoF configuration begins to plateau at low mass ratios, with an increase of 13.9% between a mass ratio of $R = 5$ and 10 and an increase of just 7% between $R = 10$ and 20. Experimental results for the 2-DoF configuration match the theoretical data well, with only a slight discrepancy between them (1–5%). The theory suggests that the addition of extra masses should increase the velocity gain at higher mass ratios, but these extra masses should offer only slight increases over the 2-DoF configurations at lower mass ratios. This is also demonstrated by the experimental data. The 4-DoF configuration actually achieves the lowest velocity gain at a mass ratio of $R = 3$, due to the extra losses caused by the higher number of impacts. At higher mass ratios, the theory demonstrates significant increases in velocity gains for the

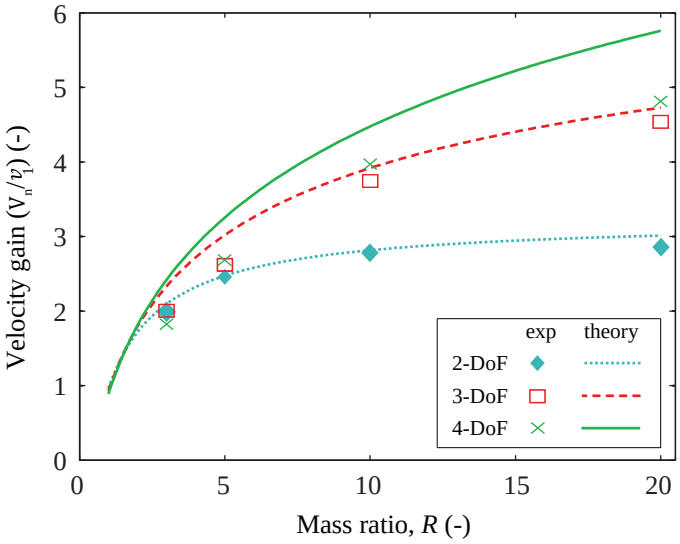

Figure 5.3: Experimental velocity gain from drop-tests for a range of mass configurations compared to theory with $e = 0.97$.

3- and 4-DoF configurations, which is also evident in the experimental data. The highest velocity gain of a factor of 4.8 was achieved by the 4-DoF $R = 20$ system. Experimental velocity gains of the 3-DoF configuration are 4–14% less than that described by the theory, while the 4-DoF configuration achieves 11–24% less than the theory predicts. Evidently, the losses in the system increase with number of DoFs due to the additional impacts. Moreover, the impacts between the masses further along the chain are less restitutive (transfer less energy). This is due to the masses becoming less stable at the higher velocities associated with the 4-DoF configuration—with more lateral motion—resulting in greater contact between the masses and the shaft and, consequently, more friction. Lateral motion also results in the interposed springs impacting the masses at a slight angle rather than squarely, which increases energy losses further. This lateral motion was observed via high-speed imagery.

5.3 Forced excitation

It was shown in the preceding section that, under the optimal pairwise impacts in a drop-test, velocity increases with increasing mass ratio and number of DoFs. In

this section, the relative performances of VAEGs with different mass configurations are analysed under forced excitation, in terms of system dynamics and the resulting generated voltage. A fixed transducer size (fixed magnet-coil combination) was used to understand the effect of mass ratio and number of masses (section 5.3.1). A similar test series was analysed through simulation in section 4.2.2, with the results predicting that velocity and voltage increases with mass ratio, and that 2-DoF configurations outperform configurations with greater numbers of DoFs—the validity of these results are investigated experimentally here. Systems where the magnet volume was increased in direct proportion to the final mass are also investigated (section 5.3.2). Velocity amplification theory states that higher mass ratios will achieve more amplification. However, increasing the mass ratio also decreases the size of the final mass, which limits the magnet volume and, therefore, the amount of electromagnetic coupling (Cugat *et al.*, 2003). To investigate if the velocity amplification of larger mass ratio systems can compensate for their smaller transducers, the magnet size was changed in proportion to the mass ratio. The experimental set-up which provided the sinusoidal excitation to the VAEGs was illustrated in figure 3.5 in section 3.2.

5.3.1 Fixed transducer size

The same magnet-coil configuration was used for each system in this test series, ensuring that the electromagnetic coupling in each system was equal for a given magnet position relative to the coil. As a consequence, any increase in voltage achieved by one system over another can be accounted for by an increased rate of change of magnetic flux. This is largely dependent on the magnitude of the relative velocity between the magnetic field and coil (equation 2.15), which, in these tests, is controlled by the velocity of the final mass.

The voltage signal from the transducer was measured across a potentiometer (0–1 kΩ), which allowed the resistive load to be varied. The load resistance at which maximum power was achieved by each system did not vary significantly; because of this, a constant load resistance of 425 Ω was used.

This test series seeks to compare the optimal performance of each system, that is, the output voltage and corresponding RMS velocity from high speed camera

recordings. This required the optimisation of a number of coupled parameters. These parameters were the frequency of vibration, the position of the cap (which, as mentioned previously, controls the initial gap, g_0), and the position of the coil (see figure 5.2). The optimisation process involved incrementally changing one of the variable parameters while holding the others constant, measuring the output voltage and iterating this process for each variable parameter.

- The frequency was changed in 0.5 Hz increments. This was a sufficiently high resolution, as only slight variations in the measured voltage output were observed in the frequency range around the optimal frequency. Only results at the optimal frequencies—which were in the range of 11–16 Hz for each system—are presented.

- The initial gap, g_0 was changed in ~ 1 mm increments. g_0 had a significant effect on the performance of each system, both in terms of dynamics (optimal frequency, velocity amplification achieved) and the voltage generated. The influence of this parameter on the response of multi-dof VAEGs was analysed through simulations in section 4.2.2, and receives further attention in section 6.3 with an experimental investigation of a 2-DoF VAEG for varying gap lengths.

- The coil position relative to the magnet stack (also changed in ~ 1 mm increments) was used to maximise the rate of change of magnetic flux in the coil and, consequently, the generated voltage.

The optimal system parameters (frequency, initial gap and coil position) were determined through voltage measurements rather than the velocity measurements, as the processing time for the voltage data was orders of magnitude lower than that of the high-speed videos. Once the optimal system parameters were determined, the output voltage of each system was recorded for 40 s and repeated four times for those optimal parameters.

In order to better understand the dynamics of the VAEGs under forced excitation, the systems in operation were recorded using a high speed camera:

- The coil was removed from the test for this step such that the high-speed camera had an unobstructed view of each of the masses. As the magnet used was relatively low strength, the electromagnetic damping was low; therefore, the system dynamics demonstrated without the coil would not be significantly different to the dynamics of the system with the coil present. For example, for the 2-DoF $R = 3$ configuration, the average mechanical power of the smallest mass was 6.2 mW (calculated from the total energy—kinetic and potential—from the data recorded by the high speed camera), while the average electrical power was 0.24 mW (from the voltage data). The electrical power represents 3.9% of the available mechanical power for this configuration. This value is sufficiently low that the results achieved from the voltage data can be assumed to qualitatively represent the performance of the mechanical system.

- With the systems configured to the optimal parameters, the high-speed camera was used to track the position of each of the masses, through the image processing technique described in section 3.1.2. The camera recorded images at a rate of 1000 fps for 20 s. Due to memory limitations of the camera, this was the maximum length of time the camera could record and store data at this frame rate and image size. As the points of peak velocity were not as pivotal for the forced excitation test as in the drop-test, the frame rate of 1000 fps—which was significantly higher than the frequency of excitation—was sufficient to accurately track the masses.

A peak acceleration level of 1 g was chosen as it ensured that each system would achieve large oscillations at the optimal frequency, despite the masses always starting from rest. An interesting effect was observed when the system first began to oscillate. The masses were initially demonstrating small oscillations, before the masses furthest up the chain began experiencing slightly larger oscillations. These masses continually transferred energy back down the chain to the lower masses until the base mass began to exhibit large amplitude oscillations, resulting in high velocities. This effect is significant for real applications because, at the optimal frequency, the response is stationary random, resulting in the RMS output being independent of initial conditions. This contrasts with

other broadband systems reported in the literature where the system response in regions of non-unique solutions is dependent on the initial conditions (Mallick *et al.*, 2015; Ramlan *et al.*, 2010). This independence from initial conditions exhibited by VAEGs has previously been referred to in the simulation results in section 4.2.2, and is discussed further using experimental bidirectional frequency sweeps in section 6.3.

The results of the load voltage tests, with each system optimally configured in terms of frequency of excitation, g_0 and coil position, are shown in figure 5.4a, while the corresponding RMS velocities of the final mass in each system are shown in figure 5.4b. This plot demonstrates that the increases in voltage output, as seen in figure 5.4a, are largely as a result of an increase in velocity of the final mass, with similar patterns observed between figure 5.4a and 5.4b. However, the velocity of the final mass does not completely determine the output voltage, as the voltage is also dependent on the magnetic flux gradient (equation 2.15). Larger displacement ranges, corresponding to higher values of g_0, result in the flux gradient experienced by the coil decreasing, due to the relative position of the magnet and coil deviating from the optimal position for large portions of the cycle. Consequently, although the RMS velocity may increase with a higher cap height, the RMS voltage generated may be lower. Alternatively, the final mass may have a lower RMS velocity, but more frequent impacts or rapid changes in direction of motion could occur that increase the flux gradient, leading to higher output voltage. The influence of flux gradient (or the electromagnetic transduction factor, K, to which it is equivalent—equation 2.22) is discussed in greater detail in sections 6.2 and 6.3.

Figure 5.4a shows that the increase in mass ratio for the 2-DoF configuration results in a significant increase in output voltage, with the $R = 20$ system generating more than twice the output voltage of the $R = 3$ system. Increasing mass ratio for the 3- and 4-DoF configurations also results in an increase in velocity and voltage; however, the increase is not as significant as for the 2-DoF configurations. Increased output voltage with higher mass ratios was predicted in the simulations results in figures 4.17 and 4.19.

The most significant finding from these forced excitation results is that under optimal conditions, the 2-DoF configurations perform the best, achieving greater

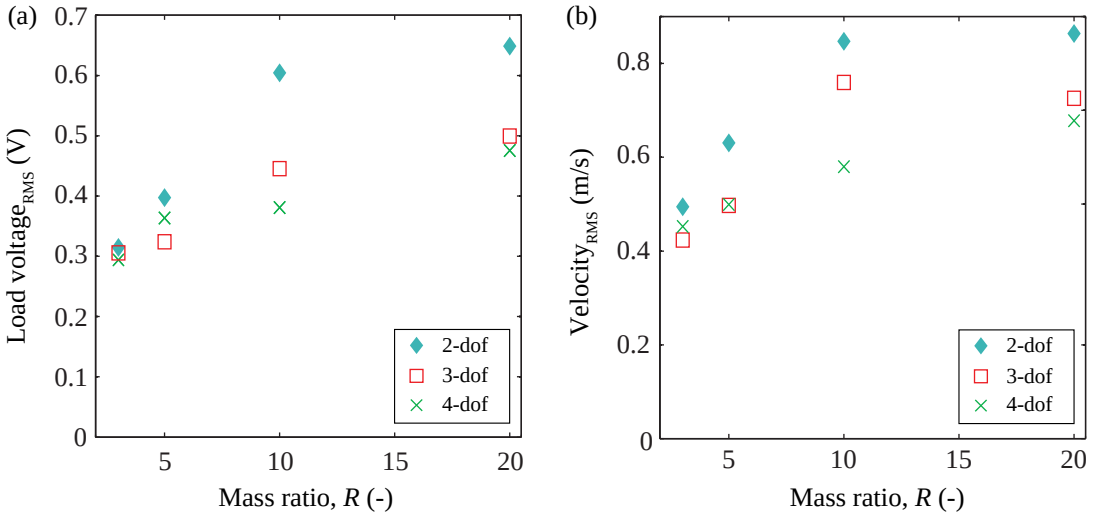

Figure 5.4: VAEG (a) RMS load voltage and (b) RMS velocity of the final mass for fixed transducer size under sinusoidal excitation—$Acc = 1$ g, $R_L = 425\ \Omega$.

velocities and output voltages than either the 3- or 4-DoF configurations. This result, which is contrary to the velocity gains described in the drop-test, was predicted in the simulation forced excitation sweeps in figure 4.19. A similar result was determined by Cottone *et al.* (2013), who compared 2- and 3-DoF VAEGs under noise excitation. The reduction in performance of the 3- and 4-DoF configurations is due to the more complex nature of the motion of the masses under forced excitation. The higher DoF configurations achieve high peaks in output voltage, compared to the 2-DoF configurations, when the sequence of impacts results in significant velocity amplification. However, these peaks occur irregularly and, as a result, the average velocity amplification achieved is significantly lower than that shown in the drop-test (figure 5.3). This was concluded from visual observation of each of the systems in operation and analysis of velocity profiles from the various systems. As a typical example, the velocity traces in figure 5.5c highlight the relatively high but irregular peaks observed for the 4-DoF system, which can be compared to the more oscillatory periodic motion of the 2-DoF system in figure 5.5a.

At lower mass ratios, particularly $R = 3$, each of the configurations generate approximately the same output voltage. This is most likely a result of the lower mass ratio systems achieving lower velocities, which causes the impacts in

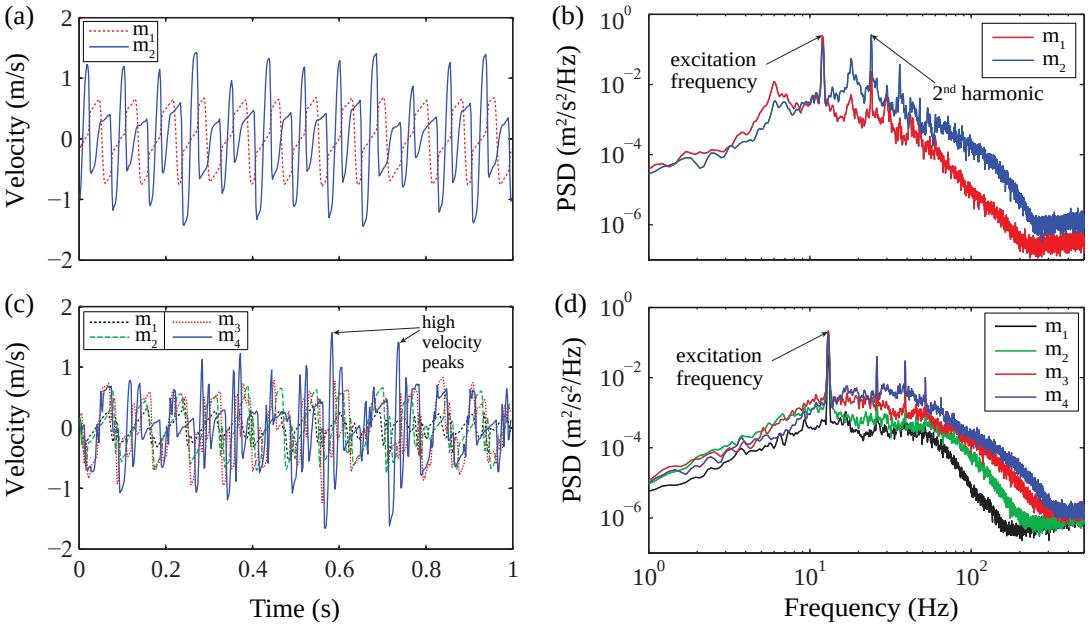

Figure 5.5: Velocity traces of each mass and corresponding power spectra for (a,b) the 2-DoF $R = 5$ system, and (c,d) the 4-DoF $R = 10$ system—$Acc = 1$ g.

these systems to be more ordered and more closely resemble the pair-wise impacts demonstrated in the drop-test. Consequently, the 3- and 4-DoF $R = 3$ configurations achieve approximately the same output voltage as the 2-DoF configuration at this mass ratio, similar to the drop-test results shown in figure 5.3.

The power spectral densities of the velocity data from the same systems are presented in figure 5.5b and d. Significant power in the frequency spectrum is present near the harmonics of the forcing frequency in each system. This is particularly the case for the 2-DoF configurations, which demonstrate the highest power near harmonics of the forcing frequency. This is shown by m_2 in the 2-DoF configuration where the peak at the 2nd harmonic is the largest peak.

The high frequency oscillations were observed to occur as follows: the final mass achieves significant velocity amplification as a result of an impact from the mass beneath it. It then impacts the cap and rebounds at high velocity. The lower mass has not yet lost all its kinetic energy and, hence, impacts the final mass once again. This process continues until the lower mass has no kinetic energy and begins to free-fall. The final mass can experience a number of these cycles for each period of the forcing frequency. These high frequency oscillations result in

greater velocities and, as a result, greater output voltages. Moreover, the total displacement of the final mass per cycle is greater than the displacement limit imposed by the cap, reducing the volume required to achieved large displacements (and velocities) at low frequencies. As a result, the power density is also increased. High frequency oscillations do not always occur, however, particularly in the 3- and 4-DoF configurations (figure 5.5c). To have a significant effect on the overall power generated, these high frequency oscillations must occur frequently. These frequency-up conversion events were previously described for simulation results in section 4.2.2.

5.3.2 Proportional transducer scaling

It has been demonstrated in the preceding section and in section 4.2.2 that, under forced excitation, increasing mass ratio increases velocity. However, increasing mass ratio also reduces the maximum possible size of the magnet due to the lighter final mass. This reduces the magnetic flux density and, consequently, the electromagnetic coupling. This final test series was, therefore, carried out in order to compare the benefits of increased velocity amplification (due to increased mass ratio) with the disadvantages of reduced magnet size.

This investigation involved making the size of the magnet within the final mass proportional to the size of that mass. This was achieved by stacking magnets together such that for each mass ratio, the same portion of the final mass consisted of magnetic material. Due to the additional material required to hold the magnets and allow them to slide freely on the central shaft, the maximum percentage of magnetic material that could be used in the smallest mass (in the $R = 20$ systems) was 70%. Hence, to make this consistent for all configurations, 70% of the final mass was composed of magnetic material for each mass ratio.

The process employed to optimise the frequency, initial gap and coil position for the investigation in the preceding section was implemented again for each configuration in the current analysis. It was not possible to reuse the same optimal parameters as the magnet stack in each system was changed, affecting both the electrical and mechanical damping, and, consequently, the optimal parameters.

Once the optimal parameters were determined, the load voltage was recorded for 40 s and four repeats were conducted.

The results of the output voltage tests from each of the optimal systems with proportional transducer scaling are shown in figure 5.6a. The 2-DoF configurations once again demonstrate the highest output voltage for each mass ratio. For this test series, however, the output voltage is at a maximum at the lowest mass ratio of $R = 3$, and decreases almost linearly with increasing R. This is due to the smaller magnet size in the transducer at higher mass ratios (lower magnetic flux density, B). Similar velocity profiles to those shown in figure 5.4b would be expected for the tests with scaled transducers, since the same mass ratios were investigated. However, it is evident that the increase in velocity amplification at higher mass ratios is not sufficient to compensate for the associated reduction in magnet size.

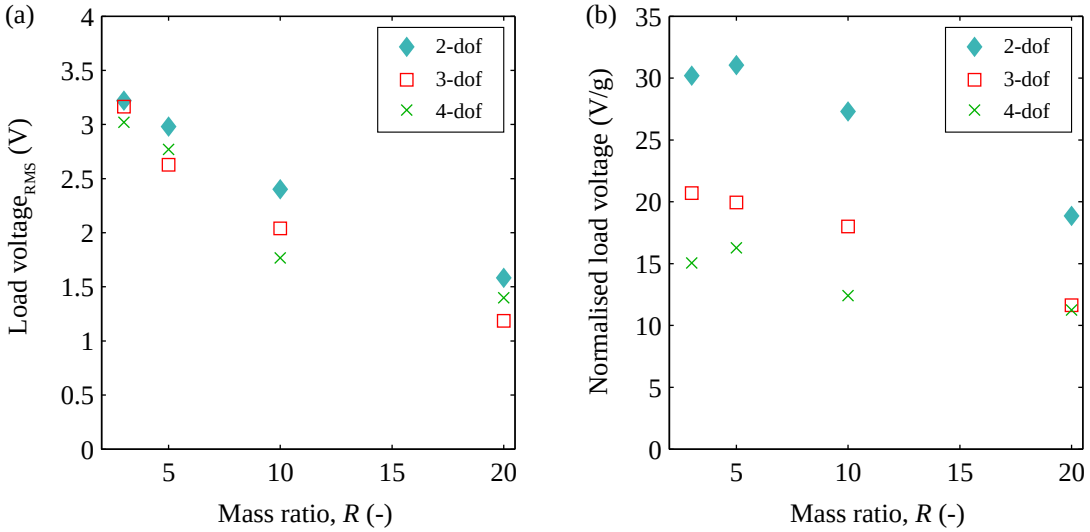

Figure 5.6: VAEG (a) RMS load voltage and (b) voltage normalised by proof mass for proportional transducer scaling under sinusoidal excitation—$Acc = 1$ g, $R_L = 425\ \Omega$.

Similar dynamics occur in these systems as were discussed for the fixed transducer size tests in the preceding section. The 2-DoF configuration has relatively less complex interactions with more velocity amplification events compared to the 3- and 4-DoF configurations, leading to higher RMS voltages. In contrast, the motion of the masses in the 3- and 4-DoF configurations is less periodic, leading

to fewer amplification events per unit time (similar to figure 5.5c) and increased losses due to larger numbers of impacts between the masses.

The RMS load voltages from figure 5.6a are normalised by the total proof mass of each system (table 5.1) in figure 5.6b. As the total mass increases with additional DoFs and reducing mass ratio, the normalised load voltage presented shifts the results from figure 5.6a towards lower numbers of DoFs and higher mass ratios. The 2-DoF configurations significantly outperform the higher DoF configurations under this metric. The normalised load voltage peaks at $R = 5$ for the 2-DoF configuration and decreases slightly as the mass ratio is reduced to $R = 3$. This suggests that the highest voltage per mass—which would translate into the highest power per volume—for a multi-DoF VAEG occurs for a 2-DoF configuration with a low mass ratio. A 2-DoF VAEG with a mass ratio of $R = 3$ is characterised in chapter 6.

5.4 Closure

A detailed experimental analysis on the influence of mass ratio and number of degrees-of-freedom (DoF) on the dynamics and voltage output of a VAEG has been carried out. Configurations with 2-, 3- and 4-Dofs, and mass ratios of $R = 3$, 5, 10 and 20 were tested under drop-test and forced excitation conditions.

- Under drop-test conditions, increasing mass ratio and number of DoFs resulted in higher velocity amplification, in accordance with theory. The 4-DoF configuration with a mass ratio of $R = 20$ demonstrated the highest velocity gain of a factor of 4.8.

- Under forced excitation, the velocity amplification the 3- and 4-DoF configurations achieved in the drop-tests was attained infrequently. This was due to the increased complexity of the impacts between masses (resulting in non-optimal sequencing), and the increased losses due to the additional impacts, compared to the 2-DoF configurations. As a consequence, the 2-DoF configurations, that exhibited fewer losses and a higher RMS velocity, achieved the highest output voltages.

- With fixed transducer size, the systems with higher mass ratios achieved higher output voltages due to the greater level of velocity amplification.
- With proportional transducer scaling, the increase in velocity of the higher mass ratio systems was not significant enough to overcome the reduction in transducer size. This resulted in the $R = 3$ systems achieving the highest output voltages for this test series.
- Normalising the output voltage to total proof mass, the greater performance of the 2-DoF configurations relative to the 3- and 4-DoF configurations was further compounded. The peak normalised voltage was then achieved by the 2-DoF $R = 5$ system.
- At 1 g of acceleration, at the optimal frequency, all of the systems entered into a state of large oscillations, despite being initiated from rest. This was due to the internal perturbations of the smaller masses in the system. This is significant as it seems to suggest the system could be deployed with the masses at rest and, if the excitation is sufficiently high and the frequency is appropriate, this effect ensures that the masses will achieve a significant response irrespective of initial conditions, allowing the system to output a reasonably high level of voltage.

Based on the findings of the current chapter, where the 2-DoF configurations generated the highest output voltages, a 2-DoF VAEG was selected for optimisation and characterisation in the following chapter. A mass ratio of $R = 3$ was employed, as it was found that the increase in velocity at higher mass ratios did not balance the reduction in the magnet size.

Chapter 6

Optimisation and characterisation of a 2-DoF VAEG

It has been demonstrated experimentally in chapter 5 and through simulations in chapter 4 that 2-DoF VAEGs can generate greater power than system with higher numbers of DoFs. As such, a 2-DoF VAEG was selected for characterisation in this chapter. A low mass ratio of $R = 3$ was chosen based on the findings of section 5.3.2, where it was determined that the increase in velocity with increasing mass ratio did not compensate for the reduction in magnet size. A range of electromagnetic transducer architectures were investigated through simulations to determine the optimal transducer design for a VAEG; the best performing transducer architecture was then optimised—outlined in section 6.2. The optimised 2-DoF VAEG was characterised using experimental and simulation frequency sweeps for a range of acceleration levels and gap lengths, discussed in section 6.3. Finally, for comparative purposes, the harvester configurations which achieved the highest NPD and FoM_V (described in section 1.5) are presented in section 6.4.

6.1 2-DoF VAEG design

A 2-DoF VAEG with mass ratio $R = 3$ was selected for further investigation in this chapter, based on the results from previous chapters which are summarised above. In chapter 7, the scaling of a 2-DoF VAEG is described. In the scaling analysis, the device was fabricated at three scales and underwent homothetic scaling, i.e. it was uniformly scaled. In this chapter, the optimisation and characterisation of one of the devices used in the scaling analysis is described. As such, a number of the design decisions implemented were based on the future use of the prototype for scaling analysis.

The process of designing the 2-DoF VAEG at the three scales can be divided into a number of subcategories:

- Active components and support structure
  - The 2-DoF VAEG consisted of a copper base mass and a lighter magnet stack. It was designed such that both the copper mass and the magnet stack oscillated within a cylindrical Teflon tube. Copper was selected for the base mass based on its high density and non-magnetic properties. The dimensions of the copper mass were selected to achieve a mass ratio of $R = 3$.
  - A model of the prototype and its support structures are illustrated in figure 6.1a (photograph of device shown in figure 6.2). This structure was able to accommodate the three prototype scales as the Teflon tubes acted as inserts to the base and cap.
  - The interior of the tube is shown in figure 6.1b, with the masses in their rest positions. As in previous designs, both masses were disconnected from the springs and were able to move freely along the inside of the Teflon tube. The springs were non-magnetic stainless steel compression springs, with the spring stiffness at each scale chosen, such that the natural frequency of an equivalent linear system remains constant.
  - A range of magnet stacks were investigated, each with the same volume (described in section 6.2). The initial design step was to select

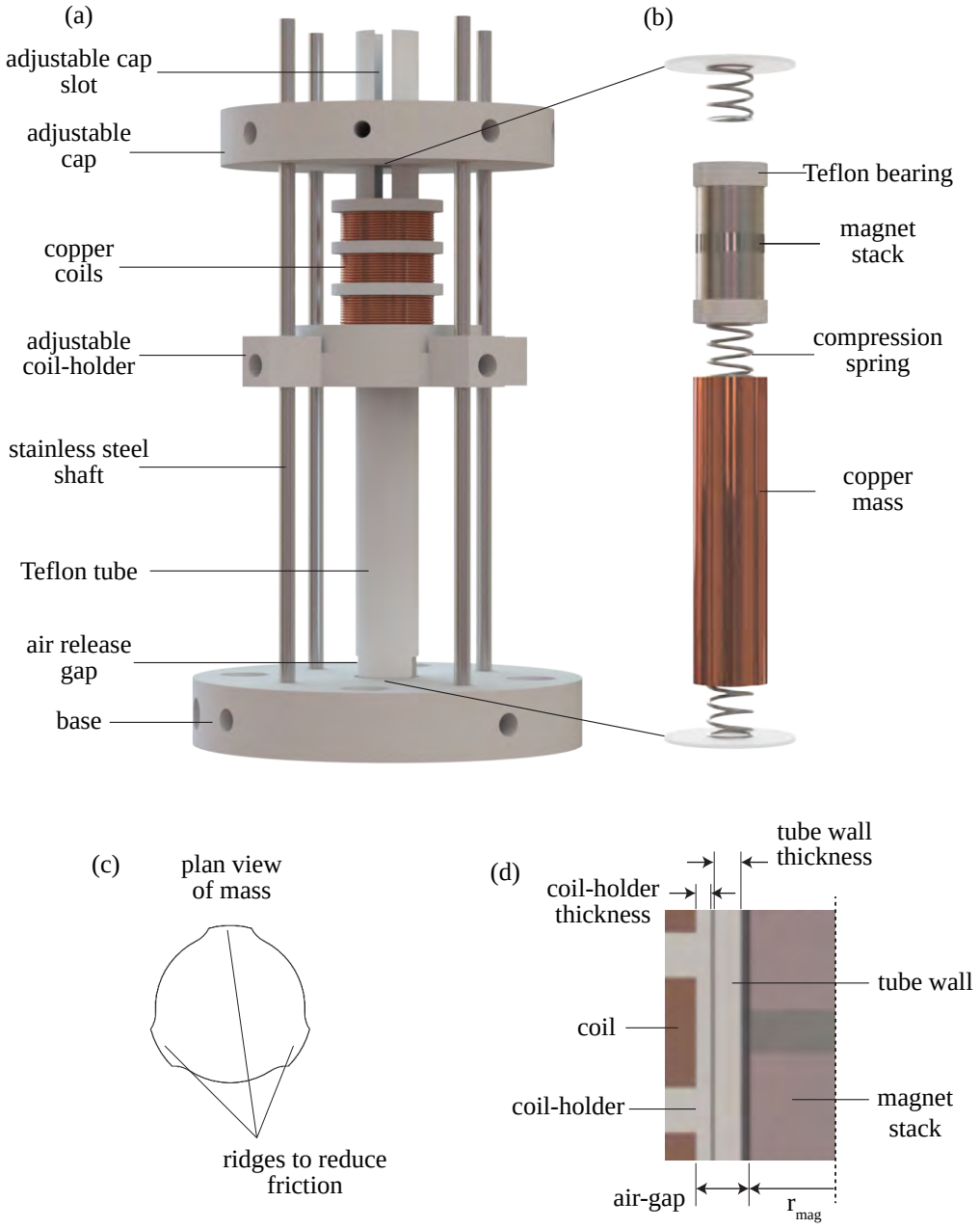

Figure 6.1: (a) Model of $d_{mag} = 8$ mm scale harvester and support structure, (b) tube inner structure showing active components, (c) plan view of inertial masses showing ridged edge design, and (d) cross section of the left half of the coil-magnet arrangement.

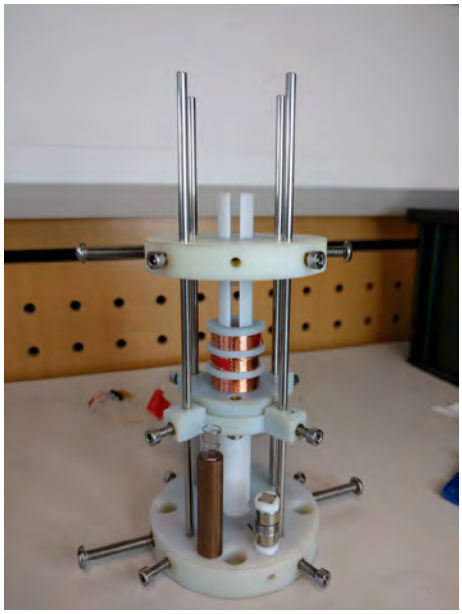

Figure 6.2: Photograph of the $d_{mag} = 8$ mm 2-DoF VAEG.

a magnet stack diameter and height. The magnets were chosen based on the availability of NdFeB magnets of certain dimensions and grade, while the height of the stack was based on a minimum desired stack aspect ratio of 1:1.5 (diameter:height). This aspect ratio was selected based on previous experience, whereby masses with low aspect ratios were affected more by rotation about the radial-axis, resulting in energy loss. Magnet diameters of $d_{mag} = 12,\ 8$ and 6 mm were chosen. As the volume changes with the cube of the dimension, the resultant transducer volumes, normalised to the volume of the largest magnet stack were 1, 0.296 and 0.125.

- Adjustable parameters—optimisation and characterisation of a VAEG requires a number of geometric parameters to be adjustable.
  - As described in chapter 4, adjusting the gap length, g_0, has a significant effect on the dynamics of both single and multi-DoF PWL oscillators. In the 2-DoF VAEG presented, g_0 was adjusted by changing the cap position. Two slots along the length of the top of the tube allowed the

cap position to be raised or lowered along the Teflon tube and stainless steel shafts.

  - The optimal position of the coil relative to the magnet stack varies with changing g_0. As such, it was also necessary to be able to adjust the coil position. The coil-holder was designed to slide along the stainless steel shafts external to the Teflon tube. Set screws were used to hold the cap and coil-holder in place.

- Mechanical damping considerations—minimising mechanical damping maximises the power generation.

  - The copper mass was designed to reduce friction with the Teflon wall. Three ridges along the length of the mass limited the surface area of the copper in contact with the tube, reducing friction (figure 6.1c).
  - A similar approach was taken in the magnet stack design. Teflon caps, with the same ridged edge design, were attached to both ends of the magnet stack to act as a bearing surface, reducing friction between the stack and tube.
  - An air-release gap was present at the base of the Teflon tube to reduce squeeze-film damping effects.

- Air-gap—in the design of an electromagnetic energy harvester, it is desirable to achieve as small an air-gap between the magnet and coil as possible. This limits the flux leakage and also minimises the volume of the device.

  - A cross section showing half of the magnet-coil set-up is shown in figure 6.1d. The ridged edges on the magnet stack increased the distance between the magnet and tube wall, and therefore, increased the air-gap. This resulted in a trade-off between reducing mechanical damping and increasing the size of the air-gap. The remainder of the air-gap consisted of the tube wall thickness, coil-holder thickness, and any space that existed between these surfaces to allow for relative movement. The highest power output for a given configuration

and excitation conditions was achievable by removing the coil-holder (reducing the air-gap), with the coil wound directly around the Teflon tube at the optimal coil position.

– The 6 mm configuration was designed initially, as the 8 mm and 12 mm configurations were simply uniformly scaled-up versions of the 6 mm configuration. The wall thickness of the 6 mm tube—determined by the limitations and difficulty of the machining process—was 1.2 mm. Taking the $d_{mag} = 6$ mm configuration: a tube wall thickness of 1.2 mm, a coil-holder thickness of 0.5 mm, and an additional gap of 0.25 mm between the magnet and inner wall of the tube resulted in a total air-gap of 1.95 mm. Consequently, to maintain the homothetic transformation between the scaled harvesters, the air-gaps in the $d_{mag} = 8$ mm and $d_{mag} = 12$ mm configurations were 2.6 mm and 3.9 mm, respectively.

6.2 Transducer design and optimisation

In the analysis of VAEGs presented thus far, a single magnet (or stack of magnets with the same polarity) oscillated relative to a single coil. It has been demonstrated in the literature that greater power densities can be achieved by implementing more complicated magnet-coil architectures (Saha *et al.*, 2008; Shahosseini and Najafi, 2015; Spreeman and Manoli, 2012; von Büren and Tröster, 2007). A range of these transducer configurations were investigated through simulation for the $d_{mag} = 12$ mm scale harvester to determine the optimal transducer design for a VAEG. These are discussed in the following subsections.

6.2.1 Transducer configurations

The range of transducer configurations investigated are illustrated in figure 6.3. There were three magnet configurations—Magnet I, II and III (shown in each column)—each having two coil configurations—Coil I and II (shown in the each row). The coils are located in regions of peak radial flux density, with the location and number of these peaks changing for each magnet configuration. Therefore,

the Coil I and Coil II configurations are different for each magnet configuration—this is expanded upon later. Each magnet-coil arrangement is referred to as the combination of the magnet and coil configurations, i.e. the magnet stack with two magnets and three coils is referred to as Magnet II - Coil II. Magnet polarisation is denoted by the white arrows. The Magnet II and III configurations consisted of oppositely polarised magnet stacks. Soft magnetic spacers—composed of low carbon steel 1020—were located between the magnets to act as flux concentrators. The magnet stacks were designed such that the peak locations were equidistant. Consequently, the coils were also equally spaced. The coils were connected in series with the winding direction alternated with each consecutive coil; coupled with the equal coil spacing, this means the voltage generated in each coil was in phase and the voltages could be superimposed.

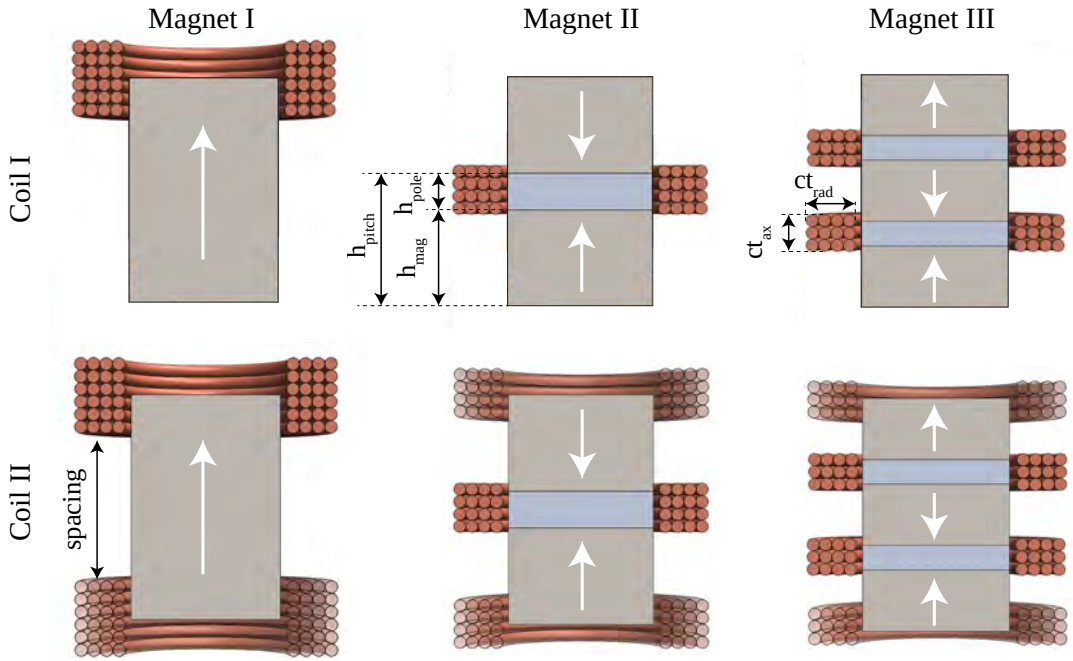

Figure 6.3: Cross sections of the three magnet configurations (Magnet I, II, III), each with two coil arrangements (Coil I—top row; Coil II—bottom row).

Figure 6.4 shows the magnetic fields generated by the magnet configurations. The Coil I and Coil II arrangements are illustrated as solid white boxes, and a combination of the dashed and solid white boxes, respectively. The average

radial magnetic flux density over the coil radial thickness, $\bar{B}_r$, for the magnet-coil configurations in figure 6.4, are shown in figure 6.5 (left column). Magnet I (the single magnet) demonstrates two peaks in $\bar{B}_r$ corresponding to the upper and lower surfaces of the magnet. Magnet II comprises two oppositely polarised magnets with a soft magnetic spacer (pole piece) between them. This pole piece concentrates the flux, increasing the radial flux leaving the magnet. This can be seen in figure 6.4b where the flux lines leave the pole perpendicular to the surface, and in figure 6.5 for Magnet II, where $\bar{B}_r$ at the pole location is significantly higher than the peak $\bar{B}_r$ for Magnet I. Increasing the number of repulsively stacked magnets to three, as in Magnet III, results in a similar effect. There are now two large peaks in $\bar{B}_r$; however, the amplitude begins to decrease due to the decreasing height of the magnets. The peaks in $\bar{B}_r$ at the ends of the magnet stack remain as the flux lines which were guided outwards from the spacers re-enter the end magnets.

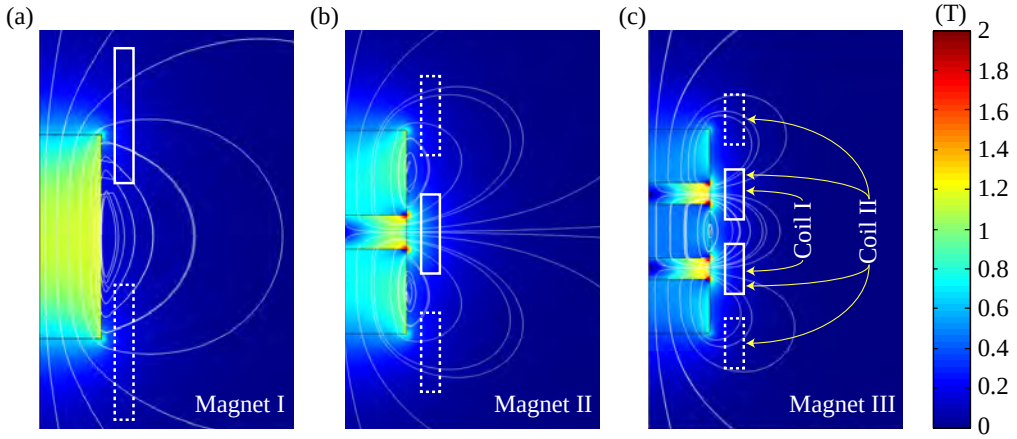

Figure 6.4: Flux distribution and density for the right half of the three magnet configurations. The coil locations implemented to find K in figure 6.5 are shown as white boxes (Coil I—solid box, Coil II—dashed and solid box).

Given the three magnet configurations, the coil arrangement resulting in the highest power generation is to be determined. The coil arrangements to be investigated locate coils in regions of high radial flux density. Coil I positions coils at the higher peak flux density locations only, while Coil II positions coils at both the higher and lower peak locations.

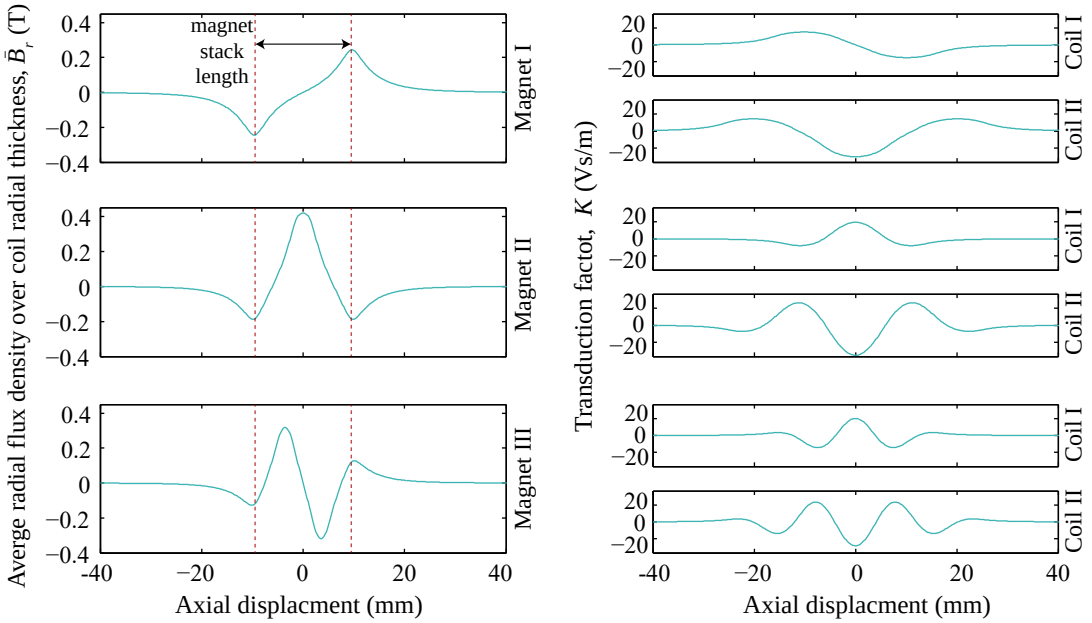

Figure 6.5: Left column: average radial flux density $\bar{B}_r$ over coil radial thickness for the three magnet configurations, Magnet I, II and III. Right column: electromagnetic transduction factor K for the two coil arrangements, Coil I and II, for each magnet configuration—d_{mag} = 12 mm, h_{mag} = 19.2 mm, ct_{rad} = 5 mm, $ct_{ax} = (2/3)h_{pitch}$ ($h_{pitch} = h_{mag} + h_{pole}$), and air-gap = 1.2 mm.

Examining the right column of figure 6.5, it is evident that the electromagnetic transduction factor, K, for the Coil II arrangements is higher than that for Coil I. This is unsurprising as the length of the coils is increased (equation 2.22). The power generated will not necessarily be higher, however, as the coil resistance also increases with the coil length. It is also worth noting that K is higher over a larger axial displacement range for Coil II than Coil I. This may benefit VAEGs, or other energy harvesters where the displacement is relatively large. The Magnet II - Coil II configuration is proven to achieve the highest power density in section 6.2.2, and is implemented experimentally in chapters 6 and 7.

Examples of the above transducer architectures from the literature are as follows: Magnet I - Coil I—Constantinou *et al.* (2012); Saha *et al.* (2008); Shahosseini and Najafi (2015); Spreeman and Manoli (2012); Magnet I - Coil II—Abed *et al.* (2016); Bonisoli *et al.* (2010); Green *et al.* (2012*b*); Mann and Owens (2010); Mann and Sims (2009); Rahimi (2012); Magnet II - Coil I—Challa *et al.*

(2013); Saha *et al.* (2008); Shahosseini and Najafi (2015); Shahosseini *et al.* (2014); Spreeman and Manoli (2012); and oppositely polarised with greater than two magnets—Abed *et al.* (2016); Cheng and Arnold (2010); Kwon *et al.* (2013); Tang *et al.* (2014); von Büren and Tröster (2007); Ylli *et al.* (2015); Zuo *et al.* (2010).

6.2.2 Transducer optimisation

The fixed parameters in the transducer optimisation were the height and diameter of the magnet stack which were 19.2 mm and 12 mm, respectively for $d_{mag} = 12$ mm, and the copper coil wire diameter, which was 100 µm. The variable parameters in each design were the coil axial thickness ct_{ax}, radial thickness ct_{rad}, and load resistance R_L, yielding a 3-dimensional search space for optimisation. The coil resistance R_C varied with the coil dimensions; hence, the optimal load resistance R_L also changed. As the coil volume increased, the ratio of optimal load resistance to coil resistance also increased. This was because the electromagnetic damping would continue to increase with coil volume if the resistance ratio remained constant. This is evident in the equation for the electrical damping coefficient, $c_e = K^2/(R_L + R_C)$, where both K and R_C are dependent on the coil length, l_w (equations 2.22 and 2.26). The squared term on the numerator results in c_e increasing with coil volume, if R_L/R_C is constant.

The variables listed above are common to each of the configurations. There are also a number of other variables to be optimised for the individual cases.

- For Magnet I - Coil II, the spacing between the coils could be varied. The optimal spacing between the centroids of the two coils was determined to be 1.5 times the magnet height.

- For the opposing polarity configurations (Magnet II and III), the magnet-pole height ratio h_{mag}/h_{pole} could be varied. The peak electromagnetic transduction factor K is plotted as a function of the magnet-pole height ratio in figure 6.6, for the Magnet II - Coil I configuration with $d_{mag} = 12$ mm. Increasing the magnet-pole height ratio increases the radial flux B_r from the pole, until the pole becomes saturated. This increasing B_r

results in K also increasing. The rate of increase of K slows with increasing ratio; beyond 3:1 the increase is small. For practical reasons—difficulty of machining the pole pieces and glueing the pole pieces to the magnets—a magnet-pole height ratio of 2.5:1 was selected.

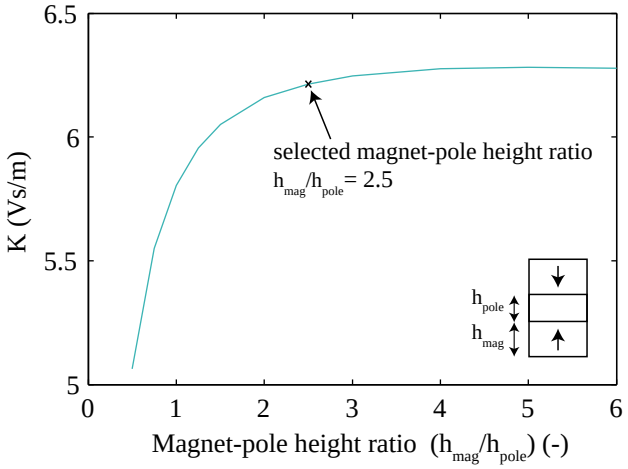

Figure 6.6: Electromagnetic transduction factor as a function of magnet-pole height ratio. Magnet stack height is constant.

The coil spacing of 1.5 h_{mag} and the magnet-pole height ratio of 2.5:1 were used in the relevant configurations in the optimisation simulations.

The single-DoF PWL oscillator described in section 4.1 was used in the optimisation sweeps. This system was used for a number of reasons:

- the number of simulations to be completed was large and the single-DoF system was much less computationally expensive than the 2-DoF system;
- the 2-DoF system response was stationary random; consequently, a significant simulation length was required to achieve a statistically significant value for the RMS voltage. In contrast, the single-DoF PWL oscillator demonstrated ranges of frequencies where the response was periodic; a much shorter simulation length was required to get an accurate value for these frequency ranges; and

- the gap length could be increased in both the 2-DoF and single-DoF PWL systems such that the displacement range was large, with the magnet stack free of any spring force over a large portion of its cycle. A linear model would not demonstrate this feature as the response is harmonic.

To determine the transducer designs which resulted in maximum power output and power density ($PD = Power/Volume$), ct_{ax} and ct_{rad} were swept through for a range of load resistances. This was done for each of the magnet-coil arrangements for the largest scale harvester ($d_{mag} = 12$ mm). The air-gap used in the simulation was the magnet radius subtracted from the outer radius of the Teflon tube—air-gap = 1.8 mm. Power (and power density) is maximised by minimising the air-gap. The lowest air-gap that could be achieved with this design (figure 6.1) was for an inner coil radius equal to the outer radius of the Teflon tube. This ignores the thickness of the adjustable coil-holder. Such an air-gap could be physically realised by taking a constant coil position and winding the coil directly around the Teflon tube.

The excitation and geometrical parameters used in the simulations were chosen to achieve large amplitude, periodic oscillations from initial conditions of $x_0 = 0$ and $\dot{x_0} = 0$. The optimal coil positions, which vary for the different magnet-coil configurations, were determined for each configuration. The fill factor of $f_f = 0.7$ was based on experimental measurements of hand-wound coils with wire diameter of 100 µm.

The coil radial thickness ct_{rad} was varied from 0.5–15 mm for each configuration. The coil axial thickness ct_{ax} was implemented in the simulations as a fraction of the pitch height $h_{pitch} = h_{mag} + h_{pole}$ (for Magnet I $h_{pitch} = h_{mag}$). The range of ct_{ax}/h_{pitch} changed with magnet-coil configuration. The configurations with multiple coils had a limited height range as beyond $ct_{ax}/h_{pitch} = 1$ the coils would overlap (this limit was 1.25 for the Magnet I - Coil II configuration due to the coil spacing of $1.5h_{mag}$). The configurations with a single coil did not have such a limit; a maximum of $ct_{ax}/h_{pitch} = 1.6$ was assessed for these configurations. A summary of the model parameters used in the optimisation tests are listed in table 6.1.

Table 6.1: Model parameters used in optimisation tests.

Parameters	Magnet I		Magnet II		Magnet III	
	Coil I	Coil II	Coil I	Coil II	Coil I	Coil II
h_{mag} (mm)	19.2	19.2	8.0	8.0	5.1	5.1
h_{pitch} (mm)	19.2	19.2	11.2	11.2	7.07	7.07
$(ct_{ax}/h_{pitch})_{max}$ (-)	1.6	1.25	1.6	1	1	1
h_{mag}/h_{pole} (-)	-	-	2.5	2.5	2.5	2.5
coil spacing (-)	-	$1.5h_{mag}$	-	-	-	-
d_{mag} (mm)	12					
B_{res} (mm)	1.35					
d_w (μm)	100					
f_f (-)	0.7					
$(ct_{rad})_{max}$ (mm)	15					
R_L/R_C range (-)	0.5–4.0					
air-gap (mm)	1.8					
m (g)	18.3					
k (N/m)	910					
Acc (m/s^2)	14					
f (Hz)	15					
g_0 (mm)	5					

Contour plots showing the power generated by each of the magnet-coil configurations for the varying coil parameters are shown in figure 6.7. The power presented is at the optimal load resistance. Contour plots of the normalised power density of each magnet-coil configuration are plotted in figure 6.8. Power density is calculated as the power per volume of the virtual cylinder surrounding the harvester. This virtual cylinder has a diameter equal to the outer diameter of the coil, and a height equal to the distance from the cap to the base, i.e. the bottom of the spring at the base to the top of the spring at the cap. The volume changes with ct_{rad} as the diameter increases with this parameter. ct_{ax}, however, does not affect the volume and, therefore, has a lesser effect on the power density. The power density presented is normalised by the highest power density achieved.

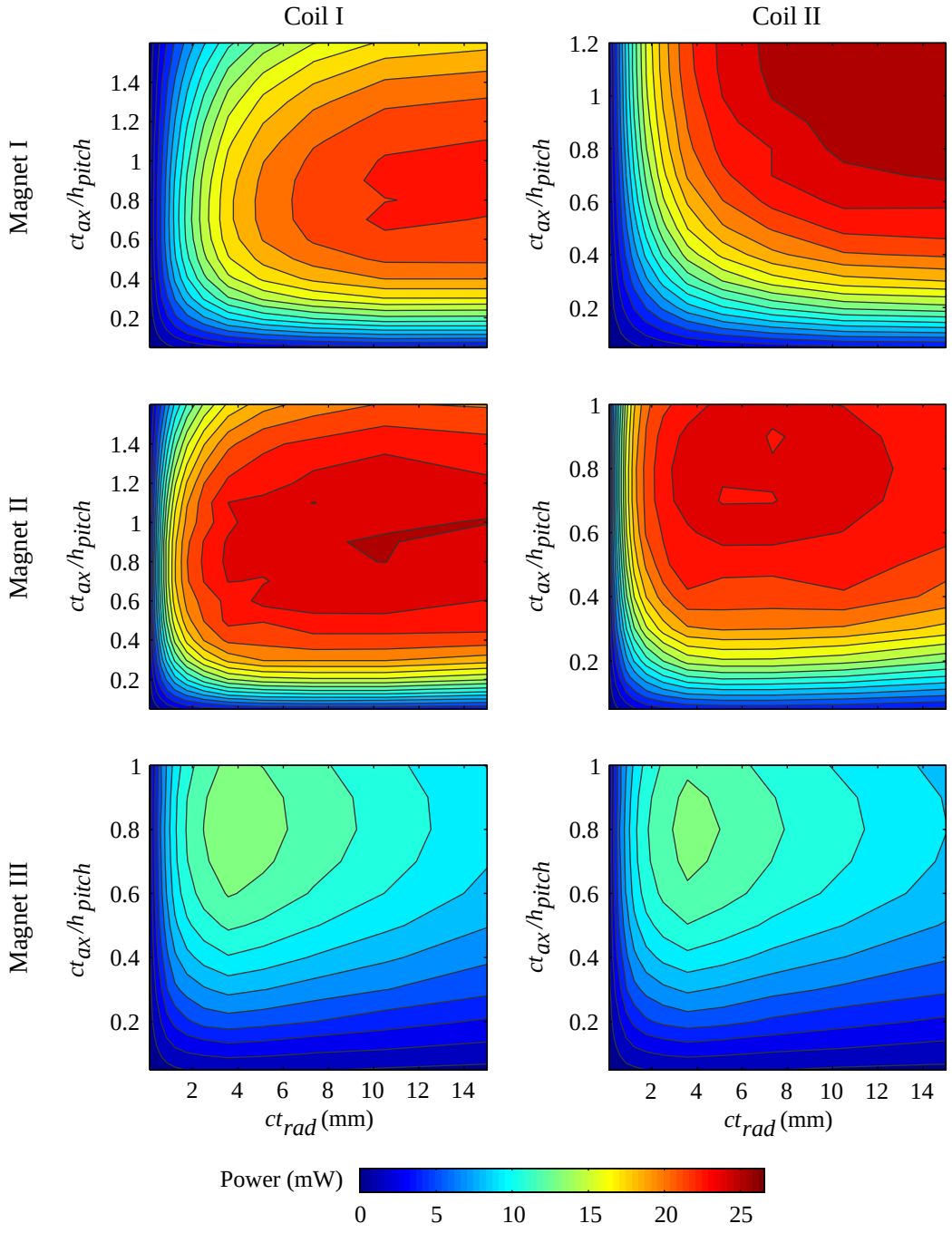

Figure 6.7: Power generated as a function of coil axial thickness ct_{ax} and coil radial thickness ct_{rad} for each of the magnet-coil configurations. Results from numerical simulation of $d_{mag} = 12$ mm system.

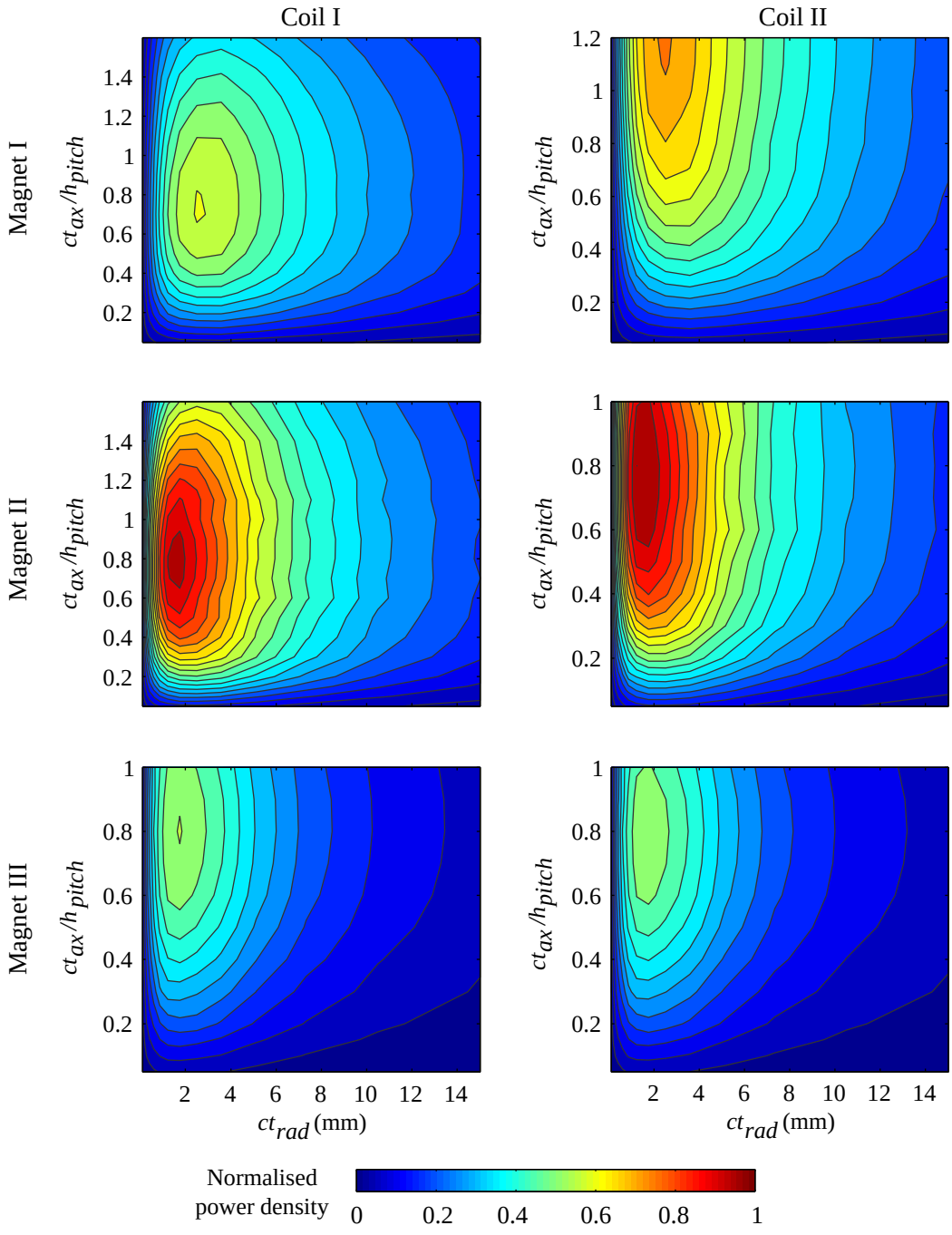

Figure 6.8: Power density as a function of coil axial thickness ct_{ax} and coil radial thickness ct_{rad} for each of the magnet-coil configurations. Results from numerical simulation of $d_{mag} = 12$ mm system.

The most significant findings from the optimisation tests series are discussed below.

- The power initially increases rapidly with both ct_{ax} and ct_{rad} for each magnet-coil configuration, due to the rate of increase of K exceeding the rate of increase of coil resistance—in terms of their influence on the power generated. The rate of increase of power then decreases and reaches a maximum in the region $ct_{ax}/h_{pitch} = 0.6$–0.9. At $ct_{ax}/h_{pitch} > 0.9$ the power generated begins to decrease. This is due to the coil length exceeding half the length of a magnetic cycle. The flux cutting the upper and lower ends of the coil starts to negate itself, reducing K and the voltage induced and, consequently, the power.

- For increasing ct_{rad}, the power reaches a maximum and then begins to decrease slowly, as beyond the value of ct_{rad} at which maximum power is generated, the increase in K no longer compensates for the increase in coil resistance. Moving from Magnet I through to Magnet III, the ct_{rad} at which maximum power is generated decreases, while the rate of decrease beyond the optimal ct_{rad} also increases. This is a result of the radial flux reducing at a greater rate in the radial direction for Magnet II than Magnet I; the radial flux from Magnet III reduces at a greater rate again.

- The Coil I and II configurations demonstrate similar maximum power and power densities for each transducer architecture. This means that the voltage generated is significantly higher in the Coil II configurations as the coil resistance is also much greater. While this investigation is interested in power and power density, in practice, the voltage may also be important as higher voltages ease AC-DC rectification and energy storage (Tang *et al.*, 2010).

- The highest power is generated by the Magnet I - Coil II configuration. However, from the power density results in figure 6.8, the highest power density is achieved by the Magnet II - Coil II configuration. Although its peak power is lower than the Magnet I - Coil II configuration, the Magnet II - Coil II configuration generates more power at lower ct_{rad}. This is due to

the radial flux of the oppositely polarised magnet stacks (Magnet II and III) being higher close to the surface of the magnet, but reducing at a greater rate than the single magnet (Magnet I) as the distance from the magnet increases. As the Magnet II - Coil II system has a higher power output at lower ct_{rad} than the Magnet I - Coil II system, the outer diameter of the virtual cylinder surrounding the coil is lower, resulting in a higher power density.

The Magnet II - Coil II configuration was implemented in the experimental characterisation in section 6.3 and the scaling analysis in chapter 7. The adjustable coil-holder was implemented in these investigations to allow the optimal coil position to be determined for each geometric and excitation condition. The ct_{ax} and ct_{rad} optimisation sweeps already described were repeated for this new arrangement with the air-gap = 3.9 mm. The harvester and transducer arrangement was, thus, optimised in terms of power density. The results of these sweeps are shown in figure 6.9. The coil parameters selected are marked by a white cross in the plots ($ct_{rad} = 2.85$ mm, $ct_{ax}/h_{pitch} = 0.714 \Rightarrow ct_{ax} = 8$ mm).

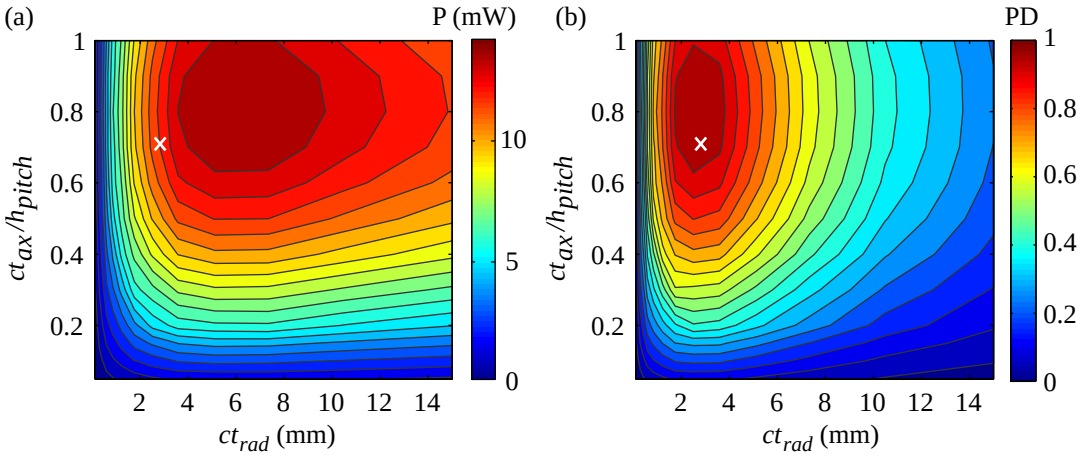

Figure 6.9: (a) Power and (b) normalised power density as a function of coil axial thickness ct_{ax} and coil radial thickness ct_{rad} for $d_{mag} = 12$ mm—magnet-coil configuration: Magnet II - Coil II, air-gap = 3.9 mm.

Repeating this analysis for the $d_{mag} = 6$ mm and $d_{mag} = 8$ mm systems—with constant coil wire diameter ($d_w = 100$ μm)—reveals that the optimal coil

geometry scales with the dimension. ct_{ax} and ct_{rad} in the scaled devices are, therefore, uniformly scaled from the values determined in figure 6.9.

6.3 Characterisation sweeps

The characterisation of the 2-DoF VAEG, with the Magnet II-Coil II transducer, is described in this section. The device used in the characterisation tests was the $d_{mag} = 8$ mm scale harvester. The system was tested experimentally using bidirectional frequency sweeps with the experimental set-up described in section 3.2 (figure 3.7). The frequency was swept from 6-45 Hz at a linear rate of 0.0733 Hz/s, giving a total sweep time of 531.8 s. The cap height was varied to achieve gap lengths of $g_0 = -0.2,\ 0.8,\ 2.5,\ 5.5,\ 10.5$ and 18.5 mm. These six configurations were tested at base acceleration levels ranging from $Acc = 2$–10 m/s^2, in increments of 2 m/s^2. The gap lengths were chosen to effectively demonstrate the range of responses shown by the device.

The hysteresis exhibited by the frequency response is negligible in most cases, as demonstrated in figure 6.10. Also, as discussed previously, the output from the harvester is stationary random, meaning, for a set of excitation conditions, the RMS of the output converges to the same value over time. This feature of the velocity amplified systems in this thesis—described previously in sections 4.2 and 5.3—is significant, as the RMS response demonstrated will be achieved irrespective of initial conditions. This is in contrast to many wideband harvesters presented in the literature (Mallick *et al.*, 2015; Mann and Sims, 2009; Ramlan *et al.*, 2010), where a softening or hardening stiffness allows the bandwidth to be widened for reverse- and forward-frequency sweeps, respectively. Entry into the high-energy state of oscillation is dependent on the initial conditions in these systems. Forward-frequency sweeps only are presented in the characterisation sweeps in this section.

Prior to performing an experimental sweep, the coil position and load resistance were optimised. This process contained a number of steps:

- An initial frequency forward-sweep was performed—the frequency at which the highest power is generated was determined (optimal frequency).

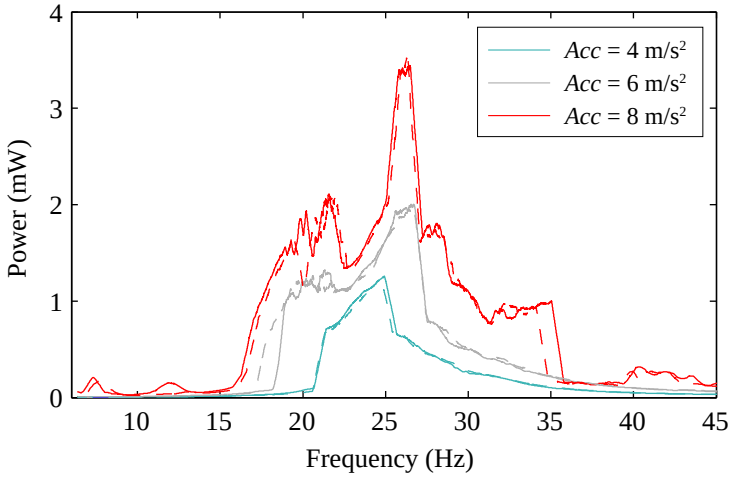

Figure 6.10: Experimental forward (——) and reverse (- - -) frequency sweeps showing load power for a range of acceleration levels; $g_0 = 2.2$ mm. Results from experimental testing of $d_{mag} = 8$ mm system.

- The system was excited under harmonic excitation at the optimal frequency. The coil position was varied in increments of ~ 1 mm, allowing the position at which maximum power is generated to be determined.
- A load resistance sweep was then performed with the coil in its optimal position, at the optimal frequency previously determined. This allowed the optimal load resistance to be determined. A sample load resistance sweep is shown in figure 6.11.

The coil position was optimised before the load resistance because changing the coil position resulted in the optimal load resistance shifting significantly, while changing the load resistance did not result in a significant change in optimal coil position.

These optimised parameters maximised the peak output power generated for each configuration and excitation condition. It should also be noted that although the peak power generated is maximised, the total power generated over the frequency range may actually be reduced. For example, for a relatively high g_0, the optimal coil position may be significantly higher than the rest position of the magnet stack. For frequencies which generate large displacements of the

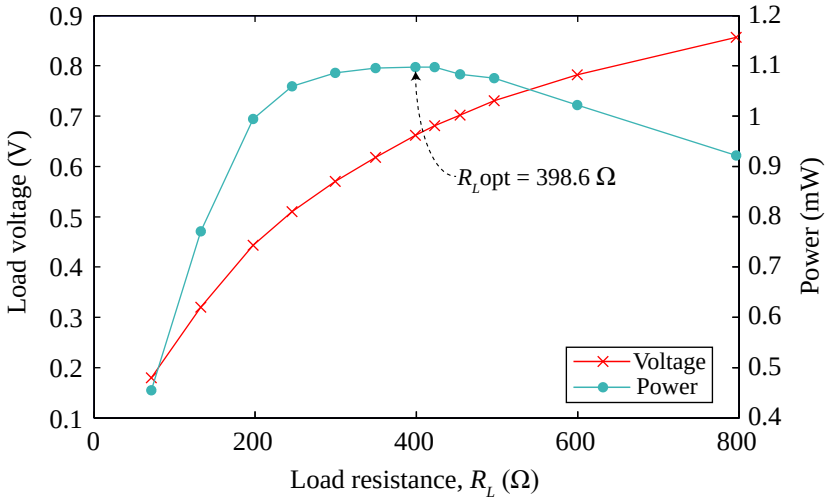

Figure 6.11: Sample load resistance sweep—$Acc = 4$ m/s^2, $g_0 = 0.8$ mm, $f = 24$ Hz. Results from experimental testing of $d_{mag} = 8$ mm system.

magnet stack, this results in increased power. However, for frequencies where the displacement of the magnet stack is lower, the coil will experience a low flux gradient, resulting in low power output.

The power generated for forward-frequency sweeps at the three lower and three higher gap lengths are plotted in figures 6.12 and 6.13, respectively. The corresponding RMS absolute velocities of the magnet stack (m_2) are shown in figures 6.14 and 6.15. Experimental frequency sweeps are shown in the left column, while simulated frequency sweeps are shown in the right column. The power and velocity values demonstrated in figures 6.12–6.15 are calculated from the RMS voltages and RMS velocities, respectively. The RMS is taken over a 10 s window using a simple moving average (SMA). The stationary random nature of the response means that, over time, the RMS response tends towards a certain value, for given excitation conditions. The SMA averaging method helps to reduce noise in the data. This applies to both the voltages and velocities in the experimental and simulation results.

The parameters used in the model, which are representative of the experimental system, are given in table 6.2. On visual inspection, it is evident that the model captures both the dynamic and electrical behaviour of the harvester, with the changing shape of the frequency response curve with g_0 evident in both the

experimental and simulation sweeps. For a more quantitative analysis, table 6.3 provides a comparison of the peak power, and the corresponding velocity and frequency for the range of g_0 values. The frequency at which the peak power occurs is predicted to within 1.3 Hz in each case. The predicted amplitude of the peak power and corresponding velocity varies more significantly than the predicted frequency, with the largest variation being 27.8%. The predicted peak power for the remaining g_0 values are all within 16%.

Table 6.2: Model parameters used in forward-frequency sweeps.

Parameter	Value	Unit
m_1	16.725	g
m_2	5.433	g
k_1	910	N/m
k_2	570	N/m
k_3	910	N/m
d_{mag}	8	mm
B_{res}	1.35	T
r_i	6.6	mm
r_o	8.5	mm
ct_{ax}	5.333	mm
N	2763	-
R_c	307.2	Ω
ζ_{s_1}	0.02	-
ζ_{s_2}	0.01	-
ζ_{f_1}	7.73	1/s
ζ_{f_2}	6.79	1/s

The results shown in figures 6.12–6.15 demonstrate the change in response with changing acceleration level and gap length.

- At 2 m/s^2, the acceleration is not high enough to induce large oscillations, irrespective of g_0. As a result, the masses remain in contact with the springs and the system behaves similarly to a linear harvester. As the acceleration

Table 6.3: Comparison of peak power and corresponding RMS absolute velocity and frequency in experimental and simulation frequency sweeps, for $Acc = 10\ \mathrm{m/s^2}$.

g_0 (mm)	Power (mW)			Velocity (m/s)			Frequency (Hz)		
	Exp	Sim	%	Exp	Sim	%	Exp	Sim	%
-0.2	7.14	7.60	6.5	0.42	0.41	-3.05	26.00	26.33	1.3
0.8	5.54	4.66	-15.9	0.35	0.32	-10.17	27.02	26.36	-2.4
2.5	6.25	5.29	-15.3	0.43	0.36	-16.54	22.95	22.68	-1.2
5.5	6.25	4.51	-27.8	0.45	0.39	-13.58	19.39	18.22	-6.0
10.5	6.26	5.26	-15.9	0.52	0.44	-15.57	15.41	15.71	1.9
18.5	5.72	5.12	-10.6	0.54	0.49	-9.85	12.28	10.96	-10.7

is increased, the masses leave the springs, impacting one another, resulting in velocity amplification of the magnet stack, m_2—provided m_1 is on an upward trajectory ($\dot{z}_1 > 0$). The harvester's behaviour becomes increasingly non-linear with increasing acceleration, with both the amplitude and bandwidth of the response increasing.

- As g_0 is increased, the optimal frequency shifts downwards due to the decreasing effective stiffness (for positive gap lengths). Effective stiffness reduces as a result of the masses spending a portion of each cycle out of contact with the springs; the higher g_0, the greater this portion is; thus, the greater the reduction. The synchronisation of impacts between the masses, base, and cap are dependent on g_0 (and, hence, the effective stiffness), with maximum energy transfer to the magnet stack occurring at a frequency below the linear resonant frequency. The influence of g_0 on a 2-DoF PWL harvester was described in detail for simulation results in section 4.1.2 (figure 4.8).

  It is notable, that the rate of change of optimal frequency decreases with increasing g_0, i.e. as g_0 is increased, achieving the same frequency shift requires the gap length to be increased by an ever greater amount. A shift in

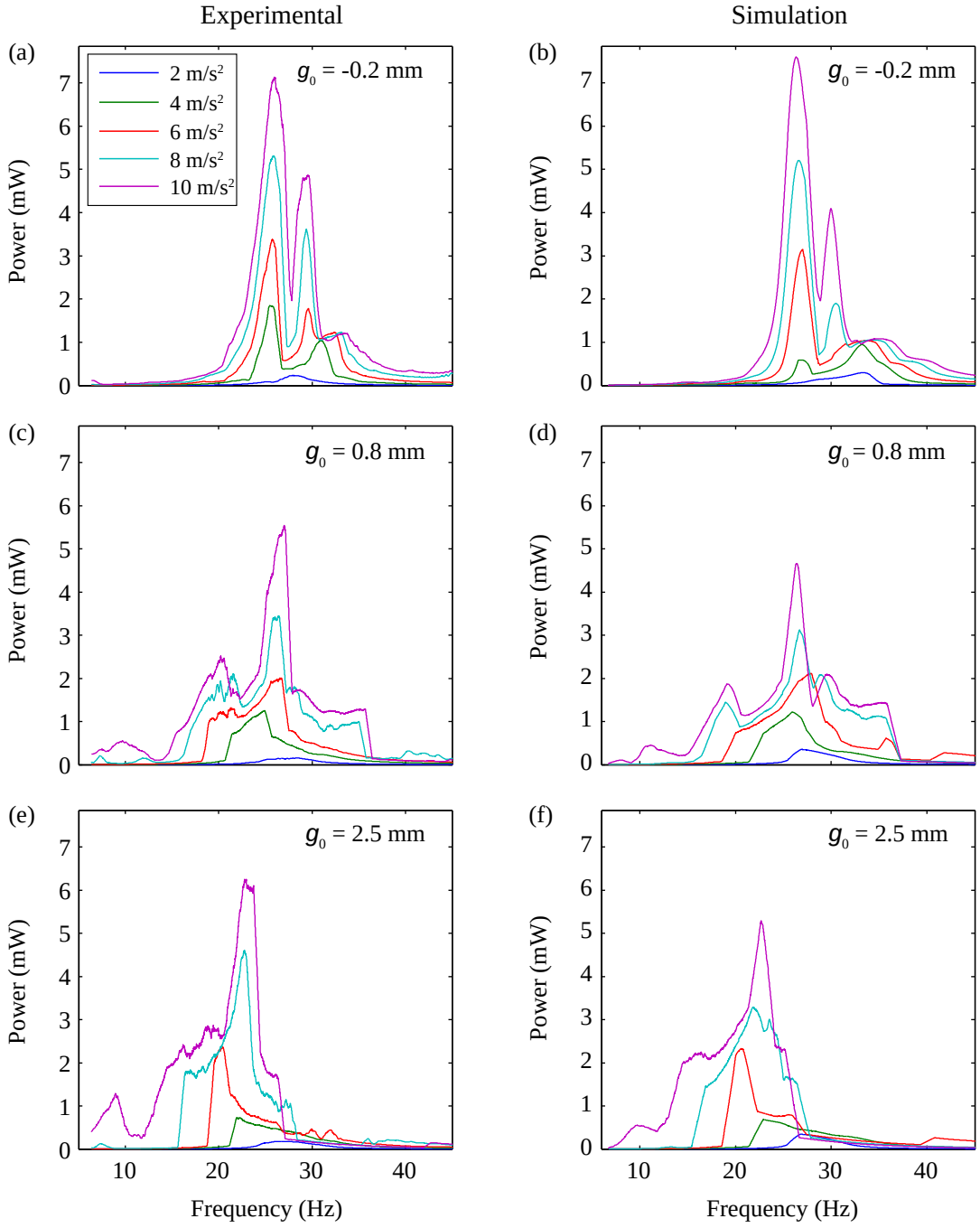

Figure 6.12: Experimental power (left column (a), (c), (e)) and simulated power (right column (b), (d), (f)) versus frequency forward-sweeps—Acc = 2–10 m/s^2, $g_0 = -0.2,\ 0.8,\ 2.5$ mm. Results from $d_{mag} = 8$ mm system.

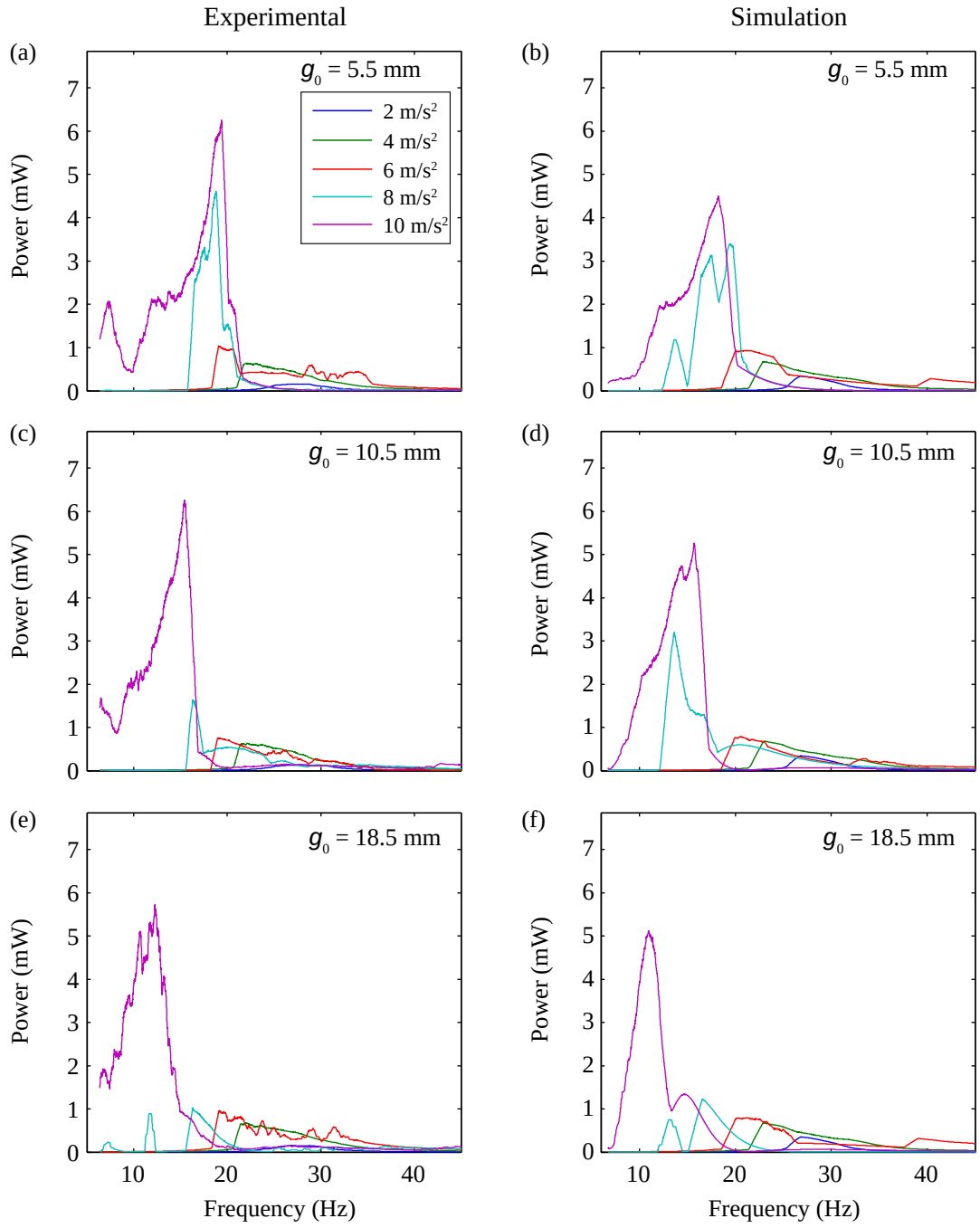

Figure 6.13: Experimental power (left column (a), (c), (e)) and simulated power (right column (b), (d), (f)) versus frequency forward-sweeps—Acc = 2–10 m/s^2, $g_0 = 5.5,\ 10.5,\ 18.5$ mm. Results from $d_{mag} = 8$ mm system.

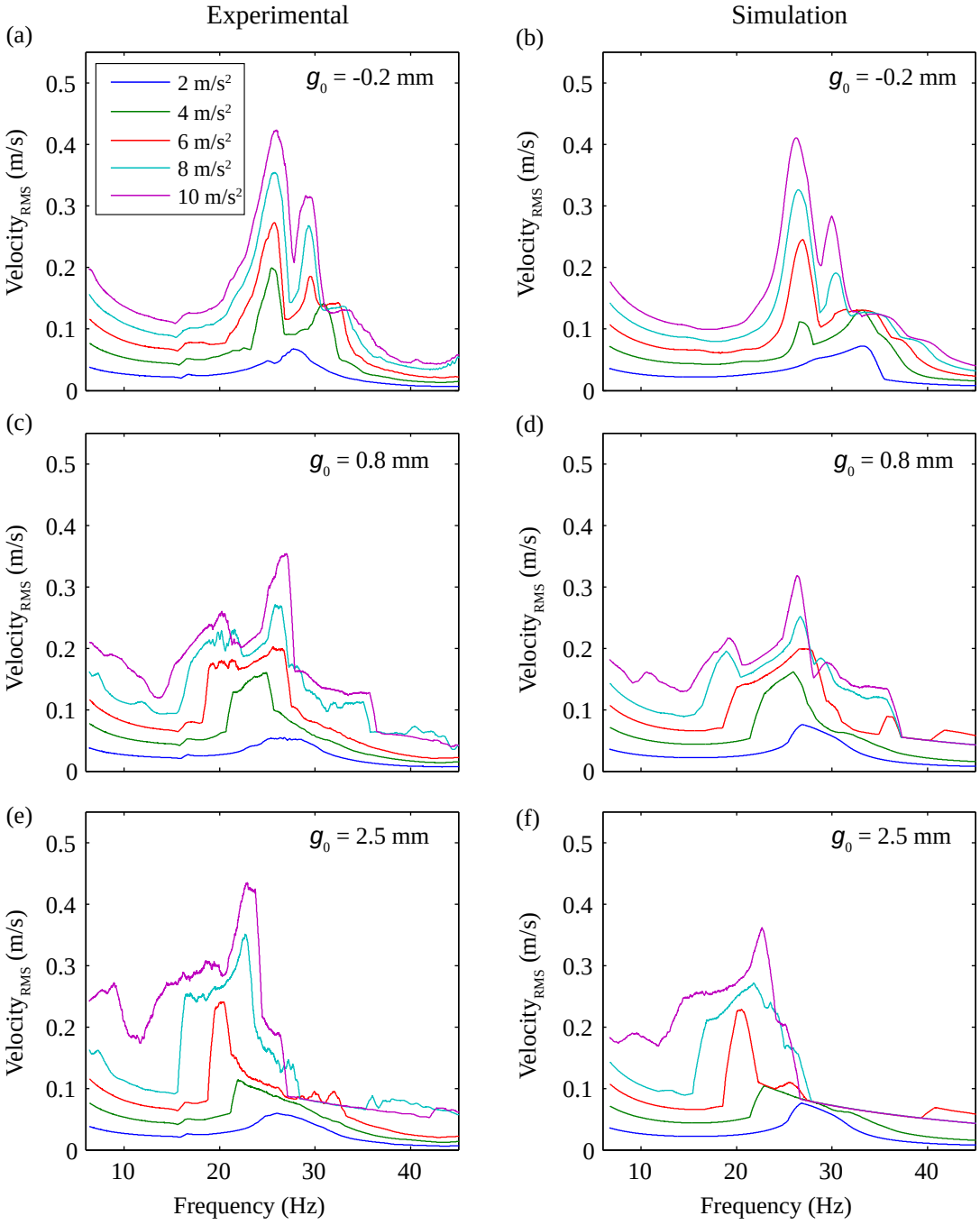

Figure 6.14: Experimental (left column (a), (c), (e)) and simulated absolute velocity (right column (b), (d), (f)) versus frequency forward-sweeps—Acc = 2–10 m/s^2, $g_0 = -0.2,\ 0.8,\ 2.5$ mm. Results from $d_{mag} = 8$ mm system.

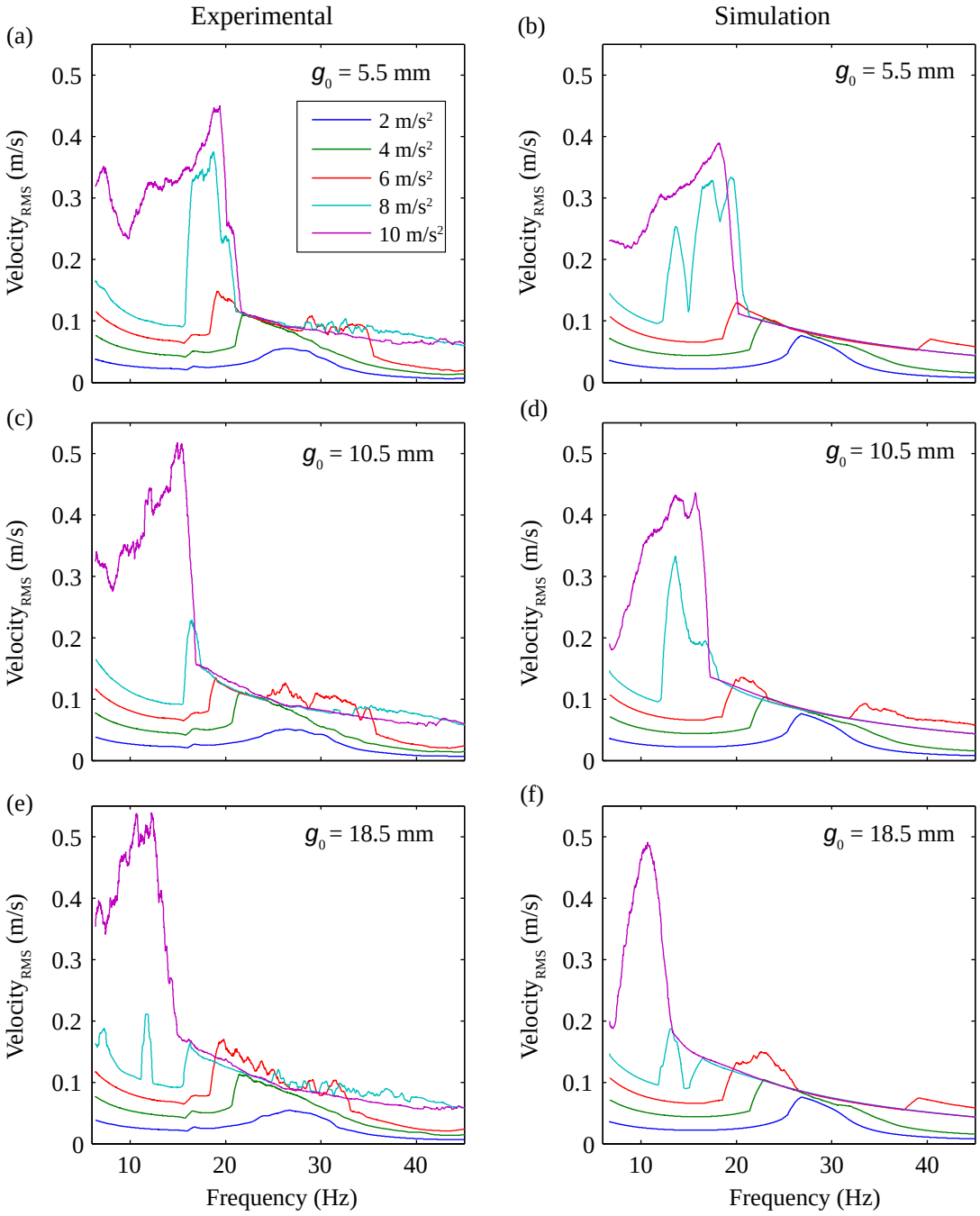

Figure 6.15: Experimental (left column (a), (c), (e)) and simulated absolute velocity (right column (b), (d), (f)) versus frequency forward-sweeps—Acc = 2–10 m/s^2, $g_0 = 5.5,\ 10.5,\ 18.5$ mm. Results from $d_{mag} = 8$ mm system.

the optimal frequency from 26 Hz to 12.3 Hz—a reduction of 52.7%—is evident in the experimental frequency sweeps at $Acc = 10$ m/s^2, moving from $g_0 = -0.2$ to 18.5 mm. This significant reduction in optimal frequency with increasing g_0 is an impressive feature of VAEGs, which could potentially be implemented as a tuning parameter (the issues with tuning of energy harvesters were discussed in sections 1.4.1 and 4.1.2). It is also an important feature of VAEGs. Achieving a low resonant frequency with a linear energy harvester becomes increasingly challenging as scale is reduced. VAEGs offer potential in this application area.

- As g_0 is increased, the acceleration level required to induce large oscillations also increases. For both $g_0 = 10.5$ and 18.5 mm, an acceleration level of 10 m/s^2 is required to achieve a high RMS velocity response. At acceleration levels lower than this, the magnet stack does not engage the stopper spring and high velocities are not achieved. This requirement of a large input acceleration to achieve a significant response is a major issue affecting the applicability of VAEGs, as the acceleration levels present in most application environments are much lower than the necessary $Acc = 10$ m/s^2 for the configurations with a large g_0.

- Provided the stopper spring is reached, and a RMS high velocity response is achieved, the amplitude of the velocity of the magnet stack increases with increasing g_0. This is due to the greater displacement range available for the masses to oscillate within. The increase in velocity is evident in the velocity sweeps, where the highest RMS velocity is achieved at the highest gap length, $g_0 = 18.5$ mm. However, this does not directly translate into higher power. As g_0 increases, the displacement range of the magnet stack also increases. Consequently, the magnet stack spends a larger portion of its cycle in regions where the flux gradient experienced by the coil is low. Therefore, despite the relative velocity between the coil and magnetic field increasing with g_0, the power generated does not increase proportionally.

- In terms of dynamics, increasing g_0 also increases the non-linear behaviour. Voltage time-traces for $g_0 = -0.2$ and 10.5 mm are shown in figure 6.16

to qualitatively demonstrate the change in response with increasing gap lengths. Both configurations are excited at $Acc = 10$ m/s^2. Evidently, the harvester behaves more periodically at lower gap lengths (figure 6.16a). In contrast, provided the acceleration level is sufficient, the higher gap lengths result in increasingly chaotic motion (figure 6.16b). An in-depth discussion on the non-linear dynamics of 2-DoF velocity amplified energy harvesters was provided through simulation in section 4.2.

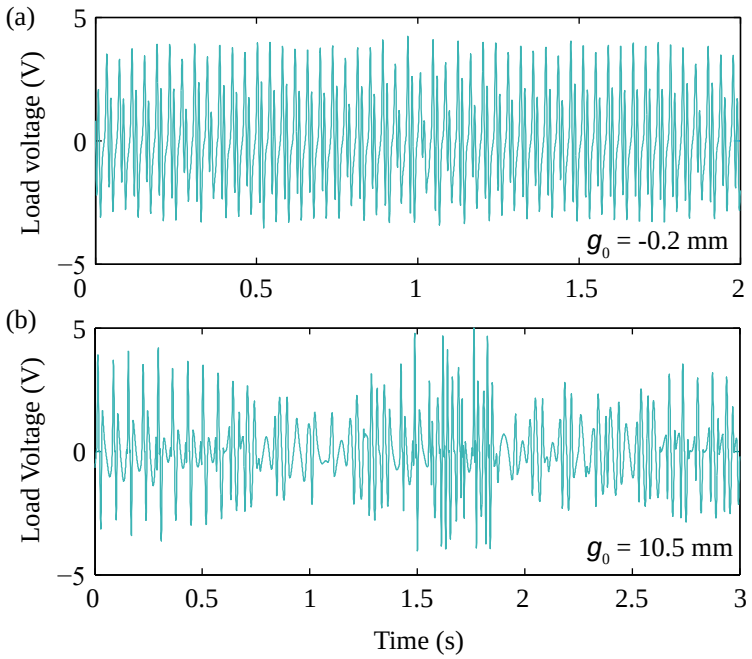

Figure 6.16: Voltage-time trace for (a) $g_0 = -0.2$ mm and (b) $g_0 = 10.5$ mm at $Acc = 10$ m/s^2. Results from experimental testing of $d_{mag} = 8$ mm system.

6.4 Performance metrics

The performance of the 2-DoF VAEG is described using the metrics NPD and FoM_V, which are described in section 1.5. The highest NPD and FoM_V from the results in figure 6.12 and 6.13, and the corresponding geometric and excitation conditions are listed in table 6.4. The VAEG volume prescribes the virtual

cylinder surrounding the device, with diameter equal to the outer coil diameter, and height equal to the distance from the top of the base to the bottom of the cap.

A number of interesting inferences can be taken from these results.

- Clearly, the geometric and excitation conditions which maximise NPD and FoM_V are not the same. As NPD is normalised to Acc^2, the highest NPD tends towards lower acceleration values.
- FoM_V, meanwhile, is normalised to Acc and ω, meaning that the highest values tend toward lower frequencies and higher accelerations, relative to NPD.

Table 6.4: Highest NPD and FoM_V for $d_{mag} = 8$ mm, air-gap = 2.6 mm.

g_0 (mm)	Volume (cm^3)	Acc (m/s^2)	f (Hz)	Power (mW)	NPD (kg s/m^3)	FoM_V (%)
-0.2	17.42	4	25.5	1.850	6.64	0.53
10.5	20.08	10	15.4	6.255	3.12	0.98

As mentioned in section 6.2.2, the power density of the current device is maximised by minimising the air-gap. In the results presented in figures 6.12 and 6.13, the coil is wound around an adjustable coil holder. Winding the coil directly around the Teflon tube allows this air-gap to be reduced; consequently, the power is increased, the device volume is decreased, and a gain in power density is achieved. The issue with this arrangement is that the coil position can no longer be adjusted.

Simulation forward-frequency sweeps were completed for the $d_{mag} = 12$ mm harvester with an air-gap equivalent to if the coil was wound directly around the Teflon tube (air-gap = 1.8 mm). The $d_{mag} = 12$ mm system was chosen because it had the smallest minimum air-gap, relative to the overall dimension. The model parameters used were the acceleration, gap length and coil position resulting in maximum NPD and maximum FoM_V in table 6.4. For both tests, the coil was

located in the optimal position. The simulation results predict that by winding the coil directly around the tube, the highest FoM_V and NPD values can be increased by factors of 2.89 and 4.42, respectively. The highest predicted NPD and FoM_V values and the corresponding geometric and excitation parameters for the $d_{mag} = 12$ mm system are listed in table 6.5.

Table 6.5: Highest NPD and FoM_V for $d_{mag} = 12$ mm predicted from simulation sweeps—coil wound directly around the Teflon tube, air-gap = 1.8 mm.

g_0 (mm)	Volume (cm^3)	Acc (m/s^2)	f (Hz)	Power (mW)	NPD (kg s/m^3)	FoM_V (%)
-0.2	28.2	6	29.6	29.98	29.54	2.59
10.5	31.1	10	16.4	34.51	11.10	2.83

Considering the frequency range in which the harvester operates (< 30 Hz), the predicted performance values presented are reasonably high (see table 1.1 in section 1.5 to compare the presented performance metrics with those from the literature). The predicted high FoM_V in the $d_{mag} = 12$ mm system at $Acc = 10$ m/s^2, $g_0 = 10.5$ mm, and $f = 16.4$ Hz suggests that velocity amplification is an effective method of achieving high power output at low frequencies, provided the acceleration is sufficiently high to achieve large amplitude oscillations.

6.5 Closure

A 2-DoF VAEG with mass ratio $R = 3$ was selected for investigation. Simulations were employed to aid in the design and optimisation process.

- A range of transducer configurations were tested through simulations.
- The transducer resulting in the highest power density was found to consist of two oppositely polarised magnets with a soft-magnetic spacer between them, accompanied by three coils with alternate winding direction (Magnet II-Coil II).

- A 2-DoF VAEG, which incorporating the optimised transducer design, was fabricated.

The harvester was characterised using forward-frequency sweeps for a range of cap heights and acceleration levels through simulation and experimentation.

- Hysteresis in response to bidirectional frequency sweeps was observed to be small; hence, forward-frequency sweeps only were presented. The lack of hysteresis is significant for an application environment, as the response demonstrated is not dependent on initial conditions.

- A shift in optimal frequency to lower frequencies with increasing gap length, g_0, was demonstrated. This shift was a result of reducing effective stiffness, with the masses spending a smaller portion of each cycle in contact with the springs. The frequency which resulted in the highest energy transfer to the magnet stack was then lower than the equivalent linear resonant frequency.

- At low accelerations (< 4 m/s^2) the response was relatively small. Increasing the acceleration, large oscillations began to occur. As g_0 was increased, the acceleration level required to achieve large oscillations also increased. VAEGs require a large input acceleration to achieve a significant response if g_0 is high. This issue affects the applicability of VAEGs as the acceleration levels present in many application environments are typically low.

- The velocity also increased with increasing g_0, provided the excitation conditions were sufficient to engage the stopper spring. This did not necessarily increase the power, as the flux gradient reduced with increasing displacement range.

- Respective NPD and FoM_V values of 29.54 kg s/m^3 and 2.83% were predicted for the lowest air-gap—with the coil wound directly around the tube in the optimal position, rather than around the adjustable coil holder. The relatively high FoM_V suggests velocity amplification is an effective method of achieving high power output at low frequencies.

Chapter 7

Scaling of a 2-DoF VAEG

The effect of scaling on linear electromagnetic energy harvesters has been well documented in the literature (Arnold, 2007; Cepnik and Wallrabe, 2013; Mitcheson *et al.*, 2008; Moss *et al.*, 2014; O'Donnell *et al.*, 2007). In section 7.1 of this chapter, an overview of the state-of-the-art in the scaling of electromagnetic energy harvesters is presented. The critical parameters are introduced and their scaling relationships are discussed. As this is in relation to linear systems, the scaling of the mechanical and electrical systems can easily be considered by analysis of the complete system. Section 7.2 addresses the influence of scaling on a 2-DoF VAEG. The device characterised in chapter 6 was fabricated at three scales, with the device undergoing homothetic scaling, i.e. it was scaled equally in all directions. The three device scales ranged in volume from ~ 4.5–60 cm^3. These systems were non-linear which increases the complexity of the scaling analysis, compared to linear systems. Consequently, to investigate the influence of scaling on the VAEGs, the electrical and mechanical systems are considered separately. In section 7.2.1, the influence of scaling on energy conversion in the transducer of a VAEG is considered. A number of deviations from linear scaling theory were made in order to maintain the velocity-frequency response across scales, allowing the electrical system to be considered separately. Experimental and numerical methods were employed in this analysis. The influence of the mechanical damping scaling rate on the velocity-frequency response of a 2-DoF VAEG is addressed, through simulation, in section 7.2.2. Finally, the influence of scale on the power generated in a 2-DoF VAEG is discussed.

7.1 Scaling theory

Summarised in this section is the scaling theory of linear inertial energy harvesters, as presented in the literature. The scaling relationships of the parameters of significance are discussed in section 7.1.1. In section 7.1.2, an analytical approach to explore the boundary of what happens at different mechanical damping scaling relationships is presented, with two scaling relationships considered—$c_m \propto s$ and $c_m \propto s^3$—the significance of these relationships is discussed in detail later.

7.1.1 Scaling of a linear electromagnetic harvester

The length scale, s, of a harvester is defined as the cubed root of the device volume ($s = Volume^{1/3}$). Mitcheson *et al.* (2008) showed that the maximum average power dissipated by a linear energy harvester per cycle at resonance is $P_{max} = (1/2)m\omega_n^3 Y Z_{lim}$—this was derived in equation 2.9. The displacement limit of the mass Z_{lim} scales with the length scale ($Z_{lim} \propto s$), while the mass scales with the volume ($m \propto s^3$). The excitation amplitude Y and resonant frequency ω_n are independent of scale; therefore, it is stated that the maximum power scales as $P_{max} \propto s^4$. However, the mechanical damping c_m is not accounted for in the analysis of Mitcheson *et al.* (2008).

Arnold (2007) demonstrated that the scaling rate of the actual displacement amplitude, Z_{max}, is affected by the mechanical damping, while c_m also affects the electrical damping, c_e, required to maximise the power delivered to the load (EDAM load matching condition, see section 2.1). Consequently, although Z_{lim}—the maximum possible displacement of the mass within a device volume—scales with s, the assumption that $Z_{max} \propto s$ may not be valid. Equation 2.14 gives the power delivered to the load at optimal load resistance. Rearranging this equation yields:

$$P_L = \frac{m^2 Acc^2}{8c_m(\frac{c_m R_C}{K^2} + 1)} \tag{7.1}$$

Assuming all of the harvester components are scaled uniformly with s, the scaling relationships of the parameters in equation 7.1 and other relevant parameters are as follows: mass $m \propto s^3$, base acceleration Acc is independent of scale, coil

volume $V_{coil} \propto s^3$, coil wire diameter $d_w \propto s$, coil wire area $A_w = \pi d_w^2/4 \propto s^2$, coil wire length $l_w = V_{coil} f_f / A_w \propto s$ where f_f is the fill-factor, coil resistance $R_C = \rho_{cop} l_w / A_w \propto s^{-1}$ where ρ_{cop} is the resistivity of copper, and $K = B_r l_w \propto s$ as the radial flux density, B_r, is independent of scale (Cugat *et al.*, 2003; O'Donnell *et al.*, 2007). Clearly, in order to determine the load power scaling rate from equation 7.1, the scaling relationship of the mechanical damping must be known. This is discussed in the following subsection.

7.1.2 Mechanical damping scaling

In the following analysis, the influence of the mechanical damping coefficient, c_m, on scaling is considered. The scaling of c_m is more difficult to define than the previously discussed parameters as it comprises a number of damping mechanisms including thermoelastic damping, friction, squeeze-film damping, and air resistance (see section 2.1 for more details on mechanical damping). The dominant damping mechanism is dependent on the device design and fabrication. Arnold (2007) states that viscid damping is usually dominant, and scales as $c_m \propto s$. This scaling relationship is also taken by Cepnik and Wallrabe (2013).

In this analysis, two mechanical damping scaling rates are considered—$c_m \propto s$ and $c_m \propto s^3$. The former, $c_m \propto s$, is the scaling relationship which is typically employed. The latter mechanical damping scaling condition, $c_m \propto s^3$, is discussed here as it is employed in the investigation into energy conversion in the transducer of a VAEG in section 7.2.1, and it is of interest to investigate this effect on linear systems so comparisons can be drawn to the VAEG systems.

$\boldsymbol{c_m \propto s}$: Inserting $c_m \propto s$ (Arnold, 2007) into equation 7.1 yields the scaling relationship for linear oscillatory energy harvesters for the given mechanical damping scaling relationship:

$$P_L \propto \frac{s^7}{s^2 + 1} \tag{7.2}$$

As the denominator of equation 7.2 contains a sum, two asymptotic scaling rela-

tionships can be determined:

$$P_L \propto s^5 \quad for\ s \to \infty \tag{7.3a}$$

$$P_L \propto s^7 \quad for\ s \to 0 \tag{7.3b}$$

These scaling relationships, described by Arnold (2007) based on analysis of the equations derived by Stephen (2006), are visualised in figure 7.1.

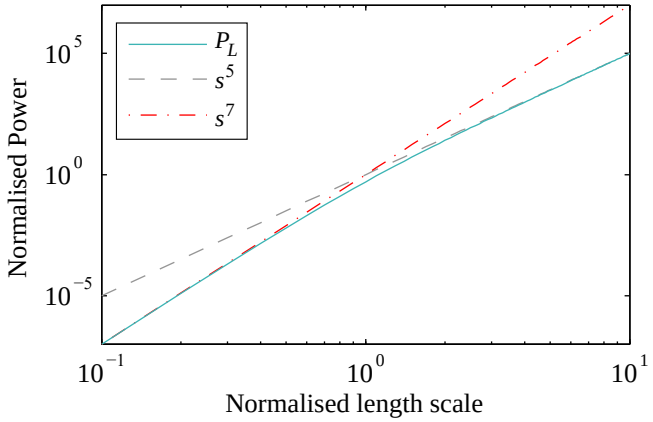

Figure 7.1: Normalised power as a function of length scale showing asymptotic scaling relationships $P_L \propto s^5$ and $P_L \propto s^7$, for linear inertial energy harvesters.

From equation 7.2, where the electrical damping dominates ($K^2/R_C \gg c_m$) the scaling relationship approaches $P_L \propto s^5$. If, however, the mechanical damping dominates ($c_m \gg K^2/R_C$) the scaling relationship approaches $P_L \propto s^7$. Examination of the scaling relationships of these terms—$K^2/R_C \propto s^3$ and $c_m \propto s$—suggests that at larger scales electrical damping will dominate, while at smaller scales mechanical damping will dominate.

The amplitude of the mass displacement scales at a minimum rate of $Z_{max} \propto s^2$, i.e. the displacement of the mass decreases at a greater rate than the displacement limit, Z_{lim}. This is determined by inputting the scaling relationships described above into the equation for maximum displacement amplitude, $Z_{max} = Y/2\zeta_T$. Clearly, assuming $c_m \propto s$, scaling has a highly negative effect on the power density of a linear VEH, with a minimum load power scaling rate of $P_L \propto s^5$.

$\boldsymbol{c_m \propto s^3}$: This scaling relationship is unlikely to occur in reality, as the difficulty of fabricating devices with moving components increases as scale is reduced, while aspects of the device such as surface finish become more significant. However, it is informative to understand the influence of the damping scaling relationship. In this instance, the mechanical damping and, consequently, the electrical and total damping scales with the volume ($c_{m,e,T} \propto s^3$)—EDAM load matching condition (section 2.1). The total damping ratio ζ_T is, therefore, independent of scale ($\zeta_T = c_T/2m\omega_n = const.$, where $m \propto s^3$ and $\omega_n = const.$), Z_{max} remains constant ($Z_{max} = Y/2\zeta_T = const.$), and $P_L \propto s^3$ (equation 7.1). Z_{max} does not scale under the current mechanical damping scaling conditions as the total damping force acting on the mass scales in proportion to the volume, resulting in the motion of the mass (its velocity-frequency response) remaining constant with scale (this is shown explicitly in figure 7.6a for a 2-DoF VAEG). This is only possible if the displacement limits do not scale with the other harvester dimensions. If the spring deflection limit, Z_{lim}, is less than Z_{max}, obviously, the mass would not be able to oscillate to its maximum displacement.

7.2 Scaling of a 2-DoF VAEG

The scaling relationship for linear inertial energy harvesters was described in section 7.1. As the systems were linear, the influence of scale on the individual parameters could be determined readily through analysis of the coupled system, i.e. the scaling relationships of the individual parameters and their influence on the response was available from analysis of the relatively simple equations presented in section 7.1, and earlier in section 2.1. In the scaling analysis of a 2-DoF VAEG, described in this section, the non-linear behaviour does not allow the influence of scale on the individual parameters to be determined readily from the system equations. This is because the relationships between the individual parameters and the harvester response vary non-linearly. For example, scaling the gap length to smaller dimensions would result in the optimal frequency shifting towards higher frequencies, which, depending on the initial gap length, may result in the amplitude of the peak response increasing or decreasing (section 6.3). Moreover, the amplitude and profile of the displacement of the individual masses

in the 2-DoF VAEG change non-linearly with the input excitation level, which has a direct effect on the harvested power. Linear systems do not contain parameters of such complexity. Clearly, determining the causes of variations in VAEG response at different scales while considering the entire system would be difficult. Consequently, to determine the influence of the individual parameters on the response as scale is reduced, particularly the gap length and excitation amplitude, the electrical and mechanical responses are decoupled and examined separately at different scales. This reduces the number of parameters which may be affecting the response in each case, allowing the influence of the individual parameters to be assessed more directly.

Section 7.2.1 explores the influence of scaling on energy conversion in the transducer of a 2-DoF VAEG by isolating the electrical system from the mechanical domain. A number of differences to linear scaling methodologies are employed to achieve this isolation of the electrical system. The majority of these differences are designed to achieve a mechanical damping scaling relationship of $c_m \propto s^3$. Experimentation and simulations are employed, with the electromagnetic transduction factor used to allow for comparison between the experimental and simulation results, which are also compared to the scaling behaviour of a linear system. An analysis of the influence of the mechanical damping scaling rate on the velocity-frequency response of a 2-DoF VAEG is presented in section 7.2.2. Simulation only is employed in this section, as fabricating an experimental energy harvester with a desired mechanical damping ratio would be extremely challenging.

7.2.1 Influence of scaling on energy conversion in a VAEG

In the analysis of the influence of scaling on energy conversion in the transducer of a VAEG, presented in this subsection, a number of deviations from the linear scaling theory of Arnold (2007) are employed. The purpose of these deviations is to achieve, as closely as possible, conditions where a mechanical damping scaling relationship of $c_m \propto s^3$ can be put in effect; hence, maintaining the velocity-frequency response across scales. This allows the effect of scaling on energy conversion in the transducer to be considered separately from the mechanical

system, i.e. any difference in energy converted in the transducer is a result of the electrical, rather than the mechanical system. The deviations employed in the analysis of the influence of scaling on the electrical system of a 2-DoF VAEG are discussed below.

- The mechanical damping coefficient was assumed to scale with volume ($c_m \propto s^3$) in the simulations, rather than the dimension ($c_m \propto s$) as in Arnold (2007). This scaling relationship was discussed in the previous section, where it was noted that the amplitude of the mass displacement in a linear harvester, Z_{max}, would remain constant with scale; however, this would only be possible if the displacement limits were not reached. Such a condition was realised physically by maintaining the spring length with scale—described in greater detail in a later point. According to EDAM, under this mechanical damping scaling rate, the electrical damping coefficient would then scale at the same rate ($c_e \propto s^3$). This means that the total damping force acting on the mass would scale proportionally, i.e. the effect of the damping force on the velocity of the mass would remain constant with scale.

- Uniform scaling of the dimensions of a uni-axially loaded spring—which can be of cantilever, helical, or planar form—results in the spring stiffness scaling as $k \propto s$ (Rao, 2011). Consequently, the natural frequency is inversely proportional to length scale ($w_n \propto s^{-1}$). In this analysis, the spring stiffness, k, was scaled as $k \propto s^3$, such that the natural frequency of an equivalent linear system would remain constant with scale ($\omega_n(s) = (k/m)^{1/2} = const.$). Although uniform scaling of a spring results in an increase in natural frequency as dimension is reduced, low stiffness materials can be implemented in the spring design allowing low natural frequencies to be achieved at small scales. An example of this is FR4, employed by Hatipoglu and Ürey (2010) and Mallick *et al.* (2015), among others, due to its relatively low Young's modulus (21 GPa).

- As described in section 7.1.2, under the damping scaling rate $c_m \propto s^3$, the displacement amplitude does not scale. To accommodate this, the spring

height was not reduced with scale ($h_{spring} = const.$) in both the experimental and simulated scaling analysis. This avoided the possibility of the displacement exceeding the maximum spring compression, and also increased the available compression spring selection range. Additional height contributed by the springs was not considered in the volume and corresponding length scale. The volume used to define the length scale ($s = Volume^{1/3}$) was, therefore, the product of the area within the outermost coil, and the summed height of the copper mass, magnet stack and gap. A schematic showing the influence of scaling on the geometry of the 2-DoF VAEG in the current experimental and simulation scaling analysis is illustrated in figure 7.2, with the area contributing to volume highlighted. Evidently, the copper mass and transducer dimensions scale with s, while the spring height does not scale. Initial gap, g_0, does not scale either—the reason for this is described in the following point.

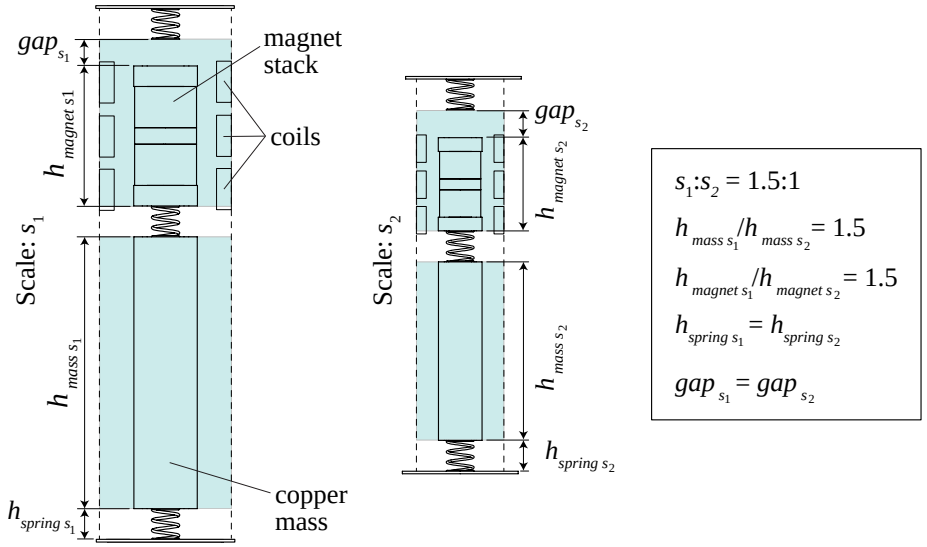

Figure 7.2: Schematic showing the cross section of a 2-DoF VAEG at scales s_1 and s_2, with the dimensional scaling relationships.

- The geometric feature of a VAEG which differs most significantly to a linear energy harvester is the presence of an initial gap, g_0, between the masses and springs. As g_0 is a component of the displacement range, it does not

scale; this means that the change in dynamics with g_0 is independent of scale. For example, for a certain scale VAEG with an arbitrary g_0: if the harvester dimensions are scaled, g_0 must remain constant to maintain the velocity-frequency response. This is a consequence of the effective stiffness of the harvester being dependent on the portion of the cycle the masses spend attached/detached from the springs during operation. For the effective stiffness to be maintained and, consequently, the velocity-frequency response to be the same across scales, the portion of each cycle the masses spend in contact with the springs must remain constant. The length of g_0 determines what this portion is for given excitation conditions and, therefore, g_0 must be kept constant to achieve the same velocity-frequency response. Consequently, in the analysis presented, g_0 remains constant with scale. As a result of this, the rate of change of volume with magnet-coil dimension decreases as g_0 increases, i.e. the larger g_0, the smaller the influence of scaling on its volume. The scaling relationship is described for a range of g_0 values.

As a result of the scaling conditions described above, the system dynamics—amplitude and frequency of velocity and displacement responses—were not affected by scale in the scaling analysis of VAEGs presented. The electrical system was, thus, isolated from the mechanical system. Any deviations from linear scaling theory were then a result of the effect of scaling on energy conversion in the transducer. The difference in the effect of scaling on a linear system and a VAEG can, therefore, be determined solely in terms of the transduction properties. This is the defining feature of the scaling analysis presented in this section, allowing the mechanical and electrical systems to be considered separately across scales.

As previously stated, if the transducer is scaled uniformly, the transducer properties scale as follows: $d_w \propto s$, $l_w \propto s$, $A_w \propto s^2$, $R_C \propto s^{-1}$ and $K \propto s$. In the scaling analysis presented in this section, the coil wire diameter was kept constant ($d_w = const.$) so that the coil fill factor would be the same for each scale; whereas, if the coil wire diameter was scaled, the fill factor would likely have changed and this would have affected the uniform scaling of the VAEGs. Applying the same analysis as above to the systems with constant coil wire diameter gives: $l_w \propto s^3$,

$A_w = const.$, $R_C \propto s^3$ and $K \propto s^3$. Inserting these scaling relationships into equation 7.1 yields the same scaling relationships described for $d_w \propto s$, i.e. the load power scales at the same rate for both $d_w \propto s$ and $d_w = const.$ ($P_L \propto s^3$). The peak electromagnetic transduction factor, K, and the coil resistance are plotted as functions of the scale length in figure 7.3, for both scaled wire diameter ($d_w \propto s$) and constant wire diameter ($d_w = const.$). The load power scaling rate remained the same for both constant and scaled coil wire diameter, despite the scaling rates of K and R_C changing, as the scaling rate of the R_C/K^2 term in equation 7.1 remained the same for both cases, i.e. $R_C/K^2 \propto s^{-3}$. A constant coil wire diameter of $d_w = 100$ µm was used in this analysis.

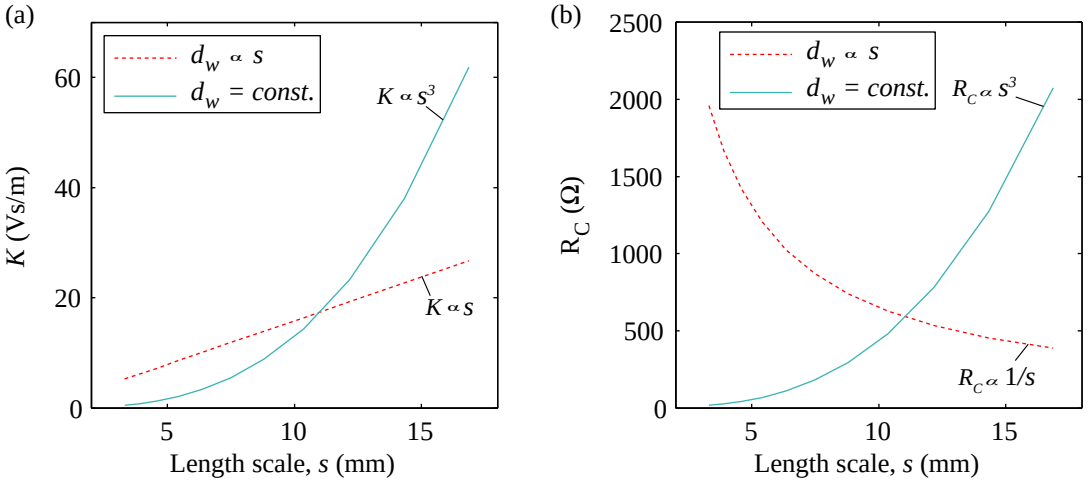

Figure 7.3: (a) Peak electromagnetic transduction factor K and (b) coil resistance R_C as a function of length scale s for scaled wire diameter ($d_w \propto s$ - - -) and constant wire diameter ($d_w = const.$ ——).

The scaling relationships employed in the scaling analysis of a 2-DoF VAEG are summarised in table 7.1. Parameters described as irregular are those which do not conform to homothetic scaling, or the scaling relationships employed by Arnold (2007), while the regular and resultant parameters are those which are a consequence of homothetic scaling, or the irregular parameters already listed.

Examining equation 7.1, with $c_m \propto s^3$, the only parameter which could cause a deviation from $P_L \propto s^3$—the linear scaling relationship—is K, as the remaining parameters are rigidly defined. A variable K becomes K_{eff}, the effective

Table 7.1: Scaling relationships employed in the simulation scaling analysis of a 2-DoF VAEG.

	Parameter	Scaling relationship
Irregular	c_m	$\propto s^3$
	d_w	$= const.$
	g_0	$= const.$
	k	$\propto s^3$
Regular/Resultant	m	$\propto s^3$
	w_n	$= const.$
	V_{coil}	$\propto s^3$
	l_w	$\propto s^3$
	A_w	$= const.$
	R_C	$\propto s^3$
	c_e	$\propto s^3$
	B_r	$= const.$
	K	$\propto s^3$

electromagnetic transduction factor, which is the RMS of K over a period of excitation.

$$K_{eff} = \sqrt{\frac{\omega}{2\pi} \int_0^{\frac{2\pi}{\omega}} K^2 dt} \tag{7.4}$$

Although the peak K is proportional to the length scale cubed, K_{eff} can scale at a greater rate. The peak K occurs when the coil and magnet stack are located at the optimal relative position—which is determined by the geometry of the transducer. For small displacement ranges, K_{eff} remains close to this peak value. In VAEGs, the displacement range varies with g_0; the larger g_0, the greater the displacement range (provided the excitation conditions result in large amplitude oscillations). Large displacements result in values of K_{eff} which are considerably lower than the peak value. The relative position of the magnet and coil which results in maximum average power generation, for a set of excitation conditions and a given g_0, differs from the optimal relative magnet coil position under very

low displacements. In this case, the optimal magnet coil position is the one that results in the highest RMS load voltage, which is a function of K and relative velocity.

In the simulations, $c_m \propto s^3$ and the velocity-frequency response remained constant with scale (the equations used in the simulations are the same as those employed in chapter 6, presented in equation 4.13). In the experimental data (figure 7.5), this was not the case; c_m scaled at a lower rate, resulting in the mechanical damping effect increasing as scale was reduced. Consequently, the experimental velocity response did not remain constant with reduced scale; its amplitude reduced. To allow the experimental and simulation results to be compared across scales, rather than using the load power, the effective transduction factor was employed. This was appropriate as K_{eff} is normalised by velocity, which mitigates the issue of the experimental velocity-frequency response amplitude changing with scale.

The voltage induced in the electrical circuit was derived using Kirchhoff's voltage law in equation 2.25. As the harvester is designed to operate at low frequencies (< 30 Hz), the effect of the coil inductance was small and, hence, was neglected in the current analysis—the inductor impedance of the largest coil was $Z_L = 56\ \Omega$ at 30 Hz, compared to a coil resistance of $R_C = 938.9\ \Omega$. Rearranging equation 2.25 allows an expression for the load voltage to be found:

$$V_L = Kv\left(\frac{R_L}{R_L + R_C}\right) \tag{7.5}$$

where v is the relative velocity between the magnet and coil. The effective transduction factor K_{eff} is calculated from both simulation and experimental data by rearranging equation 7.5:

$$K_{eff} = \frac{V_L}{v}\left(\frac{R_L + R_C}{R_L}\right) \tag{7.6}$$

In this case V_L is the RMS load voltage, while v is the RMS velocity.

The experimental K_{eff} is calculated from the peak RMS load voltage and the corresponding RMS velocity in the experimental frequency sweeps. Although the

RMS relative and absolute velocities vary significantly at frequency ranges above and below the peak frequency, the deviation between them is small at the peak frequency. This is illustrated in figure 7.4 for simulation frequency sweeps at a range of g_0 values, and the findings are valid for all scales—under the mechanical damping conditions employed. As the LDV measures the absolute velocity of the mass, and due to the small difference in absolute and relative RMS velocities at the peak response, the RMS absolute velocity is used in the calculation of the experimental K_{eff}.

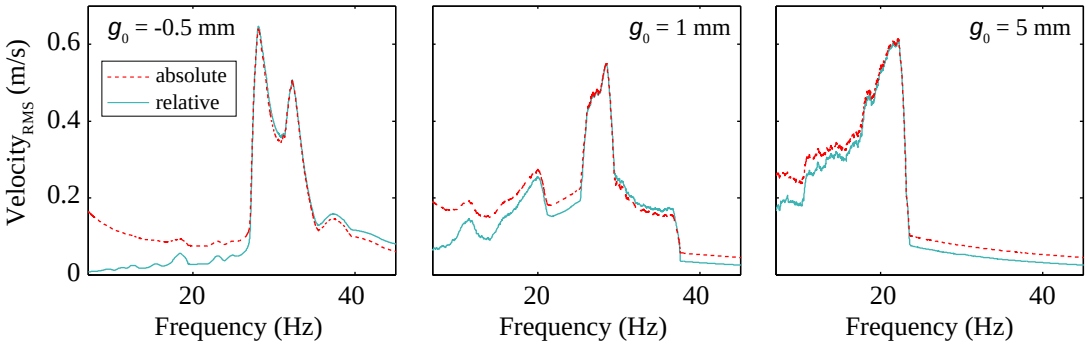

Figure 7.4: Absolute (- - - -) and relative (——) RMS velocity of m_2 for simulation forward frequency sweeps at a range of gaps—$Acc = 10$ m/s^2, $R = 3$, $s \approx 19$ mm.

The simulation and experimental K_{eff} are plotted as functions of the length scale in figure 7.5 for acceleration levels of $Acc = 10$ and 6 m/s^2, for gap lengths ranging from $g_0 = -0.2$ to 10.5 mm. The experimental data is plotted for the three magnet diameters, $d_{mag} = 6$, 8, and 12 mm, while the simulation data is presented for magnet diameters in the range $d_{mag} = 4.26$–15.63 mm. The simulation data was taken at a single frequency which varied for each g_0 and acceleration. The selected frequency remained constant with scale, however. This single frequency was selected based on the frequency response showing a high amplitude over the entire range of scales at this frequency.

The results of the scaling analysis of a 2-DoF VAEG are discussed below.

- The linear scaling relationship, $K \propto s^3$, is plotted as two dashed lines from the maximum and minimum K_{eff} values, respectively.

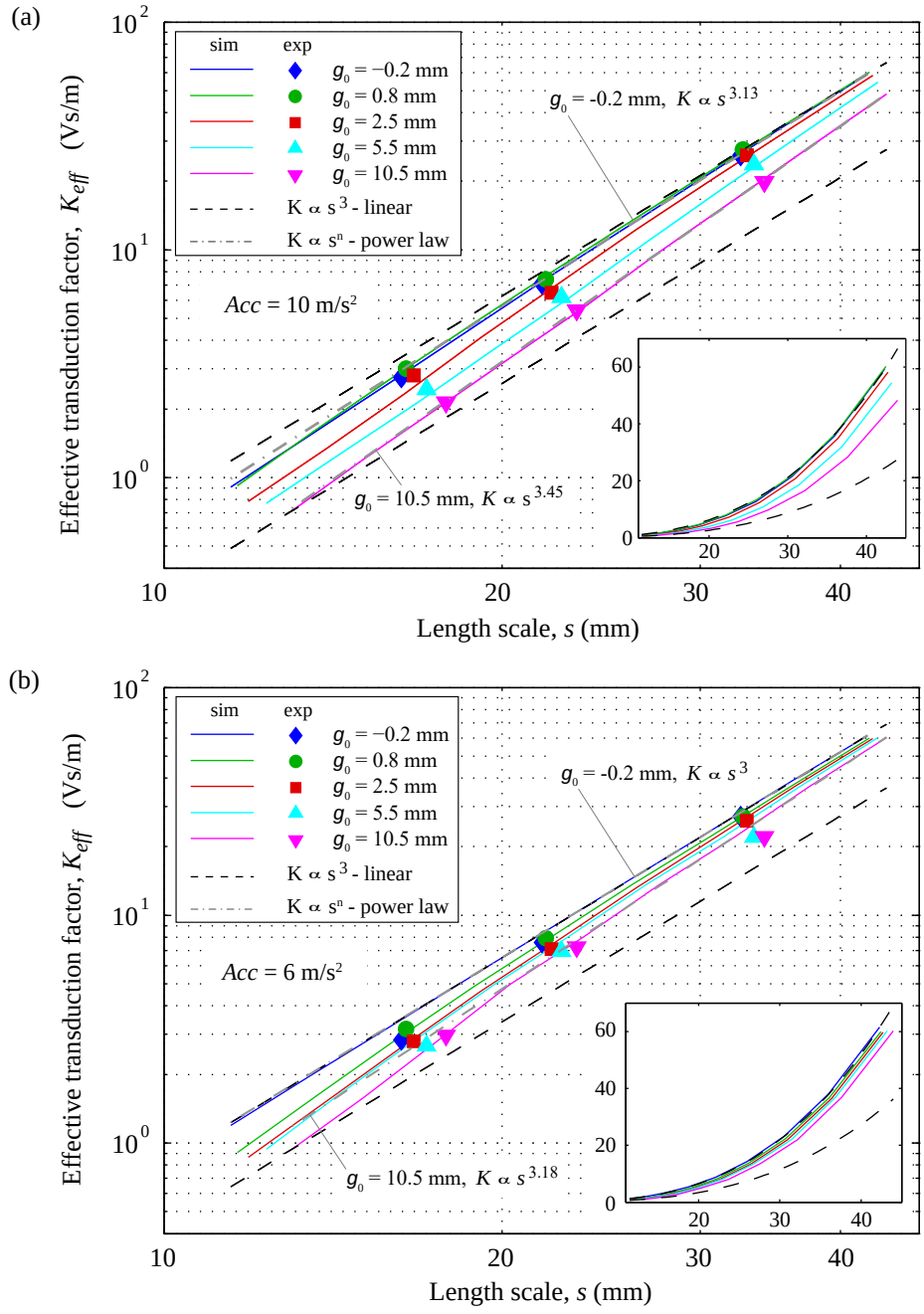

Figure 7.5: Experimental and simulation effective transduction factor, K_{eff}, as a function of length scale, for a range of g_0; (a) $Acc = 10$ m/s^2 and (b) $Acc = 6$ m/s^2. Experimental results from $d_{mag} = 6$, 8, and 12 mm systems. The main graphs are plotted on logarithmic scales, while the embedded graph are plotted on linear scales.

  - Evidently, K_{eff} scales at a greater rate than the linear relationship. This is due to the aforementioned reduction in K_{eff} with increased displacement range, which is a consequence of the relative motion of the magnet stack and coils being in sub-optimal locations for portions of each cycle.
  - As g_0 is increased, the scaling rate of K_{eff} is increased further. This is a result of g_0 remaining constant with length scale, with the volume then decreasing at a slower rate. The increased scaling rate of K_{eff} is seen in the shift in experimental data points to higher length scales with increasing g_0, and in the divergence of the simulation results from each other and the linear scaling relationships as length scale is decreased.
  - Furthermore, as the magnet stack and coil dimensions are reduced, K_{eff} is effectual over a smaller range, which becomes an ever smaller portion of the displacement range.

- Power law relationships are fitted to the simulation results for the highest and lowest gap lengths.
  - In the simulation results, at the lowest acceleration level ($Acc = 6$ m/s^2) and the lowest gap ($g_0 = -0.2$ mm), the scaling rate is effectively the same as a for a linear system ($K \propto s^3$). This is because, under these excitation and geometric conditions, the harvester effectively behaves as a linear system, i.e. the masses are always connected to a spring.
  - As g_0 and the acceleration level are increased, the displacement range rises and the system no longer behaves linearly. The scaling rate increases as a result of this larger displacement range. At the highest acceleration level ($Acc = 10$ m/s^2) and the highest gap size ($g_0 = 10.5$ mm) the highest scaling rate of $K \propto s^{3.45}$ is seen.

The scaling analysis described here relates to VAEGs; however, the results are also relevant for other electromagnetic energy harvesters which operate at low frequencies featuring large displacement amplitudes (Bedekar *et al.*, 2009;

Mann and Sims, 2009). In these systems, K_{eff} will be lower than the peak K, and will scale at a greater rate than a system featuring lower displacement amplitudes. This indicates that inertial generators operating at low frequencies will scale poorly, compared to devices operating at higher frequencies.

7.2.2 Influence of scale on mechanical damping in a VAEG

The influence of the mechanical damping scaling rate on the velocity-frequency response of a 2-DoF VAEG is investigated in this subsection. This analysis is of interest as it explores the limits of damping on the dynamic response of a VAEG. The focus of the scaling analysis presented thus far has been on the influence of geometry and acceleration level on the scaling of the electrical system of a VAEG, relative to that of a linear system. The scaling of mechanical damping was not the main objective of this investigation; therefore, only a brief analysis is discussed. Simulation only is employed in this analysis; the experimental mechanical damping scaling rate is not considered, as the mechanical damping parameters are highly dependent on the fabrication quality. A sample of three fabricated devices is, consequently, not significant enough to draw conclusions of significance from. This section compares the velocity-frequency response of 2-DoF VAEGs at four length scales for three mechanical damping scaling rates, through simulation.

The most common types of mechanical damping were discussed in section 2.1, while the scaling of the mechanical damping coefficient was discussed briefly in section 7.1. The dominant component of mechanical damping in a VEH is highly dependent on the device design. In the VAEG demonstrated herein, the most significant components of the mechanical damping were thermoelastic damping in the springs, and friction between the masses and Teflon tube. It was assumed that the mechanical damping could be sufficiently modelled by a discontinuous viscous damper, with a single viscous damping force applied to a mass when disconnected from the springs, and an additional viscous damping force applied when in contact with the springs:

$$F_c(z) = \begin{cases} c_{m_f}\dot{z} & \text{if disconnected from spring} \\ (c_{m_s} + c_{m_f})\dot{z} & \text{if connected to a spring} \end{cases} \tag{7.7}$$

where c_{m_f} was in effect constantly, and c_{m_s} was in effect when the mass experienced a spring force. The equations of motion of a 2-DoF system with discontinuous damping were described fully in equation 4.13.

Simulation velocity-frequency responses for a range of mechanical damping scaling rates and length scales are presented in figure 7.6. This test series was completed to show the influence of the mechanical damping scaling rate on the frequency response of a 2-DoF VAEG. Scaling rates of $c_m \propto s^3$, $c_m \propto s^2$, and $c_m \propto s$ are presented for four length scales. The reasons these scaling rates were selected are as follows: $c_m \propto s^3$—the ideal scenario, with the velocity-frequency response remaining constant as scale is reduced; $c_m \propto s$—the scaling rate stated by Arnold (2007); and $c_m \propto s^2$—shows the transition between the two previously described scaling rates. The length scales presented are lower than those in figure 7.5, as there is no coil present—the dynamics only are under investigation—which decreases the device volume.

If $c_m \propto s^3$, the system velocity-frequency response does not change with scale (figure 7.6a)—as discussed in section 7.2.1. Lowering the scaling rate results in the RMS velocity significantly decreasing with scale. The mechanical damping dominates, such that the masses no longer achieve high velocity impacts that result in velocity amplification. This is particularly evident in figure 7.6c, where the peak demonstrated at higher length scales is no longer present at $s = 7.2$ mm. Comparing the highest and lowest length scales presented for $c_m \propto s$, the peak RMS velocity of the magnet stack goes from 0.436 to 0.121 m/s, which is a reduction of 72.4%. This has a devastating effect on the potential energy which can be harvested from a VAEG, particularly approaching MEMS scale.

Considering, finally, the scaling of the load power in a 2-DoF VAEG, assuming $c_m \propto s$. Incorporating a transducer in the model used in figure 7.6 allowed the power generated at each scale to be simulated. Going from a length scale of $s = 18.7$ to 8.4 mm (the increase in volume with the addition of the coil is ignored to keep the length scales consistent with figure 7.6), the simulated peak power generated drops from $P_L = 12.48$ to 0.152 mW. This corresponds to a scaling rate of $P_L \propto s^{5.51}$, which is in the range specified by Arnold (2007) (equation 7.3). Decreasing the scale further, this power scaling relationship continues to increase, as the influence of the mechanical damping increases relative to the

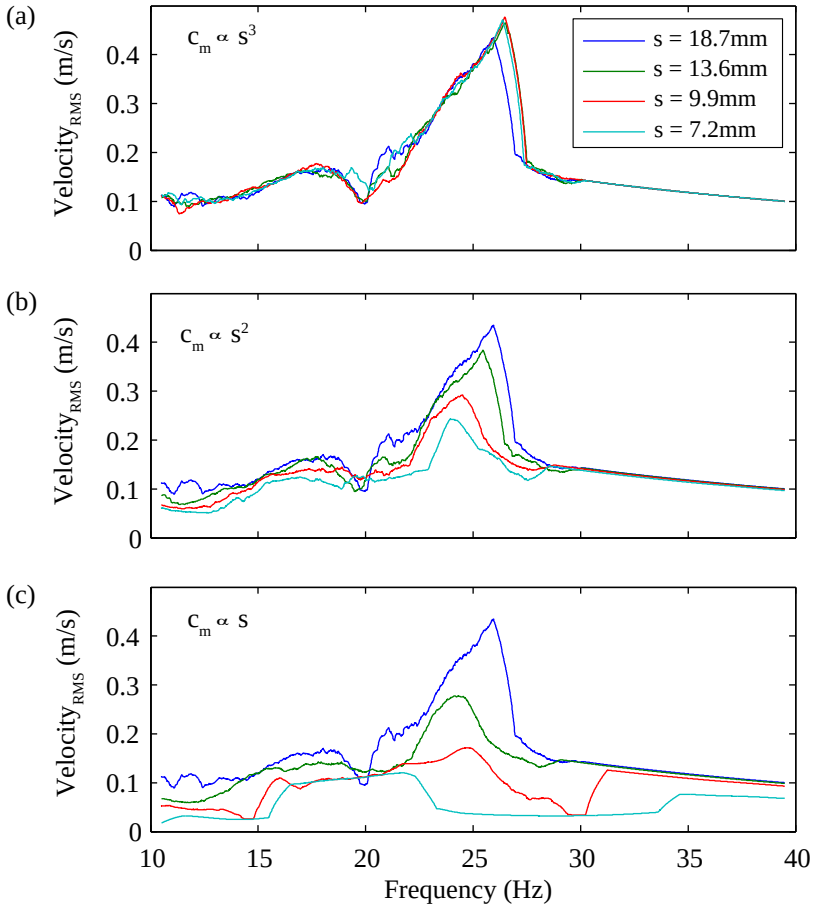

Figure 7.6: Simulation frequency forward-sweeps showing RMS velocity of magnet stack for a range of length scales; (a) $c_m \propto s^3$, (b) $c_m \propto s^2$, and (c) $c_m \propto s$—$Acc = 10$ m/s^2, $g_0 = 2.2$ mm.

electrical damping, becoming the dominant damping mechanism. This is further compounded by the volume decreasing at a lower rate than the transducer dimensions, due to g_0 remaining constant with scale.

7.3 Closure

The 2-DoF VAEG characterised in chapter 6 was uniformly scaled and fabricated at two further scales. The three harvesters—with length scales ranging from $s = 16.26$–34.48 mm—were tested to determine the influence of scale on a VAEG,

relative to a linear energy harvester.

- The electromagnetic transduction factor K was employed in the scaling analysis instead of the load power P_L, as K is normalised by velocity. This allowed the experimental and simulation results to be compared.

- It was found that g_0 does not scale. To maintain the dynamics, g_0 must be kept constant. Consequently, the total device volume does not scale at the same rate as the transducer dimensions.

- The effective transduction factor K_{eff} decreases with increasing g_0, as the position of the magnet relative to the coil corresponds to a high flux gradient over a smaller portion of its cycle. Scaling has a compounding effect on this, as K is significant over a smaller displacement range.

- The scaling rate of K_{eff} in a linear energy harvester, with $c_m \propto s^3$ and constant coil wire diameter, is $K_{eff} \propto s^3$. Under the same conditions, a VAEG demonstrates a scaling rate of $K_{eff} \propto s^{3-3.45}$. The scaling rate increases with increasing g_0 and increasing acceleration, as the displacement range increases. The scaling rate approaches the linear scaling rate at low accelerations and low g_0, as the displacement range is small.

- It has been shown through simulation that if the mechanical damping coefficient scales as $c_m \propto s$, as is stated by Arnold (2007), the effect on the dynamics of a VAEG are devastating. A 72.4% reduction in the peak RMS velocity of the magnet stack was observed going from a length scale of $s = 18.7$ to 7.2 mm. Unless a design which features very low mechanical damping levels can be fabricated, VAEGs at MEMS scale would not be feasible.

- Simulated frequency sweeps were employed to determine the scaling rate of load power in a 2-DoF VAEG, for a mechanical damping scaling rate of $c_m \propto s$. For a decrease in scale from $s = 18.7$ to 8.4 mm, a scaling rate of $P_L \propto s^{5.51}$ was determined. This scaling rate would continue to increase with reducing scale, as the mechanical damping would become increasingly dominant over the electrical damping.

Chapter 8

Conclusions and recommendations

This thesis investigated the behaviour of multi-DoF velocity amplified electromagnetic generators (VAEGs) under sinusoidal forced excitation, through experimental and numerical methods. A broad range of critical parameters were investigated including the number of DoFs and mass ratio, a geometric parameter referred to as the initial gap, and the frequency and acceleration of the excitation. It was determined that 2-DoF VAEGs with low mass ratios achieve the highest power densities. Higher numbers of DoFs result in lower RMS velocities and voltages due to the complexity of the impact sequences. The optimal frequency was observed to decrease with increasing gap, while the acceleration level required to achieve a large amplitude response increased. It was found that scaling greatly reduces the power density of a VAEG, which means developing an effective VAEG at very low scales is likely to be challenging. In this chapter, conclusions are drawn from the investigation, and recommendations are made for future work.

8.1 Conclusions

The influences of mass configuration (mass ratio and number of DoFs), a geometric parameter (initial gap), as well as excitation parameters (base frequency and acceleration) on the dynamic and electrical response of VAEGs were analysed

experimentally and numerically in this thesis. The effect of scaling on a 2-DoF VAEG was also investigated. Sinusoidal forced excitation was employed in each case.

Although the springs employed in the harvesters in this thesis were linear, the masses were able to detach from the springs, resulting in a piecewise linear (PWL) stiffness and overall non-linear behaviour. A PWL model was firstly developed, which allowed the dynamic and electrical behaviour of single- and multi-DoF PWL harvesters to be investigated through simulation. Non-linear analysis techniques were employed to analyse the behaviour of the PWL systems.

Prior to the analysis of the more complex multi-DoF systems, a single-DoF PWL oscillator was modelled to investigate the influence of a range of parameters on the system behaviour. The following conclusions were drawn for single-DoF systems:

- The device demonstrated three distinct periodic modes of operation, as well as higher period and chaotic modes.
- A downward shift in frequency was observed with increasing initial gap, g_0, due to the decreasing effective stiffness. It was also noted that the acceleration required to achieve high amplitude oscillations of the inertial mass increased with increasing g_0.
- Hysteresis in bidirectional sweeps of the frequency, acceleration and initial gap was also observed. The presence of regions with non-unique coexisting responses reduced the applicability of this harvester design—similarly to many of the non-linear energy harvesters presented in the literature—as the response achieved was dependent on the initial conditions and the basin of attraction.

The non-linear analysis techniques discussed above were also employed to analyse multi-DoF PWL oscillators. Most attention was given to 2-DoF PWL systems, and 3- and 4-DoF PWL harvesters were also investigated.

- For the set of model parameters investigated, the response was found to be chaotic for most operating conditions, i.e. the range of excitation frequencies, accelerations, and initial gaps tested.

- The hysteresis exhibited by the single-DoF PWL harvester was either severely reduced or no longer present in the bidirectional sweeps of the 2-DoF PWL system (figure 4.13). Also, the chaotic response of the harvester was stationary random, meaning, over time, the RMS harvester output converged to the same value, for a set of excitation conditions. The significance of the above points is that the RMS response of the multi-DoF system is independent of initial conditions.

- As for the single-DoF PWL system, increasing g_0 resulted in the optimal frequency shifting downwards. Again, the acceleration level required to engage the stopper spring and achieve high velocity oscillations also increased with g_0.

- Assuming a constant electromagnetic transduction factor, K, the model predicted that—under forced excitation—the RMS velocity and, consequently, voltage would increase with mass ratio—the ratio of the largest to smallest mass in the system. This was a result of greater velocity amplification on impact, resulting in high frequency oscillations with multiple impacts per cycle.

- Significantly, the model predicted that under forced excitation, contrary to the theory of velocity amplification, velocity does not increase with additional DoFs beyond 2-DoF. This is caused by the more complex impact sequences which occur in higher DoF systems, resulting in lower RMS velocities.

The influence of mass configuration—mass ratio and number of DoFs—on the performance of multi-DoF VAEGs (2-, 3-, and 4-DoFs) was investigated experimentally through drop-test and forced excitation.

- A drop-tester was developed which allowed sequential pairwise collisions between masses to be achieved. Consistent with velocity amplification theory, the velocity gain increased with both mass ratio and number of DoFs, although the losses in the system also increased with additional impacts.

- Under forced excitation, RMS velocity also increased with mass ratio; RMS velocity decreased with additional DoFs beyond 2-DoFs, however, as predicted by the multi-DoF PWL model. Therefore, the 2-DoF VAEG was found to be the optimal configuration for a multi-DoF harvester.

- Two transducer implementations were employed in this analysis. The first employed the same magnet, coil, and load resistance (i.e. same value of K) in each VAEG configuration. In this case, the RMS load voltage increased with greater mass ratio, due to the higher RMS velocity. In the second case, the magnet size within the final mass was scaled proportionally to the mass. In this case, the reduction in K with increasing mass ratio—due to the smaller magnet size—resulted in the output voltage decreasing with increasing mass ratio. This suggests that lower mass ratios will result in higher power outputs.

- A lack of hysteresis in the response was observed experimentally in this investigation, as the multi-DoF PWL model predicted.

Based on the results of the mass configuration analysis, a 2-DoF VAEG with a mass ratio of $R = 3$ was selected for optimisation and characterisation.

- Simulations were employed to design an optimised transducer. An oppositely polarised magnet stack with two magnets and three coils demonstrated the highest power density for large displacements of the inertial mass, which contained the magnet stack.

- Characterisation sweeps were performed experimentally and numerically at a range of accelerations and initial gaps. The downwards shift in optimal frequency with increasing g_0—due to the decreasing effective stiffness—was observed experimentally. It was also observed that the input acceleration level required to generate large amplitude oscillations at the optimal frequency increased with g_0. RMS velocity was observed to increase with g_0, provided large amplitude oscillations were achieved. This did not necessarily result in an increase in RMS voltage, however, as the larger displacements of the magnet stack resulted in the magnet and coil oscillating

relative to one another in regions of low flux gradient over large portions of the cycle.

- Again, the hysteresis in response to experimental and simulation bidirectional sweeps was found to be negligible. Coupled with the stationary random nature of the response, this means the RMS output from the harvester is independent of initial conditions.

- NPD and FoM_V values of 6.64 kg s/m^3 and 0.98% were reported, respectively. Adjusting the internal coil diameter to its minimum possible value, it was predicted through simulation that an increase to values of 29.84 kg s/m^3 and 2.83% could be achieved—impressive in the context of the state-of-the-art.

The final investigation undertaken in this thesis was to determine the influence of scaling on the behaviour of a 2-DoF VAEG, relative to a linear harvester. The device characterised in the optimisation study, fabricated at two further scales, was employed in the scaling analysis.

- It was determined that if the frequency response of a VAEG is to be maintained with scale, the initial gap, g_0, must be kept constant, i.e. g_0 does not scale. A consequence of this is that the total device volume scales at a slower rate than the transducer dimensions, which reduces the power density as scale is reduced.

- The scaling rate of the effective electromagnetic transduction factor, K_{eff}, is greater than that of a linear system ($K_{eff} \propto s^3$), with rates of $K_{eff} \propto s^{3-3.45}$ predicted. This is due to the larger displacement range, with the magnet and coil spending large portions of each cycle in sub-optimal relative positions. The scaling rate of K_{eff} in a VAEG increases with increasing g_0 and excitation acceleration as the effect of the sub-optimal coil magnet position is compounded.

- Considering the scaling of the mechanical system, if the mechanical damping scales at $c_m \propto s$, the effect on the RMS velocity of the transducer mass

are severe, with a reduction of 72.4% in peak RMS velocity predicted in reducing from a length scale of $s = 18.7$ to 7.2 mm.

- Recombining the mechanical and electrical systems for the same mechanical damping parameters, the load power was predicted to scale as $P_L \propto s^{5.51}$. Clearly, this has negative implications for the feasibility of a 2-DoF VAEG at micro-scales.

It has been demonstrated that a 2-DoF system with a low mass ratio ($R \approx 3$) is the optimal configuration for a VAEG. The gap which should be employed is dependent on the excitation conditions, with the optimal gap length increasing with excitation acceleration. However, as the effects of mechanical damping increase with reducing scale, it is likely to be extremely challenging to develop a high power density 2-DoF VAEG approaching micro-scales.

The ultimate goal of this research is to develop an energy harvester employing velocity amplification capable of powering a sensor node in a practical environment. The volume requirements of the harvester would depend on the sensor functionality and the application location, i.e. a device for monitoring human health should ideally have a small form factor ($\sim 10^0$ cm^3), whereas a device for monitoring the structural health of a bridge or building may not have such strict volume requirements ($\sim 10^1$–10^2 cm^3).

8.2 Recommendations for future work

This thesis focused on investigating the influence of a range of parameters on the response of VAEGs under sinusoidal excitation. A number of analyses which may be of interest, but were beyond the scope of this thesis, are listed below:

- The experimental analysis presented in this thesis focused on sinusoidal forced excitation. Most real world vibration sources, however, feature some level of noise, or may even be random in nature. It is recommended that a future investigation into VAEGs would focus on coloured noise, white noise, and sinusoidal excitation with varying degrees of noise as inputs.

- Potential improvements in power density could be made by improving the magnetic circuitry. This could potentially be achieved by implementing a Halbach array magnet stack, which have been shown to achieve high flux gradients within a confined volume.

- A more volumetrically efficient design could also be implemented in a 2-DoF VAEG by employing an embedded mass design, i.e. the smaller mass would be located within a cavity in the larger mass.

- As the results of the scaling analysis demonstrate, achieving a significant response from a VAEG at small scales would be extremely challenging. Future VAEG designs should focus on achieving an extremely low mechanical damping to achieve a reasonable output approaching micro-scales. Methods of achieving this may include the use of rolling bearing elements, lubrication, low friction materials, and improved surface finish.

- Magnetic springs—which utilise the repulsive force between oppositely polarised magnets—could be employed as an alternative to mechanical springs. A significant advantage of magnetic springs is they eliminate the thermoelastic damping that occurs in the stretching of a mechanical spring. If the linear compression springs employed in this thesis were replaced by magnetic springs, the harvesters would no longer be PWL. Obviously, this would lead to significantly different dynamics than those presented in this thesis.

Finally, the output voltage from the harvesters in this thesis were measured across a load resistor. This was deemed sufficient for the investigation, as the dynamics of multi-DoF VAEGs were of primary interest. The proportion of the RMS voltage output from a VAEG which could be converted into useful DC voltage has yet to investigated. Furthermore, the output signal from the harvester is chaotic under most operating conditions, which may increase the complexity of load optimisation and conditioning. Future work could investigate power conditioning circuitry for processing the output voltage from a VAEG to determine the actual useful power generated from a chaotic signal.

References

Abed, I., Kacem, N., Bouhaddi, N. and Bouazizi, M. L. (2016), 'Multi-modal vibration energy harvesting approach based on nonlinear oscillator arrays under magnetic levitation', *Smart Materials and Structures* **25**(2), 13. 125, 126

Ahmed Seddik, B., Despesse, G. and Defay, E. (2011), 'Increased bandwidth of mechanical energy harvester', *Sensors & Transducers Journal* **13**, 73–86. 2, 19

Arnold, D. P. (2007), 'Review of Microscale Magnetic Power Generation', *IEEE Transactions on Magnetics* **43**(11), 3940–3951. 4, 149, 150, 151, 152, 154, 155, 158, 165, 167

Ashraf, K., Khir, M. H. M., Dennis, J. O. and Baharudin, Z. (2013), 'A wideband, frequency up-converting bounded vibration energy harvester for a low-frequency environment', *Smart Materials and Structures* **22**(2), 13. 21

Baert, K., Gyselinckx, B., Torfs, T., Leonov, V., Yazicioglu, F., Brebels, S., Donnay, S., Vanfleteren, J., Beyne, E. and Van Hoof, C. (2006), 'Technologies for highly miniaturized autonomous sensor networks', *Microelectronics Journal* **37**(12), 1563–1568. 1

Barton, D. A. W., Burrow, S. G. and Clare, L. R. (2010), 'Energy Harvesting From Vibrations With a Nonlinear Oscillator', *Journal of Vibration and Acoustics* **132**(2), 7. 14, 72

Bedekar, V., Oliver, J. and Priya, S. (2009), 'Pen harvester for powering a pulse rate sensor', *Journal of Physics D: Applied Physics* **42**(10), 9. 163

Beeby, S. P., Torah, R. N., Tudor, M. J., Glynne-Jones, P., O'Donnell, T., Saha, C. R. and Roy, S. (2007), 'A micro electromagnetic generator for vibration energy harvesting', *Journal of Micromechanics and Microengineering* **17**, 1257–1265. 4, 8, 20, 21

REFERENCES

Beeby, S. P., Tudor, M. J. and White, N. M. (2006), 'Energy harvesting vibration sources for microsystems applications', *Measurement Science and Technology* **17**(12), R175. 5

Bendame, M., Abdel-rahman, E. and Soliman, M. (2014), Test and Validation of a Nonlinear Electromagnetic Energy, *in* 'Proceedings of the ASME 2014 International Design Engineering Technical Conferences & Computers and Information in Engineering Conference IDETC/CIE', Buffalo, pp. 1–9. 56, 65, 69

Bendat, J. S. and Piersol, A. G. (1971), *Random Data: Analysis and Measurement Procedures*, 4th edn, Wiley. 93

Blystad, L.-C. J. and Halvorsen, E. (2011), 'A piezoelectric energy harvester with a mechanical end stop on one side', *Microsystem Technologies* **17**(4), 505–511. 18

Blystad, L. C. J., Halvorsen, E. and Husa, S. (2010), 'Piezoelectric MEMS energy harvesting systems driven by harmonic and random vibrations', *IEEE Transactions on Ultrasonics, Ferroelectrics, and Frequency Control* **57**(4), 908–919. 19

Bonisoli, E., Canova, A., Freschi, F., Moos, S., Repetto, M. and Tornincasa, S. (2010), 'Dynamic simulation of an electromechanical energy scavenging device', *IEEE Transactions on Magnetics* **46**(8), 2856–2859. 125

Bracke, W., Merken, P., Puers, R. and Van Hoof, C. (2007), 'Generic architectures and design methods for autonomous sensors', *Sensors and Actuators, A: Physical* **135**(2), 881–888. 1

Budd, C., Dux, F. and Cliffe, a. (1995), 'The effect of frequency and clearance variations on single-degree-of-freedom impact oscillators', *Journal of Sound and Vibration* **184**, 475–502. 56, 65

Burrow, S. G. and Clare, L. R. (2007), A resonant generator with non-linear compliance for energy harvesting in high vibrational environments, *in* 'Proceedings of IEEE International Electric Machines and Drives Conference, IEMDC 2007', Vol. 1, pp. 715–720. 14

Cepnik, C., Radler, O., Rosenbaum, S., Ströhla, T. and Wallrabe, U. (2011), 'Effective optimization of electromagnetic energy harvesters through direct computation of the electromagnetic coupling', *Sensors and Actuators A: Physical* **167**(2), 416–421. 4, 21

Cepnik, C. and Wallrabe, U. (2011), 'A flat high performance micro energy harvester based on a serpentine coil with a single winding', *2011 16th International Solid-State Sensors, Actuators and Microsystems Conference, TRANSDUCERS'11* pp. 661–664. 21

Cepnik, C. and Wallrabe, U. (2013), 'Approaches for a fair comparison and benchmarking of electromagnetic vibration energy harvesters', *Micromachines* **4**(3), 286–305. 149, 151

Challa, V. R., Cheng, S. and Arnold, D. P. (2013), 'The role of coupling strength in the performance of electrodynamic vibrational energy harvesters', *Smart Materials and Structures* **22**(2), 11. 125

Challa, V. R., Prasad, M. G. and Fisher, F. T. (2011), 'Towards an autonomous self-tuning vibration energy harvesting device for wireless sensor network applications', *Smart Materials and Structures* **20**(2), 11. 10, 74, 86

Challa, V. R., Prasad, M. G., Shi, Y. and Fisher, F. T. (2008), 'A vibration energy harvesting device with bidirectional resonance frequency tunability', *Smart Materials and Structures* **17**(1), 10. 10

Cheng, S. and Arnold, D. P. (2010), 'A study of a multi-pole magnetic generator for low-frequency vibrational energy harvesting', *Journal of Micromechanics and Microengineering* **20**(2), 10. 31, 126

Ching, N. N. H., Wong, H. Y., Li, W. J., Leong, P. H. W. and Wen, Z. (2002), 'A laser-micromachined multi-modal resonating power transducer for wireless sensing systems', *Sensors and Actuators A* **98**, 685–690. 7, 21

Constantinou, P., Mellor, P. H. and Wilcox, P. D. (2012), 'A magnetically sprung generator for energy harvesting applications', *IEEE/ASME Transactions on Mechatronics* **17**(3), 415–424. 125

Cottone, F., Frizzell, R., Goyal, S., Kelly, G. and Punch, J. (2013), 'Enhanced vibrational energy harvester based on velocity amplification', *Journal of Intelligent Material Systems and Structures* **0**(0), 1–9. 19, 22, 36, 111

Cottone, F., Vocca, H. and Gammaitoni, L. (2009), 'Nonlinear Energy Harvesting', *Physical Review Letters* **102**(8), 4. 15, 16, 17

Cugat, O., Delamare, J. and Reyne, G. (2003), 'Magnetic micro-actuators and systems (MAGMAS)', *IEEE Transactions on Magnetics* **39**(6), 3607–3612. 107, 151

Daqaq, M. F. (2011), 'Transduction of a bistable inductive generator driven by white and exponentially correlated Gaussian noise', *Journal of Sound and Vibration* **330**(11), 2554–2564. 17

Daqaq, M. F. (2012), 'On intentional introduction of stiffness nonlinearities for energy harvesting under white Gaussian excitations', *Nonlinear Dynamics* **69**(3), 1063–1079. 5, 17

Daqaq, M. F., Masana, R., Erturk, A. and Dane Quinn, D. (2014), 'On the Role of Nonlinearities in Vibratory Energy Harvesting: A Critical Review and Discussion', *Applied Mechanics Reviews* **66**(4), 23. 15, 72

Dhakar, L., Liu, H., Tay, F. and Lee, C. (2013), 'A new energy harvester design for high power output at low frequencies', *Sensors and Actuators A: Physical* **199**, 344–352. 18

di Bernardo, M., Budd, C. J. and Champneys, A. R. (2001), 'Normal form maps for grazing bifurcations in n-dimensional piecewise-smooth dynamical systems', *Physica D-Nonlinear Phenomena* **160**(3-4), 222–254. 68

El Aroudi, a., Ouakad, H., Benadero, L. and Younis, M. (2014), 'Analysis of Bifurcation Behavior of a Piecewise Linear Vibrator with Electromagnetic Coupling for Energy Harvesting Applications', *International Journal of Bifurcation and Chaos* **24**(5), 20. 56

El-hami, M., Glynne-jones, P., White, N. M., Hill, M. and Beeby, S. (2001), 'Design and fabrication of a new vibration-based electromechanical power generator', **92**, 335–342. 8, 21

Elvin, N. G. and Elvin, A. a. (2011), 'An experimentally validated electromagnetic energy harvester', *Journal of Sound and Vibration* **330**(10), 2314–2324. 4, 21

Erturk, A., Hoffmann, J. and Inman, D. J. (2009), 'A piezomagnetoelastic structure for broadband vibration energy harvesting', *Applied Physics Letters* **94**(25), 92–95. 15, 16

Erturk, A. and Inman, D. J. (2011), 'Broadband piezoelectric power generation on high-energy orbits of the bistable Duffing oscillator with electromechanical coupling', *Journal of Sound and Vibration* **330**(10), 2339–2353. 16

Erturk, A., Renno, J. M. and Inman, D. J. (2009), 'Modeling of Piezoelectric Energy Harvesting from an L-shaped Beam-mass Structure with an Application to UAVs', *Journal of Intelligent Material Systems and Structures* **20**(5), 529–544. 12, 15, 74

Ferrari, M., Ferrari, V., Guizzetti, M., Andò, B., Baglio, S. and Trigona, C. (2010), 'Improved energy harvesting from wideband vibrations by nonlinear piezoelectric converters', *Sensors and Actuators A: Physical* **162**(2), 425–431. 17

Ferrari, M., Ferrari, V., Guizzetti, M. and Marioli, D. (2009), 'An autonomous battery-less sensor module powered by piezoelectric energy harvesting with RF transmission of multiple measurement signals', *Smart Materials and Structures* **18**(8), 9. 6

Ferro (2009), 'Ferro Solutions VEH-460'. 21

Fore, L. B. (2010), 'Reduction of peak-locking errors produced by Gaussian sub-pixel interpolation in cross-correlation digital particle image velocimetry', *Measurement Science and Technology* **21**(3), 6. 46

Forliti, D. J., Strykowski, P. J. and Debatin, K. (2000), 'Bias and precision errors of digital particle image velocimetry', *Experiments in Fluids* **28**(5), 436–447. 53

Friswell, M. I., Ali, S. F., Bilgen, O., Adhikari, S., Lees, a. W. and Litak, G. (2012), 'Non-linear piezoelectric vibration energy harvesting from a vertical cantilever beam with tip mass', *Journal of Intelligent Material Systems and Structures* **23**(13), 1505–1521. 17

Frizzell, R., Kelly, G., Cottone, F., Boco, E., Nico, V., O'Donoghue, D. and Punch, J. (2016), 'Experimental characterisation of dual-mass vibration energy harvesters employing velocity amplification', *Journal of Intelligent Material Systems and Structures* p. 17. 19, 22, 49, 56

Galchev, T., Kim, H. and Najafi, K. (2009), 'A Parametric Frequency Increased Power Generator for Scavenging Low Frequency Ambient Vibrations', *Procedia Chemistry* **1**(1), 1439–1442. 84

Galchev, T., Kim, H. and Najafi, K. (2011), 'Micro power generator for harvesting low-frequency and nonperiodic vibrations', *Journal of Microelectromechanical Systems* **20**(4), 852–866. 21

Gammaitoni, L., Neri, I. and Vocca, H. (2009), 'Nonlinear oscillators for vibration energy harvesting', *Applied Physics Letters* **94**(16), 4–7. 17

Gilbert, J. M. and Balouchi, F. (2008), 'Comparison of energy harvesting systems for wireless sensor networks', *International Journal of Automation and Computing* **5**(4), 334–347. 2

Glynne-Jones, P., Tudor, M., Beeby, S. and White, N. (2004), 'An electromagnetic, vibration-powered generator for intelligent sensor systems', *Sensors and Actuators A: Physical* **110**(1-3), 344–349. 8

Green, P. L., Worden, K., Atallah, K. and Sims, N. D. (2012*a*), 'The benefits of Duffing-type nonlinearities and electrical optimisation of a mono-stable energy harvester under white Gaussian excitations', *Journal of Sound and Vibration* **331**(20), 4504–4517. 47

Green, P. L., Worden, K., Atallah, K. and Sims, N. D. (2012*b*), 'The effect of Duffing-type non-linearities and Coulomb damping on the response of an energy harvester to random excitations', *Journal of Intelligent Material Systems and Structures* **23**(18), 2039–2054. 125

Gu, L. (2011), 'Low-frequency piezoelectric energy harvesting prototype suitable for the MEMS implementation', *Microelectronics Journal* **42**(2), 277–282. 19, 84

Gu, L. and Livermore, C. (2011), 'Impact-driven, frequency up-converting coupled vibration energy harvesting device for low frequency operation', *Smart Materials and Structures* **20**(4), 10. 84

Haroun, A., Yamada, I. and Warisawa, S. (2015), 'Study of electromagnetic vibration energy harvesting with free/impact motion for low frequency operation', *Journal of Sound and Vibration* **349**, 389–402. 56

Hart, J. and Herman, R. (1968), 'Energy transfer in one- dimensional collisions of many objects', *American Journal of Physics* **36**, 46–48. 39

Hatipoglu, G. and Ürey, H. (2010), 'FR4-based electromagnetic energy harvester for wireless sensor nodes', *Smart Materials and Structures* **19**(1), 11. 21, 155

Hinrichs, N., Oestreich, M. and Popp, K. (1997), 'Dynamics of oscillators with impact and friction', *Chaos, Solitons and Fractals* **8**(4 SPEC. ISS.), 535–558. 56

Hoffmann, D., Folkmer, B. and Manoli, Y. (2009), 'Fabrication, characterization and modelling of electrostatic micro-generators', *Journal of Micromechanics and Microengineering* **19**(9), 11. 6, 19

Holman, J. P. (1971), *Experimental methods for engineers*, 8 edn, McGraw Hill. 50

Hu, Y., Xue, H. and Hu, H. (2007), 'A piezoelectric power harvester with adjustable frequency through axial preloads', *Smart Materials and Structures* **16**(5), 1961–1966. 9

Iannacci, J., Sordo, G., Serra, E. and Schmid, U. (2016), 'The MEMS four-leaf clover wideband vibration energy harvesting device: design concept and experimental verification', *Microsystem Technologies* **22**(7), 1865–1881. 12

Ing, J., Pavlovskaia, E., Wiercigroch, M. and Banerjee, S. (2008), 'Experimental study of impact oscillator with one-sided elastic constraint', *Philosophical Transactions of the Royal Society A - Mathematical Physical and Engineering Sciences* **366**(1866), 679–704. 56, 68

Inman, D. J. and Erturk, A. (2009), 'An experimentally validated bimorph cantilever model for piezoelectric energy harvesting from base excitations', *Smart Materials and Structures* **18**(2), 18. 5

James, E., Tudor, M., Beeby, S., Harris, N., Glynne-Jones, P., Ross, J. and White, N. (2004), 'An investigation of self-powered systems for condition monitoring applications', *Sensors and Actuators A: Physical* **110**(1-3), 171–176. 4, 6

Jordan, D. and Smith, P. (1977), *Nonlinear Ordinary Differential Equations: An Introduction for Scientists and Engineers*, 4th edn, Oxford, Ney York. 58, 59, 84

Kerwin, J. D. (1972), 'Velocity, Momentum, and Energy Transmissions in Chain Collisions', *American Journal of Physics* **40**(8), 1152–1158. 39

Kim, I.-H., Jung, H.-J., Lee, B. M. and Jang, S.-J. (2011), 'Broadband energy-harvesting using a two degree-of-freedom vibrating body', *Applied Physics Letters* **98**(21), 3. 12

Kleczka, M., Kreuzer, E. and Schiehlen, W. (1992), 'Local and Global Stability of a Piecewise Linear Oscillator', *Philosophical Transactions of the Royal Society A: Mathematical, Physical and Engineering Sciences* **338**(1651), 533–546. 56, 58

Kline, S. and McClintock, F. (1953), 'Describing uncertainties in single-sample experiments', *Mechanical engineering* **75**(1), 3–8. 50, 51

Koukharenko, E., Beeby, S. P., Tudor, M. J., White, N. M., O'Donnell, T., Saha, C., Kulkarni, S. and Roy, S. (2006), 'Microelectromechanical systems vibration powered electromagnetic generator for wireless sensor applications', *Microsystem Technologies* **12**(10-11), 1071–1077. 7

Kulkarni, S., Koukharenko, E., Torah, R., Tudor, J., Beeby, S., O'Donnell, T. and Roy, S. (2008), 'Design, fabrication and test of integrated micro-scale vibration-based electromagnetic generator', *Sensors and Actuators A: Physical* **145-146**, 336–342. 4, 21

Kulkarni, S., Roy, S., O'Donnell, T., Beeby, S. and Tudor, J. (2006), 'Vibration based electromagnetic micropower generator on silicon', *Journal of Applied Physics* **99**(8), 97–100. 7

Kwon, S.-D., Park, J. and Law, K. (2013), 'Electromagnetic energy harvester with repulsively stacked multilayer magnets for low frequency vibrations', *Smart Materials and Structures* **22**(5), 13. 126

Le, C. P. and Halvorsen, E. (2012), 'MEMS electrostatic energy harvesters with end-stop effects', *Journal of Micromechanics and Microengineering* **22**(7), 12. 19

Le, C. P., Halvorsen, E., Yeatman, E. M. and Sorasen, O. (2012), 'Microscale electrostatic energy harvester using internal impacts', *Journal of Intelligent Material Systems and Structures* **23**(13), 1409–1421. 6, 19, 56

Le, T. T., Han, J., Von Jouanne, A., Mayaram, K. and Fiez, T. S. (2006), 'Piezoelectric micro-power generation interface circuits', *IEEE Journal of Solid-State Circuits* **41**(6), 1411–1419. 6

Leland, E. S. and Wright, P. K. (2006), 'Resonance tuning of piezoelectric vibration energy scavenging generators using compressive axial preload', *Smart Materials and Structures* **15**(5), 1413–1420. 9, 86

Libelium (2013), 'Top 50 Internet of Things Applications - Ranking — Libelium'. 1

Lin, J. T., Lee, B. and Alphenaar, B. (2010), 'The magnetic coupling of a piezoelectric cantilever for enhanced energy harvesting efficiency', *Smart Materials and Structures* **19**(4), 7. 5

Litak, G., Friswell, M. I. and Adhikari, S. (2010), 'Magnetopiezoelastic energy harvesting driven by random excitations', *Applied Physics Letters* **96**(21), 18–21. 17

Liu, H., How Koh, K. and Lee, C. (2014), 'Ultra-wide frequency broadening mechanism for micro-scale electromagnetic energy harvester', *Applied Physics Letters* **104**(5), 4. 4

Liu, H., Lee, C., Kobayashi, T., Tay, C. J. and Quan, C. (2012*a*), 'Investigation of a MEMS piezoelectric energy harvester system with a frequency-widened-bandwidth mechanism introduced by mechanical stoppers', *Smart Materials and Structures* **21**(3), 12. 19

Liu, H., Lee, C., Kobayashi, T., Tay, C. J. and Quan, C. (2012*b*), 'Piezoelectric MEMS-based wideband energy harvesting systems using a frequency-up-conversion cantilever stopper', *Sensors and Actuators A: Physical* **186**, 242–248. 84

Liu, W. Q., Badel, A., Formosa, F., Wu, Y. P. and Agbossou, A. (2013), 'Novel piezoelectric bistable oscillator architecture for wideband vibration energy harvesting', *Smart Materials and Structures* **22**(3), 11. 63

Mallick, D., Amann, A. and Roy, S. (2015), 'A nonlinear stretching based electromagnetic energy harvester on FR4 for wideband operation', *Smart Materials and Structures* **24**(1), 14. 4, 15, 66, 74, 110, 134, 155

Mann, B. P. and Owens, B. a. (2010), 'Investigations of a nonlinear energy harvester with a bistable potential well', *Journal of Sound and Vibration* **329**(9), 1215–1226. 62, 63, 125

Mann, B. and Sims, N. (2009), 'Energy harvesting from the nonlinear oscillations of magnetic levitation', *Journal of Sound and Vibration* **319**(1-2), 515–530. 14, 125, 134, 164

Marin, A., Turner, J., Ha, D. S. and Priya, S. (2013), 'Broadband electromagnetic vibration energy harvesting system for powering wireless sensor nodes', *Smart Materials and Structures* **22**(7), 075008. 6

Marinkovic, B. and Koser, H. (2009), 'Smart Sanda wide bandwidth vibration energy harvesting platform', *Applied Physics Letters* **94**(10), 3. 15

Masana, R. and Daqaq, M. F. (2011*a*), 'Electromechanical Modeling and Nonlinear Analysis of Axially Loaded Energy Harvesters', *Journal of Vibration and Acoustics* **133**(February 2011), 10. 15

Masana, R. and Daqaq, M. F. (2011*b*), 'Relative performance of a vibratory energy harvester in mono- and bi-stable potentials', *Journal of Sound and Vibration* **330**(24), 6036–6052. 5, 15, 16, 63

Masana, R. and Daqaq, M. F. (2012), 'Energy harvesting in the super-harmonic frequency region of a twin-well oscillator', *Journal of Applied Physics* **111**(4), 11. 9

Meninger, S., Mur-miranda, J. O., Amirtharajah, R., Chandrakasan, A. P. and Lang, J. H. (2001), 'Vibration-to-Electric Energy Conversion', *IEEE Transactions on Very Large Scale Integration (VLSI) Systems* **9**(1), 64–76. 6

Miorandi, D., Sicari, S., De Pellegrini, F. and Chlamtac, I. (2012), 'Internet of things: Vision, applications and research challenges', *Ad Hoc Networks* **10**(7), 1497–1516. 1, 2

Mitcheson, P. D., Green, T. C. and Yeatman, E. M. (2007), 'Power processing circuits for electromagnetic, electrostatic and piezoelectric inertial energy scavengers', *Microsystem Technologies* **13**(11-12), 1629–1635. 6

Mitcheson, P. D., Toh, T. T., Wong, K. H., Burrow, S. G. and Holmes, A. S. (2011), 'Tuning the Resonant Frequency and Damping of an Electromagnetic Energy Harvester Using Power Electronics', *IEEE Transactions on Circuits and Systems II: Express Briefs* **58**(12), 792–796. 10

Mitcheson, P. D., Yeatman, E. M., Rao, G. K., Holmes, A. S. and Green, T. C. (2008), Human and Machine Motion for Wireless Electronic Devices, *in* 'Proceedings of the IEEE', Vol. 96, pp. 1457–1486. 5, 6, 20, 149, 150

Moffat, R. J. (1988), 'Describing the uncertainties in experimental results', *Experimental Thermal and Fluid Science* **1**(1), 3–17. 50

Moss, S. D., Payne, O. R. and Hart, G. A. (2014), 'Scaling and power density metrics of electromagnetic vibration energy harvesting devices', *Smart Materials and Structures* **24**(2), 14. 149

Munaz, A., Lee, B.-C. and Chung, G.-S. (2013), 'A study of an electromagnetic energy harvester using multi-pole magnet', *Sensors and Actuators A: Physical* **201**, 134–140. 21

Naruse, Y., Matsubara, N., Mabuchi, K., Izumi, M. and Suzuki, S. (2009), 'Electrostatic micro power generation from low-frequency vibration such as human motion', *Journal of Micromechanics and Microengineering* **19**(9), 5. 6

Nico, V., Boco, E., Frizzell, R. and Punch, J. (2016), 'A high figure of merit vibrational energy harvester for low frequency applications', *Applied Physics Letters* **108**(1), 5. 19, 21, 22

NiPS (2012), 'Real Vibrations'. xiii, 3

Nobach, H. and Honkanen, M. (2005), 'Two-dimensional Gaussian regression for subpixel displacement estimation in particle image velocimetry or particle position estimation in particle tracking velocimetry', *Experiments in Fluids* **38**(4), 511–515. 46

O'Donnell, T., Saha, C., Beeby, S. and Tudor, J. (2007), 'Scaling effects for electromagnetic vibrational power generators', *Microsystem Technologies* **13**(11-12), 1637–1645. 149, 151

Park, J. C., Bang, D. H. and Park, J. Y. (2010), 'Micro-Fabricated Electromagnetic Power Generator to Scavenge Low Ambient Vibration', *IEEE Transactions on Magnetics* **46**(6), 1937–1942. 4, 21

Penella, M. T., Albesa, J. and Gasulla, M. (2009), Powering wireless sensor nodes: Primary batteries versus energy harvesting, *in* '2009 IEEE Intrumentation and Measurement Technology Conference, I2MTC 2009', number May, pp. 1625–1630. 1

Perpetuum (2013), 'Perpetuum Data Sheet'. 21

Peterka, F. (2000), 'Dynamics of Double Impact Oscillators', *Facta Universitatis - Mechanics, Automatic Control and Robotics* **2**(10), 1177–1190. 67, 68

Peters, C., Maurath, D., Schock, W., Mezger, F. and Manoli, Y. (2009), 'A closed-loop wide-range tunable mechanical resonator for energy harvesting systems', *Journal of Micromechanics and Microengineering* **19**(9), 9. 10, 86

Qi, S., Shuttleworth, R., Olutunde Oyadiji, S. and Wright, J. (2010), 'Design of a multiresonant beam for broadband piezoelectric energy harvesting', *Smart Materials and Structures* **19**(9), 10. 12

Quinn, D. D., Triplett, A. L., Bergman, L. a. and Vakakis, A. F. (2011), 'Comparing Linear and Essentially Nonlinear Vibration-Based Energy Harvesting', *Journal of Vibration and Acoustics* **133**(1), 8. 15, 72, 73

Rahimi, A. (2012), 'Fully Self-Powered Electromagnetic Energy Dual Rail Output', *IEEE Sensors Journal* **12**(6), 2287–2298. 6, 125

Ramlan, R., Brennan, M. J., Mace, B. R. and Kovacic, I. (2010), 'Potential benefits of a non-linear stiffness in an energy harvesting device', *Nonlinear Dynamics* **59**(4), 545–558. 72, 110, 134

Rao, S. S. (2011), *Mechanical Vibrations*, 5th edn, Prentice Hall. 155

Rodgers, B., Goyal, S., Kelly, G. and Sheehy, M. (2009), 'The dynamics of multiple pair-wise collisions in a chain for designing optimal shock amplifiers', *Shock and Vibration* **16**(1), 99–116. 19, 37, 40, 101, 104

Roundy, S. (2005), 'On the Effectiveness of Vibration-based Energy Harvesting', *Journal of Intelligent Material Systems and Structures* **16**(10), 809–823. 4, 5

Roundy, S. and Wright, P. K. (2004), 'A piezoelectric vibration based generator for wireless electronics', *Smart Materials and Structures* **13**(5), 1131–1142. 5

Roundy, S., Wright, P. K. and Rabaey, J. (2003), 'A study of low level vibrations as a power source for wireless sensor nodes', *Computer Communications* **26**(11), 1131–1144. 5

Saha, C. R., O'Donnell, T., Wang, N. and McCloskey, P. (2008), 'Electromagnetic generator for harvesting energy from human motion', *Sensors and Actuators A: Physical* **147**(1), 248–253. 21, 122, 125, 126

Sari, I., Balkan, T. and Kulah, H. (2008), 'An electromagnetic micro power generator for wideband environmental vibrations', *Sensors and Actuators, A: Physical* **145-146**(1-2), 405–413. 11

Sasaki, K., Osaki, Y., Okazaki, J., Hosaka, H. and Itao, K. (2005), 'Vibration-based automatic power-generation system', *Microsystem Technologies* **11**(8-10), 965–969. 21

Sebald, G., Kuwano, H., Guyomar, D. and Ducharne, B. (2011), 'Simulation of a Duffing oscillator for broadband piezoelectric energy harvesting', *Smart Materials and Structures* **20**(7), 10. 15

Shahosseini, I. and Najafi, K. (2015), Cylindrical Halbach magnet array for electromagnetic vibration energy hrvesters, *in* 'The 28th IEEE International Conference on Micro Electro Mechanical Systems', Estoril, pp. 1051–1054. 122, 125, 126

Shahosseini, I., Peterson, R. L., Aktakka, E. E. and Najafi, K. (2014), Electromagnetic Generator Optimization for Non- Resonant Energy Harvester, *in* 'SENSORS, 2014 IEEE', p. 4. 126

Shahruz, S. M. (2006), 'Design of mechanical band-pass filters for energy scavenging', *Journal of Sound and Vibration* **292**(3-5), 987–998. 11

Shaikh, F. K. and Zeadally, S. (2016), 'Energy harvesting in wireless sensor networks: A comprehensive review', *Renewable and Sustainable Energy Reviews* **55**, 1041–1054. 1, 2

Shaw, S. W. and Holmes, P. J. (1983), 'A periodically forced piecewise linear oscillator.pdf', *Journal of Sound and Vibration* **90**(1), 129–155. 56

Sneller, A. J., Cette, P. and Mann, B. P. (2011), Experimental investigation of a post-buckled piezoelectric beam with an attached central mass used to harvest energy, *in* 'Proceedings of the Institution of Mechanical Engineers, Part I: Journal of Systems and Control Engineering', Vol. 225, pp. 497–509. 5, 15

Soliman, M. S. M., Abdel-Rahman, E. M., El-Saadany, E. F. and Mansour, R. R. (2008), 'A wideband vibration-based energy harvester', *Journal of Micromechanics and Microengineering* **18**, 11. 18, 21

Soliman, M. S. M., Abdel-rahman, E. M., El-saadany, E. F., Member, S. and Mansour, R. R. (2009), 'A Design Procedure for Wideband Micropower Generators', *Journal of Microelectromechanical Systems* **18**(6), 1288–1299. 18, 56

Spreeman, D. and Manoli, Y. (2012), *Electromagnetic Vibration Energy Harvesting Devices: Architectures, Design, Modeling and Optimization*, Springer. 122, 125, 126

Spreemann, D., Folkmer, B., Manoli, Y. and Technology, I. (2008), Comparative study of electromagnetic coupling architectures for vibration energy harvesting devices, *in* 'Proceedings of PowerMEMS 2008+ microEMS2008,', pp. 257–260. 31

Spreemann, D., Manoli, Y., Folkmer, B. and Mintenbeck, D. (2006), 'Non-resonant vibration conversion', *Journal of Micromechanics and Microengineering* **16**(9), 169–173. 21

Stanton, S. C., McGehee, C. C. and Mann, B. P. (2009), 'Reversible hysteresis for broadband magnetopiezoelastic energy harvesting', *Applied Physics Letters* **95**(17), 2013–2016. 15

Stanton, S. C., McGehee, C. C. and Mann, B. P. (2010), 'Nonlinear dynamics for broadband energy harvesting: Investigation of a bistable piezoelectric inertial generator', *Physica D: Nonlinear Phenomena* **239**(10), 640–653. 5, 16

Stephen, N. G. (2006), 'On energy harvesting from ambient vibration', *Journal of Sound and Vibration* **293**(1-2), 409–425. 29, 152

Tang, L., Yang, Y. and Soh, C. K. (2010), 'Toward Broadband Vibration-based Energy Harvesting', *Journal of Intelligent Material Systems and Structures* **21**(18), 1867–1897. 132

Tang, L., Yang, Y. and Soh, C.-K. (2012), 'Improving functionality of vibration energy harvesters using magnets', *Journal of Intelligent Material Systems and Structures* **23**(13), 1433–1449. 12

Tang, X., Lin, T. and Zuo, L. (2014), 'Design and optimization of a tubular linear electromagnetic vibration energy harvester', *IEEE/ASME Transactions on Mechatronics* **19**(2), 615–622. 126

Thorsten, P. and Brilliantov, N. V. (2001), 'Extremal collision sequences of particles on a line: Optimal transmission of kinetic energy', *Physical Review E* **63**(3), 10. 39

Tichý, J., Erhart, J., Kittinger, E. and Pívratská, J. (2010), *Fundamentals of piezoelectric sensorics: Mechanical, dielectric, and thermodynamical properties of piezoelectric materials*. 5

Torah, R. (2007), Energy aware wireless microsystem powered by vibration energy harvesting, *in* 'PowerMEMS', Freiburg, pp. 323–326. 8

Tvedt, L. G. W., Nguyen, D. S. and Halvorsen, E. (2010), 'Nonlinear Behavior of an Electrostatic Energy Harvester Under Wide- and Narrowband Excitation', *Journal of Microelectromechanical Systems* **19**(2), 305–316. 6

von Büren, T. and Tröster, G. (2007), 'Design and optimization of a linear vibration-driven electromagnetic micro-power generator', *Sensors and Actuators A: Physical* **135**(2), 765–775. 122, 126

Wang, P., Tanaka, K., Sugiyama, S., Dai, X., Zhao, X. and Liu, J. (2009), 'A micro electromagnetic low level vibration energy harvester based on MEMS technology', *Microsystem Technologies* **15**(6), 941–951. 4

Westerweel, J. (1997), 'Fundamentals of digital particle image velocimetry', *Measurement Science and Technology* **8**(12), 1379–1392. 46

Wheeler, H. A. (1928), 'Simple inductance formulas for radio coils', *Proceedings of the Institute of Radio Engineers* **16**(10), 1398–1400. 35

Williams, C. B. and Yates, R. B. (1996), 'Analysis of a micro-electric generator for microsystems', *Sensors and Actuators A* **52**, 8–11. 7, 26

Williams, C., Shearwood, C., Harradine, M., Mellor, P., Birch, T. and Yates, R. (2001), 'Development of an electromagnetic micro-generator', *IEE Proceedings - Circuits, Devices and Systems* **148**(6), 337. 7

Williams, C. and Yates, R. (1995), Analysis Of A Micro-electric Generator For Microsystems, *in* 'Proceedings of the International Solid-State Sensors and Actuators Conference', Vol. 1, pp. 8–11. 6, 7

Wu, H., Tang, L., Yang, Y. and Soh, C. K. (2012), 'A novel two-degrees-of-freedom piezoelectric energy harvester', *Journal of Intelligent Material Systems and Structures* **24**(3), 357–368. 12

Wu, M., Ou, Y., Mao, H., Li, Z., Liu, R., Ming, A. and Ou, W. (2015), 'Multi-resonant wideband energy harvester based on a folded asymmetric M-shaped cantilever', *AIP Advances* **5**, 7. 12

Wu, W.-J., Chen, Y.-Y., Lee, B.-S., He, J.-J. and Peng, Y.-T. (2006), Tunable resonant frequency power harvesting, *in* 'SPIE Proceedings', Vol. 6169, San Diego, p. 8. 10

Wu, Y., Badel, A., Formosa, F., Liu, W. and Agbossou, A. (2014), 'Nonlinear vibration energy harvesting device integrating mechanical stoppers used as synchronous mechanical switches', *Journal of Intelligent Material Systems and Structures* **25**(14), 1658–1663. 56, 73

Xing, X., Lou, J., Yang, G. M., Obi, O., Driscoll, C. and Sun, N. X. (2009), 'Wideband vibration energy harvester with high permeability magnetic material', *Applied Physics Letters* **95**(13), 3. 21

Xue, H., Hu, Y. and Wang, Q. M. (2008), 'Broadband piezoelectric energy harvesting devices using multiple bimorphs with different operating frequencies', *IEEE Transactions on Ultrasonics, Ferroelectrics, and Frequency Control* **55**(9), 2104–2108. 11

Yamamoto, B. E. and Trimble, A. Z. (2016), 'An experimentally validated analytical model for the coupled electromechanical dynamics of linear vibration energy harvesting systems', *Journal of Intelligent Material Systems and Structures* pp. 1–20. 31

Yang, Z. and Yang, J. (2008), 'Connected Vibrating Piezoelectric Bimorph Beams as a Wide-band Piezoelectric Power Harvester', *Journal of Intelligent Material Systems and Structures* **20**(5), 569–574. 5

Ylli, K., Hoffmann, D., Willmann, A., Becker, P., Folkmer, B. and Manoli, Y. (2015), 'Energy harvesting from human motion: exploiting swing and shock excitations', *Smart Materials and Structures* **24**(2), 12. 126

Yuen, S., Lee, J., Li, W. and Leong, P. (2007), 'An AA-Sized Vibration-Based Microgenerator for Wireless Sensors', *IEEE Pervasive Computing* **6**(1), 64–72. 21

Zhu, D., Beeby, S. P., Tudor, M. J. and Harris, N. R. (2011), 'A credit card sized self powered smart sensor node', *Sensors and Actuators A: Physical* **169**(2), 317–325. 6

Zhu, D., Beeby, S., Tudor, J. and Harris, N. (2012), 'Vibration energy harvesting using the Halbach array', *Smart Materials and Structures* **21**(7), 075020. 21

Zorlu, Ö., Topal, E. T. and Külah, H. (2011), 'A Vibration-Based Electromagnetic Energy Harvester Using Mechanical Frequency Up-Conversion Method', *IEEE Sensors Journal* **11**(2), 481–488. 21

Zuo, L., Scully, B., Shestani, J. and Zhou, Y. (2010), 'Design and characterization of an electromagnetic energy harvester for vehicle suspensions', *Smart Materials and Structures* **19**(4), 10. 126

Appendix A: Publications

Journal papers

1. O'Donoghue, D., Frizzell, R., Kelly, G., Nolan, K., and Punch, J. (2016). The influence of mass configurations on velocity amplified vibrational energy harvesters. Smart Materials and Structures, 25(5), 13.

2. Frizzell, R., Kelly, G., Cottone, F., Boco, E., Nico, V., O'Donoghue, D., and Punch, J. (2016). Experimental characterisation of dual-mass vibration energy harvesters employing velocity amplification. Journal of Intelligent Material Systems and Structures, 17.

Conference papers

1. O'Donoghue, D., Nico, V., Frizzell, R., Kelly, G., and Punch, J. (2014). A multiple degree-of-freedom velocity amplified vibrational energy harvester part A: experimental analysis. In Proceedings of the ASME 2014 Conference on Smart Materials, Adaptive Structures and Intelligent Systems (p. 9). Newport.

2. Nico, V., O'Donoghue, D., Frizzell, R., Kelly, G., and Punch, J. (2014). A multiple degree-of-freedom velocity-amplified vibrational energy harvester: Part B: Modelling. In Proceedings of the ASME 2014 Conference on Smart Materials, Adaptive Structures and Intelligent Systems, SMASIS 2014 (p. 10). Newport.

3. O'Donoghue, D., Frizzell, R., and Punch, J. (2015). The influence of mass configuration on bandwidth in velocity amplified vibrational energy harvesters. In Proceedings of the ASME 2015 Conference on Smart Materials, Adaptive Structures and Intelligent Systems (p. 8). Colorado Springs.

4. Boco, E., Nico, V., O'Donoghue, D., Frizzell, R., Kelly, G., and Punch, J. (2015). Optimization of coil parameters for a nonlinear two Degree-of-Freedom (2DOF) velocity-amplified electromagnetic vibrational energy harvester. In Smart Cities and Green ICT Systems (SMARTGREENS), 2015 International Conference on (p. 10). Lisbon.